Global glacier mass change by spatiotemporal analysis of digital elevation models

Romain Hugonnet

Université Fédérale
Toulouse Midi-Pyrénées

ETH zürich

THÈSE

En vue de l'obtention du

DOCTORAT DE L'UNIVERSITÉ DE TOULOUSE

Délivrée par : **l'Université Toulouse 3 Paul Sabatier (UT3 Paul Sabatier)**
Codirection internationale ETH Zürich

Présentée et soutenue le **19 mai 2022** par :

Romain Hugonnet

Changement de masse des glaciers à l'échelle mondiale par analyse spatiotemporelle de modèles numériques de terrain

Global glacier mass change by spatiotemporal analysis of digital elevation models

JURY

Irena Hajnsek	Professeure, DLR & ETH Zürich	Rapportrice
Jonathan Bamber	Professeur, Université de Bristol	Rapporteur
Juan I. López-Moreno	Directeur de recherche, IPE-CSIC	Examinateur
Anny Cazenave	Chercheuse émérite, CNES	Présidente du jury
Jean-Marc Delvit	Ingénieur CNES	Invité
Etienne Berthier	Directeur de recherche, CNRS	Directeur de thèse
Daniel Farinotti	Professeur, ETH Zürich	Co-directeur de thèse

École doctorale et spécialité :
SDU2E : Océan, Atmosphère, Climat
Unité de recherche :
LEGOS (UMR 5566)
Directeurs de thèse :
Etienne Berthier et Daniel Farinotti
Rapporteurs :
Irena Hajnsek et Jonathan Bamber

Résumé —

Les glaciers de la planète rétrécissent rapidement, avec des impacts qui s'étendent de la hausse du niveau de la mer et la modification des risques cryosphériques jusqu'au changement de disponibilité en eau douce. Malgré des avancées significatives durant l'ère satellitaire, l'observation des changements de masse des glaciers est encore entravée par une couverture partielle des estimations de télédétection, et par une faible contrainte sur les erreurs des évaluations associées. Dans cette thèse, nous présentons une estimation mondiale et résolue des changements de masse des glaciers basée sur l'analyse spatio-temporelle de modèles numériques de terrain. Nous développons d'abord des méthodes de statistiques spatio-temporelles pour évaluer l'exactitude et la précision des modèles numériques de terrain, et pour estimer des séries temporelles de l'altitude de surface des glaciers. En particulier, nous introduisons un cadre spatial non stationnaire pour estimer et propager des corrélations spatiales multi-échelles dans les incertitudes d'estimations géospatiales. Nous générons ensuite des modèles numériques de terrain massivement à partir de deux décennies d'archives d'images optiques stéréo couvrant les glaciers du monde entier. À partir de ceux-ci, nous estimons des séries temporelles d'altitude de surface pour tous les glaciers de la Terre à une résolution de 100 m sur la période 2000–2019. En intégrant ces séries temporelles en changements de volume et de masse, nous révélons une accélération significative de la perte de masse des glaciers à l'échelle mondiale, ainsi que des réponses régionalement distinctes qui reflètent des changements décennaux de conditions climatiques. En utilisant une grande quantité de données indépendantes et de haute précision, nous démontrons la validité de notre analyse pour produire des incertitudes fiables et cohérentes à différentes échelles de la structure spatio-temporelle de nos estimations. Nous espérons que nos méthodes favorisent des analyses spatio-temporelles robustes, en particulier pour identifier les sources de biais et d'incertitudes dans les études géospatiales. En outre, nous nous attendons à ce que nos estimations permettent de mieux comprendre les facteurs qui régissent le changement des glaciers et d'étendre nos capacités de prévision de ces changements à toutes échelles. Ces prédictions sont nécessaires à la conception de politiques adaptatives sur l'atténuation des impacts de la cryosphère dans le contexte du changement climatique.

Mots clés : glacier, cryosphère, bilan de masse, statistiques spatiotemporelles, modèle numérique de terrain, mondial, télédétection, analyse d'incertitude, big data.

Abstract —

The world's glaciers are shrinking rapidly, with impacts ranging from global sea-level rise and changes in freshwater availability to the alteration of cryospheric hazards. Despite significant advances during the satellite era, the monitoring of the mass changes of glaciers is still hampered by a fragmented coverage of remote sensing estimations and a poor constraint of the errors in related assessments. In this thesis, we present a globally complete and resolved estimate of glacier mass changes by spatiotemporal analysis of digital elevation models. We first develop methods based on spatiotemporal statistics to assess the accuracy and precision of digital elevation models, and to estimate time series of glacier surface elevation. In particular, we introduce a non-stationary spatial framework to estimate and propagate multi-scale spatial correlations in uncertainties of geospatial estimates. We then massively generate digital elevation models from two decades of stereo optical archives covering glaciers worldwide. From those, we estimate time series of surface elevation for all of Earth's glaciers at a resolution of 100 m during 2000–2019. Integrating these time series into volume and mass changes, we identify a significant acceleration of global glacier mass loss, as well as regionally-contrasted responses that mirror decadal changes in climatic conditions. Using a large amount of independent, high-precision data, we demonstrate the validity of our analysis to yield reliable and consistent uncertainties at different scales of the spatiotemporal structure of our estimates. We expect our methods to foster robust spatiotemporal analyses, in particular to identify sources of biases and uncertainties in geospatial assessments. Furthermore, we anticipate our estimates to advance the understanding of the drivers that govern glacier change, and to extend our capabilities of predicting these changes at all scales. Such predictions are critically needed to design adaptive policies on the mitigation of cryospheric impacts in the context of climate change.

Keywords: glacier, cryosphere, mass balance, spatiotemporal statistics, digital elevation model, global, remote sensing, uncertainty analysis, big data.

Acknowledgments

Look deep into nature, and then you will understand everything better.
—*Albert Einstein*

A few introductory words

I was looking at the wonders of the night sky from the Manú National Park, Madre de Dios, at the end of an intense experience with researchers in the Peruvian side of the primary Amazon rainforest, when I realized that I finally knew, after being somewhat lost since young, what I wanted to devote my life's work to: the study of the universe and environment.

What I did not know then, immersed in that tropical warmth, was that chance and opportunity would eventually launch me toward studying the coldest regions on Earth. For this unexpected development, I am glad, as I was one who always loved venturing far in the backcountry, to the mountains. But also because I could never suffer the heat anyway!

I undertook this thesis with a true fascination in the mathematics to better measure and describe our physical world. As time passed, I became increasingly motivated by the impact on water policies and its potential influence on the daily lives of millions of people in our urgent climate crisis. This thesis is but a drop in an ocean of science, but I still hope that it will, somewhere down that line, somehow, contribute to helping those in need.

Three and half years of experiences, and more

First and foremost, I would like to thank Etienne for being such an incredible supervisor. For believing in me, and supporting me even when I was straying off the initial path. It is quite unbelievable to look back and realize how much I have learned during this adventure thanks to you, both scientifically and humanly. I see the big family of past students you have created, still growing throughout the years, and I simply think: "there it is, the testimony of your deep care and kindness". And I am very happy to be part of that family. Merci infiniment, vénérable Berthix !

Secondly, I thank my supervisor Daniel for his continued support since the very beginning, ensuring my well-being and integration at VAW glaciology during Covid times. I have learned a great deal from you, complementarily than in Toulouse: being part of the dynamic of a larger research group, interacting with the wider nonscientific community and, of course, always paying attention to produce clear scientific writing (this sentence is at the limit of the 3-line rule! let's make it a little longer... that breaks it!). Here again, the long family of remaining, coming-back, or "recovered from other institutions" members in the group testifies of your thoughtfulness. Thank you so much for everything you do!

I thank Philippe, with whom I started in Toulouse for my end-of-study internship at the French Space Agency, which constituted my first steps in remote sensing and glaciology. It was this discovery of the research world, with your encouragement and interest, that helped me realize that everyday work can become a passion. This spark caught into flame during my stay in Prince George with Brian (probably because of one of your crazy hot homegrown peppers—I'm never trying those again!). Four intense months of science, and much more. Thank you infinitely for supporting me, in so many ways, throughout the thesis! I also thank all the people who inspired me to pursue in science, in particular my maths sup teacher Vincent Bayle and my Delphi supervisor Matthew Fairbairn.

I thank my close co-authors. Bob for the coding (or English wording) sessions, never losing his sense of humor. The future is indeed now. I thank the past students for welcoming me into the Berthix family. Ines for her natural kindness and honesty, and for guiding me on my first-ever ski tour! Fanny, always finding a great laugh, yet also straightforwardly sharing her thoughts on how to best move forward (or on how to argue a "taillage de short"!). César for being always funny, easygoing, and warming the bed at conferences. I thank Maxence and Zhouyi for working by my side during their thesis, and Will, Georg and David for the trust and opportunity to work on their great projects.

I thank the Cryosphere team of the University of Northern British Columbia for their warm welcome! Roger for the great squash games, Ben and Joe for the lunch-time runs in the forest, Kriti and Christina for the visiting trips (Ancien Forest!). I thank Susanne, Martin, and Liam for welcoming me into their family. Our Mount Robson long-distance trail project marked the beginning of a running passion (and was good training for cross-crountry, I hope)! I thank Shayne for helping me discover British Columbia, and sharing these memorable adventures across the European Alps, including our first foot on a glacier.

I thank the LEGOS doctoral students in Toulouse for two great years of shared soirées, weekends, and holidays! Pierre (*see picture above, venturing in the Vanoise*), you are the one who pushed us to do so many things (even if you won't acknowledge it). After-work climbing, holidays in the mountain... Thank you for everything, and don't ever change! Manon and Flo, for hosting us almost weekly and feeding us with a very diverse diet of pizza and croziflette. Le fromage c'est la vie ! While playing truly unchallenging board games, bien évidemment. And also Lisa (hmmm... no, a glacier is not exactly a mountain of ice), Gabriela (with Genesis and Guillermo, of course), Adé and Nolwenn (co-bureau préférées !). Marion for the confabulation tea breaks. And Audrey and Lise, les anciennes (yes... we are the old ones now!).

I thank the VAW doctoral students and colleagues in Zürich for a year and a half of (despite-Covid) great fun! Chris, we made VAW into our (sports) quarters—the French way of following pandemic rules. Definitely brightened that time. Sure, sure 36–27... but brace yourself, man, I'll be back in the game soon! Amaury and Melissa, for welcoming me warmly in Switzerland, hosting and hiking! Jane, Dominik, Manuela for the great ski tours (man did those Walden poles travel back and forth from France). Matt aka The King, for always reminding us of humility in tennis. Johannes, Loris, Michaela for their everyday cheerfulness. Lea, for sharing a flat (beware, no salt!) and taking me as apprentice sewer. Matthias, for his continuous support, and for taking me to my first winter and summer field trips!

I thank my long-time friends. Lucas, c'est dimanche: cuissots ! Who would have thought, nearly 20 years ago, that we'd both end up doctors? Bertrand, for always being there. I didn't get to say hi on Mumble so often... we'll need to speedrun those new FFs soon! Manu, for the company and discussions in lonely times... just one more game? Hicham and Julie, for staying enthusiastic even in hard times, and always feeding me! Morgan, Pierre and Adrien: without consult, we all ended up doing a doctorate, did that stem from our shared taste of adventure? Delphine, Greg, Flora, Marie, Aude, Laetita, Thomas, Pauline, for the reunions, the holidays, and perpetual encouragement for me to find something that I like.

Finally, I thank my family. My parents for hosting me (and bearing with me) "temporarily" in Toulouse, between travels, rare jungle diseases, pandemic and sports injuries. With the current perspective of moving to another continent, I am happy to have been able to spend more time together than anticipated. My sister, Marie, for her never-ending sarcasm (I know you're laughing at my jokes... internally) and her constructive aesthetical analysis of my "science artwork". Annegret, for sharing a bit of life together, and continuing. You made these years in Switzerland indescribably brighter. And my grandparents for supporting me in all my endeavors, even when those might be hard to grasp.

I love you all.

Acronyms

AIS	Antarctic Ice Sheet
ASTER	Advanced Spaceborne Thermal Emission and Reflection Radiometer
ASP	Ames Stereo Pipeline
DEM	Digital Elevation Model
GDAL	Geospatial Data Abstraction Library
GDEM	ASTER Global Digital Elevation Model
GIS	Greenland Ice Sheet
GlaThiDa	Glacier Thickness Database
GLIMS	Global Land Ice Measurements from Space
GLOF	Glacier Lake Outburst Flood
GRACE	Gravity Recovery and Climate Experiment
ICESat	Ice, Cloud and land Elevation Satellite
IPCC	Intergovernmental Panel on Climate Change
KH-9	KeyHole-9 (aka Hexagon)
NetCDF	Network Common Data Form
NMAD	Normalized Median Absolute Deviation
OSGeo	Open Source Geospatial Foundation
RCP	Representative Concentration Pathway
REMA	Reference Elevation Model of Antarctica
RGI	Randolph Glacier Inventory
SAR	Synthetic-Aperture Radar
SETSM	Surface Extraction from TIN based Search-space Minimization
SILCAST	Sensor Information Laboratory Corporation ASTER
SPOT	Satellite Pour l'Observation de la Terre
SRTM	Shuttle Radar Topography Mission
SSP	Shared Socioeconomic Pathway
TIN	Triangulated Irregular Network
TWS	Terrestrial Water Storage

Contents

List of Figures

List of Tables

Introduction générale

Que sont les glaciers et pourquoi les étudier ?

Les glaciers sont les masses de glace terrestres ayant un écoulement, et distinctes des calottes glaciaires du Groenland et de l'Antarctique. Ils sont un élément essentiel de la cryosphère qui, avec l'hydrosphère, l'atmosphère, la biosphère et la lithosphère, constituent les cinq principales composantes du système climatique. En raison de leur sensibilité aux changements climatiques, les glaciers constituent à la fois un moyen d'étudier le climat passé et présent à partir d'observations, et également une variable qui nécessite d'être prédite pour atténuer l'impact de leurs changements futurs au sein du système climatique.

Les glaciers sont en effet associés à un large éventail d'impacts imbriqués avec les autres composantes du système climatique. Dans le cadre du cycle global de l'eau, les glaciers fournissent des ressources saisonnières en eau douce aux systèmes en aval qui, lorsqu'elles sont déséquilibrées, sont soit ajoutés à l'hydrosphère, soit retenus par celle-ci, ce qui entraîne des changements de niveaux des lacs et des mers. Le ruissellement de l'eau de fonte régule également la composition relative de l'eau douce et salée dont dépendent les populations humaines et les écosystèmes, et affecte ainsi la diversité dans la biosphère. La réflectance du rayonnement solaire sur les surfaces glaciaires affecte l'équilibre énergétique avec la surface terrestre et l'atmosphère. De plus, l'interaction entre les glaciers et la lithosphère est caractérisée par un large éventail de risques naturels tels que les vidanges de lacs glaciaires ou les glissements de terrain.

Pour évaluer et prévoir l'éventail de ces impacts, les glaciers doivent être surveillés. Les mesures de terrain fournissent une base d'observation s'étendant sur plus d'un siècle dans certaines régions, mais qui demeure éparse. Le début de l'ère satellitaire dans les années 1990 a donné naissance à des moyens révolutionnaires d'observation de la Terre à l'échelle planétaire. À la fin des années 2010, la plupart des caractéristiques des glaciers, telles que leur emplacement et leur superficie, l'épaisseur de glace ou la couverture de débris, étaient estimés mondialement à l'échelle de glaciers individuels, soit directement par des observations, soit par leur intégration dans des modèles. Cependant, les évaluations de changements de volume et de masse des glaciers sont encore entravées par une couverture incomplète des observations et par de grandes incertitudes. Pour y remédier, une voie prometteuse est celle des mesures d'altitude de la surface de la Terre qui ne cessent de croître en disponibilité et en résolution, notamment à travers des modèles numériques de terrain.

Que sont les modèles numériques de terrain et pourquoi les utiliser ?

Les modèles numériques de terrain sont des représentations numériques de l'altitude de surface, en soit des cartes digitales de topographie. Leur propriété unique de décrire l'altitude de manière contiguë, qui s'exempte généralement de données manquantes et est cohérente dans l'espace, les a rapidement rendus omniprésents que ce soit dans les domaines scientifiques ou commerciaux. Ainsi, les modèles numériques de terrain sont de plus en plus utilisés dans un nombre croissant de domaines des sciences du système terrestre, notamment en géomorphologie, hydrologie, volcanologie, foresterie et glaciologie.

En glaciologie, la description contiguë de l'altitude de surface d'un glacier, mesurée à une certaine date, est essentielle pour l'estimation de l'épaisseur de glace ou pour la conception de modèles d'écoulement et de bilan de masse permettant de prévoir l'évolution des glaciers. Afin d'estimer les changements de volume et de masse des glaciers, il est nécessaire de disposer de plusieurs modèles numériques de terrain générés à partir d'acquisitions de différentes dates. Les changements d'altitude des glaciers sont mesurés entre les deux dates, et peuvent être intégrés en un changement de volume, ensuite converti en changement de masse équivalent en eau selon des hypothèses de densité.

L'utilisation de modèles numériques de terrain s'accompagne toutefois d'un grand nombre de défis. Ceux-ci sont générés à partir d'une gamme variée de capteurs aériens ou spatiaux, qui possèdent un niveau différent de couverture, d'exactitude et de précision. Bien qu'il existe des archives disponibles en libre accès pour générer des modèles numériques de terrain à l'échelle planétaire, leur utilisation est largement entravée par des bruits instrumentaux ou par des biais spécifiques à l'observation de la neige et de la glace. L'influence de ces erreurs et leur structure spatio-temporelle complexe nécessitent davantage de clarifications pour pouvoir fournir des estimations fiables.

Objectif

Dans cette thèse, notre objectif est de fournir une évaluation globale et cohérente du changement de masse des glaciers récent en se basant sur des modèles numériques de terrain disponible librement et à grande échelle, ainsi que sur des statistiques spatio-temporelles robustes. Pour cela, notre plan se divise en deux étapes : (i) caractériser la structure d'erreur des modèles numériques de terrain, proposer des méthodes robustes de propagation d'incertitude et évaluer l'impact sur les hypothèses d'études précédentes ; et (ii) cartographier à répétition l'altitude de surface de tous les glaciers de la Terre en générant et en corrigeant les biais de modèles numériques de terrain à partir d'archives inexploitées d'images stéréo, pour estimer l'altitude de surface, le volume et les changements de masse depuis l'échelle du pixel jusqu'à l'échelle du glacier, de la région et du monde entier, et d'analyser mondialement ces estimations avec des données de réanalyse météorologique.

Cette thèse est organisée en trois chapitres. Le **Chapitre 1** présente une introduction sur les défis associés aux glaciers et à leur surveillance, aux modèles numériques de terrain et à leur utilisation, ainsi qu'un aperçu sur les statistiques spatio-temporelles et obstacles à leur accessibilité. Le **Chapitre 2** est basé sur un article accepté sur l'analyse d'incertitude des modèles numériques de terrain, et présente des articles en co-auteur sur la propagation d'incertitude d'autres problèmes géospatiaux, y compris les épaisseurs et les vitesses de glace, et les méthodes d'interpolation pour le changement d'altitude des glaciers. Le **Chapitre 3** est basé sur deux articles publiés sur des estimations régionales et globales des changements de masse des glaciers. Il comprend des articles en co-auteur sur les estimations régionales des changements de masse des glaciers, la modélisation globale des glaciers, les changements de l'eau terrestre et les risques naturels. Dans **Conclusions et perspectives**, nous concluons en résumant les principaux résultats de ce travail et les éventuelles directions de future recherche.

General introduction

What are glaciers and why study them?

Glaciers are the flowing land ice masses distinct from the ice sheets of Greenland and Antarctica. They are a core constituent of the cryosphere which, with the hydrosphere, atmosphere, biosphere and land surface, make up the five major components of the climate system. Due to their sensitivity to changes in climatic conditions, glaciers constitute both a means to study past and present climate from observational knowledge, and a variable requiring prediction to mitigate the impact of their future changes within the climate system.

Glaciers are indeed associated with a wide range of impacts intertwined with other components of the climate system. As part of the global water cycle, glaciers provide seasonal freshwater resources to downstream systems which, when imbalanced, are either added to or impounded from the hydrosphere causing changes in lake and sea levels. Meltwater runoff also regulates the relative composition of fresh- and saltwater on which human populations and ecosystems are reliant, and thereby affects diversity in the biosphere. The reflectance of solar radiation from glacierized surfaces affects the energy balance with the land surface and atmosphere. Additionally, the interaction between glaciers and land surface systems is characterized by a wide range of natural hazards such as outburst floods or slope failures.

To assess and predict the range of these impacts, glaciers have to be monitored. Records of field measurements provide an observational baseline that is century-long in some regions, but spatially sparse. The beginning of the satellite era in the 1990s gave rise to revolutionary means of Earth observation at the planetary scale. By the end of the 2010s, most glacier characteristics such as their location and area, ice thickness or debris-cover were estimated at the global scale for individual glaciers, either directly by observations or through their integration into models. Yet, assessments of the changes in volume and mass of glaciers are still impeded by an incomplete observational coverage and large uncertainties. To address this, a promising avenue is that of increasingly available and resolved measurements of Earth's surface elevation and, most specifically, digital elevation models.

What are digital elevation models and why use them?

Digital elevation models are numerical representations of surface elevation, essentially digital maps of topography. Their unique property of providing contiguous elevation, largely gap-free and consistent in space, has rapidly brought about their ubiquity in both scientific and commercial fields. As such, digital elevation models are increasingly used in an expanding range of Earth system sciences fields, including notably geomorphology, hydrology, volcanology, forestry, and glaciology.

In glaciology, the contiguous description of the surface elevation of a glacier measured at a single epoch is critical to the estimation of ice thickness, or to the design of flow and mass balance models to predict glacier evolution. In order to estimate glacier volume and mass changes, multiple digital elevation models generated from acquisitions of different epochs are necessary. Changes in glacier elevation are measured between epochs, which can be integrated into volume changes, and later converted into water-equivalent mass changes using density assumptions.

Using digital elevation models comes with a wide range of challenges, however. They are generated from a diverse range of air- or space-borne sensors that possess a different level of coverage, accuracy, and precision. While several openly available archives exist to generate digital elevation models at the planetary scale, their use is largely hampered by either patterns of instrument noise, or biases specific to the observation of snow and ice. The influence of these errors and their complex spatiotemporal structure require clarification to provide reliable estimations.

Objective

In this thesis, our objective is to provide a global and consistent assessment of recent glacier mass change based on large-scale and openly available digital elevation models and robust spatiotemporal statistics. To this end, our plan is twofold: (i) to characterize the patterns of errors in digital elevation models, to propose robust methods of uncertainty propagation, and to assess its impact on previous assumptions; and (ii) to repeatedly map the surface elevation of Earth's glaciers by generating and bias-correcting digital elevation models from untapped archives of stereo-imagery, to estimate surface elevation, volume and mass changes from pixel-scale to glacier-, regional- and global-scale, and to analyze these estimations globally with meteorological reanalysis data.

This thesis is organized in three chapters. **Chapter 1** presents an introduction on the challenges associated with glaciers and their monitoring, digital elevation models and their usage, as well as background on spatiotemporal statistics and the barriers to its accessibility. **Chapter 2** is based on an accepted article on the uncertainty analysis of digital elevation models, and features co-authored articles on the uncertainty propagation of other geospatial problems including ice thicknesses and velocities, and interpolation methods for glacier elevation change. **Chapter 3** is based on two published articles on regional and global glacier mass change estimates, and features co-authored articles on regional glacier mass change estimations, global glacier modeling, terrestrial water changes, and natural hazards. In **Conclusions and outlook**, we conclude by summarizing the main results of this work and possible future research directions.

Chapter 1

Monitoring Earth's glaciers: an observational challenge rooted in space and time

Contents

1.1 Glaciers in a changing climate

1.1.1 The ice giants that are disappearing

Glaciers are *perennial masses of ice, and possibly firn and snow, originating on the land surface by the recrystallization of snow or other forms of solid precipitation, and showing evidence of past or present flow* (Cogley et al., 2011). Together with the Greenland and Antarctic land ice masses, defined separately as ice sheets owing to their *continental size* (>50,000 km²), they constitute nearly all of the mass of ice bodies on land. Glaciers are formed and evolve under a large set of physical processes which, for mass considerations, can be grouped into accumulation, i.e. gain of water mass such as snowfall, and ablation, i.e. loss of water mass such as surface melt (Fig. 1.1). The balance between accumulation, ablation, and flow of ice regulates the extent and topographical distribution of glaciers on land, making them a visual indicator of climatic conditions and, nowadays, an icon of climate change.

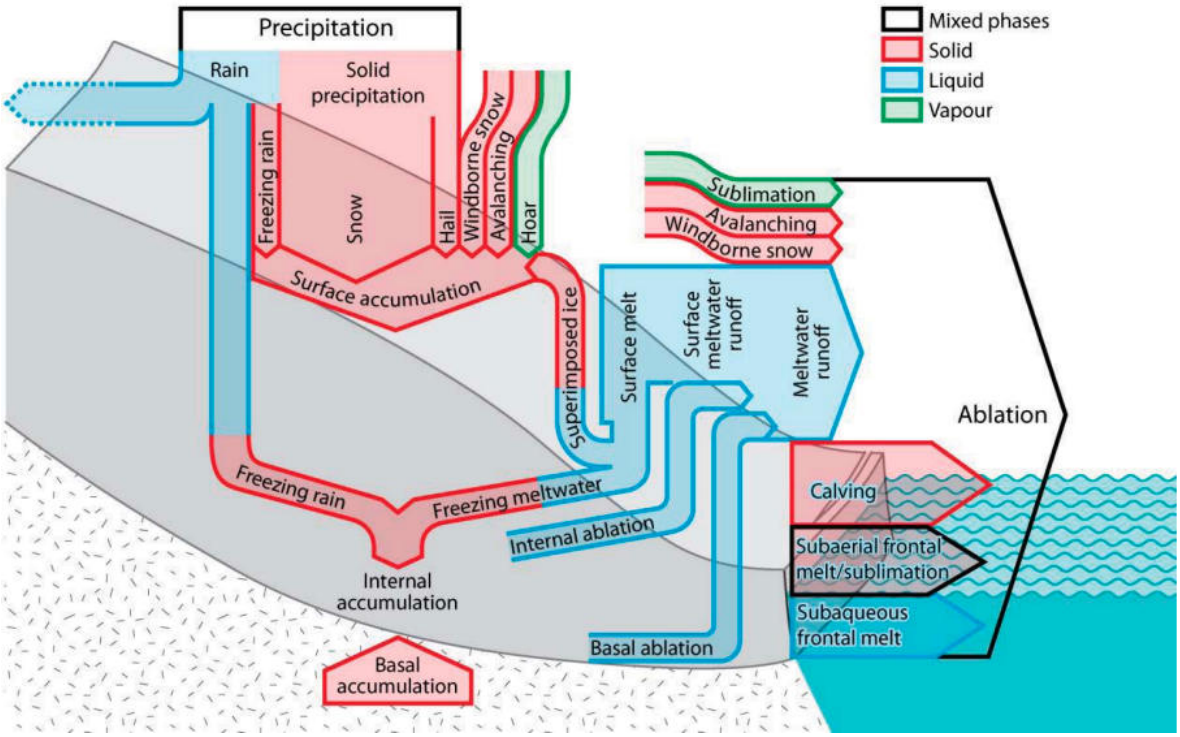

Figure 1.1: Processes of glacier mass balance. From Cogley et al. (2011).

Earth's climate fluctuated across geological times, and with it the extent and volume of glaciers and ice sheets. Quaternary ice ages with a characteristic periodicity of ~100,000 years caused large ice volume fluctuations which amounted to ~100 m of changes in global sea-level (Lambeck et al., 2002; Meyssignac and Cazenave, 2012). Shorter, millenia-scale climatic fluctuations were responsible for changes of smaller magnitude, such as the controversially-named Little Ice Age observed in historical times (Grove, 2019). Since the mid-1950s, glaciers have been retreating globally (Parkes and Marzeion, 2018; Zemp et al., 2019). This mass loss

is largely attributable to climate change (Marzeion et al., 2014) and, without anthropogenic influence, many glacierized regions could even be growing nowadays (Painter et al., 2013; Roe et al., 2021). The continuing changes in our planet's climate (IPCC, 2021) thus call for an understanding of the range of underlying impacts that can arise from changing glaciers.

1.1.2 The impacts of glacier changes

Glaciers are interlinked to many other constituents of the Earth system, in particular within the global water cycle (Fig. 1.2). Glaciers globally hold a mass of ice that, if completely melted, could rise sea levels by about a third of a meter (Farinotti et al., 2019a). While this potential sea-level rise is lower than the ~7 m and ~58 m of the Greenland and Antarctic ice sheets, respectively (Vaughan et al., 2013; Morlighem et al., 2017, 2019), glaciers currently lose mass at faster rates than either of the ice sheets (Bamber et al., 2018; Zemp et al., 2019). They are expected to remain the primary sea-level rise contributor after thermal expansion until the end of the century (Edwards et al., 2021), yet could be overcome by unstable dynamic processes of the ice sheets (Fürst et al., 2016; Garbe et al., 2020) that entail high mass loss uncertainties (WCRP, 2018; Bamber et al., 2019).

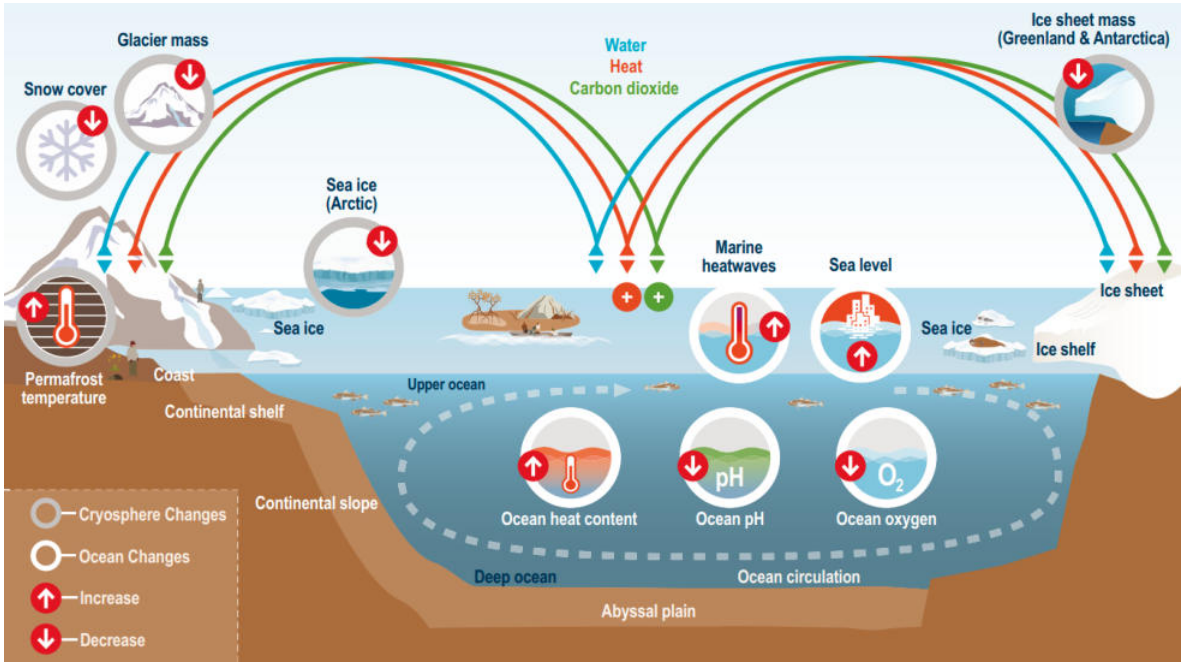

Figure 1.2: Climate change effects on the ocean and cryosphere. From IPCC (2019).

Glaciers are also one of the most climate-sensitive components of the natural water towers of the world (Immerzeel et al., 2020) i.e. the mountainous areas that store water in solid form during the winter and release it as meltwater during the summer. The retreat of glaciers, combined with the decline in seasonal snow, modifies the timing and amount of meltwater release (Kaser et al., 2010), altering downstream runoff that is increasingly relied on by hundreds of millions of people worldwide (Pritchard, 2019; Viviroli et al., 2020). Higher

melting rates temporarily increase runoff, but this short-lived effect will eventually decline with glacier shrinkage. Current predictions anticipate that this *peak water* turning point will be reached this century for all low-latitude, populated glacierized regions, if it has not already passed (Huss and Hock, 2018). These hydrological changes do not only affect the amount of released water, but also its organic composition and carbon cycle (Fell et al., 2021) which, in turn, alters riverine and near-shore ecosystems (Vörösmarty et al., 2010; Milner et al., 2017) with many threats to biodiversity (Jacobsen et al., 2012; Cauvy-Fraunié and Dangles, 2019).

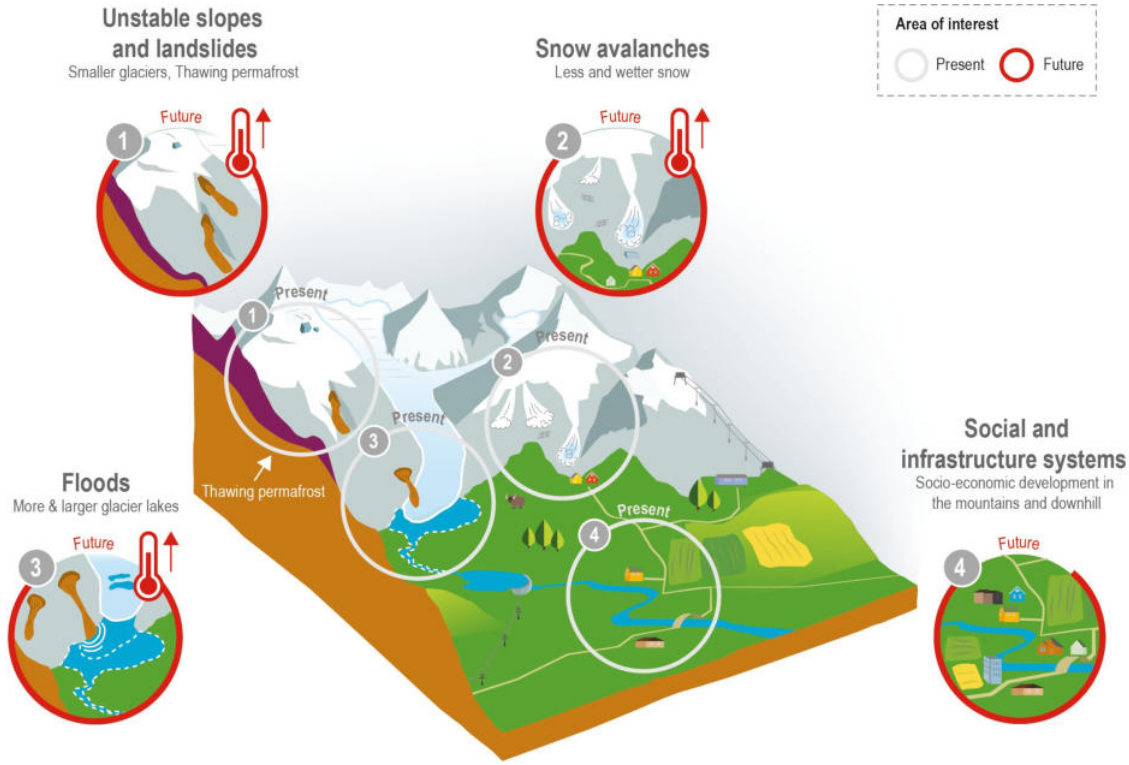

Figure 1.3: Anticipated changes in high mountain hazards under climate change. From IPCC (2019), upper panel only.

Glaciers are additionally associated with a wide range of natural hazards (Fig. 1.3). The sudden release of water stored in ice- or moraine-dammed lakes through outburst floods (Veh et al., 2020; Stuart-Smith et al., 2021) and the collapses or avalanches of rock and ice (Kääb et al., 2018; Shugar et al., 2021) have devastated infrastructures and claimed many victims in populated mountain regions, with thousands of documented events. While it is yet unclear if climate change is exacerbating the frequency and magnitude of glacier lake outburst floods (Veh et al., 2022), the increased mass movements in mountainous areas, such as slope instabilities, have been largely attributed to glacier retreat and a warming environment (Stoffel and Huggel, 2012). Some opportunities also arise from glacier changes, for example the facilitated damming of future ice-free basins for water storage and hydropower production (Farinotti et al., 2019b). Ultimately, to address the identification and mitigation of this wide range of impacts, it is crucial to improve our understanding of glacier processes and therefore to monitor glaciers worldwide.

1.1.3 Observing glaciers in the satellite area

Historically, glaciers were monitored by in-situ measurements, which started as soon as the early 19th century in some regions (Huss et al., 2021). In-situ measurements consist mostly of front positions, snow depths of winter accumulation and ablation at ice stakes locations (WGMS, 2019). The substantial resources required to perform glacier surveys resulted in large differences in observational coverage between regions. Globally, less than a hundred glaciers are surveyed continuously (WGMS, 2019). Consequently, in-situ measurements are delicate to utilize to estimate glacier changes at large scales (Gardner et al., 2013), despite being crucial to study climatic signals over long time scales and to provide a historic baseline of glacier variability (Zemp et al., 2013; Vincent et al., 2017).

With the advent of numerical satellites in the 1980s came a revolution in the means of monitoring the Earth system, with a potential for consistent observations at the continental and planetary scales. Unfortunately, many of those satellite archives remained closed or used only commercially until the 2010s, which limited their scientific use (Kääb, 2008). In 2008, the opening of the Landsat archive created unprecedented potential for studying the Earth surface and, a few years later, largely enabled the first mapping of all glaciers around the globe (Pfeffer et al., 2014; RGI Consortium, 2017) (Fig. 1.4). More than 200,000 glaciers were inventoried, covering ~715,000 km^2 of land surface in the early 2000s, which is about 30% larger than the area of France (RGI Consortium, 2017).

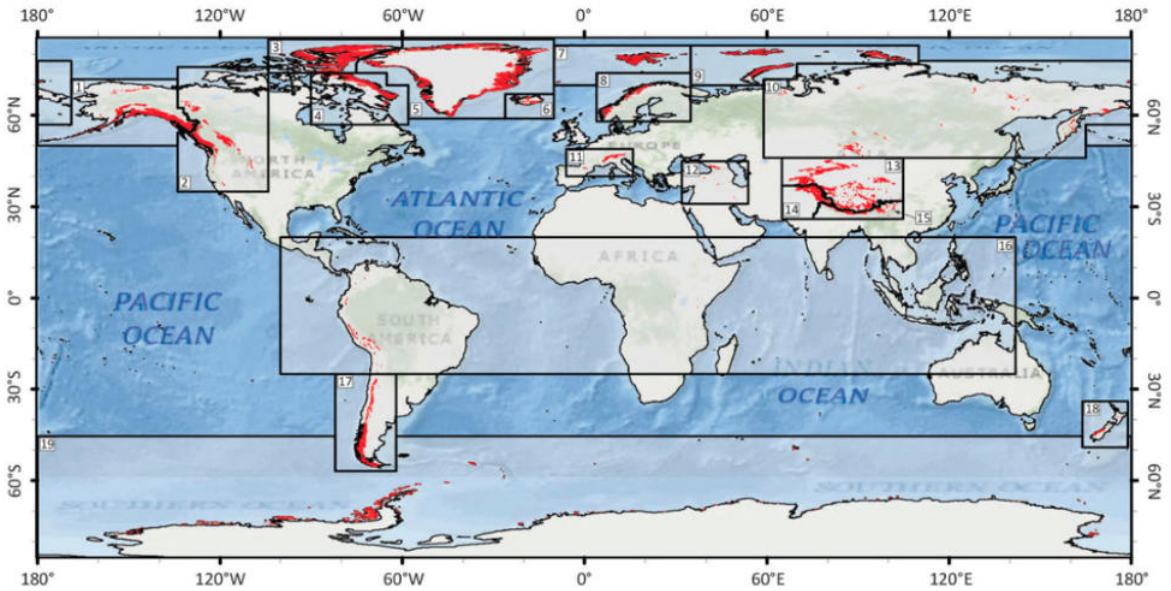

Figure 1.4: A globally complete inventory of the world's glaciers. From Pfeffer et al. (2014).

Satellite sensors are diverse and can be used to observe many variables of interest. For glaciers, surface albedo (Naegeli et al., 2017; Shaw et al., 2021) and ice velocity (Altena et al., 2019; Dehecq et al., 2019) can notably be derived from optical sensors. Glacier elevation and its changes through time can be estimated from radar, stereo optical sensors, or altimetry (Berthier et al., 2010; Kääb et al., 2012; Rankl and Braun, 2016; Leinss and Bernhard,

2021), and the topographical information extracted can be utilized to estimate ice thicknesses (Farinotti et al., 2009). During the 2010s, the increased availability of satellite data coupled to scalable processing methods enabled the estimation of most of these variables at the global scale, including for instance ice velocity (Gardner et al., 2018a, 2019), ice thickness (Huss and Farinotti, 2012; Farinotti et al., 2019a), or debris cover (Scherler et al., 2018; Herreid and Pellicciotti, 2020). However, glacier volume and mass changes are variables that remain only partially measured, owing to difficulties in resolving the changes in Earth's mass or topography over the fragmented expanse of glacierized surfaces.

1.1.4 Constraining recent glacier mass change

Large-scale glacier mass changes have been quantified using two types of instruments: gravimetric sensors that directly detect changes in Earth's mass distribution (Jacob et al., 2012; Gardner et al., 2013); and sensors capable of measuring surface elevation, with repeat acquisitions to derive volume changes (Schiefer et al., 2007; Bauder et al., 2007), which are later converted to mass changes based on density assumptions (Huss, 2013). Each sensor possesses different spatiotemporal coverage, resolution and precision (Table 1.1).

Table 1.1: Coverage, resolution and precision of sensors used for glacier mass balance estimation. Only large-scale sensors are listed. Targeted temporal resolution refers to sensors with only targeted times and locations of acquisitions. Resolution and precision are simplified averages from the literature in gravimetry (Wouters et al., 2019), stereo-photogrammetry (Kääb, 2008; Korona et al., 2009; Berthier et al., 2014; Girod et al., 2017; Perko et al., 2019; Dehecq et al., 2020), radar interferometry (Carabajal and Harding, 2005; Rizzoli et al., 2017; Zink et al., 2021), laser altimetry (Fricker, 2005; Brunt et al., 2019) and radar altimetry (Wang et al., 2015; Morris et al., 2022). In practice, these metrics are influenced by many factors. Coverage of ICESat-1 and ICESat-2 corresponds to the average density of points and photons, respectively, in mid-latitudes (40–60°).

Sensor type	Specific sensor	Spatial coverage	Temporal coverage	Spatial resolution	Temporal resolution	Average precision[1]
Gravimetry	GRACE (F-O)	Global	2002–	~300 km	~Monthly	±1 Gt yr^{-1}
Optical stereo-photogrammetry	ASTER	Global	2000–	~30 m	~Biannual	±10 m
	SPOT5-HRS	Global	2002–2015	30 m	**Targeted**	±5 m
	SPOT6-7	Global	2013–	~2 m	**Targeted**	±1 m
	Pléiades	Global	2011–	~2 m	**Targeted**	±1 m
	WorldView	Global	2012–	~2 m	**Targeted**	±2 m
	Corona, KH-9	Global	1960–1975	~5–30 m	**Targeted**	±5 m
Radar interferometry	SRTM	Low-latitudes	2000	~30 m	-	±10 m
	TanDEM-X	Global	2012–	~12 m	~Annual	±4 m
Laser altimetry	ICESat	~5 pt km^{-2}	2003–2009	60 m footprint	~Biannual	±0.2 m
	ICESat-2	~5,000 pt km^{-2}	2018–	17 m footprint	~Monthly	±0.1 m
Radar altimetry	CryoSat-2	Global	2010–	~200 m swath	~Annual	±0.5 m

[1]Average precision corresponds to a symmetrical 95% confidence interval for a study area at the reported spatial resolution (i.e. 1 pixel or 1 point).

Gravimetric sensors directly measure changes in mass, but their low spatial resolution of ~300 km until fully decorrelated, implies that the signals of different sources are easily entangled. While the uncertainty in signals other than ice mass loss is sufficiently small to provide valuable estimates for the Greenland and Antarctic ice sheets (van den Broeke et al., 2009; Velicogna et al., 2020), it renders estimations unfeasible for individual glaciers. At the scale of glacier regions, only isolated, mainly ice-covered polar areas of the Arctic are measured confidently, while others suffer from large sources of uncertainties associated with the deconvolution of mass changes from hydrology and neighbouring ice sheets (Wouters et al., 2019; Ciracì et al., 2020), in addition to the inherent uncertainties from geocenter motion and glacial isostatic adjusment (Blazquez et al., 2018).

As an alternative to gravimetric measurements, a wide variety of sensors measuring surface elevation have been used (Table 1.1). Laser altimetry precisely measures surface elevation, but with a sampling which is sparse over glaciers, especially at lower latitudes (Kääb et al., 2012; Gardner et al., 2013). Radar interferometry and altimetry provide global-scale, repeat surface elevation measurements that are unaffected by cloud cover (Braun et al., 2019; Jakob et al., 2021), but are hampered by biases from the penetration of radar signals into firn and ice (Berthier et al., 2006; Fischer et al., 2020). These biases of typically 5–15 m, depending on the radar frequency, vary seasonally with the surface conditions and snow density profile of the glaciers, and remain therefore hard to correct. While penetration biases of radar altimetry are generally low, they suffer from a poor coverage in steep and rugged mountainous terrain (Wang et al., 2015). Optical photogrammetry has a temporal coverage highly dependent on cloud cover, and suffers from data gaps in the bright accumulation areas of glaciers that lack the texture necessary in stereo-correlation (McNabb et al., 2019).

In this thesis, we focus on digital elevation models (DEMs), that correspond to the surface elevations generally derived from optical or radar imaging (Table 1.1), and aim to harness their dense spatial sampling and large-scale availability to estimate global glacier mass changes.

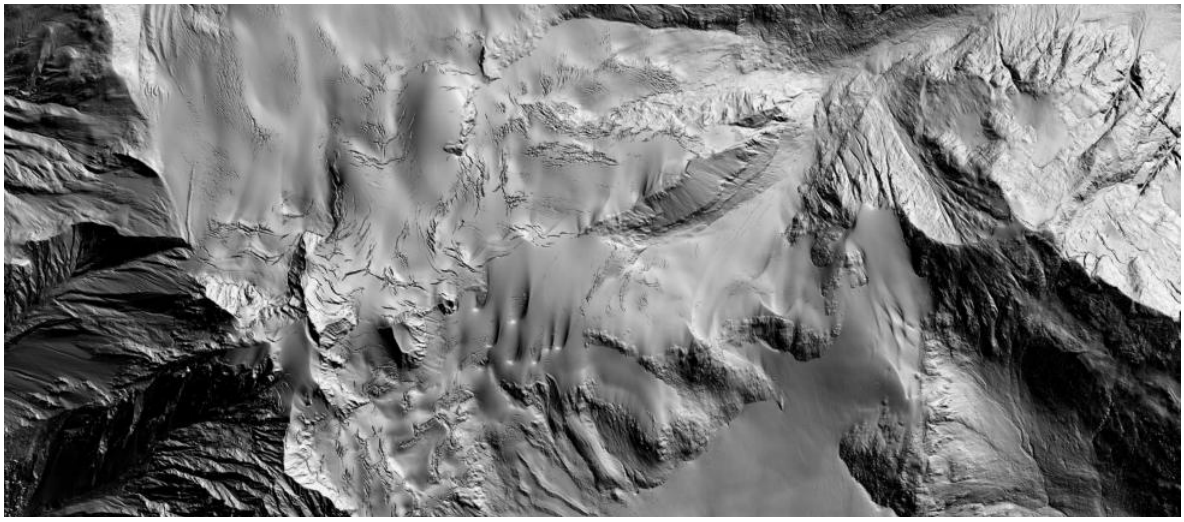

Figure 1.5: Hillshade generated from a DEM. Targeted lidar acquisition at 1 m posting on Sentinel Glacier and surroundings, British Columbia, Canada (Menounos et al., 2019).

1.2 Digital elevation models at the core of Earth Observation

1.2.1 The rise of digital elevation models

Digital elevation models are gridded, numerical representations of surface elevation. Historically, DEMs were derived by interpolation of point measurements or historical maps (Taud et al., 1999; Weng, 2002). Nowadays DEMs are most often generated from radar interferometry (Rosen et al., 2000; Bürgmann et al., 2000), optical stereo-photogrammetry (Walker, 1995; Mikhail et al., 2001) or laser scanning (Baltsavias, 1999; Dubayah and Drake, 2000) of a planetary surface. Several radar and optical sensors board satellites, but laser scanning (i.e. lidar) is mostly utilized in local aerial surveys of very high resolution (e.g., Menounos et al., 2019; Vionnet et al., 2021; Vidaller et al., 2021, Fig. 1.5)).

Since the first mapping of near-global land topography by the Shuttle Radar Topography Mission (SRTM) in February 2000 (Farr et al., 2007), the resolution and coverage of global DEMs has been rapidly increasing (Bhushan et al., 2021) and assessments have largely grown from opportunistic case studies to routine monitoring, particularly for radar interferometry (Biggs and Wright, 2020; Rosen, 2021). Additionally, the declassification of historical archives of aerial imagery and spy satellites is unlocking a goldmine of data to study the planet's topography of the last century (Galiatsatos et al., 2007; Dehecq et al., 2020; Geyman et al., 2022). The number of studies relying on DEMs has been increasing exponentially (Hebeler and Purves, 2009), a trend that matches recent satellite launches (e.g., Fig. 1.6 for synthetic aperture radar (SAR)) that are increasingly aimed at commercial applications.

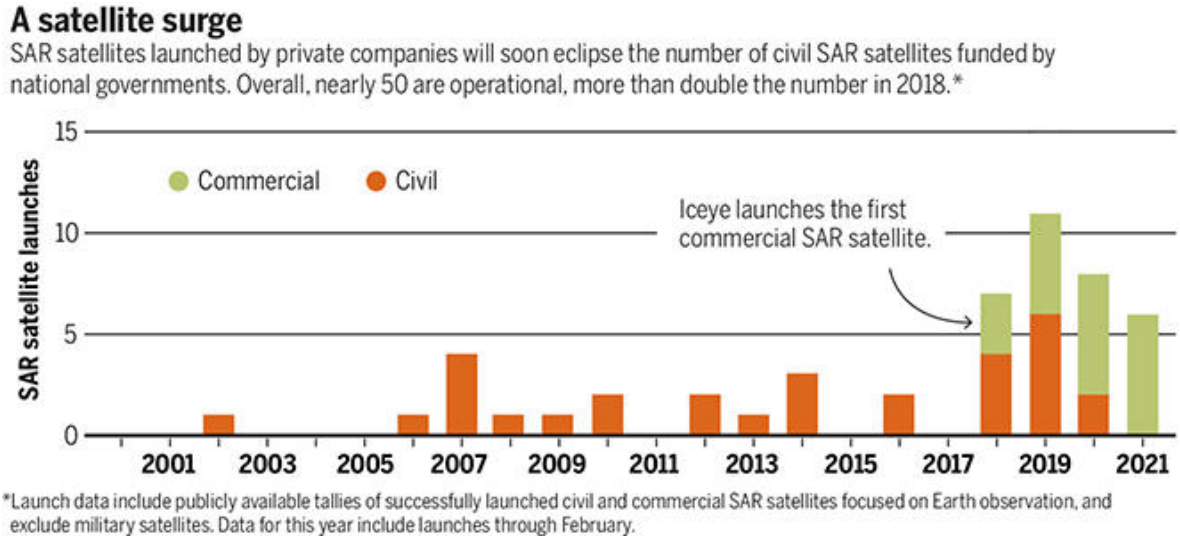

Figure 1.6: A satellite surge. From Rosen (2021), lower panel only.

1.2.2 A multitude of instruments for diverse applications

DEMs have become ubiquitous across a wide and expanding range of fields, notably in Earth system science such as geomorphology, hydrology, glaciology, forestry, seismology and volcanology. The ability of DEMs to represent surface elevation contiguously in space and at large scales, thereby capturing a complete picture of the topography (Fig. 1.7), is essential to many applications such as onshore inundation forecasting (Oksanen and Sarjakoski, 2005; Kulp and Strauss, 2019), hydrological modelling (Oksanen and Sarjakoski, 2005; Hawker et al., 2018) or avalanche risk prediction (Bühler et al., 2013).

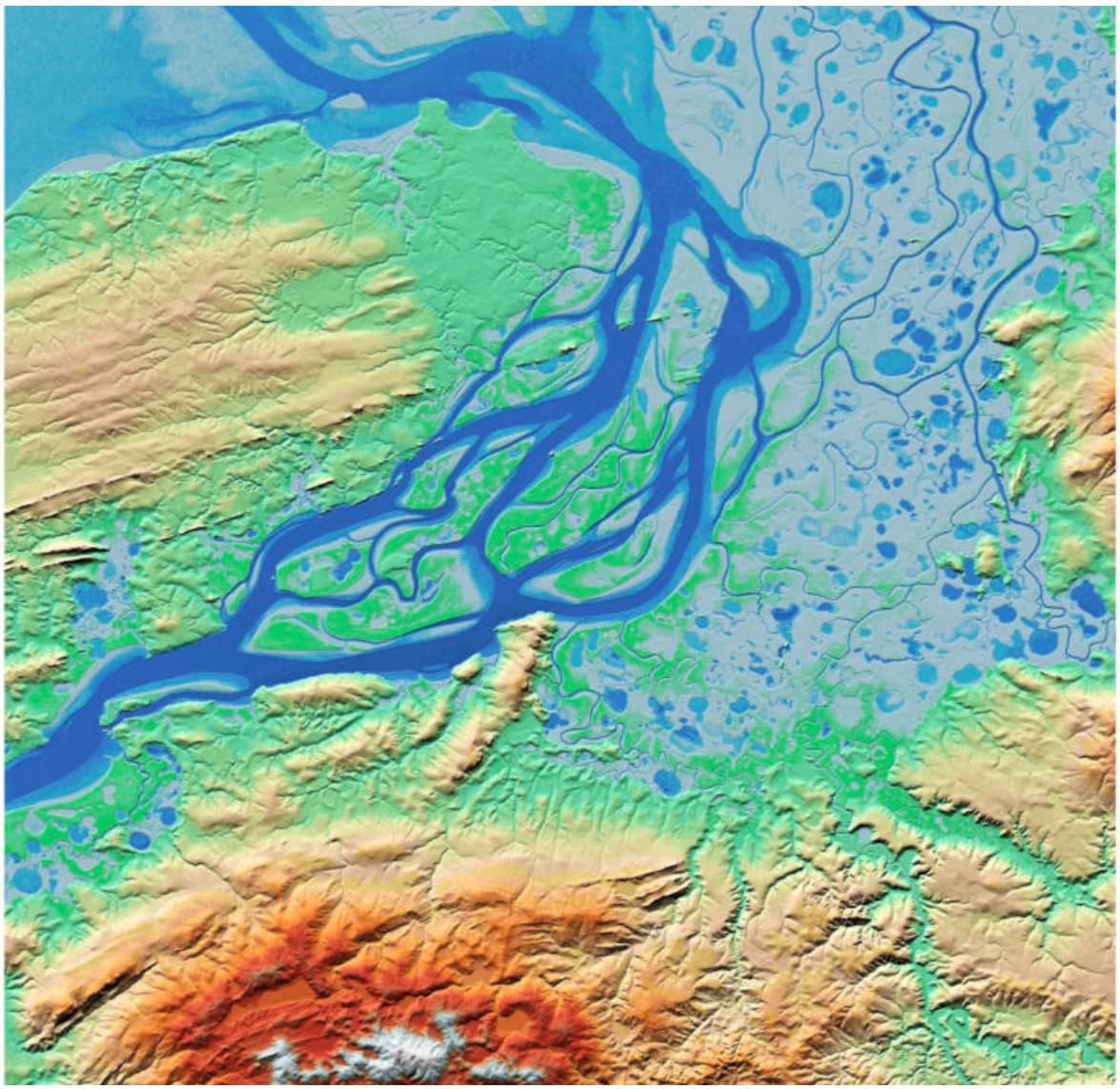

Figure 1.7: Large-scale digital elevation models. From Zink et al. (2021). TanDEM-X DEM covering 73°–74° North, 86°–88° East in Russia. The completely frozen river Pjasina meanders into the Kara Sea. Height varies between 0 m and 280 m.

The focus of certain applications is not only surface elevation, however, but also its changes through time. For this, multiple DEMs acquired at different epochs are required. Unfortunately, DEMs other than the SRTM (Farr et al., 2007) remained largely inaccessible until the mid-2010s. Only the Advanced Spaceborne Thermal Emission and Reflection Radiometer (ASTER) provided repeat, large-scale imagery to produce DEMs until the late 2000s. This imagery remained only accessible commercially (Kääb, 2008), or as a temporal mosaic (Tachikawa et al., 2011). In 2016, the ASTER archive was opened, and followed by other DEM products such as TanDEM-X DEM (Krieger et al., 2007), or WorldView in polar regions through the ArcticDEM (Porter et al., 2018) and Reference Elevation Model of Antarctica (REMA) (Howat et al., 2019) efforts. These openings provided, for the first time, the materials to study changes in elevation at large scales. Yet, for such assessments, DEMs of sufficient quality are required to detect elevation changes within the error of measurements.

1.2.3 The patterns of errors in digital elevation models

DEMs sometimes suffer from poor accuracy directly related to their georeferencing, in particular when derived from spaceborne instruments. Limited constraints over sensor positioning, orientation and processing artefacts can lead to erroneous horizontal referencing (Girod et al., 2017; Guan et al., 2020), vertical shifts (Mukherjee et al., 2013; Kulp and Strauss, 2019) and tilts (Gruber et al., 2012; Dehecq et al., 2016). The misalignment created by these shifts propagates into large elevation biases that hindered early elevation change analyses (Surazakov and Aizen, 2006; Racoviteanu et al., 2007). Nowadays, those are addressed by coregistration methods that 3-dimensionally correct DEMs for shifts and rotations, using terrain assumed stable such as bare-rock (Nuth and Kääb, 2011; Noh and Howat, 2014).

Despite having addressed these widespread DEM biases, other complex patterns of errors remain. DEMs of different native resolutions resampled on the same grid consistently exhibit biases in terrains of high curvature such as peaks and cavities (Gardelle et al., 2012). Acquisitions from many sensors are plagued by along-track undulations of magnitude of 2–10 m and wavelengths of 1–10 km, including the widely used DEMs from ASTER (Girod et al., 2017) and SRTM (Farr et al., 2007), but also modern sensors such as SPOT-6 or Pléiades (Fig. 1.8). These patterns of errors are inherent to the DEMs and thus impact negatively all applications. And, in the case of glaciers, they cumulate with other specific challenges.

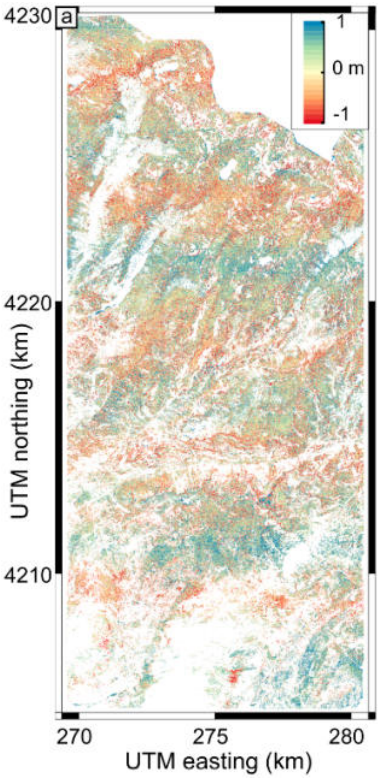

Figure 1.8: Errors from along-track undulations. From Deschamps-Berger et al. (2020), Pléiades DEM noise compared to lidar.

1.2.4 The specificity of glacier elevation changes

The surface elevation of glaciers is subject to changes of different magnitudes that occur over a wide range of time scales. In winter times, a thick (>1 m) snow layer can be deposited in a matter of days and start to densify into firn. In summer, ablation processes continuously remove mass from the glacier surface over the course of several months, with higher melt on warm days. These mechanisms of thickening and thinning vary strongly along the altitudinal distribution of a glacier (Huss and Hock, 2015). To adjust their geometry to climatic conditions, glaciers have longer response time of several years to decades (Jóhannesson et al., 1989; Cuffey and Paterson, 2010; Miles et al., 2021). Furthermore, glaciers are constantly flowing at velocities that vary by several orders of magnitude between glaciers or regions, and between years. All of these processes translate into surface elevation changes.

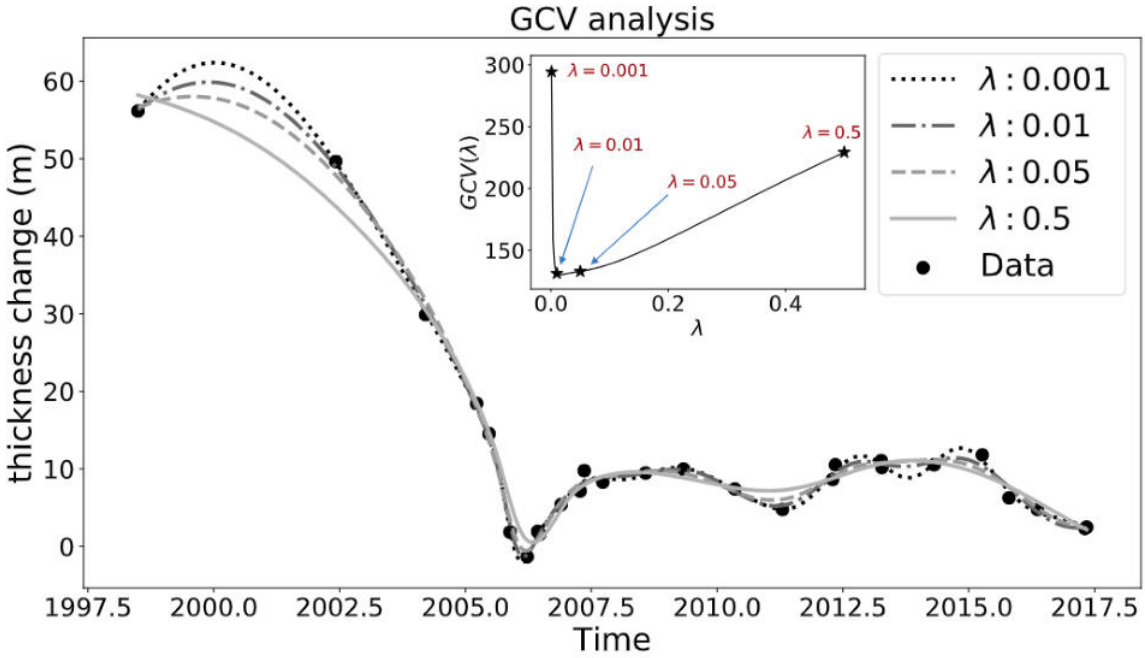

Figure 1.9: Fitting a time series to glacier elevation. From Shekhar et al. (2021), example of a localized penalized spline fit wit different smoothing parameters λ. GCV stands for the generalized cross-validation criterion used to select the best fit, here $\lambda = 0.01$ that has the lowest GCV value.

For many large-scale monitoring sensors, there is little control over when imagery will be acquired, and the state of the glacier surface and its recent changes are generally unknown. Consequently, it is delicate to deconvolve seasonal signals (Belart et al., 2017; Pelto et al., 2019) or fill spatial gaps in elevation data (McNabb et al., 2019; Seehaus et al., 2020) to estimate yearly volume changes, as well as perform density conversion to estimate mass changes (Huss, 2013). Furthermore, these variations in surface state can negatively affect the sensor measurements, including the previously mentioned biases from radar penetration (Dehecq et al., 2016; Li et al., 2021). Most critically, many assessments wish to report estimates for a fixed, consistent period of study (e.g. January 2000 to January 2010), despite large seasonal

and yearly spread of underlying DEM acquisitions (Braun et al., 2019; Dussaillant et al., 2019). To remedy this, time series estimation of surface elevation have emerged, from robust linear fits (Nuimura et al., 2012; Willis et al., 2012) to more complex quadratic or spline functions (Wang et al., 2015; Shekhar et al., 2021)) (Fig. 1.9). However, temporal biases due to overfitting, sparse data, or uneven temporal sampling have to be carefully considered with such parametric methods.

In this thesis, we aim to address the two challenges of (i) the spatial estimation of robust uncertainties for the patterns of errors in DEMs and (ii) the temporal estimation of glacier surface elevation. To this end, we turn towards spatiotemporal statistical methods.

1.3 Spatiotemporal statistics for geospatial assessments

1.3.1 An inherent multi-dimensionality in geospatial analysis

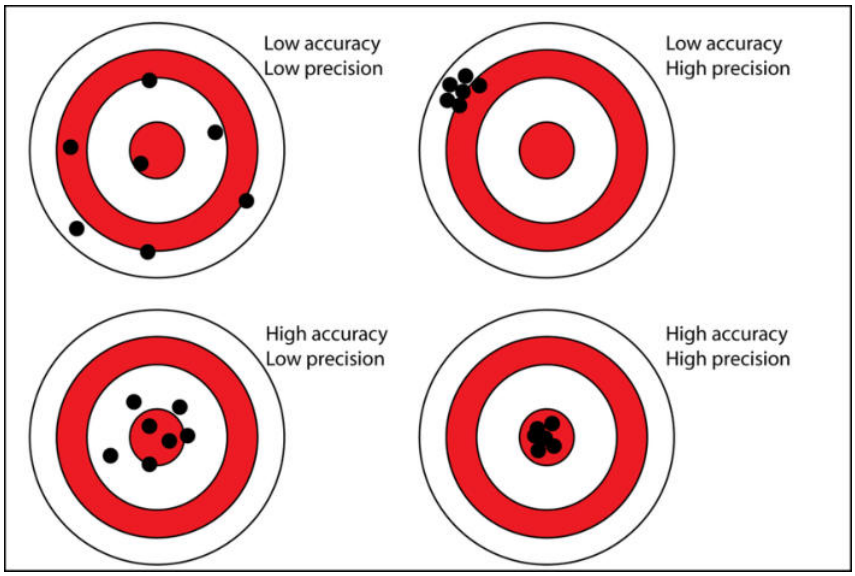

Figure 1.10: Precision versus accuracy. The bullseye represents the true value. From `https://www.antarcticglaciers.org/`, Bethan Davies.

Whether observation- or model-based, geospatial assessments are anchored in space and time. Geospatial assessments consider a certain spatiotemporal domain, i.e. study area and time period, and yield estimations at a certain spatiotemporal resolution, i.e. spatial sampling distance and time step. The underlying scales can vary across several orders of magnitude, e.g. from seasonal point measurements on a glacier (Huss et al., 2021) to a worldwide assessment (Zemp et al., 2019). Traditional estimation statistics provide the means to study a variable of interest based on a population of other observed or modelled input variables, which can be as simple as computing the average and spread of a sample population. For geospatial data, however, these methods rapidly become limited to describe the complex, multi-dimensional structure of a geospatial estimation with respect to space and time.

Estimations rely on input variables that possess a certain level of spatiotemporal accuracy and precision that propagates to the estimation of the variable of interest. Accuracy relates to biases, i.e. systematic errors, while precision relates to uncertainty, i.e. random errors (ISO, 1994, Fig. 1.10). Within a multi-dimensional framework, single metrics to estimate biases (such as the average difference), or to describe the uncertainty (such as the standard error of the mean) do not always reliably consider the entire structure of error, as highlighted by Canters et al. (2002) for geographical information system applications: *in most cases meta-information on the accuracy of spatial data is lacking or is limited to simple, overall measures that do not describe spatial variation in error.* To address this, the inter-dependency that input variables may have in the dimensions of space and time has to be considered. In glaciology, the problem of extrapolating few in-situ measurements to the regional scale (Kaser et al., 2006; Zemp et al., 2019) is an observation-based example of such an issue, and estimating the biases of ice thickness due to inconsistent dates of glacier outlines and DEMs (Farinotti et al., 2019a) is a model-based example of another one. The dependency of DEM errors in space (Fig. 1.8) and the temporal estimation of glacier elevation changes (Fig 1.9) are two problems that are intertwined with space and time, and therefore require to be addressed with adapted statistical approaches to provide robust estimations.

1.3.2 Spatiotemporal statistics for robust assessments

Spatiotemporal statistics (Cressie and Wikle, 2015) provide a body of theory and methods to address spatiotemporal problems. The underlying concepts are largely extended from spatial statistics, also known as geostatistics (Cressie, 1993; Goovaerts, 1997) which first emerged from the concepts of regionalized variables and kriging in mining applications (Matheron, 1965; Journel and Huijbregts, 1978). With the advent of the numerical era, the rise of machine learning methods has extended the core concepts of spatial statistics to any type of dimensions through Gaussian Processes (Williams and Rasmussen, 2006). While spatiotemporal statistics focus on the estimation and modelling of covariances typical to space and time with predefined models (Cressie and Wikle, 2015), Gaussian Processes combine those concepts with learning algorithms to optimize the form of the covariance, its parametrization, and to better scale with big data (Gardner et al., 2018b; Pleiss et al., 2018).

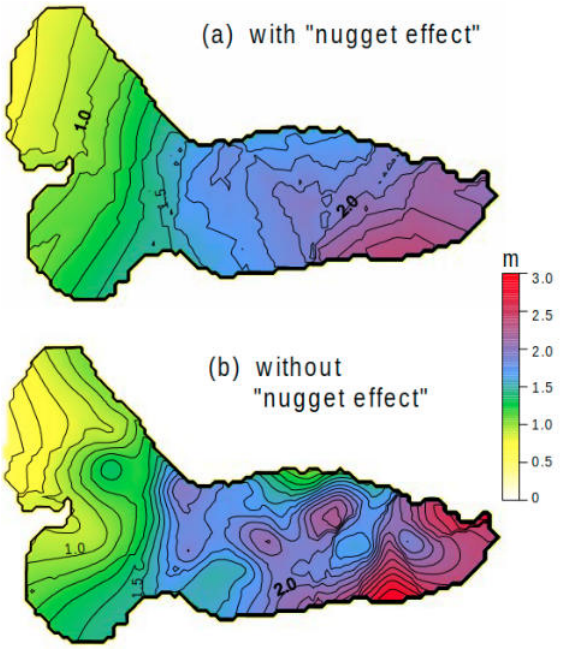

Figure 1.11: Kriging for glacier summer thinning. Interpolation of point measurements of summer ablation of Storglaciären, 1994 from Hock and Jensen (1999).

Spatiotemporal statistics methods have been mostly used for spatial and temporal interpolation using kriging (Burgess and Webster, 1980; Webster and Oliver, 2007), and also to address uncertainty analyses of geospatial data (Heuvelink et al., 1989; Heuvelink, 1998; Wang et al., 2005). While many applications have picked up interpolation methods (Fig. 1.11), both for DEMs (Reuter et al., 2007; Heritage et al., 2009) and glacier variables (Hock and Jensen, 1999; Schiefer et al., 2008; Fischer, 2009), uncertainty analyses that rely on spatial statistics are more scarce (Kyriakidis et al., 1999; Oksanen, 2006; Rolstad et al., 2009). Most critically, several glaciological and DEM-based studies erroneously applied existing formulations of uncertainty analyses (Schiefer et al., 2007; Gardelle et al., 2013; Fischer et al., 2015) which were reproduced and disseminated through hundreds of studies in the literature. Statistical validation exercises can help identify such issues, but are inconsistently performed. All these limitations seem to have stemmed from two barriers of spatial statistics: the theoretical complexity and the lack of accessible tools.

1.3.3 The theoretical complexity barrier of uncertainty analysis

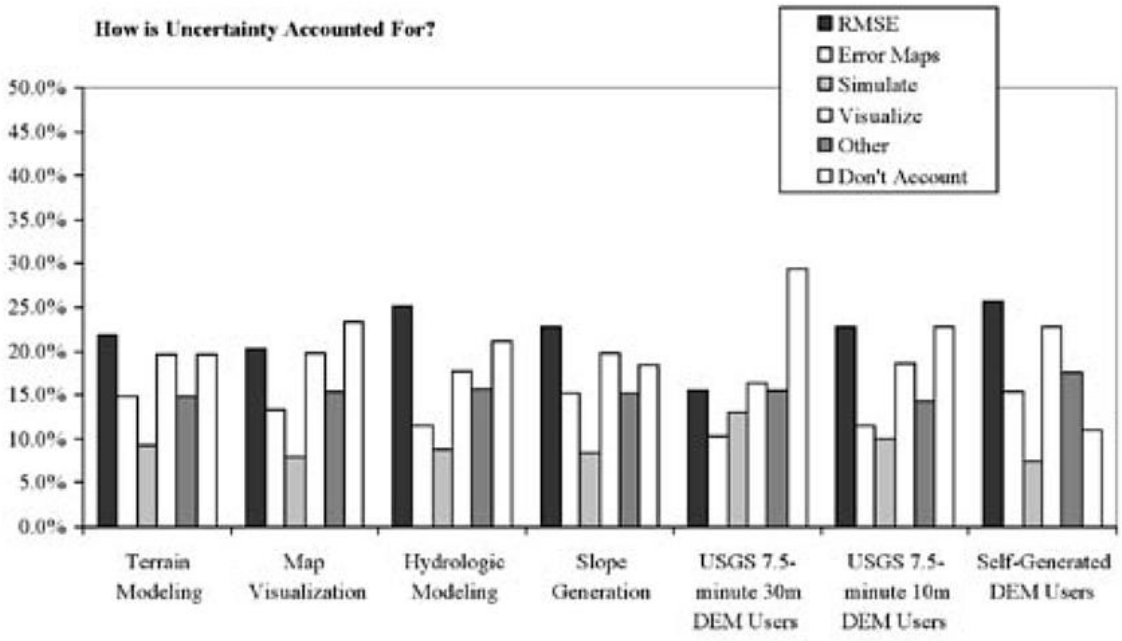

Figure 1.12: How is uncertainty accounted for by DEM users. From Wechsler (2003). Bar plot of uncertainty methods used by different DEM users, from a survey of 216 users.

Despite the formulation and demonstration of geospatial uncertainty methods as soon as the early 1990s, including several examples specific to DEMs (Kyriakidis et al., 1999; Heuvelink, 1998), these dedicated analyses were disseminated to relatively few applications. A survey conducted by Wechsler (2003) concluded that *although many DEM users deem uncertainty in the DEMs they use to be somewhat important, they indicated an unwillingness to devote much time to evaluate the impact that this uncertainty might have on their applications*, using simplified approaches instead (Fig. 1.12). This output resonated with that of

Heuvelink (2006) on the broader application of uncertainty analysis in all geographical information systems considered *as yet unrealized*, despite high efforts and hopes expressed more than a decade earlier (Goodchild and Gopal, 1989). And this, notwithstanding the increasingly high relevance to many applications thanks to a *body of theory and methods encompassed by geostatistics that is large and continues to grow*, and that allows handling of more complex problems including anisotropy, non-stationarity and non-normality (Heuvelink, 2006).

One of the major issues identified by Heuvelink (2006) on the failure to reach spatial data users was that the statistical background necessary to apply spatial statistics tools was too high. Most studies and tools *more or less expect the user to be an expert in (geo)statistics, or at least to have an expert in his or her immediate surrounding* (Heuvelink, 2006). While this is, to some extent, unavoidable, some steps were identified to facilitate such analyses, notably including a *dramatic simplification* of the error propagation analysis that *may still be preferred over a complete ignorance of how errors propagate in GIS analyses* (Heuvelink, 2006). Those steps would require an evolution of existing tools for spatial statistics and uncertainty analysis to reach a broader community.

1.3.4 The lack of accessible tools that pair with remote sensing

Another issue raised by Wechsler (2007) concerned the consistency and availability of spatial statistical tools. Only a few open-source and documented tools in spatial statistics have been readily available since the advent of numerical spatial analysis (e.g. Pebesma and Wesseling, 1998). Most importantly, the gap between programming languages where these statistical tools were typically developed (e.g. R) and those where geographic information systems data were increasingly analyzed (e.g. IDL, Python, QGIS) is likely to have been the main obstacle to the dissemination and reproduction of spatial statistics methods in the community. The discrepancies among DEM studies of the past decades testify to this, with many modern assessments with objective to quantify DEM accuracy and precision that fully omit spatial correlations (e.g. Uuemaa et al., 2020; Eberhard et al., 2021; Magruder et al., 2021).

The recent emergence of geostatistics packages (Mälicke and Schneider, 2019; Müller et al., 2021) and Gaussian Processes packages (Pedregosa et al., 2011; Gardner et al., 2018b) in high-level programming languages that pair efficiently with remote sensing such as Python (Fig. 1.13) holds a strong potential to favor accessible, reproducible and consistent spatiotemporal analyses. Those tools are mostly directed at problems of spatial interpolation, however, rather than towards uncertainty propagation. Yet, they provide a technical basis to quantify the spatiotemporal structure of variance that is necessary to further develop tools for uncertainty analysis and propagation.

In this thesis, we aim to build upon these tools to provide open, documented, and tested methods for DEMs, including the analysis of patterns of DEM errors and the temporal estimation of glacier elevation, to yield a robust assessment of recent global glacier mass changes.

```python
import numpy as np
import gstools as gs
# load 3D anisotrope field
x, y, z, field = np.loadtxt("directional.txt")
# define main axes by yaw, pitch and roll
angles = np.deg2rad([90, 45, 22])
model = gs.Gaussian(dim=3, angles=angles)
main_axes = model.main_axes()
# estimate variogram along all axes
bin_center, dir_vario = gs.vario_estimate(
    (x, y, z), field,
    direction=main_axes,
    bandwidth=10,
    angles_tol=np.deg2rad(22),
)
# fitting directional variogram
model.fit_variogram(bin_center, dir_vario)
```

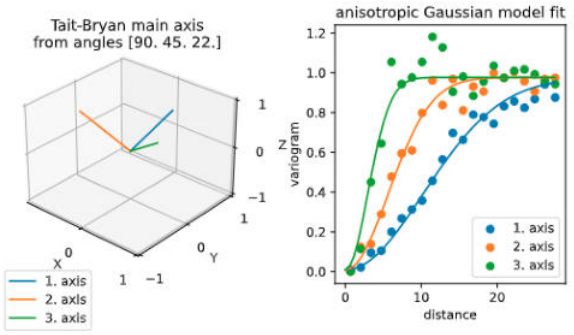

Figure 1.13: Directional variogram estimation for 3D data in Python. From Müller et al. (2021). Estimation of directional variograms for given main axes. The code snippet shows the setup for estimating and fitting the variogram to an anisotropic field. The figures show the main axes of the rotated model and the fitting results. Plotting commands have been omitted.

Chapter 2

Analysis of accuracy and precision of digital elevation models

Contents

2.1 Early advances on the uncertainty analysis of elevation changes

In this section, we summarize work on the uncertainty analysis of elevation changes estimated from DEMs performed in an early stage of the thesis. We address the issue of correlated noise in DEMs and compare inconsistent analytical formulations that were used in glaciology during the last two decades. Owing to its exclusive relevance to glaciology, some of this work was not included in the accepted article *Uncertainty analysis of digital elevation models by spatial inference from stable terrain* later presented in this chapter. Additionally, this work was paused during ~2 years to focus on the global glacier estimation presented in the next chapter, in the hope of meeting the IPCC Sixth Assessment Report deadline of January 2021. During this break, our work was partly integrated in the study of Dehecq et al. (2020) focusing on spy optimal imagery from Hexagon (KH-9), featured below.

2.1.1 Satellite instrument noise and digitization artefacts

Instrument noises such as along-track undulations, also sometimes referred to as jitter for undulations of short wavelength (<1 km), are omnipresent in many DEMs including ASTER and SRTM. They also plague modern, high-resolution sensors such as SPOT-6 or Pléiades (Fig. 2.1). Besides, other correlated noise can stem from digitization and processing artefacts, common in historical or modern DEMs (examples from the accepted article of this chapter on Figs. 2.7 and A1). To mitigate these correlated errors, bias corrections methods have emerged such as least-square polynomial fits (Brun et al., 2017) and sum of sinusoids (Girod et al., 2017), both based on independent elevation data assumed unbiased. Most notably, a recent effort of NASA reprocessed the SRTM with an in-depth "ripple" correction relying on ICESat data to produce the NASADEM (NASA JPL, 2020).

All these methods rely on a large amount of independent data acquired on stable ground, however, which is scarce in many regions of the world including, for example, ice sheet margins or expansive woodlands. Thankfully, correlated errors are generally consistent among acquisitions of the same instrument. This consistency can be used to infer the potential noise in DEMs in regions where bias-correction methods perform poorly, by estimating it in areas with a large amount of stable ground. Thus, even though some of these patterns can be corrected for some DEMs, we need to understand how these correlated errors can still affect largely uncorrected ones.

To this end, our objective is to estimate an uncertainty for a spatial average of elevation changes $\overline{dh}$ inside an area A of N pixels:

$$\overline{dh} = \frac{1}{N} \sum_{i=1}^{N} dh_i. \tag{2.1}$$

The classical formulation of the standard error of the mean implies that the uncertainty of the spatial average of elevation changes $\sigma_{\overline{dh}}$ depends on the dispersion of elevation σ_{dh} generally estimated by the standard deviation, and an effective number of samples N_{eff} which represents the number of independent samples within the N pixels:

$$\sigma^2_{\overline{dh}} = \frac{\sigma^2_{dh}}{N_{eff}}. \tag{2.2}$$

In practice, applying Eq. 2.2 using N as the effective number of samples N_{eff} yields small uncertainties, orders of magnitude below what would be expected from a visual inspection of the noises (Fig. 2.1). We must therefore turn towards methods that account for spatial correlations.

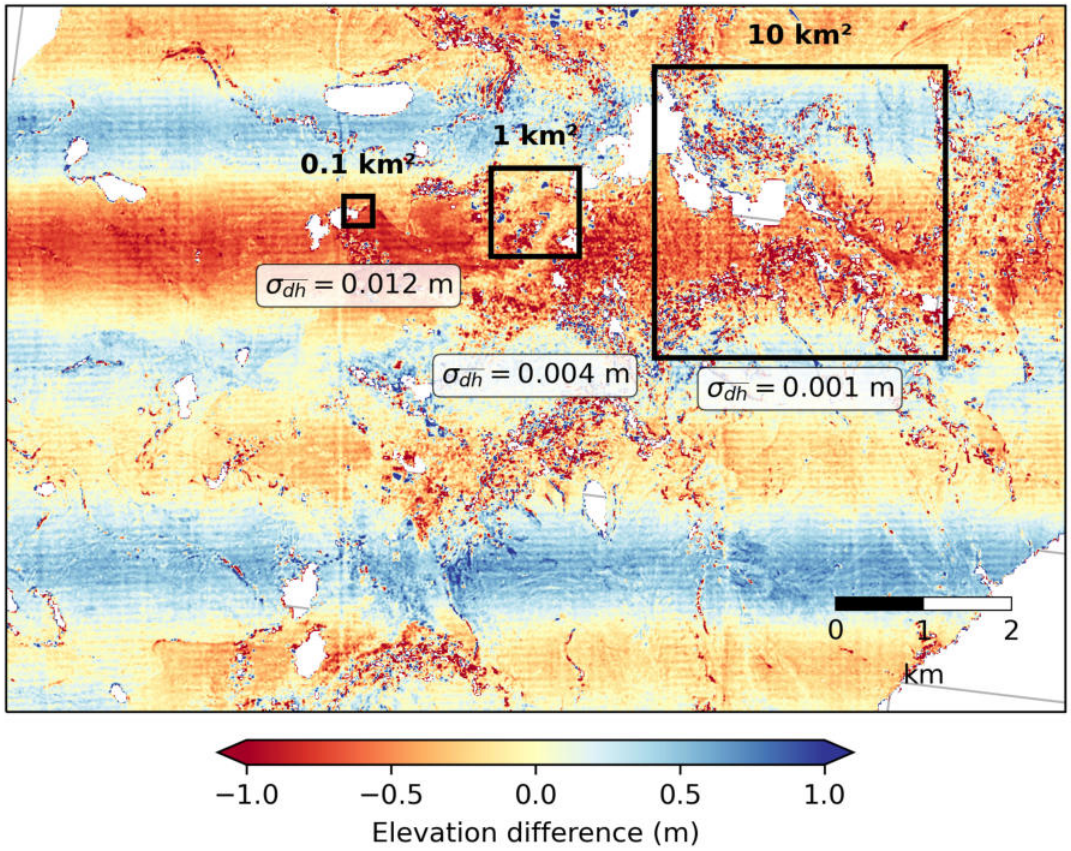

Figure 2.1: Jitter and classical standard error. Elevation differences from two Pléiades DEMs acquired 10 days apart in Peru, adapted from Fig. 2.7. The dispersion σ_{dh} is of 0.4 m. The standard error $\sigma_{\overline{dh}}$ is computed by Eq. 2.2 using the number N of 10 m x 10 m pixels for N_{eff} for three subset of different sizes. It is clear that the resulting standard error is way too small compared to the expected errors from the undulation in the elevation difference map.

2.1.2 Unraveling inconsistent approaches disseminated in glaciology

During early work in the studies of Menounos et al. (2019) and Dussaillant et al. (2019) on regional glacier mass changes later detailed in Chapter 3, we were confronted to different published approaches for uncertainty analysis. In the glaciological literature, a large number of studies have reproduced analyses from a few selected studies in order to estimate their uncertainty on elevation changes derived from DEMs. Tracing back the trail, we identified a first group that relies on a formula introduced by Schiefer et al. (2007) and Gardelle et al. (2013) based on the study by Bretherton et al. (1999):

$$N_{eff} = \frac{r \cdot N}{2d}, \tag{2.3}$$

where r is the spatial resolution i.e. pixel size, and d is the correlation length.

A second group of studies reproduces a formula introduced by Rolstad et al. (2009) and, in several occurences, modified by Fischer et al. (2015) as:

$$\begin{cases} N_{eff} = \frac{5A}{\pi d^2} & \text{if } d^2 > \frac{A}{\pi}, \\ N_{eff} = 1 & \text{otherwise.} \end{cases} \tag{2.4}$$

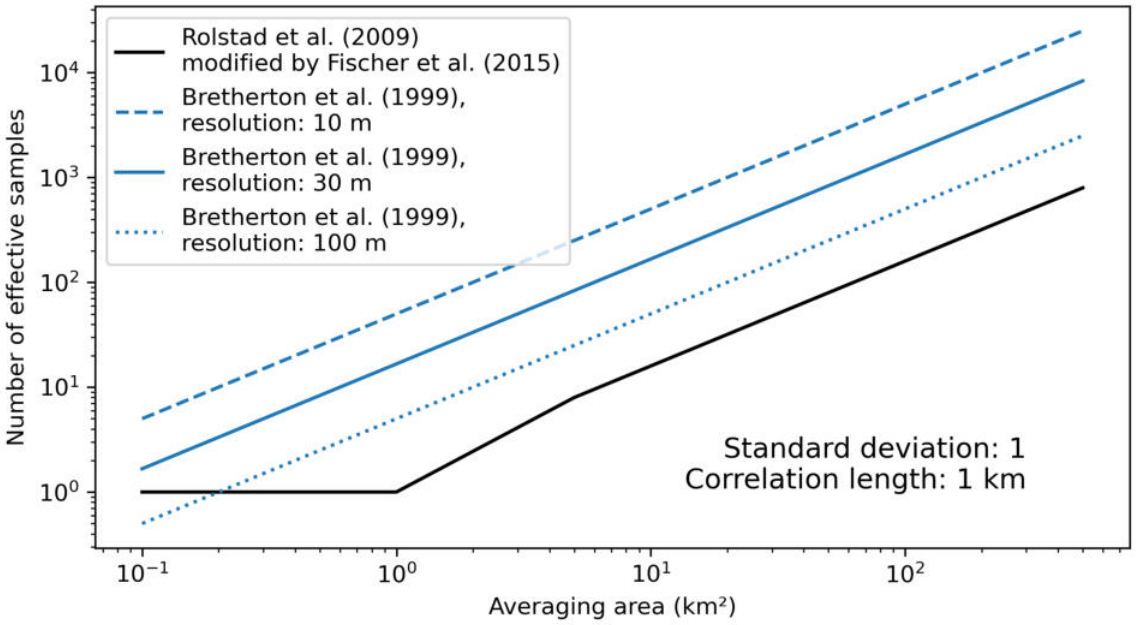

Figure 2.2: Differences between spatial correlation propagation formulas used in glaciology. A standard deviation of 1 and correlation length of 1 km are used for demonstration purposes. Note the logarithmic scale of both axes. The modification by Fischer et al. (2015) of the approach by Rolstad et al. (2009) is used, creating a break around 1 km².

By comparing the output of these two formulas, we found differences spanning orders of magnitude in the number of effective samples (Fig. 2.2). Once propagated through Eq. 2.2, the uncertainty of the spatial average $\sigma_{\overline{dh}}$ also varies by several orders of magnitude, which is manifestly problematic.

Several aspects are inconsistent with these two approaches. Firstly, spatial correlations stem from correlated noises which occur randomly in space, but have a fixed correlation range. Hence, these correlated noises do not vary with the resolution. Thus, while the area $A = r^2 N$ undoubtedly plays a role in the uncertainty of the spatial average over an area A, the spatial resolution r should not have any impact at all for a fixed area A. The approach of Bretherton et al. (1999), which considers only a one-dimensional space, shows such a dependency on the spatial resolution r, and therefore appears to have been misadapted. Secondly, correlated noises are modelled by functions that are continuous in space (Rolstad et al., 2009). Consequently, there is no statistical justification for the discontinuity introduced by Fischer et al. (2015). To elucidate those aspects, we explore simulation methods of spatial statistics.

We used the spatial statistics package *gstat* (Pebesma and Wesseling, 1998; Gräler et al., 2016) in R to analyze empirical variograms and explore simulation methods. First, we used unconditional Gaussian simulation (Goovaerts, 1997) to test the robustness of the different analytical formulation detailed above. In these simulations, we provided the same model of spatial correlation assumed in the analytical formulations, and simulated correlated noise randomly for 1,000 realizations (Fig. 2.3). We computed the spatial average for each realization, and estimated the uncertainty as the standard deviation of these averages. We found that only the original formulation of Rolstad et al. (2009) was the only one completely consistent with model parameters matching that of the simulation, while other formulations were erroneous. While the formulation of Rolstad et al. (2009) closely matched the simulation results for any variogram parameters, it always produced smaller values than expected intuitively for correlated errors over large areas using the empirical variogram estimated from DEMs (Fig. 1.1). To improve our estimation, we therefore delve into more details in the estimated empirical variograms.

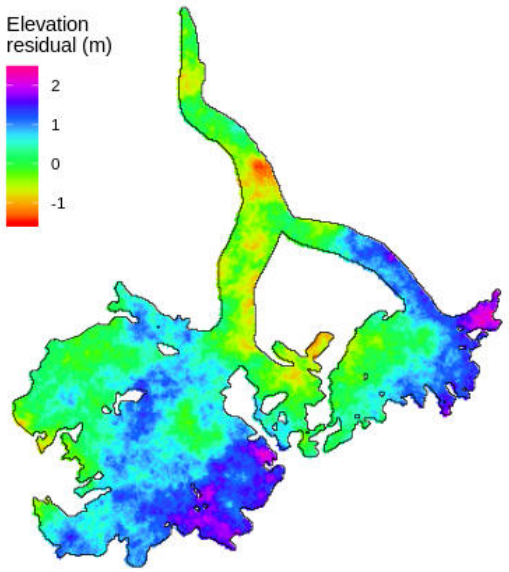

Figure 2.3: Unconditional simulation example. Example of single realization of unconditional Gaussian simulation for the Mer de Glace glacier, from an exponential model with sill (correlated variance) of 1 m and range (correlation length) of 5 km chosen for demonstration purposes.

2.1.3 The improvement brought by multi-range variogram models

Published article as co-author featured in this section: Dehecq, A. et al. (2020), *Automated Processing of Declassified KH-9 Hexagon Satellite Images for Global Elevation Change Analysis Since the 1970s*, Frontiers in Earth Science.[1]

We analyzed empirical variograms and identified additional, longer correlation ranges (2–20 km), orders of magnitude higher than typically used (50–500 m) for ASTER, SPOT-6 and Pléiades DEMs. The sills, i.e. correlated variances, of these long correlation ranges we identified (>2 km) were relatively small (typically 5-20% of the variance), which likely explains why those went largely unnoticed in previous studies. We later found similar results in Dehecq et al. (2020) using KH-9 DEMs, with correlation ranges spanning from 500 m to 70 km (Fig. 2.4A,B), and higher values of long-range sills (30–50% of variance) which matched the patterns of correlated noises (Fig. 2.4D).

To account for these additional correlation ranges in a formulation or simulation, they need to be modelled. Commonly, variograms are modelled by a single model of a certain form (e.g., spherical, gaussian) which, unfortunately, is the sole option of many geostatistical packages. To remedy this, we performed our own modelling of a sum of variogram models, each with a different correlation range and partial sill, i.e. correlated variance pertaining to this correlation range, using least-squares optimization. We compared our results to an empirical "patches" method (Berthier et al., 2016; Miles et al., 2018), for which we estimate the spatial average in 1,000 independent patches of stable terrain (as in Fig. 2.1, annotated "Exp. error" on Fig. 2.4C). This method essentially substitutes space for random realizations compared to Gaussian simulation methods (Fig. 2.3). We found that using a sum of variogram models yielded robust results, especially for large averaging areas, for both DEMs with along-track undulations, and for digitization artefacts in KH-9 (Fig. 2.4C).

During the study of Dehecq et al. (2020), the recent emergence of a Python package for spatial statistics (Mälicke and Schneider, 2019) enabled us to migrate several statistical tools from R to Python, more efficiently pairing with existing remote sensing tools. In the following, we describe how we continued with this endeavor with the aim of providing open, tested and documented tools for DEMs including uncertainty analysis based on spatial statistics.

[1] Contribution: in the study of Dehecq et al. (2020), I contributed literature and methodological discussions on spatial statistics and uncertainty propagation, including standard error formulation, multi-range variogram and validation methods, and I shared code.

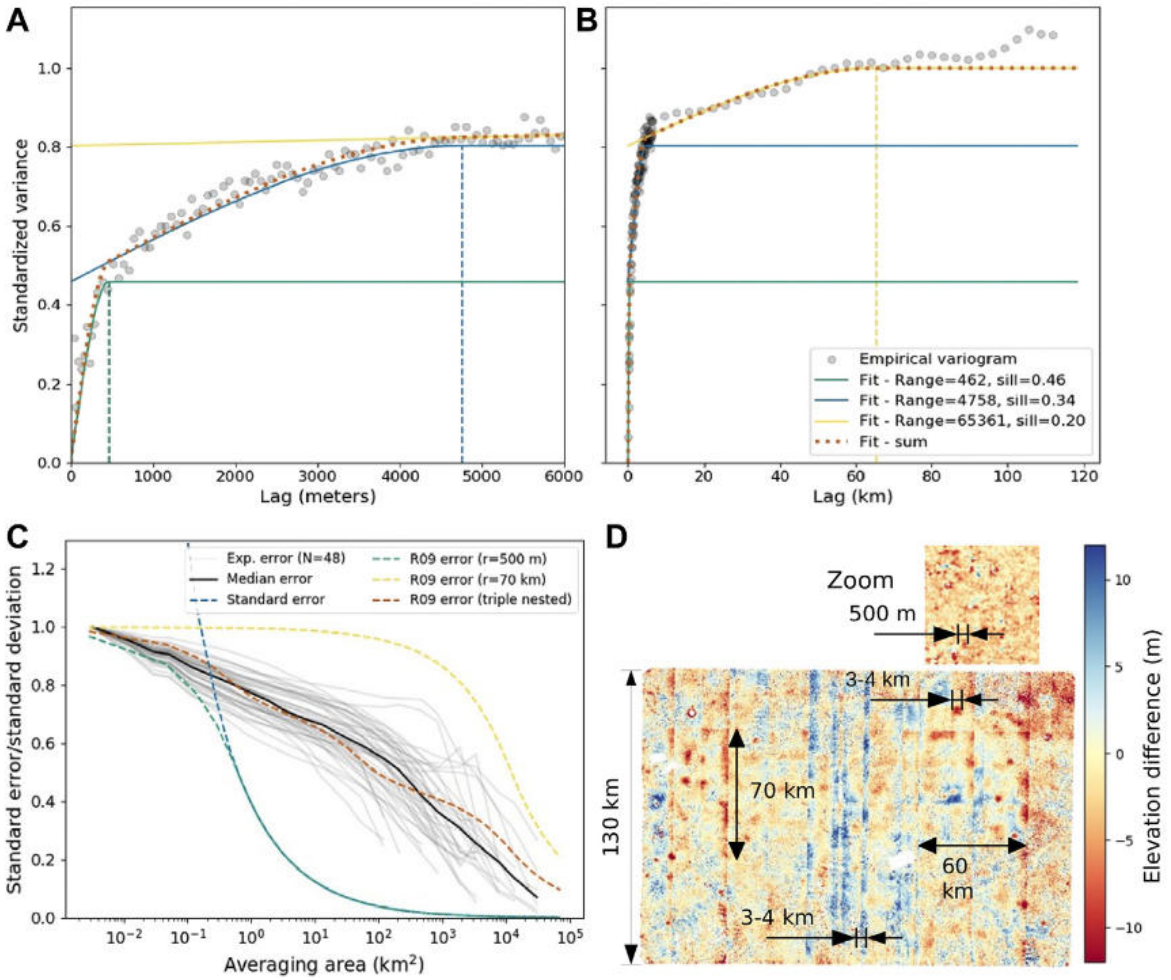

Figure 2.4: Spatial correlation of DEM errors in KH-9 DEMs. From Dehecq et al. (2020). Observed (gray dots) and modeled (lines) variograms for elevation differences between 48 KH-9 DEMs and ArcticDEM mosaic over Alaska for **(A)** short lag distances (<6 km) and **(B)** all lag distances. The best fit variogram model (orange dashed lines) is the sum of three nested spherical models (green, blue and yellow lines). **(C)** Empirical standard error of the mean as a function of the averaging area for all 48 DEM differences (gray lines) and the median values (black line) compared to several analytical estimates (R09 refers to Rolstad et al. (2009) model for corresponding range r) and our best-fit triple-nested variogram model (orange dashed line), and the classical standard error using all pixel samples for N_{eff} (see Eq. 2.2). **(D)** Sample elevation difference map for a KH-9 pair on an ice-free area, with typical artifact length scales noted.

2.2 Development of open tools for geospatial and elevation data analysis

2.2.1 *geoutils*: an open and accessible Python package for geospatial data

DEMs are georeferenced rasters, generally provided in the GeoTIFF or Hierarchical Data Format metadata standards. In geospatial data analysis, georeferenced rasters are analyzed with other georeferenced data, including point or vector data. Such analysis is complex and requires specific software support. The leading and widely used open software library for translating and manipulating geoferenced data, initially released in 2000, is the Geospatial Data Abstraction Library (GDAL) (GDAL/OGR contributors, 2022) of the Open Source Geospatial Foundation (OSGeo). Since its release, GDAL has provided free and increasingly performant geospatial tools, now widely used and fostering accessible, reproducible and consistent analyses.

GDAL provides routines that have a low level of operation, however, especially in its integration in high-level programming languages such as R or Python. Performing a relatively simple operation such as reprojecting a raster onto another one to compare the two underlying data grids, or rasterizing a georeferenced vector on the extent of a raster to mask a specific area, is not always straightforward. It generally requires a solid knowledge of georeferenced metadata in GDAL syntax, and possibly a long series of commands. And this despite the success and practicality of its command line interface, which is unfortunately not well suited to automate complex analyses. To address this, many researchers have built their own libraries on top of GDAL, to facilitate their georeferenced operations and improve efficiency. For example, in glaciology alone, about half a dozen of such packages[2] were developed including notably *pygeotools* (`https://github.com/dshean/pygeotools`; Shean and Lilien (2019)), a deprecated *geoutils* (`https://github.com/GeoUtils/geoutils`) homonymous with the new package later detailed in this section, *pybob* (`https://github.com/iamdonovan/pybob`) and *salem* (`https://github.com/fmaussion/salem`; Maussion et al. (2021)).

These efforts provide valuable open tools for the community, yet they also raise the issues of having limited intercompatibility and a lack of tested and consistent workflows. Additionally, several packages are mixing tools that are aimed at different applications. Most of these tools have also become incompatible with recent packages that provide easier data handling and big data scaling of arrays such as *xarray* (Rocklin, 2015; Hoyer and Hamman, 2017), or enable a facilitated raster and vector manipulations such as *rasterio* and *geopandas* (Gillies and Others, 2013; Jordahl et al., 2020). The now widely used package *rasterio*, build on top of GDAL, somewhat simplifies raster manipulations but still has a relatively low level of operation, owing to its function-based structure. It therefore brings about the same problem as GDAL to an extent and, additionally, has an inter-operability with *geopandas* that is not straightforward to perform coupled raster–vector manipulation .

[2] In the early stages of this thesis, I also developed my own routines from GDAL at `https://github.com/rhugonnet/rh_pygeotools`, later put aside to focus on collaborative efforts.

```python
import rasterio
from rasterio.warp import calculate_default_transform, \
    reproject, Resampling

dst_crs = 'EPSG:4326'

with rasterio.open('raster1.tif') as src:
    transform, width, height = calculate_default_transform(
        src.crs, dst_crs, src.width, src.height, *src.bounds)
    kwargs = src.meta.copy()
    kwargs.update({
        'crs': dst_crs,
        'transform': transform,
        'width': width,
        'height': height
    })

    with rasterio.open('raster2.tif', 'w', **kwargs) as dst:
        for i in range(1, src.count + 1):
            reproject(
                source=rasterio.band(src, i),
                destination=rasterio.band(dst, i),
                src_transform=src.transform,
                src_crs=src.crs,
                dst_transform=transform,
                dst_crs=dst_crs,
                resampling=Resampling.nearest)
```

```python
from geoutils import Raster

r1 = Raster('raster1.tif')
dst_crs = 'EPSG:4326'

r2 = r1.reproject(dst_crs=dst_crs)
r2.save('raster2.tif')
```

Figure 2.5: Simple class-based operations in *geoutils*. Code example to reproject a raster to a new projection based on (left) *rasterio* and (right) *geoutils*. Note that the *geoutils* shows class-based operations, where a Raster class object is created, manipulated into a new object, then saved. This approach differs both technically and conceptually from the function-based structure of *rasterio*.

To remedy this, we developed a new package *geoutils* (`https://github.com/GlacioHack/GeoUtils`) in the frame of the collaborative effort GlacioHack initiated by Amaury Dehecq (VAW, Zürich and IGE, Grenoble). This package provides object-based manipulation of rasters and vectors, constructed as classes built on top of *rasterio* and *geopandas*. These allow single-line operations to perform the most common manipulation of raster and vector data (Fig. 2.5), and integrates an arithmetic interface for raster objects (e.g. addition, multiplication). Another part of the package, that might in time become its own project, focuses on extraction of metadata (e.g. date, instrument, spatial extent) from the filename or ancillary files used by various remote sensing data products. Most importantly, all functionalities *geoutils* are tested, and tests are assembled in a continuous integration workflow that ensures their perennity. Our package in still in its infancy, and might evolve depending on the direction of similar efforts such as *rioxarray* (Snow et al., 2022), but provides at present a solid core to perform simplified geospatial analysis. In a concomitant effort to *geoutils*, and by utilizing its simplified geospatial routines, we developed a package for DEM analysis: *xdem*.

2.2.2 *xdem*: an open and modular Python package for DEM analysis

Few high-level programming packages provide tools for the analysis of DEMs, with only a few packages available for terrain analysis (e.g., slope, curvature, and basin delineation) (Barnes, 2016) or DEM alignement (Shean et al., 2021). In *xdem* (xdem contributors, 2021), which stands for "cross-DEM" analysis, we aim to provide open, modular and tested tools for analyzing either a single DEM, or several DEMs among themselves. While *xdem* is still in development, it already provides the core tools for DEM analysis (Fig. 2.6).

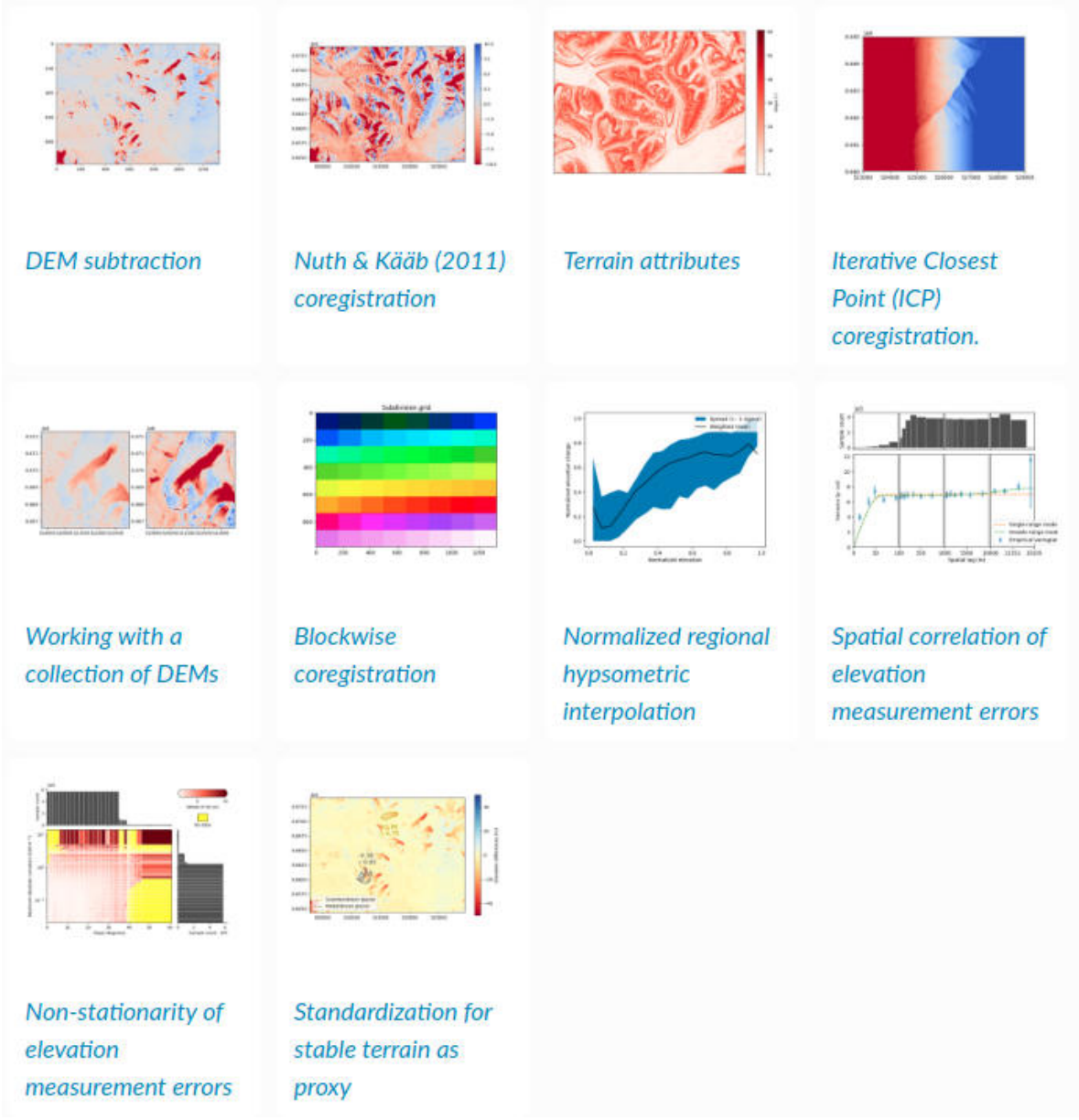

Figure 2.6: Gallery of documentation examples in *xdem*. Thumbnails pointing to detailed code examples of DEM alignment, interpolation, terrain attributes and spatial statistics, from `https://xdem.readthedocs.io/en/latest/auto_examples/index.html`.

Through *xdem*, we first provide the means to perform vertical system transformation based on translation grids from PROJ, a library of cartographic projections (PROJ contributors, 2022) that is now also a project of OSGeo, as for GDAL. The nature of DEMs entails additional metadata than that of a typical raster, with vertical systems of reference described by ellipsoids or geoids, including a multitude of geoids models used in different regions of the world. Our routines attempt to identify the vertical system from the DEM product name, in order to ensure that different DEMs are analyzed on the same reference.

We additionally implement algorithms to estimate DEM terrain attributes. Those methods are widely used but limited to specific softwares such as GDAL or the System for Automated Geoscientific Analyses (SAGA) package. Based on published works, we enable the computation of the attributes of terrain slope and aspect (Horn, 1981), profile and planform curvatures (Zevenbergen and Thorne, 1987; Wilson et al., 2007), ruggedness (Riley et al., 1999), roughness (Dartnell and Gardner, 2004) and topographic position indexes (Weiss, 2001). To our knowledge, those algorithms were not implemented directly in Python before, or only by binding Python to C++ implementations Barnes (2016), despite being at the basis of DEM analysis.

We also provide DEM alignment methods described in the literature, including horizontal alignment using the relation between aspect and slope (Nuth and Kääb, 2011) or iterative closest point cloud registration (Besl and McKay, 1992; Bradski, 2000). We also include bias correction methods based on robust polynomial and sinusoid fitting, including directional biases (e.g. Girod et al. (2017)) or terrain biases (e.g. Gardelle et al. (2012)). For modularity, we implement a "pipeline" object, inspired by the machine learning package *scikit-learn* (Pedregosa et al., 2011), that allows combining any number of steps of alignment, bias correction, or filtering in any order, and with any parameter.

Finally, we implement spatial statistics methods for the uncertainty analysis of DEMs and their derivatives, which are based on the article presented below.

2.3 Accepted article: *Uncertainty analysis of digital elevation models by spatial inference from stable terrain*

Accepted article as main author featured in this section: Hugonnet, R. et al. (accepted 27.06.22), *Uncertainty analysis of digital elevation models by spatial inference from stable terrain*, IEEE Journal of Selected Topics in Applied Earth Observations and Remote Sensing.[3]

In the following article, we expand on our work by proposing a non-stationary spatial statistical framework, which clarifies the concepts of accuracy and precision for DEMs, and accounts for error variability in addition to the spatial correlation of errors during uncertainty analysis. We also generalize the uncertainty analysis of DEM differences to the case of any DEM, we present and validate robust estimation methods, and we verify that stable terrain can be used as a proxy to infer elevation errors on other types of terrain by utilizing nearly simultaneous DEM acquisitions. Ultimately, we analyze the impact of our validated methods on the analysis of pixel-scale DEM derivatives such as terrain slope and aspect, and the analysis of spatially integrated DEM derivatives such as glacier volume changes.

[3]Contribution: the article of Hugonnet et al. (accepted) is my own work that stemmed from early analyses started alongside Fanny Brun. I largely conceptualized the final study. I solely performed the literature review from which analytical formulations are developed, wrote all associated code, performed the analysis of all data and wrote the initial version of the manuscript. More details on co-author contributions in the "Authors contributions".

Uncertainty analysis of digital elevation models by spatial inference from stable terrain

Romain Hugonnet, Fanny Brun, Etienne Berthier, Amaury Dehecq, Erik Schytt Mannerfelt, Nicolas Eckert and Daniel Farinotti

***Abstract*—The monitoring of Earth's and planetary surface elevations at larger and finer scales is rapidly progressing through the increasing availability and resolution of digital elevation models (DEMs). Surface elevation observations are being used across an expanding range of fields to study topographical attributes and their changes over time, notably in glaciology, hydrology, volcanology, seismology, forestry and geomorphology. However, DEMs frequently contain large-scale instrument noise and varying vertical precision that lead to complex patterns of errors. Here, we present a validated statistical workflow to estimate, model, and propagate uncertainties in DEMs. We review the state-of-the-art of DEM accuracy and precision analyses, and define a conceptual framework to consistently address those. We show how to characterize DEM precision by quantifying the heteroscedasticity of elevation measurements, i.e. varying vertical precision with terrain- or sensor-dependent variables, and the spatial correlation of errors that can occur across multiple spatial scales. With the increasing availability of high-precision observations, our workflow based on independent elevation data acquired on stable terrain can be applied almost anywhere on Earth. We illustrate how to propagate uncertainties for both pixel-scale and spatial elevation derivatives, using terrain slope and glacier volume changes as examples. We find that uncertainties in DEMs are largely underestimated in the literature, and advocate that new metrics of DEM precision are essential to ensure the reliability of future Earth and planetary surface elevation assessments.**

***Index Terms*—Geostatistics, error propagation, remote sensing, variogram, spatial correlation, surface height.**

I. Introduction

DIGITAL elevation models (DEMs) are gridded, numerical representations of surface elevation. DEMs have a long history of interpolation from point measurements and digitized historical maps [1], [2]. Nowadays, DEMs are mostly generated from radar interferometry [3], [4], optical stereophotogrammetry [5], [6] or laser scanning [7], [8] of a planetary surface. When produced from these remote sensing techniques, DEM grid cells essentially represent surface elevations timestamped to the date of instrument acquisition. With the ever-improving coverage and precision of satellite and airborne sensors [9], land surface assessments based on DEMs are advancing towards estimates that are both more spatially and more temporally resolved [10], [11]. Additionally, the recent unlocking of historical optical archives has created unprecedented potential for studying half a century of Earth's surface elevation [12]–[14].

Studies that harness elevation observations can generally be divided into two groups. The first group relies on single-acquisition and often gap-filled DEMs to extract essential topographic characteristics, e.g., in river discharge and flood modelling [15]–[17], geomorphological terrain analysis [18]–[21], tectonic monitoring [22]–[25], avalanche risk prediction [26], land classification [27], [28], onshore inundation and sea-level rise forecasting [29]–[31] and planetary surface characterization [32], [33]. The second group requires multiple acquisitions to study surface elevation changes over time, e.g., for landslide and rock avalanche detection [34]–[36], seasonal snow depth assessment [37]–[39], lava flow volume quantification [40], [41], canopy height evolution [42]–[44] and glacier, ice sheet and ice shelf mass balance estimation [45]–[47]. In both groups, and for all applications, the interpretation of results and its robustness are inextricably intertwined with the accuracy and precision of the underlying DEMs.

Accuracy and precision are related to systematic and random errors. In the case of DEMs, they have been the focus of specific research [48]–[51], software development [52] and questioning [53]–[56] since the beginning of the numerical era. Yet, these efforts are dwarfed by the tremendous increase of studies that rely on DEMs [57] and the processing of ever larger data volumes [58]–[60]. Most critically, the analysis of many modern studies is still confined to simplified metrics for accuracy and precision (e.g., [61]–[63]) that mix systematic and random errors and fail to describe the strong spatial variations and correlations in errors observed in DEMs (e.g., [64]–[66]).

Here, we present a statistical workflow to robustly estimate and propagate uncertainties in DEMs; most specifically, we:

- perform a literature review of analyses dealing with DEM accuracy and precision;
- propose a framework based on spatial statistics to consistently address DEM accuracy and precision;
- present robust inferential methods to estimate elevation heteroscedasticity and spatial correlation of errors;
- analyze the impact on the uncertainty of elevation derivatives, using terrain slope and glacier volume changes as examples;
- provide access to our methods through the open, tested and documented Python package xDEM.

R. Hugonnet and E. Berthier are with the LEGOS, Université de Toulouse, CNES, CNRS, IRD, UPS, F-31400 Toulouse, France (e-mail: romain.hugonnet@gmail.com).

R. Hugonnet, A. Dehecq, E.S. Mannerfelt and D. Farinotti are with the Laboratory of Hydraulics, Hydrology and Glaciology (VAW), ETH Zurich, Zurich, Switzerland, and the Swiss Federal Institute for Forest, Snow and Landscape Research (WSL), Birmensdorf, Switzerland.

F. Brun and A. Dehecq are with the IGE, Université Grenoble Alpes, CNRS, IRD, Grenoble INP, Grenoble, France.

N. Eckert is with the Université Grenoble Alpes, INRAE, UR ETNA, Grenoble, France.

Manuscript received March 23, 2022; revised June 10, 2022.

II. Literature review

A. Mitigating poor DEM accuracy before studying precision

The term accuracy has been used to describe either systematic errors or, in some instances, both systematic and random errors, leading to some confusion. In the present article, we define accuracy as the description of systematic errors only, also known as "trueness" [67], which is related to elevation biases. Poor accuracy is common in DEMs and has been a major source of error in elevation assessments, particularly during the advent of space-borne DEMs. Limitations in instrument positioning, orientation, or post-processing often lead to erroneous horizontal referencing [66], [68], vertical shifts [69], [70] or tilts [71], [72] that propagate into elevation biases (Fig. 1a). By utilizing terrain with elevation assumed stable over time, methods performing 3-dimensional alignment of DEMs have flourished, relying on either generic registration methods [73]–[75], least squares approaches [71], [76] or specifically-developed DEM registration based on terrain constraints [77], [78]. These methods proved robust for aligning a DEM either to an external reference DEM, or to accurate geolocated point elevation data such as space-borne laser altimetry [79], [80]. The above registration methods are only successful at correcting elevation biases common to the entire DEM grid, however. Other biases remain present once 3-dimensional alignment is attained and can arise from resolution [81], [82], specific image deformations and instrument biases [13], [66] or physical properties of the observed terrain such as radar penetration into snow and ice [83], [84] or into forest canopy [43]. Most of these biases are instrument- or application-dependent and, therefore, require specific considerations. Notwithstanding those, poor DEM accuracy has been largely addressed by the robustness of registration methods that have become increasingly widespread, thereby shifting the focus towards the next limiting factor: better quantifying DEM precision.

B. The inherent variability of vertical precision

Precision describes random errors [67] and is related to elevation variance. One aspect of DEM precision consists of the pixel-scale dispersion of elevations that we refer to as "vertical precision". DEMs are generated from acquisitions that possess intrinsic, random measurement errors. At the pixel scale, instrument resolution, spectral range, and encoding depth of optical sensors directly affect the quality of stereo-correlation [5], [6], [85], radar slant angle and height of ambiguity play an important role in interferometric coherence [86], [87] while laser wavelength, sunlight background radiation, target reflectivity, and backscattering properties modulate laser signal-to-noise ratio [88], [89]. Many instrument- or processing-related metrics constitute quality indicators of the estimated elevations. These indicators have been almost exclusively used for the filtering of observations of lesser quality, however, and only occasionally as a tool towards improved modelling of sensor-specific variability in vertical precision (e.g, [90]). Besides, the geometry of instrument acquisition can exacerbate random errors depending on the relief of the observed landforms (Fig. 1a). Vertical precision has indeed been long shown to decrease with terrain slope [48], [91]–[94]. Several assessments account for this variability by partitioning the elevation variance into categories of flat and steep terrain (e.g., [59]). Most studies use a single metric to describe vertical precision, however, often reporting a standard deviation (e.g., ± 2 meters). Such simple metrics are insufficient in describing the heteroscedasticity of elevation measurements, i.e. the variability in vertical precision. Although some studies quantified and modelled this heteroscedasticity [64], [95], [96], this modelling was generally performed without validation of the underlying methodology and, most critically, without considering the effect of spatial correlations.

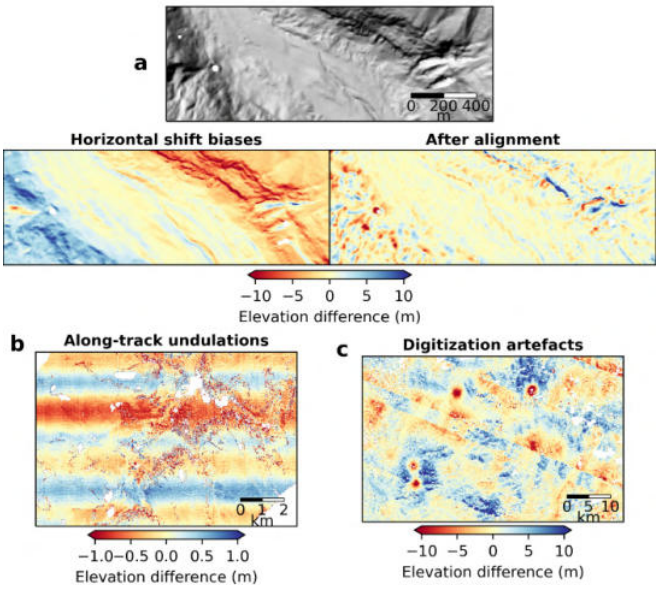

Fig. 1. **Patterns of random and systematic errors in DEMs. a,** Elevation differences of horizontal shifts (left) and after alignment (right) with terrain hillshade (top), extracted from the data in Table I. The horizontal shift between Pléiades and SPOT-6 DEMs is of 2 m east and 4 m north, creating large biases despite being relatively small (half a pixel). **b-c,** Noise owed to **(b)** along-track undulations in a Pléiades–Pléiades DEM difference and to **(c)** digitization artefacts in a KH-9–ArcticDEM DEM difference [13], after alignment.

C. The correlated noises that plague DEMs

Another aspect of DEM precision concerns the inter-pixel spatial dependency of random errors, here referred to as "spatial correlations". Spatial correlations describe structures of noise that show a location-dependent pattern, which can often be traced back to limitations during acquisition or post-processing. Along-track undulations have been observed in many DEMs generated from air- and space-borne sensors (Fig. 1b), including the Advanced Spaceborne Thermal Emission and Reflection Radiometer (ASTER) [47], [66], the Satellite Pour l'Observation de la Terre (SPOT) [97], [98], Pléiades [39], [99] and the Shuttle Radar Topography Mission (SRTM) [58], [100], [101] (Fig. S1). Processing noise is common in DEMs requiring image digitization including aerial photographs [102], [103] or historical satellite imagery such as Corona and Hexagon KeyHole-9 (KH-9) [13], [104] (Fig. 1c). To mitigate these correlated noises, DEM correction methods have emerged [82], [105] but are still burgeoning for specific

types of errors [66], [106], [107], and their performance is highly dependent on the type of terrain. Furthermore, nearly all DEMs contain structural short-range correlation of errors. The degree to which a DEM grid spacing represents its native resolution [108], [109] and how that resolution has possibly been degraded through interpolation [110] determine the severity of these short-range correlations. When upsampled to a larger grid spacing, vertical precision improves directly as a function of the underlying spatial correlations [111]. Spatial correlations are generally quantified using an empirical variogram [112], [113] estimated either on the basis of differences with independent elevation observations [2], [114] or those with simulated elevation surfaces [115], [116]. Many studies have used variograms, but have almost exclusively used short range models (i.e. 5 to 20 times the pixel size). Few studies modelled longer-range correlations, that is, correlations that persist over distances several orders of magnitude larger than the pixel size [13], [47], [65]. The widespread occurrence of long-range noise in DEMs thus constitutes a critical limitation in the analysis of DEM precision, and one that directly affects uncertainty propagation.

D. Uncertainty propagation to elevation derivatives

To propagate elevation variance into uncertainties of elevation derivatives (i.e. variables that are derived from elevations), a large set of methods has been applied that generally relies on spatial statistics. Spatial statistics, also known as geostatistics [112], [113], [117], provide a large body of theories and methods that, among others, can address spatial uncertainty analyses [118]–[120] by characterizing spatial correlations that depend only on the distance between observations. These uncertainty propagation methods can be subdivided into two groups: (i) Monte Carlo techniques that simulate multiple random realizations of correlated error fields [121]–[123], notably including Sequential Gaussian simulation [117] and Fourier randomization [124]; and (ii) gradient techniques that analytically approximate the variance of a derivative through simplified equations, that can be either based on Taylor series expansion [121] for any derivative of elevation, or approximations of variogram integration [65] for spatial derivatives. The first group has been widely used for topographic variables, notably in hydrology [16], [57], [125], [126] and occasionally for spatial derivatives in glaciology [127]. The second group is used less frequently, both for Taylor series expansions developed in few applications [128]–[131], and for variogram integration implemented mainly in glaciology and geomorphology [65], [132]. Although both groups are expected to perform similarly, Monte Carlo techniques are computationally expensive, especially at fine resolution. Analytical approximations, instead, require a theoretical description of variance propagation that can reach a high degree of complexity for some derivatives [133]. To our knowledge, few studies [132] constrained these propagation methods with estimates of heteroscedasticity and spatial correlation of errors into a single framework for DEMs, and none tested the underlying assumptions of spatial statistics. In the following, we propose such a framework, and later describe methods to robustly estimate its key components.

III. Problem formulation

A. Elevation bias and variance at each location

We consider the elevation observation $\hat{h}(x, y, t)$ located at (x, y) in space and t in time, and pertaining to the DEM $\mathcal{D}$. Annotating the true unknown elevation at the same location $h(x, y, t)$, we can state that the elevation observation has a bias $\delta h(x, y, t)$ if, over a large number of repeated measurements $i \in \mathcal{I}$ of elevation $\hat{h}(x, y, t)_i$ at (x, y, t), we have:

$$\overline{\hat{h}(x, y, t)_i|_{\mathcal{I}}} - h(x, y, t) = \delta h(x, y, t). \quad (1)$$

The repeat elevation measurements around the bias $\delta h(x, y, t)$ are subject to random measurement errors $\epsilon_h(x, y, t)$ with variance $\sigma_h^2(x, y, t)$, whose distribution is not necessarily normal and might depend on time and location:

$$\hat{h}(x, y, t) = h(x, y, t) + \delta h(x, y, t) + \epsilon_h(x, y, t). \quad (2)$$

In practice, acquiring a large number of repeat measurements at both the same location and time is not feasible, and we therefore turn towards inferential methods to estimate these biases and variance.

B. Inference from stable terrain

DEMs benefit from a great asset, largely uncommon to other remote sensing data, which is that large proportions of planetary surface elevations remain virtually unchanged through time. In fact, elevation changes caused by erosion, short vegetation growth, or continental drift are typically small compared to the precision of the measurement. Terrains such as bare rock or grasslands – later referred to as "stable terrain" – thus provide the means of analyzing multiple elevation measurements acquired at different points in time as if they were acquired from simultaneous measurements $\hat{h}(x, y, t)_i$:

$$\frac{dh(x, y, t)}{dt} \approx 0 \,\text{for}\, (x, y) \in \text{stable terrain}. \quad (3)$$

While this temporal consistency unlocks the potential to analyze elevation acquisitions independently of time t, it is impeded by the number of required DEMs. For each location (x, y), the number of samples to perform the statistical analysis would always be at best equal to the total number of independent acquisitions, requiring a large number of DEMs. Therefore, we investigate the spatial properties of elevation biases and variance.

C. Spatial homogeneity after affine alignment

Elevation biases and variance are inherent to instrumental limitations, to the physical properties of the observed terrain, as well as its topography (see previous Sections II-A and II-B). Among many types of location-specific biases, a general exception is that of grid misalignment to the true elevations $h(x, y, t)$ that follows specific geometric distributions linked to the gridded nature of DEMs (Fig. 1a). In our framework, we therefore split elevation biases into two categories: affine biases $\delta h_{\mathcal{A}}$ that are common to the entire DEM (e.g., translation, rotation, scaling), and non-affine "specific" biases $\delta h_{\mathcal{S}}$

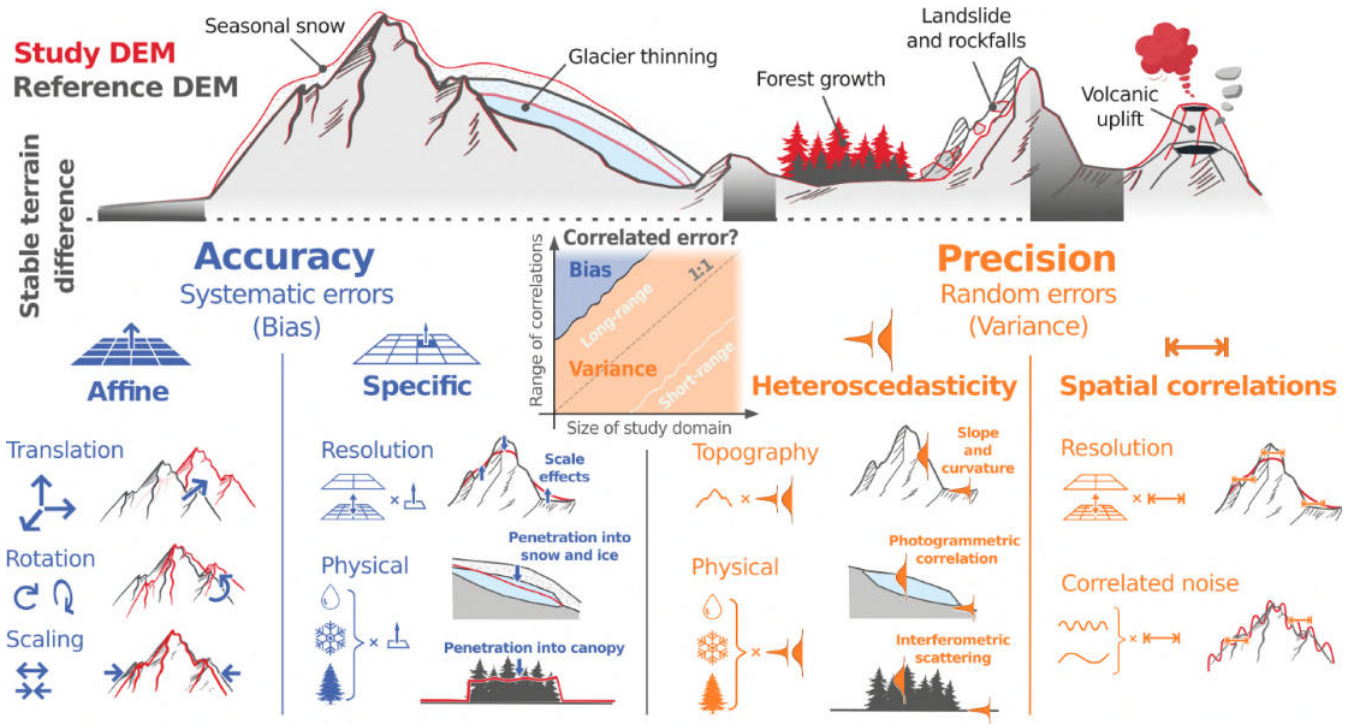

Fig. 2. **A framework for uncertainty analysis of DEMs.** Non-stationary spatial framework to analyze the accuracy and precision of DEMs based on elevation differences on stable terrain (Sections III-A–III-D), with accuracy divided into affine and specific biases (Section III-C), and precision divided into heteroscedasticity and spatial correlation of errors (Section III-F).

that occur at the grid cell level and vary with instrumental and topographical effects (Fig. 2):

$$\delta h(x,y,t) = \delta h_{\mathcal{A}}(x,y,t) + \delta h_{\mathcal{S}}(x,y,t). \quad (4)$$

Once an alignment is attained by the affine transformation $\mathcal{A}$ giving $\mathcal{A}(x,y,t) = \delta h_{\mathcal{A}}(x,y,t)$, we assume that, for a single DEM $\mathcal{D}$, specific elevation biases $\delta h_{\mathcal{S}}$ and elevation variance σ_h^2 have a spatial distribution that is homogeneous with the properties of the instrument and the observed terrain $\mathcal{P}$. We use this spatial homogeneity to substitute space for time. For example, we consider that elevations $h(x_1,y_1,t)$ and $h(x_2,y_2,t)$ of $\mathcal{D}$ acquired on the same surface type (e.g., bare rock), and under the same topographical attributes (e.g., flat) will have similar specific biases and variance:

$$\left.\begin{aligned}\delta h_s(x_1,y_1) &\approx \delta h_s(x_2,y_2)\\ \sigma_h(x_1,y_1) &\approx \sigma_h(x_2,y_2)\end{aligned}\right\} \text{for } \mathcal{P}(\mathrm{x_1},\mathrm{y_1}) = \mathcal{P}(\mathrm{x_2},\mathrm{y_2}). \quad (5)$$

Combining the assumptions of Eqs. 3 and 5, and provided that we describe all the properties $\mathcal{P}$ of spatial homogeneity, a large sample size can be used to infer δh and σ_h at each location (x,y) from a single difference between a DEM and an independent source of elevation data. The properties of spatial homogeneity $\mathcal{P}$ could differ between biases and variance. In the following, we assume that specific elevation biases, if they exist, are independently corrected and focus on characterizing the elevation variance σ_h^2.

D. Elevation difference with an independent source

After performing affine alignment of elevations $\hat{h}_1(x,y,t_1)$ from a first source $\mathcal{D}_1$ and elevation $\hat{h}_2(x,y,t_2)$ of a second source $\mathcal{D}_2$, we subtract them to derive elevation differences $dh_{1-2}(x,y)$. Assuming independence between the error of each elevation source, the variance of the difference is:

$$\sigma^2_{dh_{1-2}}(x,y) = \sigma^2_{h_1}(x,y) + \sigma^2_{h_2}(x,y). \quad (6)$$

By selecting a second source to observe $\hat{h}_2$ that is of higher precision than the first source that observes $\hat{h}_1$, the analysis of the differences $\hat{h}_2 - \hat{h}_1$ will largely capture the variance of the first source. For example, if the second source is three times more precise than the first, Eq. 6 implies that about 95% of the variance of the elevation difference will originate from the first source, yielding:

$$\sigma_{h_1}(x,y) \approx \sigma_{dh_{1-2}}(x,y). \quad (7)$$

Alternatively, if h_1 and h_2 originate from independent acquisitions of the same instrument and processing, we have:

$$\sigma_{h_1}(x,y) = \frac{\sigma_{dh_{1-2}}(x,y)}{\sqrt{2}}. \quad (8)$$

Thus, we use elevation differences to infer on σ_h, which can be converted from either Eqs. 7 or 8.

E. Discriminating elevation bias from variance in spatial statistics

To further analyze elevation variance, we need to discriminate bias from variance. When analyzing elevation differences, what appears as a bias at the local scale could also be a form of long-range correlation at larger scales (Fig. 1b-c). This distinction is directly related to the assumption of second-order stationarity of spatial statistics. For elevation differences, second-order stationarity implies that the following assumptions should be fulfilled (see Supplementary Section II-A):

1) a first assumption of stationary mean, i.e. that the average of elevation differences $dh(x, y)$ is constant over large areas;
2) a second assumption of stationary variance, i.e. that the variance of elevation differences $\sigma_{dh}(x, y)$ is constant over large areas; and
3) a third assumption of spatially consistent covariance, i.e. that the correlation between random errors of elevation differences only depends on the distance between observations.

Large areas here refer to areas slightly smaller than the size of the study domain, typically within an order of magnitude. As such, a correlated error with a correlation range that is orders of magnitude larger than the size of the study domain might be considered a vertical bias common to the entire DEM grid (Fig. 2). And, inversely, such a bias placed in the context of a larger study domain might be considered as a correlated error, if the elevation differences fulfill the above assumptions.

Thanks to the affine alignment of our elevation differences, we verify the first assumption of stationary mean. However, the heteroscedasticity of elevations (see Section II-B) invalidates the second and third assumptions, and therefore a non-stationary framework needs to be defined.

F. A non-stationary spatial framework for DEM analysis

To perform spatial statistics with a non-stationary variance, transformation of the data towards a stationary variance is necessary. The transformation depends on the nature of the spatial variability and correlations. In DEMs, we identify two types of correlation: short-range ones related to resolution, and long-range ones related to correlated noise or digitization artefacts. While the latter appear unrelated to the heteroscedasticity of elevation, the former are similarly linked to local instrument- and terrain-dependent variables (see Sections II-B and II-C). We thus subdivide elevation variance into elevation heteroscedasticity and spatial correlation of errors (Fig. 2) assuming that longer-range correlations are independent of elevation heteroscedasticity, which yields:

$$\sigma^2_{dh}(x, y) = \sigma^2_{dh_{sr}}(x, y) + \sigma^2_{dh_{lr}}, \tag{9}$$

where $\sigma^2_{h_{sr}}(x, y)$ is the variable short-range variance at (x, y), $\sigma^2_{h_{lr}}$ is the constant long-range variance.

Using the variable spread $\sigma_{dh}(x, y)$, the elevation differences can be standardized into a standard score z_{dh} with unit variance, which fulfills the second assumption of second-order stationarity:

$$z_{dh}(x, y) = \frac{dh(x, y)}{\sigma_{dh}(x, y)}. \tag{10}$$

Additionally, the spatial covariance $C_{z_{dh}}$ of z_{dh}, related to the variogram $\gamma_{z_{dh}} = 1 - C_{z_{dh}}$, is also free of the influence of heteroscedasticity and now fulfills the third assumption of second-order stationarity:

$$\gamma^2_{z_{dh}}(d) = \left(\frac{\overline{\sigma_{dh_{sr}}}|_{\mathcal{D}}}{\sigma_{dh}}\right)^2 \gamma_{sr}(d) + \left(\frac{\sigma_{dh_{lr}}}{\sigma_{dh}}\right)^2 \gamma_{lr}(d), \tag{11}$$

where d is the spatial lag, i.e. the distance between two given observations, $\overline{\sigma_{dh_{sr}}}|_{\mathcal{D}}$ is the average of $\sigma_{dh_{sr}}$ in the DEM $\mathcal{D}$, and γ_{sr} and γ_{lr} are the short- and long-range variogram functions.

With all the assumptions in our framework fulfilled, we can now reliably use spatial statistics for uncertainty propagation. To this end, we require an estimate of the elevation dispersion $\sigma_{dh}(x, y)$ and of the variogram of the standard score $\gamma_{z_{dh}}(d)$, which describe the heteroscedasticity and the spatial correlation of errors, respectively. We also need to ensure that our assumption of spatial homogeneity remains valid when using stable terrain as an error proxy to infer heteroscedasticity and spatial correlations on moving terrain. In the following, we address these aspects by utilizing near-simultaneous data and implementing robust methods.

IV. Data

A. Mont-Blanc case study: simultaneous DEMs

To demonstrate the methods associated with our proposed framework, we present a case study of two DEMs generated one day apart in the Mont-Blanc massif, French Alps (Fig. 3b, Table I). These DEMs were produced with a spatial posting of 5 m from SPOT-6 and Pléiades stereo images using the Ames Stereo Pipeline [134]. We utilize the temporal closeness of the two acquisitions to assess if stable terrain can be used as a proxy for moving terrain, considering a negligible elevation change on moving terrain.

We present an additional case study in the Northern Patagonian Icefield to illustrate the influence of the quality of stereo-correlation, a sensor-dependent variable, on elevation heteroscedasticity (Supplementary Section I-A with additional refs. [66], [135], [136]). This case study is based on simultaneously acquired ASTER [47] and SPOT-5 images. Furthermore, the DEMs used to illustrate noise patterns (Figs. 1 and S1) are described in the Supplementary Section I-B with additional refs. [137]–[139].

TABLE I
Nearly-simultaneous Pléiades and SPOT-6 DEMs used for the Mont-Blanc case study.

Instrument	Acquisition time	Resolution of stereo-pair
Pléiades	24/10/2017, 12:00 CET	1.5 m
SPOT-6	25/10/2017, 12:30 CET	0.7 m

B. Inventory and land cover products

We define moving terrain as glacierized, forested and seasonally snow-covered terrain, and exclude water bodies from our analysis. The remaining terrain is assumed to be stable. We mask glaciers using the Randolph Glacier Inventory 6.0 (RGI 6.0) outlines [140], which are delineated from images with a typical resolution of 15–30 m. We mask forests and water bodies using the ESA Climate Change Initiative Land Cover version 2.0.7 [141] which has a resolution of 300 m. Forested terrain corresponds to either broadleaved, needle-leaved, evergreen, or deciduous tree cover classes.

We identify specific elevation biases over forested terrain between the SPOT-6 and Pléiades DEMs – likely owing to different native resolution, orientation and spectral bands (Fig. S3a) – and thus exclude this terrain from our analysis. Our end-of-summer acquisitions contain little snow outside of glacierized surfaces. Therefore, we did not mask off-ice snow cover. Ultimately, in our analysis, moving terrain corresponds to glacierized terrain.

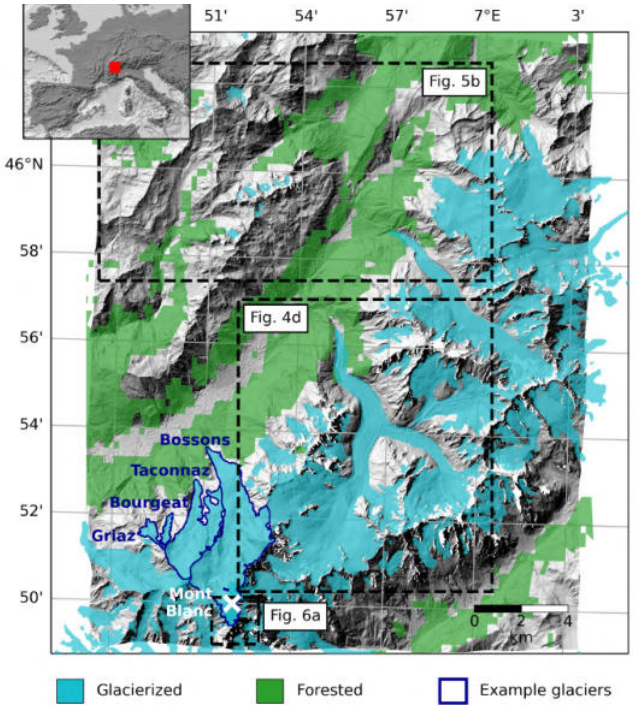

Fig. 3. **Mont-Blanc case study.** Hillshade of Pléaides DEM and land cover for the Mont-Blanc case study. Example glaciers serve to illustrate Section VI-C.

V. Methods

A. Robust statistics and alignment

We use the median instead of the mean as a robust estimator of central tendency, and the normalized median absolute deviation (NMAD) instead of the standard deviation as a measure of statistical dispersion. Both choices are to mitigate the effects of frequent outliers in DEMs [142]. Combining these estimators with the dense sampling of stable terrain also ensures robustness to elevation changes of potentially unmasked moving terrain. This includes rare events such as landslides or ground subsidence, or events that can occur over a small portion of the analyzed terrain such as volcanic uplift or sediment transport. We coregister DEMs on stable terrain for horizontal and vertical shifts following the aspect-slope relation described in [77] and we correct for possible tilts through least squares optimization of a plane [71].

B. Heteroscedasticity

We estimate elevation heteroscedasticity by sampling an empirical dispersion of elevation differences $\hat{\sigma}_{dh}$ using the NMAD of binned categories along the terrain slope α [143] and the terrain maximum absolute curvature c (Figs. 4a-c and S4). Maximum absolute curvature is defined as the maximum of the absolute profile curvature and the absolute planform curvature at each location [144]. All terrain attributes are estimated from the Pléiades DEM that contains the least data gaps. When available, the binning can also include an instrument quality factor q, such as the quality of stereo-correlation (Supplementary Section I-A, Figs. S5–S7) or interferometric coherence.

We numerically model the empirical dispersion $\hat{\sigma}_{dh}$ as a function σ_{dh} of the terrain- and sensor-dependent variables (α, c, q) by multidimensional linear interpolation of the binned data (Fig. S8). The modelling of this variability can also be performed by fitting parametric models, for example an exponential model with the slope or a linear model with the maximum curvature (Fig. S9). These are more robust in the case of small sample sizes of elevation differences.

We standardize the elevation differences dh following Eq. 10, using the modelled dispersion $\sigma_{dh}(\alpha, c, q)$:

$$z_{dh} = \frac{dh}{\sigma_{dh}(\alpha, c, q)}. \tag{12}$$

After standardization, we verify that the standard score of the elevation differences matches a normal distribution by quantile-quantile plotting, and by comparison to a normal distribution fit [142], [145] (Fig. S10). The substantial improvement validates our choice of terrain slope and maximum curvature as key variables to describe elevation heteroscedasticity, as those largely explain the departure of random elevation errors from normality.

C. Spatial correlations

We estimate spatial correlations by sampling an empirical variogram $\hat{\gamma}$ on the standard score z_{dh} using Dowd's estimator [146], [147] (Fig. 5a):

$$2\hat{\gamma}_{z_{dh}}(d) = 2.198 \cdot \text{median}(z_{dh}(x, y) - z_{dh}(x', y'))^2, \tag{13}$$

where z_{dh} is the standard score of elevation differences, and locations (x, y) and (x', y') are separated by a spatial lag d.

Dowd's estimator is based on median absolute deviations, and consequently more robust than the Matheron [148] or Cressie-Hawkins [149] estimators classically used (see Supplementary Section II-B based on additional ref. [150]). We

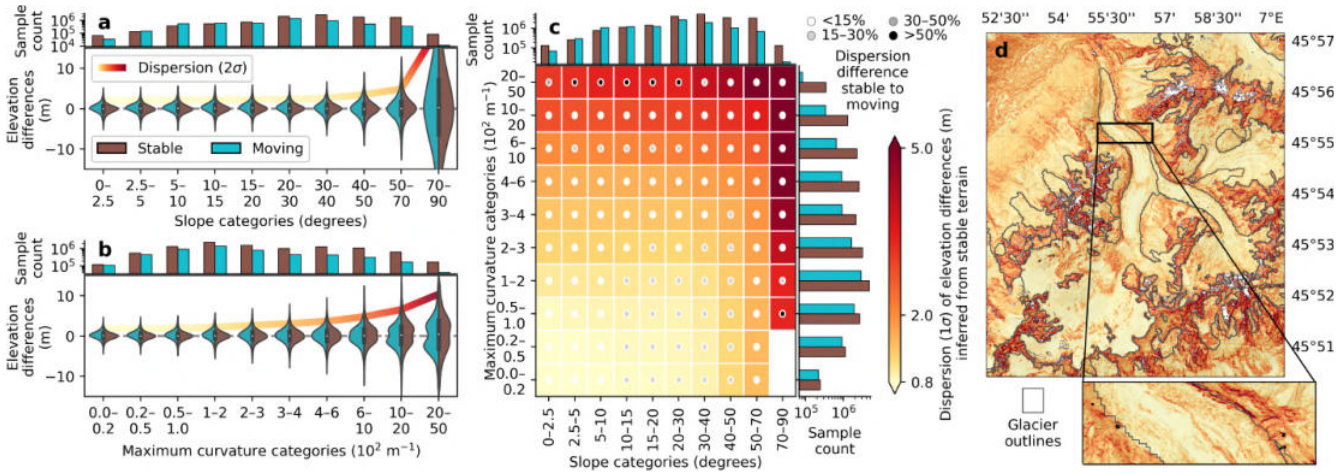

Fig. 4. **Heteroscedasticity inference from stable terrain as function of slope and curvature for the Mont-Blanc case study. a-b,** Violin plots of elevation differences on stable and moving terrain by bins of **(a)** slope and **(b)** maximum curvature. Dispersion inferred from stable terrain is showed by a thick line with color matching other panels. Note the logarithmic scales of histograms. **c,** Heatmap of stable terrain dispersion for slope and maximum curvature. Bins with a relative dispersion difference between stable and moving terrain greater than 30% (dark gray and black dots) contain less than 1% of samples. **d,** Inferred spatial distribution of vertical precision for all terrain, with inset that matches Fig. 1a.

verify the increased robustness of Dowd's estimator for the Mont-Blanc case study (Figs. S11 and S12).

To improve the variogram estimation, we introduce a pairwise subsampling method based on iterative subsetting of pairwise combinations between a disk and multiple rings centered on a random point (see Supplementary Section II-C). As variograms were historically sampled from point measurements [112], traditional sampling methods are less computationally efficient on large grids. Most critically, they are inefficient at sampling pairwise distances evenly across spatial scales, which is substantially improved by our method to estimate more reliably both short-range and long-range correlations (Fig. S13). Finally, we derive empirical variograms for 100 independent realizations with the same binning. We estimate our final empirical variogram by the mean of all realizations at each spatial lag with, as an empirical uncertainty, the standard error of the mean.

To derive a spatially continuous representation of the variogram, we calibrate an analytical model γ_{zdh} with the empirical variogram $\hat{\gamma}_{z_{dh}}$. We fit a sum of k variogram models $V(s_k, r_k, d)$, optimizing their partial sills s_k (i.e. correlated variance) and ranges r_k (i.e. correlation length) simultaneously by weighted least squares, using as weights the squared inverse of the empirical uncertainties previously detailed (Fig. 5a):

$$\gamma_{z_{dh}}(d) = \sum_k V_k(s_k, r_k, d). \tag{14}$$

For the Mont-Blanc study, we find no significant improvement in least-squares residuals when fitting more than three models, which are capable of capturing one short-range and two long-range correlations (Fig. S14, Table S2). The two long-range correlations match the along- and cross-track lengths of low-amplitude undulations in the elevation differences (Fig. 5b). We thus use three models to avoid the possible overfitting of a larger number of summed models. Generally, k should be chosen to reflect the number of distinct ranges in the patterns of DEM noise. For instance, ASTER undulations are characterized by two wavelengths of 1–2 km and 5–10 km in the along-track direction, and a cross-track distance of 60 km (Fig. S1a), which better fits three distinct long-range models [47] for a total of four ranges.

We also identify a low sensitivity to different variogram model types (Fig. S15, Tables S3 and S4), which shows that adequately modelling the multi-range nature of the spatial correlations is more important than refining that of their spatial form (Fig. 5b). For the Mont-Blanc case study, we reached the smallest least-squares residuals using a gaussian model $G(s, r, x - x')$ at short ranges, and spherical models $S(s, r, x - x')$ at long ranges [151] and used those henceforth:

$$G(s, r, d) = s\left(1 - e^{-\left(\frac{2d}{r}\right)^2}\right), \text{ and} \tag{15}$$

$$S(s, r, d) = \begin{cases} s\left(\frac{3}{2}\frac{d}{r} - \frac{1}{2}\left(\frac{d}{r}\right)^3\right) & \text{if } 0 < d < r, \\ s & \text{if } d \geq r. \end{cases} \tag{16}$$

D. Uncertainty propagation

1) Simulation methods for elevation derivatives: For derivatives of elevation with a complex spatial gradient, such as terrain slope and aspect later analyzed, we use simulation methods. We find similar results using Fourier randomization [124], [152] and unconditional Gaussian simulation [117], [153], and thus only use the former in the following. For 1,000 realizations, we simulate a random correlated error field of the standard score z_{dh} based on the modelled spatial correlation $\gamma_{z_{dh}}$ in Eq. 14. We then de-standardize z_{dh} using Eq. 12, and add the resulting elevation error field to the studied DEM. For each of these DEM realizations with an added error field, we then compute the terrain attribute of interest (e.g., terrain slope or aspect), for which we can study the distribution of errors.

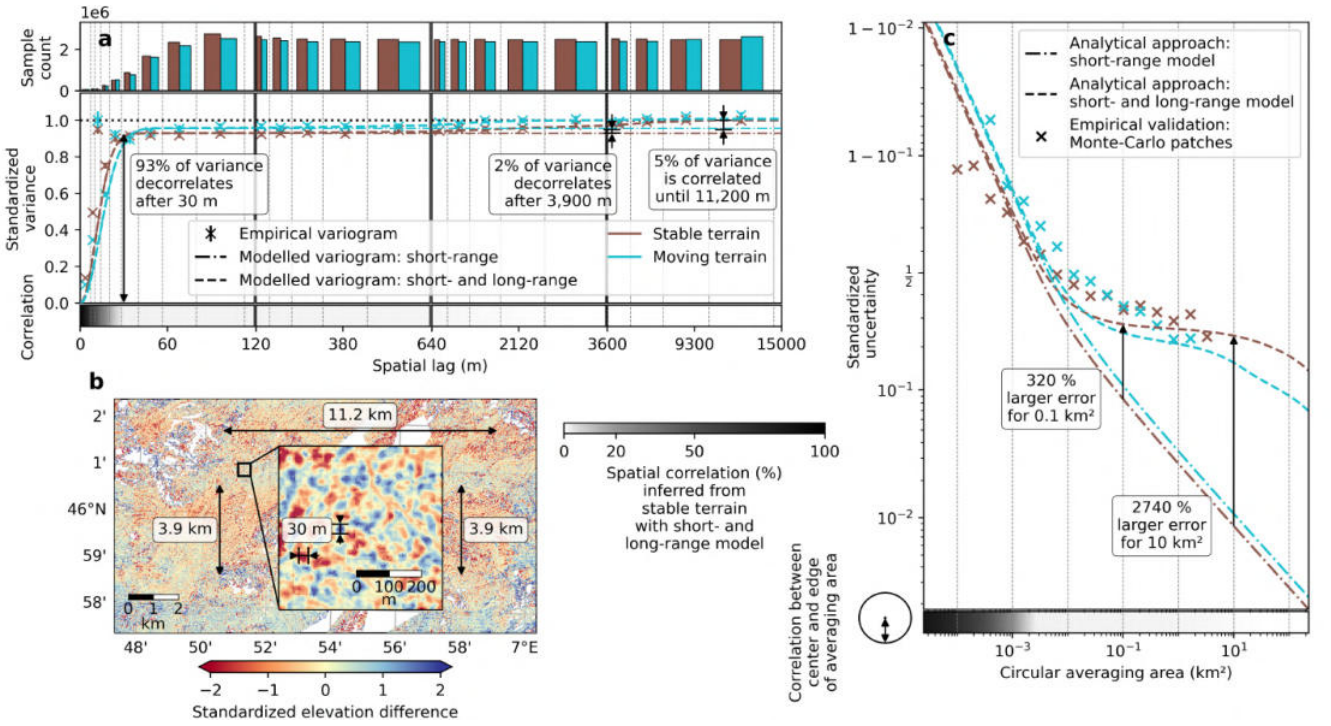

Fig. 5. **Spatial correlation inference from stable terrain for the Mont-Blanc case study. a,** Spatial variogram of standardized elevation differences on stable and moving terrain. The empirical variogram is based on Dowd's estimator [146] and modelled by either a short-range spherical model or the sum of short- and long-range spherical models. **b,** Excerpt of the standardized elevation difference map, which highlights the correlated signals at both short-range (30 meters) and long-range (3.9 km in the along-track direction, 11.2 km in the cross-track direction). **c,** Standardized elevation uncertainty with increasing circular averaging area validated by empirical Monte Carlo sampling. Note the logit scale of the Y-axis.

2) Theoretical approximation methods for spatial derivatives: For spatial derivatives such as the average $\overline{dh}$ of elevation changes dh in an area A, we derive an exact analytical solution of the uncertainty in the spatial average $\sigma_{\overline{dh}}$:

$$\sigma^2_{\overline{dh}} = \frac{1}{N^2}\sum_{i=1}^{N}\sum_{j=1}^{N}\rho_{ij}\sigma_{dh_i}\sigma_{dh_j}, \tag{17}$$

where N denotes the number of samples i falling in the area A, σ_{dh_i} is the vertical precision of pixel i, and $\rho_{ij} = (1-\gamma_{z_{dh}}(d))$ is the spatial correlation between pixel i and pixel j based on their distance d.

In practice, Eq. 17 raises the issue of scaling exponentially with the number of samples, possibly resulting in trillions of calculations. To remedy this, we propose an approximation for spatially contiguous areas, inspired by the approach of [65] that computes a single aerial integral by approximating the area A by a disk of the same area. Here, for each pixel k of a random subset of K pixels within the N pixels, we compute the single aerial integral of the variogram numerically. We then approximate the variogram integral by the average of these subset aerial integrations (see Supplementary Section II-E):

$$\sigma^2_{\overline{dh}} \approx \overline{\sigma^2_{dh}}|_A \frac{1}{N}\frac{1}{K}\sum_{k=1}^{K}\sum_{i=1}^{N}\left(1-\gamma_{z_{dh}}(x_k-x_i)\right), \tag{18}$$

where $\overline{\sigma^2_{dh}}|_A$ is the average variance of the elevation differences of pixels i in the area A:

$$\overline{\sigma^2_{dh}}|_A = \frac{1}{N}\sum_i \sigma^2_{dh_i}. \tag{19}$$

We show that our method improves the accuracy of the theoretical approximation of [65] by accounting for more complex area shapes than disks while maintaining computational efficiency (Fig. S16). Additionally, these formulations can be linked to a number of effective samples, which describes the number of samples among the N pixels in area A that are statistically independent based on the spatial correlations modelled by $\gamma_{z_{dh}}$ (see Supplementary Section II-D).

Once uncertainties have been integrated from a spatial support (e.g., pixels) to a larger spatially contiguous ensemble (e.g., glaciers), they can be propagated again to a larger ensemble (e.g., all glaciers in a region) following Krige's relation of transitivity [112], [154]. For this, Eq. 17 can be applied for each pair of spatially contiguous ensembles i and j of area A_i with the same variogram $\gamma_{z_{dh}}$ composed of the k summed models $V_k(s_k, r_k, d)$:

$$\begin{aligned}\sigma_{\overline{dh}} = \frac{1}{(\sum_i A_i)^2}\sum_k\sum_i\sum_j\Big(&\sigma_{\overline{dh}_{k,i}}\sigma_{\overline{dh}_{k,j}} \\ &-V_k(\sigma_{\overline{dh}_{k,i}}\sigma_{\overline{dh}_{k,j}}, r_k, d_{i-j})\Big)A_iA_j,\end{aligned} \tag{20}$$

where d_{i-j} is the distance between the centroids of ensemble i and j, and $\sigma_{\overline{dh}_{k,i}}$ is the spatially integrated uncertainty

of ensemble i associated to the variogram model V_k, partial sill s_k and range r_k with pixel pairs n and m (see Eq. 17):

$$\sigma_{\overline{dh}_{k,i}} = \frac{1}{N^2} \sum_{n=1}^{N} \sum_{m=1}^{N} (s_k - V_k(s_k, r_k, x_n - x_m)) \, \sigma_{dh_n} \sigma_{dh_m}. \quad (21)$$

Furthermore, we use a Monte Carlo spatial sampling method to validate our uncertainties of spatially averaged elevations, thus indirectly verifying the robustness of our modelled spatial correlations (Fig. 5c). We randomly sample up to 10,000 circular patches of area A without replacement. We compute the mean $\overline{dh}$ inside circular patches, keeping only those with more than 80% valid elevation differences dh to mitigate the effects of missing data. We use the NMAD of 10,000 realizations to empirically estimate the uncertainty of the spatially averaged dh of area A, and repeat this procedure for varying area sizes A (Fig. 5c). This method substitutes repeated correlated simulation of Fourier randomization or Gaussian simulation by a repeated spatial sampling, relying on the assumption of spatial homogeneity of variance on stable terrain (Section III-C). As it requires a large number of independent patches to produce a robust estimate, the area size A for which it can estimate an uncertainty is limited to sizes much smaller than that of the spatial domain. It is also highly dependent on the availability of stable terrain. Therefore, we use it only for validation purposes.

VI. Results and discussion

In Section VI-A below, we discuss the use of stable terrain as an error proxy based on the methods applied to the Mont-Blanc case study. In Sections VI-B and VI-C, we then analyze the impacts of heteroscedasticity and spatial correlations when propagating elevation variance into uncertainties of pixel-scale elevation derivatives such as terrain slope, or spatial derivatives such as glacier volume changes. In those two sections, we provide examples based on the Mont-Blanc case study and determine the impact of our methods for a set of assumptions on the variance properties during uncertainty propagation:

- either homoscedastic elevation (constant variance, shortened "homosc.") or heteroscedastic elevation (variable variance, "heterosc."); and
- either no spatial correlation (shortened "no corr."), or only short-range correlations ("short-range"), or both short- and long-range correlations ("long-range").

In this exercise, the most realistic case refers to the one that accounts for potential elevation heteroscedasticity and potential short- and long-range correlations. Uncertainties are reported as a symmetric confidence interval of 1σ (68% confidence level) or 2σ (95%), specified in each case.

A. Validation of stable terrain as an error proxy

We test the validity of using stable terrain as a proxy of elevation errors for moving terrain on the nearly simultaneous DEMs of the Mont-Blanc case study. We find that elevations on moving terrain exhibit the same heteroscedasticity with slope and curvature than those on stable terrain, with less than 1% of binned samples that differ by more than 30% (Fig. 4a-c). We additionally verify that this elevation heteroscedasticity is continuous between neighbouring bins when using robust estimators, thereby consolidating our assumption of spatial homogeneity (Section III-C, Eq. 5). By extending this assumption to the case of moving terrain, we infer a complete map of vertical precision (Fig. 4d).

We find similar spatial correlations of errors between stable and moving terrain (Fig. 5a). Values of partial sills and ranges of the variogram models that describe these correlations are within the same orders of magnitude (Table II), despite greater differences at long ranges due to the limited pairwise samples available on moving terrain. Using our Monte Carlo sampling method, we validate the increased robustness of using multiple correlation ranges to estimate uncertainties across spatial scales (Fig. 5c). Our results indicate that using a short-range model alone underestimates elevation uncertainties by several orders of magnitude for areas larger than 0.1 km².

TABLE II
Estimated variogram model parameters for the spatial correlations of elevation errors in the Mont-Blanc case study. Stable and moving terrain is distinguished (columns). Gaussian components are listed for the short-range model and spherical components for the long-range ones, as in Fig. 5. Partial sills are expressed as a percentage of the total variance.

Model parameters	Stable	Moving
Sill of short-range model	93%	95%
Range of short-range model	30 m	38 m
Sill of 1st long-range model	2%	4%
Range of 1st long-range model	3,900 m	2,400 m
Sill of 2nd long-range model	5%	1%
Range of 2nd long-range model	11,200 m	10,800 m

For elevation heteroscedasticity, our results highlight the importance of elevation standardization to ensure an adequate scaling when inferring on another type of terrain (e.g., from steep, stable terrain to flat, moving terrain). Yet, our analysis only exemplifies snow- and ice-covered terrain with high-resolution stereophotogrammetric DEMs. The physical properties of the observed terrain in relation to the utilized sensor might in some cases invalidate our assumption of spatial homogeneity. For instance, we found that our standardization did not mitigate the larger errors of elevation over forested areas (Fig. S3a). In such a case, an upfront investigation of specific elevation biases is required. After these biases are corrected, a refined modelling of elevation heteroscedasticity based on sensor-dependent variables can help to reach a good description of the properties of spatial homogeneity. We indeed found a strong relationship with the quality of stereo-correlation for the case study of the Northern Patagonian Icefield (Figs. S6 and S7). The rougher resolution (15 m) and spectral range (8 bits) of the ASTER stereo images, compared to those of SPOT-6 and Pléiades (metric resolution and 12-bits), leads to a significant variability in elevation errors with terrain texture.

For spatial correlations, we highlight the value of standardization to reduce variability for empirical variogram estimation (Figs. S3b-d and S12). It is especially useful to deconvolve the long-range correlations with small magnitude to the short-range ones. Heteroscedasticity may indeed explain the short-range variogram anisotropy found by previous studies [155]. We nevertheless identify a slight difference in the well-constrained short correlation range between stable and moving terrain (30 m vs 38 m, respectively; Table II). This difference might be due to the rougher interpolation of stereophotogrammetric block-matching algorithms over bright, lower-texture glacierized terrain. In some cases, sensor properties or processing schemes influence not only the magnitude of spatial variability but also the scale of correlations. Developing a statistical framework that continuously includes these effects might be overly complex for most analyses that, instead, could adjust estimates of short-range correlation depending on the type of observed terrain.

We conclude that stable terrain is a valid proxy for error analysis, provided that elevation heteroscedasticity is taken into account. However, the quality of statistical inference from this error proxy depends directly on the number of stable terrain samples available. For some DEMs, these samples might be scarce in the proximity of continuous expanses of moving terrain (e.g., at the margins of ice sheets or large forests) and thus insufficient to perform robust inference. To address this, the stable terrain of independent DEMs, possibly located elsewhere, could be utilized if they are generated from the same instrument and processing chain. Many DEMs indeed have consistent error properties between segments acquired under similar conditions around the world (e.g., [47], [59], [156]). For instruments with correlated noise of varying amplitude, such as Pléiades or ASTER, long-range correlations can be more robustly inferred from a multiple-acquisition average of variograms.

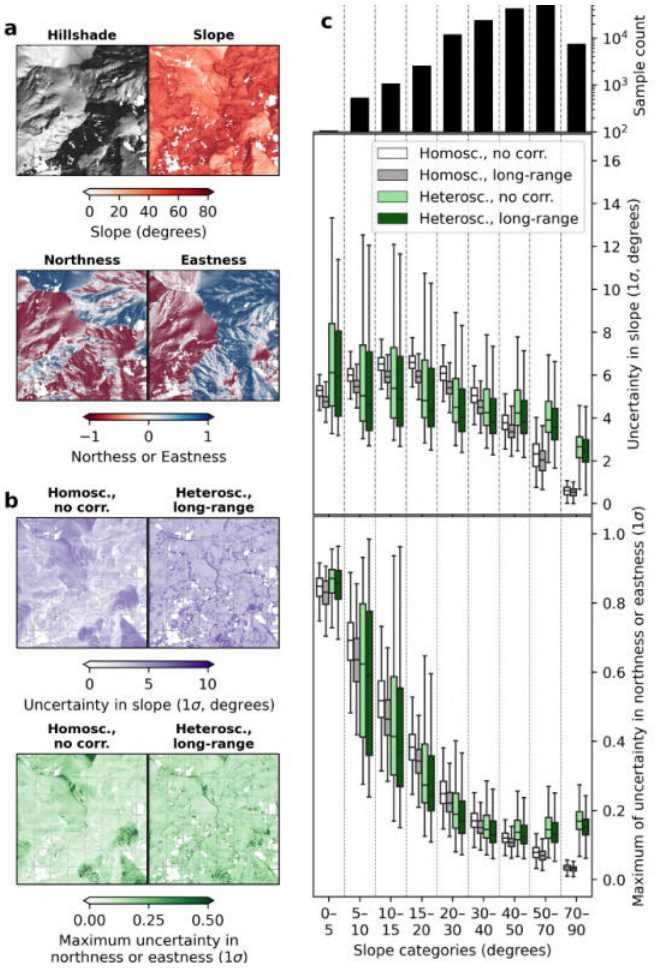

Fig. 6. **Uncertainty propagation to terrain slope and aspect at the Mont-Blanc summit. a,** Hillshade and terrain attributes based on the Pléiades DEM. **b,** Slope and aspect uncertainty estimated by the half-difference between the 16^{th} and 84^{th} percentiles of 1,000 simulated terrain attributes at each pixel. **c,** Distributions of slope and aspect uncertainties by category of terrain slope for each set of assumptions, with boxes denoting the interquartile range and whiskers extending to the entire distribution.

B. Impact on pixel-scale derivatives of elevation: example with terrain slope and aspect

We illustrate the propagation of elevation uncertainty to the slope and aspect in a 4 km² area around the Mont-Blanc summit (Fig. 6a). We select this area due to its wide range of slopes and aspects, and its small extent facilitating computationally expensive simulations. To avoid the circularity of the aspect variable when assessing uncertainty, we divide it into northness (i.e. cosine of the aspect) and eastness (i.e. sine of the aspect) which denote, respectively, the north-south and east-west tilt of the slope.

We propagate uncertainties in the Pléiades DEM by simulating random elevation error fields (see Section V-D) for every set of assumptions (Fig. S17). For this example, we assume that SPOT-6 and Pléiades have random errors of similar amplitude, and estimate the random errors of the Pléiades DEM following Eq. 8. We generally note a strong deviation from normality and asymmetry in the simulated uncertainty distribution of terrain attributes (Fig. S18). While this asymmetry requires specific considerations for in-depth terrain analysis, we here provide a simplified picture by estimating a symmetric 1-σ uncertainty derived from the half-difference between the 16th and 84th percentile of the simulated slope, northness or eastness of each pixel.

Our analysis reveals that elevation heteroscedasticity plays a major role in the spatial distribution of uncertainties in slope and aspect. In particular, it exacerbates errors in steep and rough terrain. Spatial correlations moderately affect uncertainties by slightly reducing their amplitude (Fig. 6b-c). We interpret the latter to be due to an increase in the spatial coherence of terrain derivatives when the elevation errors are spatially correlated. Since topographical attributes are derived over a 3x3 pixel window, the closer the short-range spatial correlations are to a 3-pixel length, the larger the impact on the amplitude change (Fig. S19).

By aggregating uncertainties into slope categories, we show that uncertainties in flat terrain are overestimated when assuming homoscedasticity and no spatial correlation, while those in steep terrain are underestimated by up to a factor

of 10 (Fig. 6c). Slope uncertainties decrease near slopes of 90 degrees, likely because elevation errors tilt the terrain in different orientations while generally maintaining a steep slope, which translates into aspect uncertainties. We reach similar conclusions when aggregating uncertainties by maximum absolute curvature categories, our second variable that describes elevation heteroscedasticity (Fig. S20).

C. Impact on spatial derivatives of elevation: example with glacier volume changes

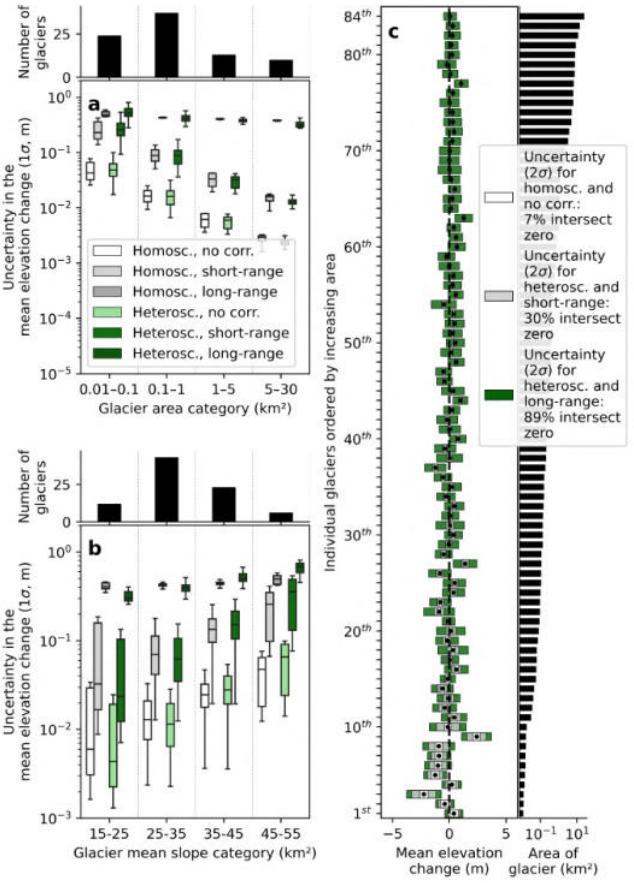

Fig. 7. **Uncertainty propagation to glacier mean elevation changes at the Mont-Blanc massif. a-b,** Distributions of uncertainty of glacier mean elevation change by category of area and average terrain slope for each set of assumption, with boxes denoting the interquartile range and whiskers extending to the entire distribution. **c,** Empirical evaluation of uncertainty ranges for mean glacier elevation changes in the Mont-Blanc case study. Correct uncertainty estimates should cross the vertical zero line in 95% of the cases.

We consider 84 glaciers in the Mont-Blanc massif that have at least 85% of their area covered by valid elevation differences. We analyze the mean elevation changes within the outline of each glacier, which can be converted to volume changes after multiplication by the glacier area, and propagate uncertainties for each set of assumptions.

We find that spatial correlations strongly hamper the decrease in uncertainty with increasing glacier area (Fig. 7a). Long-range correlations are the main contributor to uncertainty for large areas, mirroring the validation of Fig. 5c. While our case study has long-range correlations of only 7% of the variance, uncertainties of mean elevation changes for glaciers larger than 10 km² are underestimated by a factor of about 25 when based solely on short-range correlation. This is striking, and even more so when realizing that the underestimation is nearly by a factor of 150 when totally omitting spatial correlations. This dramatic increase is explained by the fact that long-range correlations essentially correspond to local biases.

Heteroscedasticity has a moderate influence on the uncertainty of each glacier, impacting its amplitude by a factor of 1 to 3. The uncertainty of glaciers located in flat areas is overestimated when using a homoscedastic assumption due to the larger average variance over rougher, stable terrain. On the contrary, the uncertainty of the steepest glaciers is underestimated (Fig. 7b). Using the empirical comparison provided by the nearly simultaneous volume changes (Fig. 7c), we show that the uncertainties for the mean elevation change are most realistic when accounting for long-range spatial correlation. In such a case, 89% of the ranges intersect zero (the true volume change) at the 2σ level (i.e. 95% confidence), in contrast to only 30% for short ranges and 7% for no correlation. Yet, our uncertainties are slightly too low.

We identify the cause of this underestimation as the omission of a longer-range correlation close to the size of the DEM and thereby difficult to constrain. This longer-range correlation arises from the fact that along-track undulations are fully correlated in the cross-track direction with 20 km swath. Directional variography could help characterize such correlations, but would lead to a more difficult uncertainty propagation, with exacerbated complexity when combining several DEMs. Instead, we maintain an omnidirectional variogram to describe correlations, but assess a conservative estimate based on artificial undulations (Fig. S21). This results in the replacement of the 11.2 km correlation with a 20 km one (DEM swath width) and a partial sill twice larger. We then find that 93% of the uncertainties for glacier larger than 0.2 km² intersect zero at the 95% confidence level, confirming the increased robustness with these considerations. Only 87% do so for smaller glaciers, however. This discrepancy might be explained by unaccounted heteroscedasticity from landform-projected shadows that particularly affects small glaciers in steep and north-facing slopes.

TABLE III
SPATIAL UNCERTAINTY PROPAGATION AMONG GLACIERS IN THE MONT-BLANC MASSIF. MEAN ELEVATION CHANGE UNCERTAINTIES $\sigma_{\overline{dh}}$ ARE PROPAGATED USING EQ. 20.

Uncertainty of spatial average	Griaz and Bourgeat	Bossons and Taconnaz	All glaciers
$\sigma_{\overline{dh}}$ no corr. (m)	0.027	0.006	0.002
$\sigma_{\overline{dh}}$ short-range corr. (m)	0.027	0.006	0.002
$\sigma_{\overline{dh}}$ long-range corr. (m)	0.061	0.049	0.024
Glacier area (km²)	0.9	16.3	131.1

When uncertainties of volume change of several glaciers are propagated into that of the massif, correlations also come into play. We illustrate the propagation at different spatial scales

by considering several glacier groups: one group with the two small neighbouring glaciers of Griaz and Bourgeat, another group with the two large neighbouring glaciers of Bossons and Taconnaz, and a third group including all 84 glaciers (Fig. 3). We find identical uncertainties when considering no correlation, or only short-range correlations (Table III). This reflects the fact that all glaciers are separated by at least 30 m, i.e. a distance larger than that of our short-range correlation (Table II). Long-range spatial correlations have a large impact on the total uncertainty, however, with a tenfold underestimation of the uncertainty for all glaciers in the massif when omitting them. Increased uncertainties from long-range correlations mostly affect large neighbouring glaciers, as shown for Bossons and Taconnaz, but also affect smaller, disconnected glaciers such as Griaz and Bourgeat. The latter is true as long as the glaciers are within the correlation range of 11.2 km.

VII. Conclusions

In this study, we reviewed the literature on the accuracy and precision of DEMs. On the basis of the raised considerations regarding variable vertical precision and correlated noises, we proposed a non-stationary spatial framework for DEM uncertainty analysis. This framework allows to perform inference on a single difference between a DEM and independent elevation data on stable terrain, and to distinguish elevation biases from elevation variance. We developed robust methods to estimate and model both elevation heteroscedasticity and spatial correlation of elevation errors. We then validated that stable terrain is a reliable error proxy for other terrain types using pairs of DEMs derived from nearly simultaneous acquisitions for the Mont-Blanc massif and the Northern Patagonian Icefield.

We illustrated the impact of our methods when propagating uncertainties to pixel-scale and spatial derivatives of elevation. For the pixel-scale terrain slope, uncertainties are underestimated by up to a factor 10 in rough and steep topography when omitting elevation heteroscedasticity. For glacier volume changes, the uncertainty of the volume change of a glacier of 10 km² is underestimated by a factor of 25 when omitting correlations with ranges of 3.9 and 11.2 km, despite their small cumulative magnitude of only 7% of the variance. This underestimation of long-range spatial correlation affects many studies relying on instruments plagued by noise, such as the widely used DEMs from SRTM and ASTER.

We provide an implementation of our methods in the Python package xDEM [157], which includes, in particular, DEM alignment, correction, and uncertainty analysis. Spatial statistics have long been used for uncertainty analysis, yet often suffered from a lack of accessibility [126]. The wider application of such analysis was still deemed as "unrealized" a decade ago [133], possibly also due to the scarcity of open-source and documented tools for spatial statistics. By providing our methodological tools within the frame of a package embedded in high-level programming languages that efficiently pairs with remote sensing analysis, we hope to foster a consistent, reproducible and accessible uncertainty analysis of DEMs.

We highlight the genericity of our spatial framework for uncertainty analysis and of our estimation methods for dense and outlier-prone grid data. Our framework holds the potential to be extended to other geospatial data. Gridded surface displacement, for instance, profit from the same error proxy of stable terrain and are increasingly used in a variety of applications. To describe the precision of such spatially structured data, we advocate for the use of additional metrics. These metrics should describe potential heteroscedasticity and spatial correlation of errors, reported, for example, in a tabular manner — parameters of variogram models; discrete categories of heteroscedasticity. Ultimately, the adoption of such new metrics is critical to progress towards a realistic description of error structure in geospatial data, and a robust propagation of uncertainties in Earth system science assessments.

Data and code availability statement

The code developed for the processing and analysis of all data, and the generation of figures and tables in this article is available at https://github.com/rhugonnet/dem_error_study, with routines implemented in the DEM analysis Python package xDEM available at https://github.com/GlacioHack/xdem with supporting documentation at https://xdem.readthedocs.io, and the spatial statistics Python package SciKit-GStat available at https://github.com/mmaelicke/scikit-gstat with supporting documentation at https://scikit-gstat.readthedocs.io.

Author contributions

R.H., F.B. and E.B. designed the study. F.B. performed an early analysis of spatial correlation for the Mont-Blanc case study. R.H. developed and tested non-stationary spatial statistics methods for DEMs with inputs from N.E., A.D., F.B. and E.B. R.H. implemented the methods in the Python package xDEM with main inputs from A.D. and E.M. All authors interpreted the results. R.H. performed the literature review and led the writing of the paper, and all other co-authors contributed.

Acknowledgments

We thank Dorde Masovic for realizing Fig. 2 with vector graphics. We thank Alexandre Wadoux for insightful exchanges on spatial statistics and Simon Gascoin for discussions on along-track undulations in Pléiades DEMs. We also thank Eyjólfur Magnússon and Joaquín Belart for providing insights into Gaussian simulations for DEMs. We thank Jonathan Bamber, César Deschamps-Berger and Matthias Huss for comments on early versions of the manuscript. SPOT6/7 data were obtained from GEOSUD (ANR-10-EQPX-20, programme 'Investissements d'Avenir'). INRAE is a member of Labex OSUG. R.H. acknowledges a fellowship from the University of Toulouse. R.H., A.D., E.M and D.F. acknowledge funding from the Swiss National Science Foundation, grant number 184634. E.B. acknowledges support from the French Space Agency (CNES) through ISIS and TOSCA programmes.

References

[1] H. Taud, J.-F. Parrot, and R. Alvarez, "DEM generation by contour line dilation," *Comput. Geosci.*, vol. 25, no. 7, pp. 775–783, Aug. 1999.

[2] Q. Weng, "Quantifying uncertainty of digital elevation models derived from topographic maps," in *Advances in Spatial Data Handling*. Springer Berlin Heidelberg, 2002, pp. 403–418.

[3] P. A. Rosen, S. Hensley, I. R. Joughin, F. K. Li, S. N. Madsen, E. Rodriguez, and R. M. Goldstein, "Synthetic aperture radar interferometry," *Proc. IEEE*, vol. 88, no. 3, pp. 333–382, Mar. 2000.

[4] R. Bürgmann, P. A. Rosen, and E. J. Fielding, "Synthetic aperture radar interferometry to measure earth's surface topography and its deformation," *Annu. Rev. Earth Planet. Sci.*, vol. 28, no. 1, pp. 169–209, May 2000.

[5] A. S. Walker, "Analogue, analytical and digital photogrammetric workstations: Practical investigations of peformance," *The Photogrammetric Record*, 1995.

[6] E. M. Mikhail, J. S. Bethel, and J. C. McGlone, *Introduction to Modern Photogrammetry*. Nashville, TN: John Wiley & Sons, Mar. 2001, vol. 19.

[7] E. P. Baltsavias, "Airborne laser scanning: basic relations and formulas," *ISPRS J. Photogramm. Remote Sens.*, vol. 54, no. 2-3, pp. 199–214, Jul. 1999.

[8] R. O. Dubayah and J. B. Drake, "Lidar remote sensing for forestry," *J. For.*, vol. 98, no. 6, pp. 44–46, Jun. 2000.

[9] S. Bhushan, D. Shean, O. Alexandrov, and S. Henderson, "Automated digital elevation model (DEM) generation from very-high-resolution planet SkySat triplet stereo and video imagery," *ISPRS J. Photogramm. Remote Sens.*, vol. 173, pp. 151–165, Mar. 2021.

[10] J. Biggs and T. J. Wright, "How satellite InSAR has grown from opportunistic science to routine monitoring over the last decade," *Nat. Commun.*, vol. 11, no. 1, p. 3863, Aug. 2020.

[11] J. Rosen, "Shifting ground," *Science*, vol. 371, no. 6532, pp. 876–880, Feb. 2021.

[12] N. Galiatsatos, D. N. M. Donoghue, and G. Philip, "High resolution elevation data derived from stereoscopic CORONA imagery with minimal ground control," *Photogrammetric Engineering & Remote Sensing*, vol. 73, no. 9, pp. 1093–1106, 2007.

[13] A. Dehecq, A. S. Gardner, O. Alexandrov, S. McMichael, R. Hugonnet, D. Shean, and M. Marty, "Automated processing of declassified KH-9 hexagon satellite images for global elevation change analysis since the 1970s," *Front Earth Sci.*, vol. 8, p. 516, 2020.

[14] E. C. Geyman, W. J J van Pelt, A. C. Maloof, H. F. Aas, and J. Kohler, "Historical glacier change on svalbard predicts doubling of mass loss by 2100," *Nature*, vol. 601, no. 7893, pp. 374–379, Jan. 2022.

[15] G. LeFavour and D. Alsdorf, "Water slope and discharge in the amazon river estimated using the shuttle radar topography mission digital elevation model," *Geophys. Res. Lett.*, vol. 32, no. 17, Sep. 2005.

[16] J. Oksanen and T. Sarjakoski, "Error propagation analysis of DEM-based drainage basin delineation," *Int. J. Remote Sens.*, vol. 26, no. 14, pp. 3085–3102, Jul. 2005.

[17] L. Hawker, P. Bates, J. Neal, and J. Rougier, "Perspectives on digital elevation model (DEM) simulation for flood modeling in the absence of a High-Accuracy open access global DEM," *Front Earth Sci.*, vol. 6, p. 233, 2018.

[18] B. Székely and D. Karátson, "DEM-based morphometry as a tool for reconstructing primary volcanic landforms: examples from the börzsöny mountains, hungary," *Geomorphology*, vol. 63, no. 1, pp. 25–37, Nov. 2004.

[19] T. Bolch, U. Kamp, J. Olsenholler, and M. Oluić, "Using ASTER and SRTM DEMs for studying geomorphology and glaciation in high mountain areas," in *New Strategies for European Remote Sensing*, M. Oluić, Ed. Rotterdam: Millpress, 2005, pp. 119–127.

[20] B. Žabota, B. Repe, and M. Kobal, "Influence of digital elevation model resolution on rockfall modelling," *Geomorphology*, vol. 328, pp. 183–195, Mar. 2019.

[21] A. Mueting, B. Bookhagen, and M. R. Strecker, "Identification of debris-flow channels using high-resolution topographic data: A case study in the quebrada del toro, NW argentina," *J. Geophys. Res. Earth Surf.*, vol. 126, no. 12, Dec. 2021.

[22] A. Ganas, G. Papadopoulos, and S. B. Pavlides, "The 7 september 1999 athens 5.9 ms earthquake: Remote sensing and digital elevation model inputs towards identifying the seismic fault," *Int. J. Remote Sens.*, vol. 22, no. 1, pp. 191–196, Jan. 2001.

[23] S. Vassilopoulou, L. Hurni, V. Dietrich, E. Baltsavias, M. Pateraki, E. Lagios, and I. Parcharidis, "Orthophoto generation using IKONOS imagery and high-resolution DEM: a case study on volcanic hazard monitoring of nisyros island (greece)," *ISPRS J. Photogramm. Remote Sens.*, vol. 57, no. 1, pp. 24–38, Nov. 2002.

[24] P. Grosse, B. van Wyk de Vries, P. A. Euillades, M. Kervyn, and I. A. Petrinovic, "Systematic morphometric characterization of volcanic edifices using digital elevation models," *Geomorphology*, vol. 136, no. 1, pp. 114–131, Jan. 2012.

[25] K. K. Singh and A. Singh, "Detection of 2011 sikkim earthquake-induced landslides using neuro-fuzzy classifier and digital elevation model," *Nat. Hazards*, vol. 83, no. 2, pp. 1027–1044, Sep. 2016.

[26] Y. Bühler, S. Kumar, J. Veitinger, M. Christen, A. Stoffel, and Others, "Automated identification of potential snow avalanche release areas based on digital elevation models," *Nat. Hazards Earth Syst. Sci.*, vol. 13, no. 5, pp. 1321–1335, 2013.

[27] A. E. Akay, H. Oğuz, I. R. Karas, and K. Aruga, "Using LiDAR technology in forestry activities," *Environ. Monit. Assess.*, vol. 151, no. 1-4, pp. 117–125, Apr. 2009.

[28] A. Räsänen, M. Kuitunen, E. Tomppo, and A. Lensu, "Coupling high-resolution satellite imagery with ALS-based canopy height model and digital elevation model in object-based boreal forest habitat type classification," *ISPRS J. Photogramm. Remote Sens.*, vol. 94, pp. 169–182, Aug. 2014.

[29] J. Griffin, H. Latief, W. Kongko, S. Harig, N. Horspool, R. Hanung, A. Rojali, N. Maher, A. Fuchs, J. Hossen, S. Upi, D. Edi, N. Rakowsky, and P. Cummins, "An evaluation of onshore digital elevation models for modeling tsunami inundation zones," *Front Earth Sci.*, vol. 3, p. 32, 2015.

[30] S. Kulp and B. H. Strauss, "Global DEM errors underpredict coastal vulnerability to sea level rise and flooding," *Front Earth Sci.*, vol. 4, p. 36, 2016.

[31] A. Hooijer and R. Vernimmen, "Global LiDAR land elevation data reveal greatest sea-level rise vulnerability in the tropics," *Nat. Commun.*, vol. 12, no. 1, p. 3592, Jun. 2021.

[32] M. K. Barker, E. Mazarico, G. A. Neumann, M. T. Zuber, J. Haruyama, and D. E. Smith, "A new lunar digital elevation model from the lunar orbiter laser altimeter and SELENE terrain camera," *Icarus*, vol. 273, pp. 346–355, Jul. 2016.

[33] Y. Wang and B. Wu, "Active machine learning approach for crater detection from planetary imagery and digital elevation models," *IEEE Trans. Geosci. Remote Sens.*, vol. 57, no. 8, pp. 5777–5789, Aug. 2019.

[34] Y.-C. Hsieh, Y.-C. Chan, and J.-C. Hu, "Digital elevation model differencing and error estimation from multiple sources: A case study from the meiyuan shan landslide in taiwan," *Remote Sensing*, vol. 8, no. 3, p. 199, Feb. 2016.

[35] P. Lacroix, "Landslides triggered by the gorkha earthquake in the langtang valley, volumes and initiation processes the 2015 gorkha, nepal, earthquake and himalayan studies: First results 4. seismology," *Earth Planets Space*, vol. 68, no. 1, pp. 1–10, 2016.

[36] D. H. Shugar, M. Jacquemart, D. Shean, S. Bhushan, K. Upadhyay, A. Sattar, W. Schwanghart, S. McBride, M. V. W. de Vries, M. Mergili, A. Emmer, C. Deschamps-Berger, M. McDonnell, R. Bhambri, S. Allen, E. Berthier, J. L. Carrivick, J. J. Clague, M. Dokukin, S. A. Dunning, H. Frey, S. Gascoin, U. K. Haritashya, C. Huggel, A. Kääb, J. S. Kargel, J. L. Kavanaugh, P. Lacroix, D. Petley, S. Rupper, M. F. Azam, S. J. Cook, A. P. Dimri, M. Eriksson, D. Farinotti, J. Fiddes, K. R. Gnyawali, S. Harrison, M. Jha, M. Koppes, A. Kumar, S. Leinss, U. Majeed, S. Mal, A. Muhuri, J. Noetzli, F. Paul, I. Rashid, K. Sain, J. Steiner, F. Ugalde, C. S. Watson, and M. J. Westoby, "A massive rock and ice avalanche caused the 2021 disaster at chamoli, indian himalaya," *Science*, Jun. 2021.

[37] M. Nolan, C. Larsen, and M. Sturm, "Mapping snow depth from manned aircraft on landscape scales at centimeter resolution using structure-from-motion photogrammetry," *The Cryosphere*, vol. 9, no. 4, pp. 1445–1463, Aug. 2015.

[38] R. Marti, S. Gascoin, E. Berthier, M. d. Pinel, T. Houet, and D. Laffly, "Mapping snow depth in open alpine terrain from stereo satellite imagery," *The Cryosphere*, vol. 10, no. 4, pp. 1361–1380, 2016.

[39] C. Deschamps-Berger, S. Gascoin, E. Berthier, J. Deems, E. Gutmann, A. Dehecq, D. Shean, and M. Dumont, "Snow depth mapping from stereo satellite imagery in mountainous terrain: evaluation using airborne laser-scanning data," *The Cryosphere*, vol. 14, no. 9, pp. 2925–2940, Sep. 2020.

[40] M. Bagnardi, P. J. González, and A. Hooper, "High-resolution digital elevation model from tri-stereo pleiades-1 satellite imagery for lava flow volume estimates at fogo volcano," *Geophys. Res. Lett.*, vol. 43, no. 12, pp. 6267–6275, Jun. 2016.

[41] G. B. M. Pedersen, J. M. C. Belart, E. Magnússon, O. K. Vilmundardóttir, F. Kizel, F. S. Sigurmundsson, G. Gísladóttir, and J. A. Benediktsson, "Hekla volcano, iceland, in the 20th century: Lava volumes, production rates, and effusion rates," *Geophys. Res. Lett.*, vol. 45, no. 4, pp. 1805–1813, Feb. 2018.

[42] C. Ticehurst, S. Phinn, and A. Held, "Using multitemporal digital elevation model data for detecting canopy gaps in tropical forests due to cyclone damage: An initial assessment," *Austral Ecol.*, vol. 32, no. 1, pp. 59–69, Feb. 2007.

[43] L. Magruder, H. Leigh, and A. Neuenschwander, "Evaluation of terrain and canopy height products in central african tropical forests," *Int. J. Remote Sens.*, vol. 37, no. 22, pp. 5365–5387, Nov. 2016.

[44] K. Gdulová, J. Marešová, V. Barták, M. Szostak, J. Červenka, and V. Moudrý, "Use of TanDEM-X and SRTM-C data for detection of

deforestation caused by bark beetle in central european mountains," *Remote Sensing*, vol. 13, no. 15, p. 3042, Aug. 2021.

[45] D. Felikson, T. C. Bartholomaus, G. A. Catania, N. J. Korsgaard, K. H. Kjær, M. Morlighem, B. Noël, M. van den Broeke, L. A. Stearns, E. L. Shroyer, D. A. Sutherland, and J. D. Nash, "Inland thinning on the greenland ice sheet controlled by outlet glacier geometry," *Nat. Geosci.*, vol. 10, no. 5, pp. 366–369, May 2017.

[46] D. E. Shean, I. R. Joughin, P. Dutrieux, B. E. Smith, and E. Berthier, "Ice shelf basal melt rates from a high-resolution digital elevation model (DEM) record for pine island glacier, antarctica," *The Cryosphere*, vol. 13, no. 10, pp. 2633–2656, 2019.

[47] R. Hugonnet, R. McNabb, E. Berthier, B. Menounos, C. Nuth, L. Girod, D. Farinotti, M. Huss, I. Dussaillant, F. Brun, and A. Kääb, "Accelerated global glacier mass loss in the early twenty-first century," *Nature*, vol. 592, no. 7856, pp. 726–731, Apr. 2021.

[48] J. Wood, "The geomorphological characterisation of digital elevation models," Ph.D. dissertation, University of Leicester (United Kingdom), Ann Arbor, United States, 1996.

[49] B. H. Carlisle, "Digital elevation model quality and uncertainty in DEM-based spatial modelling," Ph.D. dissertation, University of Greenwich, London, UK, 2002.

[50] J. Oksanen, "Digital elevation model error in terrain analysis," Ph.D. dissertation, University of Helsinki, Faculty of Science, Nov. 2006.

[51] C. Papasaika-Hanusch, "Fusion of digital elevation models," Ph.D. dissertation, ETH Zurich, 2012.

[52] D. F. Maune, *Digital elevation model technologies and applications: the DEM users manual*. Asprs Publications, 2007.

[53] P. F. Fisher and N. J. Tate, "Causes and consequences of error in digital elevation models," *Progress in Physical Geography: Earth and Environment*, vol. 30, no. 4, pp. 467–489, Aug. 2006.

[54] S. P. Wechsler, "Uncertainties associated with digital elevation models for hydrologic applications: a review," *Hydrol. Earth Syst. Sci.*, vol. 11, no. 4, pp. 1481–1500, Aug. 2007.

[55] S. E. Lakshmi and K. Yarrakula, "Review and critical analysis on digital elevation models," *Geofizika*, vol. 35, no. 2, pp. 129–157, 2018.

[56] L. Polidori and M. El Hage, "Digital elevation model quality assessment methods: A critical review," *Remote Sensing*, vol. 12, no. 21, p. 3522, Oct. 2020.

[57] F. Hebeler and R. S. Purves, "The influence of elevation uncertainty on derivation of topographic indices," *Geomorphology*, vol. 111, no. 1, pp. 4–16, Oct. 2009.

[58] T. G. Farr, P. A. Rosen, E. Caro, R. Crippen, R. Duren, S. Hensley, M. Kobrick, M. Paller, E. Rodriguez, L. Roth, D. Seal, S. Shaffer, J. Shimada, J. Umland, M. Werner, M. Oskin, D. Burbank, and D. Alsdorf, "The shuttle radar topography mission," *Rev. Geophys.*, vol. 45, no. 2, p. 1485, May 2007.

[59] P. Rizzoli, M. Martone, C. Gonzalez, C. Wecklich, D. B. Tridon, B. Bräutigam, M. Bachmann, D. Schulze, T. Fritz, M. Huber, B. Wessel, G. Krieger, M. Zink, and A. Moreira, "Generation and performance assessment of the global TanDEM-X digital elevation model," *ISPRS J. Photogramm. Remote Sens.*, vol. 132, pp. 119–139, 2017.

[60] G. Amatulli, D. McInerney, T. Sethi, P. Strobl, and S. Domisch, "Geomorpho90m, empirical evaluation and accuracy assessment of global high-resolution geomorphometric layers," *Sci Data*, vol. 7, no. 1, p. 162, May 2020.

[61] E. Uuemaa, S. Ahi, B. Montibeller, M. Muru, and A. Kmoch, "Vertical accuracy of freely available global digital elevation models (ASTER, AW3D30, MERIT, TanDEM-X, SRTM, and NASADEM)," *Remote Sensing*, vol. 12, no. 21, p. 3482, Oct. 2020.

[62] L. A. Eberhard, P. Sirguey, A. Miller, M. Marty, K. Schindler, A. Stoffel, and Y. Bühler, "Intercomparison of photogrammetric platforms for spatially continuous snow depth mapping," *The Cryosphere*, vol. 15, no. 1, pp. 69–94, Jan. 2021.

[63] L. Magruder, A. Neuenschwander, and B. Klotz, "Digital terrain model elevation corrections using space-based imagery and ICESat-2 laser altimetry," *Remote Sens. Environ.*, vol. 264, p. 112621, Oct. 2021.

[64] B. H. Carlisle, "Modelling the spatial distribution of DEM error," *Trans. GIS*, vol. 9, no. 4, pp. 521–540, Oct. 2005.

[65] C. Rolstad, T. Haug, and B. Denby, "Spatially integrated geodetic glacier mass balance and its uncertainty based on geostatistical analysis: Application to the western svartisen ice cap, norway," *J. Glaciol.*, vol. 55, no. 192, pp. 666–680, 2009.

[66] L. Girod, C. Nuth, A. Kääb, R. McNabb, and O. Galland, "MMASTER: Improved ASTER DEMs for elevation change monitoring," *Remote Sensing*, vol. 9, no. 7, p. 704, Jul. 2017.

[67] ISO (International Organisation for Standardisation), *ISO 5725-1: 1994: Accuracy (Trueness and Precision) of Measurement Methods and Results-Part 1: General Principles and Definitions*. Geneva: ISO, 1994.

[68] L. Guan, H. Pan, S. Zou, J. Hu, X. Zhu, and P. Zhou, "The impact of horizontal errors on the accuracy of freely available digital elevation models (DEMs)," *Int. J. Remote Sens.*, vol. 41, no. 19, pp. 7383–7399, Oct. 2020.

[69] S. Mukherjee, P. K. Joshi, S. Mukherjee, A. Ghosh, R. D. Garg, and A. Mukhopadhyay, "Evaluation of vertical accuracy of open source digital elevation model (DEM)," *Int. J. Appl. Earth Obs. Geoinf.*, vol. 21, pp. 205–217, Apr. 2013.

[70] S. A. Kulp and B. H. Strauss, "New elevation data triple estimates of global vulnerability to sea-level rise and coastal flooding," *Nat. Commun.*, vol. 10, no. 1, p. 4844, Oct. 2019.

[71] A. Gruber, B. Wessel, M. Huber, and A. Roth, "Operational TanDEM-X DEM calibration and first validation results," *ISPRS J. Photogramm. Remote Sens.*, vol. 73, pp. 39–49, Sep. 2012.

[72] A. Dehecq, R. Millan, E. Berthier, N. Gourmelen, E. Trouvé, and V. Vionnet, "Elevation changes inferred from TanDEM-X data over the Mont-Blanc area: Impact of the X-Band interferometric bias," *IEEE Journal of Selected Topics in Applied Earth Observations and Remote Sensing*, vol. 9, no. 8, pp. 3870–3882, Aug. 2016.

[73] P. J. Besl and N. D. McKay, "A method for registration of 3-D shapes," *IEEE Trans. Pattern Anal. Mach. Intell.*, vol. 14, no. 2, pp. 239–256, Feb. 1992.

[74] A. Myronenko and X. Song, "Point set registration: coherent point drift," *IEEE Trans. Pattern Anal. Mach. Intell.*, vol. 32, no. 12, pp. 2262–2275, Dec. 2010.

[75] Q.-Y. Zhou, J. Park, and V. Koltun, "Fast global registration," in *Computer Vision – ECCV 2016*. Springer International Publishing, 2016, pp. 766–782.

[76] T. Zhang and M. Cen, "Robust DEM co-registration method for terrain changes assessment using least trimmed squares estimator," *Adv. Space Res.*, vol. 41, no. 11, pp. 1827–1835, Jan. 2008.

[77] C. Nuth and Kääb, "Co-registration and bias corrections of satellite elevation data sets for quantifying glacier thickness change," *The Cryosphere*, vol. 5, no. 1, pp. 271–290, 2011.

[78] M.-J. Noh and I. M. Howat, "Automated coregistration of repeat digital elevation models for surface elevation change measurement using geometric constraints," *IEEE Trans. Geosci. Remote Sens.*, vol. 52, no. 4, pp. 2247–2260, Apr. 2014.

[79] J. B. Abshire, X. Sun, H. Riris, J. M. Sirota, J. F. McGarry, S. Palm, D. Yi, and P. Liiva, "Geoscience laser altimeter system (GLAS) on the ICESat mission: On-orbit measurement performance," *Geophys. Res. Lett.*, vol. 32, no. 21, 2005.

[80] W. Abdalati, H. J. Zwally, R. Bindschadler, B. Csatho, S. L. Farrell, H. A. Fricker, D. Harding, R. Kwok, M. Lefsky, T. Markus, A. Marshak, T. Neumann, S. Palm, B. Schutz, B. Smith, J. Spinhirne, and C. Webb, "The ICESat-2 laser altimetry mission," *Proc. IEEE*, vol. 98, no. 5, pp. 735–751, May 2010.

[81] J. Vaze, J. Teng, and G. Spencer, "Impact of DEM accuracy and resolution on topographic indices," *Environmental Modelling & Software*, vol. 25, no. 10, pp. 1086–1098, Oct. 2010.

[82] J. Gardelle, E. Berthier, and Y. Arnaud, "Impact of resolution and radar penetration on glacier elevation changes computed from DEM differencing," *J. Glaciol.*, vol. 58, no. 208, pp. 419–422, 2012.

[83] J. Dall, S. N. Madsen, K. Keller, and R. Forsberg, "Topography and penetration of the greenland ice sheet measured with airborne SAR interferometry," *Geophys. Res. Lett.*, vol. 28, no. 9, pp. 1703–1706, May 2001.

[84] J. Li, Z.-W. Li, J. Hu, L.-X. Wu, X. Li, L. Guo, Z. Liu, Z.-L. Miao, W. Wang, and J.-L. Chen, "Investigating the bias of TanDEM-X digital elevation models of glaciers on the tibetan plateau: impacting factors and potential effects on geodetic mass-balance measurements," *J. Glaciol.*, vol. 67, no. 264, pp. 613–626, Aug. 2021.

[85] F. Ackermann, "Digital image correlation: Performance and potential application in photogrammetry," *Photogramm. Rec.*, vol. 11, no. 64, pp. 429–439, Oct. 1984.

[86] R. M. Goldstein, H. A. Zebker, and C. L. Werner, "Satellite radar interferometry: Two-dimensional phase unwrapping," *Radio Sci.*, vol. 23, no. 4, pp. 713–720, Jul. 1988.

[87] H. Lee and J. G. Liu, "Analysis of topographic decorrelation in SAR interferometry using ratio coherence imagery," *IEEE Trans. Geosci. Remote Sens.*, vol. 39, no. 2, pp. 223–232, Feb. 2001.

[88] A. Wehr and U. Lohr, "Airborne laser scanning—an introduction and overview," *ISPRS J. Photogramm. Remote Sens.*, vol. 54, no. 2-3, pp. 68–82, Jul. 1999.

[89] F. J. Aguilar and J. P. Mills, "Accuracy assessment of lidar-derived digital elevation models," *Photogramm. Rec.*, vol. 23, no. 122, pp. 148–169, Jun. 2008.

[90] F. J. Aguilar, J. P. Mills, J. Delgado, M. A. Aguilar, J. G. Negreiros, and J. L. Pérez, "Modelling vertical error in LiDAR-derived digital elevation models," *ISPRS J. Photogramm. Remote Sens.*, vol. 65, no. 1, pp. 103–110, Jan. 2010.

[91] P. V. Bolstad and T. Stowe, "An evaluation of DEM accuracy: elevation, slope, and aspect," *Photogrammetric Engineering & Remote Sensing*, vol. 60, no. 11, pp. 1327–1332, 1994.

[92] Y. Gyasi-Agyei, G. Willgoose, and F. P. De Troch, "Effects of vertical resolution and map scale of digital elevation models on geomorphological parameters used in hydrology," *Hydrol. Process.*, vol. 9, no. 3-4, pp. 363–382, Apr. 1995.

[93] K. W. Holmes, O. A. Chadwick, and P. C. Kyriakidis, "Error in a USGS 30-meter digital elevation model and its impact on terrain modeling," *J. Hydrol.*, vol. 233, no. 1, pp. 154–173, Jun. 2000.

[94] T. Toutin, "Three-dimensional topographic mapping with ASTER stereo data in rugged topography," *IEEE Trans. Geosci. Remote Sens.*, vol. 40, no. 10, pp. 2241–2247, 2002.

[95] J. M. Wheaton, J. Brasington, S. E. Darby, and D. A. Sear, "Accounting for uncertainty in DEMs from repeat topographic surveys: improved sediment budgets," *Earth Surf. Processes Landforms*, 2009.

[96] D. J. Milan, G. L. Heritage, A. R. G. Large, and I. C. Fuller, "Filtering spatial error from DEMs: Implications for morphological change estimation," *Geomorphology*, vol. 125, no. 1, pp. 160–171, Jan. 2011.

[97] A. Bouillon, M. Bernard, P. Gigord, A. Orsoni, V. Rudowski, and A. Baudoin, "SPOT 5 HRS geometric performances: Using block adjustment as a key issue to improve quality of DEM generation," *ISPRS J. Photogramm. Remote Sens.*, vol. 60, no. 3, pp. 134–146, May 2006.

[98] I. Dussaillant, E. Berthier, and F. Brun, "Geodetic mass balance of the northern patagonian icefield from 2000 to 2012 using two independent methods," *Front Earth Sci.*, vol. 6, no. February, p. 8, 2018.

[99] R. Perko, H. Raggam, and P. M. Roth, "Mapping with Pléiades—End-to-End workflow," *Remote Sensing*, vol. 11, no. 17, p. 2052, Sep. 2019.

[100] G. Falorni, "Analysis and characterization of the vertical accuracy of digital elevation models from the shuttle radar topography mission," *J. Geophys. Res.*, vol. 110, no. F2, 2005.

[101] M. Simard, M. Neumann, and S. Buckley, "Validation of the new SRTM digital elevation model (NASADEM) with ICESAT/GLAS over the united states," in *2016 IEEE International Geoscience and Remote Sensing Symposium (IGARSS)*. ieeexplore.ieee.org, Jul. 2016, pp. 3227–3229.

[102] J. M. C. Belart, E. Berthier, E. Magnússon, L. S. Anderson, F. Pálsson, T. Thorsteinsson, I. M. Howat, G. Aðalgeirsdóttir, T. Jóhannesson, and A. H. Jarosch, "Winter mass balance of drangajökull ice cap (NW iceland) derived from satellite sub-meter stereo images," *The Cryosphere*, vol. 11, no. 3, pp. 1501–1517, Jun. 2017.

[103] L. Girod, N. I. Nielsen, F. Couderette, C. Nuth, and A. Kääb, "Precise DEM extraction from svalbard using 1936 high oblique imagery," *Geosci. Instrum. Methods Data Syst.*, vol. 7, no. 4, pp. 277–288, Oct. 2018.

[104] W. Gheyle, J. Bourgeois, R. Goossens, and K. Jacobsen, "Scan problems in digital CORONA satellite images from USGS archives," *Photogrammetric Engineering & Remote Sensing*, vol. 77, no. 12, pp. 1257–1264, 2011.

[105] J. Li, Z.-W. Li, J.-J. Zhu, X. Li, B. Xu, Q.-J. Wang, C.-L. Huang, and J. Hu, "Early 21st century glacier thickness changes in the central tien shan," *Remote Sens. Environ.*, vol. 192, pp. 12–29, Apr. 2017.

[106] M. S. Hamid and M. Safy, "InSAR image denoising filter for accurate DEM generation," in *2020 12th International Conference on Electrical Engineering (ICEENG)*, Jul. 2020, pp. 306–310.

[107] L. Bopche and P. P. Rege, "Use of noise reduction filters on stereo images for improving the accuracy and quality of the digital elevation model," *JARS*, vol. 15, no. 1, p. 014508, Feb. 2021.

[108] T. Ai and J. Li, "A DEM generalization by minor valley branch detection and grid filling," *ISPRS J. Photogramm. Remote Sens.*, vol. 65, no. 2, pp. 198–207, Mar. 2010.

[109] T. Smith, A. Rheinwalt, and B. Bookhagen, "Determining the optimal grid resolution for topographic analysis on an airborne lidar dataset," *Earth Surf. Dynam.*, vol. 7, no. 2, pp. 475–489, May 2019.

[110] J. D. Wood and P. F. Fisher, "Assessing interpolation accuracy in elevation models," *IEEE Comput. Graph. Appl.*, vol. 13, no. 2, pp. 48–56, Mar. 1993.

[111] J. Gao, "Resolution and accuracy of terrain representation by grid DEMs at a micro-scale," *Int. J. Geogr. Inf. Sci.*, vol. 11, no. 2, pp. 199–212, Mar. 1997.

[112] A. G. Journel and C. J. Huijbregts, *Mining geostatistics*. Academic press London, 1978, vol. 600.

[113] N. A. C. Cressie, *Statistics for spatial data*. New York: Wiley, 1993, vol. 4.

[114] C. R. Ehlschlaeger and A. Shortridge, "Modeling elevation uncertainty in geographical analyses," in *Proceedings of the International Symposium on Spatial Data Handling, Delft, Netherlands B*, vol. 9, 1996, pp. 15–9B.

[115] P. C. Kyriakidis, A. M. Shortridge, and M. F. Goodchild, "Geostatistics for conflation and accuracy assessment of digital elevation models," *Int. J. Geogr. Inf. Sci.*, vol. 13, no. 7, pp. 677–707, Oct. 1999.

[116] S. P. Wechsler, "Digital elevation model (DEM) uncertainty: evaluation and effect on topographic parameters," in *ESRI User Conference*. ecn.purdue.edu, 1999, pp. 1081–1090.

[117] P. Goovaerts, *Geostatistics for Natural Resources Evaluation*. Oxford University Press, 1997.

[118] G. B. M. Heuvelink, *Error propagation in environmental modelling with GIS*. CRC press, 1998.

[119] A. Shortridge, "Characterizing uncertainty in digital elevation models," in *Spatial Uncertainty in Ecology: Implications for Remote Sensing and GIS Applications*, C. T. Hunsaker, M. F. Goodchild, M. A. Friedl, and T. J. Case, Eds. New York, NY: Springer New York, 2001, pp. 238–257.

[120] G. Wang, G. Z. Gertner, S. Fang, and A. B. Anderson, "A methodology for spatial uncertainty analysis of remote sensing and GIS products," *Photogrammetric Engineering & Remote Sensing*, vol. 71, no. 12, pp. 1423–1432, 2005.

[121] G. B. M. Heuvelink, P. A. Burrough, and A. Stein, "Propagation of errors in spatial modelling with GIS," *International Journal of Geographical Information Systems*, vol. 3, no. 4, pp. 303–322, Oct. 1989.

[122] P. F. Fisher, "First experiments in viewshed uncertainty: the accuracy of the viewshed area," *Photogramm. Eng. Remote Sens.*, vol. 57, no. 10, pp. 1321–1327, 1991.

[123] S. Openshaw, M. Charlton, and S. Carver, "Error propagation: a monte carlo simulation," in *Handling geographical information: methodology and potential applications*. Longman Harlow, Essex, 1991, pp. 78–101.

[124] F. Heße, V. Prykhodko, S. Schlüter, and S. Attinger, "Generating random fields with a truncated power-law variogram: A comparison of several numerical methods," *Environmental Modelling & Software*, vol. 55, pp. 32–48, May 2014.

[125] F. Canters, W. D. Genst, and H. Dufourmont, "Assessing effects of input uncertainty in structural landscape classification," *Int. J. Geogr. Inf. Sci.*, vol. 16, no. 2, pp. 129–149, Mar. 2002.

[126] S. P. Wechsler and C. N. Kroll, "Quantifying DEM uncertainty and its effect on topographic parameters," *Photogrammetric Engineering & Remote Sensing*, vol. 72, no. 9, pp. 1081–1090, 2006.

[127] E. Magnússon, J. Muñoz-Cobo Belart, F. Pálsson, H. Ágústsson, and P. Crochet, "Geodetic mass balance record with rigorous uncertainty estimates deduced from aerial photographs and lidar data – case study from drangajökull ice cap, NW iceland," *The Cryosphere*, vol. 10, no. 1, pp. 159–177, Jan. 2016.

[128] A. Bachmann and B. Allgöwer, "Uncertainty propagation in wildland fire behaviour modelling," *Int. J. Geogr. Inf. Sci.*, vol. 16, no. 2, pp. 115–127, Mar. 2002.

[129] M. Albani, B. Klinkenberg, D. W. Andison, and J. P. Kimmins, "The choice of window size in approximating topographic surfaces from digital elevation models," *Int. J. Geogr. Inf. Sci.*, vol. 18, no. 6, pp. 577–593, Sep. 2004.

[130] C. Li, Q. Wang, W. Shi, and S. Zhao, "Uncertainty modelling and analysis of volume calculations based on a regular grid digital elevation model (DEM)," *Comput. Geosci.*, vol. 114, pp. 117–129, May 2018.

[131] C. Li, S. Zhao, Q. Wang, and W. Shi, "Uncertainty modeling and analysis of surface area calculation based on a regular grid digital elevation model (DEM)," *Int. J. Geogr. Inf. Sci.*, vol. 32, no. 9, pp. 1837–1859, Sep. 2018.

[132] S. W. Anderson, "Uncertainty in quantitative analyses of topographic change: error propagation and the role of thresholding," *Earth Surf. Processes Landforms*, vol. 44, no. 5, pp. 1015–1033, 2019.

[133] G. B. M. Heuvelink, "Analysing uncertainty propagation in GIS: Why is it not that simple?" in *Uncertainty in Remote Sensing and GIS*. Chichester, UK: John Wiley & Sons, Ltd, Jul. 2006, pp. 155–165.
[134] R. A. Beyer, O. Alexandrov, and S. McMichael, "The ames stereo pipeline: NASA's open source software for deriving and processing terrain data," *Earth and Space Science*, vol. 5, no. 9, pp. 537–548, Sep. 2018.
[135] NASA/METI/AIST/Japan Spacesystems, and U.S./Japan ASTER Science Team, "ASTER level 1A data set - reconstructed, unprocessed instrument data," 2001.
[136] E. Rupnik, M. Daakir, and M. Pierrot Deseilligny, "MicMac – a free, open-source solution for photogrammetry," *Open Geospatial Data, Software and Standards*, vol. 2, no. 1, p. 14, 2017.
[137] NASA JPL, "NASADEM SRTM-only height and height precision mosaic global 1 arc second," 2020.
[138] M.-J. Noh and I. M. Howat, "The surface extraction from TIN based search-space minimization (SETSM) algorithm," *ISPRS J. Photogramm. Remote Sens.*, vol. 129, pp. 55–76, Jul. 2017.
[139] C. Porter, P. Morin, I. Howat, M.-J. Noh, B. Bates, K. Peterman, S. Keesey, M. Schlenk, J. Gardiner, K. Tomko, M. Willis, C. Kelleher, M. Cloutier, E. Husby, S. Foga, H. Nakamura, M. Platson, M. Wethington, Jr, C. Williamson, G. Bauer, J. Enos, G. Arnold, W. Kramer, P. Becker, A. Doshi, C. D'Souza, P. Cummens, F. Laurier, and M. Bojesen, "ArcticDEM," Nov. 2018.
[140] RGI Consortium, "Randolph glacier inventory – a dataset of global glacier outlines: Version 6.0: Technical report, global land ice measurements from space, colorado, USA," 2017.
[141] ESA, "Land cover CCI product user guide version 2. tech. rep," 2017.
[142] J. Höhle and M. Höhle, "Accuracy assessment of digital elevation models by means of robust statistical methods," *ISPRS J. Photogramm. Remote Sens.*, vol. 64, no. 4, pp. 398–406, Jul. 2009.
[143] B. K. P. Horn, "Hill shading and the reflectance map," *Proc. IEEE*, vol. 69, no. 1, pp. 14–47, Jan. 1981.
[144] L. W. Zevenbergen and C. R. Thorne, "Quantitative analysis of land surface topography," *Earth Surf. Processes Landforms*, vol. 12, no. 1, pp. 47–56, Jan. 1987.
[145] M. B. Wilk and R. Gnanadesikan, "Probability plotting methods for the analysis of data," *Biometrika*, vol. 55, no. 1, pp. 1–17, Mar. 1968.
[146] P. A. Dowd, "The variogram and kriging: Robust and resistant estimators," in *Geostatistics for Natural Resources Characterization*, G. Verly, M. David, A. G. Journel, and A. Marechal, Eds. Dordrecht: Springer Netherlands, 1984, pp. 91–106.
[147] M. Mälicke and H. D. Schneider, "Scikit-GStat 0.2.6: A scipy flavored geostatistical analysis toolbox written in python," Nov. 2019.
[148] G. Matheron, *Les variables régionalisées et leur estimation: une application de la théorie de fonctions aléatoires aux sciences de la nature*. Masson et CIE, 1965, vol. 4597.
[149] N. Cressie and D. M. Hawkins, "Robust estimation of the variogram: I," *Journal of the International Association for Mathematical Geology*, vol. 12, no. 2, pp. 115–125, Apr. 1980.
[150] M. G. Genton, "Highly robust variogram estimation," *Math. Geol.*, vol. 30, no. 2, pp. 213–221, Feb. 1998.
[151] T. M. Burgess and R. Webster, "Optimal interpolation and isarithmic mapping of soil properties," *J. Soil Sci.*, vol. 31, no. 2, pp. 315–331, Jun. 1980.
[152] S. Müller and L. Schüler, "GeoStat-Framework/GSTools: v1.3.3 'pure pink'," 2021.
[153] E. J. Pebesma and C. G. Wesseling, "gstat : A program for geostatistical modelling, prediction and simulation," *Comput. Geosci.*, vol. 24, no. 1, pp. 17–31, 1998.
[154] R. Webster and M. A. Oliver, *Geostatistics for Environmental Scientists*, 2nd ed. Wiley, Nov. 2007.
[155] H. Liu and K. C. Jezek, "Investigating DEM error patterns by directional variograms and fourier analysis," *Geogr. Anal.*, vol. 31, no. 3, pp. 249–266, Sep. 2010.
[156] E. Rodríguez, C. S. Morris, and J. E. Belz, "A global assessment of the SRTM performance," *Photogrammetric Engineering & Remote Sensing*, vol. 72, no. 3, pp. 249–260, 2006.
[157] xdem contributors, "xdem," May 2021.

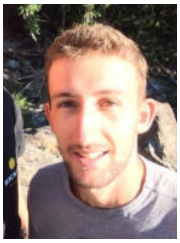

Romain Hugonnet received his MSc. degree in 2017 from Ecole Centrale de Lille, France. Since 2018, he has been working as a Ph.D. student for the Laboratory for Space Studies in Geophysics and Oceanography, Toulouse, France and the Laboratory of Hydraulics, Hydrology and Glaciology, ETH Zürich, Switzerland. His research aims at monitoring the Earth system by remote sensing, with a focus on glaciology and digital elevation models. His fields of expertise are satellite imagery and spatiotemporal analyses, including uncertainty quantification.

Fanny Brun received her Ph.D. degree in 2018 from the University Grenoble Alpes, France. Since 2020, she has been working for IRD in the Institute of Environmental Geosciences, Grenoble, France. Her research aims at observing glacier changes from remote sensing and field techniques, with a focus in Asia. She currently serves as Scientific Editor for the Journal of Glaciology.

Etienne Berthier received his Ph.D. degree in 2005 from the University of Toulouse, France. Since 2007, he has been working for CNRS in the Laboratory for Space Studies in Geophysics and Oceanography, Toulouse, France. His research aims at observing and understanding the effect of climate change on mountain glaciers and ice caps and quantifying their contribution to sea level rise. His field of expertise is satellite remote sensing, including the retrieval of ice topography from optical images to measure ice elevation changes. He currently serves as the Scientific Editor for The Cryosphere and La Météorologie (in French). He is member of the European Geophysical Union and the International Glaciological Society.

Amaury Dehecq received his Ph.D. degree in remote sensing in 2015 from the University Grenoble Alpes, France. From 2019 to 2021, he worked as a postdoctoral researcher at ETH Zurich's Laboratory of Hydraulics, Hydrology and Glaciology (VAW). Since 2021, he has been working for the French National Research Institute for Sustainable Development (IRD) and based at the Institute for Geosciences and Environmental research (IGE), Grenoble, France. His research focuses on estimating 20th century mountain glacier changes from remote sensing observations, using a combination of modern satellite, declassified spy satellite, and historical airborne/terrestrial images.

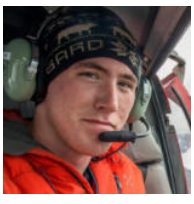

Erik Schytt Mannerfelt received his MSc degree in 2020 from UiT — The Arctic University of Norway. Between 2020 and 2022, he has worked at the Laboratory of Hydraulics, Hydrology and Glaciology, ETH Zurich, Switzerland, as a research assistant. His research focuses on fieldwork-, modelling-, and photogrammetry-based methods to constrain late Little Ice Age to contemporary glacier change and dynamics.

Nicolas Eckert received his Ph.D. degree in 2007 from AgroparisTech. Since 2008 he is researcher at INRAE Grenoble, co-head of the mountain risk team since 2018. He is also task officer in charges of Environmental risks for the AQUA department at INRAE, and for the ALLENVI research federation. He serves as Associate Chief Editor for Journal of Glaciology and as Scientific Editor for Cold Regions Science and Technology. His research is at the crossroads between geosciences and statistical modelling, with applications to mountain risks, mountain climatology and glaciers. Additional interests in the socio-historical component of risk makes him involved in interdisciplinary research addressing all dimensions of mountain risks.

Daniel Farinotti received his doctoral degree in 2010 from the Swiss Federal Institute of Technology in Zurich (ETH Zurich). Since 2016 he leads the Professorship of Glaciology at ETH Zurich's Laboratory of Hydraulics, Hydrology and Glaciology (VAW), a position jointly affiliated to the Swiss Federal Institute for Forest, Snow and Landscape Research WSL. His research focuses on the evolution of glaciers and the implications for water resources, notably including the estimation of glacier ice thickness from surface characteristics, the long-term modelling of glacier mass budgets, the estimation of the runoff contributions from glacierized catchments, or the implications for water resource management in high-mountain environments.

2.4 Extension to other types of uncertainty analyses

The spatial statistics methods implemented in our article Hugonnet et al. (accepted) rely on some assumptions specific to DEMs, but the underlying methods are generic and applicable to more diverse problems. In this section, we utilize the skills and tools developed for spatial statistics and extend their application to other challenges.

2.4.1 Uncertainties in the interpolation of glacier elevation changes

In-review article as co-author featured in this section: Mannerfelt, E.S. et al. (2022), *Halving of Swiss glacier volume since 1931 observed from terrestrial image photogrammetry*, The Cryosphere Discussions.[4]

In the recent study of Mannerfelt et al. (2022), we use historical archives of terrestrial imagery to generate DEMs all around Switzerland during 1916–1947. We then estimate elevation changes between a median year of 1931 and 2016 for most Swiss glaciers. An inherent problem with the use of terrestrial imagery is the limited amount of observed terrain in a pair of stereo images, and the low incidence angle to observe the glacier surfaces. As a result, the region-wide spatial coverage of elevation changes is of only 45%, despite a 86% theoretical coverage of the imagery, and thus arises the need for robust interpolation.

The most popular methods of interpolation, i.e. gap-filling of glacier elevation change estimates, rely on the elevation dependency of glacier elevation changes (Schwitter and Raymond, 1993). These hypsometric methods fill data gaps based on the mean elevation change within an elevation band for the glacier or the region, and have been shown as the most robust by recent comparative studies (McNabb et al., 2019; Seehaus et al., 2020). Some discrepancies arise when gap-filling at the regional-scale, however, which is necessary for large amount of gaps such as in Mannerfelt et al. (2022). To address this, we proposed a regional normalized hypsometric interpolation. This method estimates the mean distribution of normalized elevation change for all glaciers in the region from their normalized hypsometry. Then, hypsometric gap-filling is estimated by per-glacier de-normalization, i.e. scaling of the regional normalized hypsometric signal to the elevation change observations of each glacier. We qualitatively found that this method provided the most satisfying results (Fig. 2.14).

While many interpolation methods have emerged for gap-filling glacier elevation change, few uncertainty approaches have been proposed to account for its impact on final estimates. Some studies have relied on an empirical comparison to stable terrain (Berthier et al., 2016) reproduced without validation in other studies (e.g. Braun et al., 2019; Abdel Jaber et al., 2019) despite different parameters such as the size of study area, or amount of data gaps. Other studies have scaled interpolation errors on the variance on stable terrain, which overestimates errors (Malz et al., 2018). A recent study proposed an error formulation (Seehaus et al., 2020) that was not demonstrated or validated in a statistical exercise.

[4]Contribution: in the study of Mannerfelt et al. (2022), I contributed methods for both uncertainty analyses and glacier elevation change interpolation, in particular on a new approach to propagate interpolation errors.

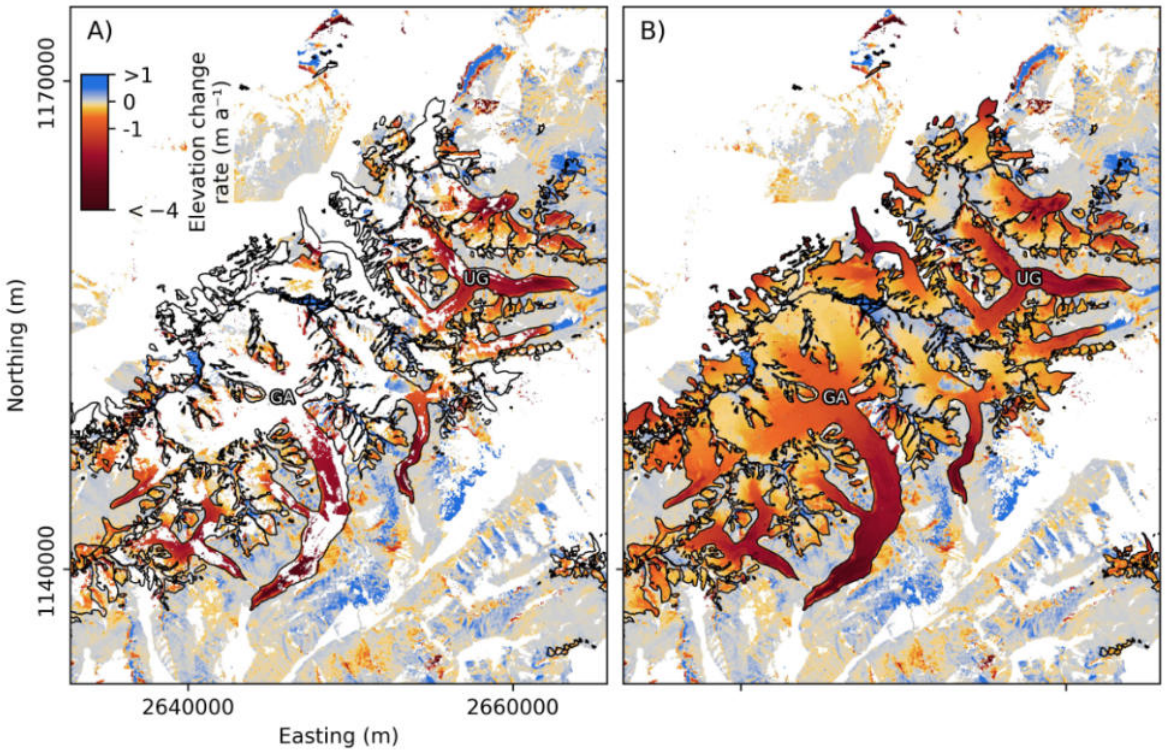

Figure 2.14: Regional normalized hypsometric interpolation. From Mannerfelt et al. (2022). Maps of elevation change rates between the historical and modern DEMs over the period 1931-–2016 **(A)** before and **(B)** after regional normalized hypsometric interpolation. The site contains Grosser Aletschgletscher (GA), Unteraargletscher (UG) and other neighbouring glaciers. Glacier outlines from ca. 1931 in black.

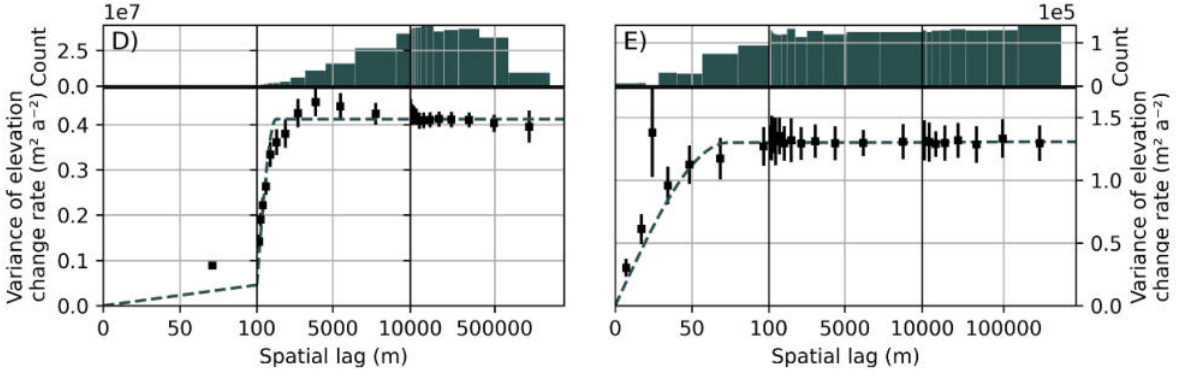

Figure 2.15: Spatial correlations of errors in interpolation and in measured elevation changes. From Mannerfelt et al. (2022). **(D,E)** Empirical and modelled variograms of interpolated **(D)** and stable-terrain **(E)** elevation difference errors, showing the variance of all pairs of pixels at a given spatial lag. The interpolated errors are estimated from artificial gaps in the 2000-2019 elevation changes of Hugonnet et al. (2021). The individual markers show the empirically derived variance, their error bars show their 95% confidence intervals, and the dashed line shows the variogram model (sum of two spherical models). The histograms show the pairwise sample counts.

In the study of Mannerfelt et al. (2022), we introduce an approach based on spatial statistics relying on an empirical comparison to independent estimates. We copy the extent of data gaps of the 1931–2016 elevation changes estimates (Fig. 2.14) and artificially introduce them in the nearly-complete 2000–2019 elevation change rates of Hugonnet et al. (2021). We then perform the interpolation using the 46% remaining spatial coverage of the 2000–2019 data. Finally, we subtract the artificially interpolated 2000–2019 elevation change rates with their original 2000–2019 estimates to study the interpolation errors, similarly as elevation differences are used to study elevation error (Hugonnet et al., accepted). We find no regional bias (~0.01 m yr^{-1}), and estimate the spatial correlations from these errors using the methods previously developed for DEMs. We find that interpolation errors remain correlated until ~2 km with a magnitude of error of ±0.5 m yr^{-1}, while 1931–2016 elevation change errors are only correlated until ~100 m with a magnitude of ±1.5 m yr^{-1} (Fig. 2.15). Our results highlight that interpolation errors are correlated within each glacier, but largely independent in between glaciers. This confirms the performance of our regional interpolation method which, by scaling the hypsometric interpolation with the estimates of each glacier, does not create large-scale errors as did the global hypsometric method (McNabb et al., 2019). Once propagated, our interpolation errors constitute the primary source (~90% and ~50% at glacier- and regional-scale respectively) of uncertainty in the 1931–2016 elevation change estimates (Mannerfelt et al., 2022).

In the early stages of this thesis, we started an analysis on the artificial generation of random data gaps with respect to a certain spatial correlation (Fig. 2.16). This artificial generation enables to control the extent and spatial distribution of these artificial gaps, and therefore test a wider range of parameters. Using this approach to create gaps on complete glacier elevation change maps for a large number of simulations (typically ~1,000) allows to estimate the bias that each interpolation method might have, and assess the robustness of different uncertainty approaches. Coupling this simulation approach with our recent modular integration of interpolation methods in *xdem* (xdem contributors, 2021) and our proposed uncertainty analyses based on spatial statistics (Hugonnet et al., accepted), these recent developments should help to further clarify the impact that interpolation methods have on glacier estimates and better constrain their uncertainties for all types of gaps.

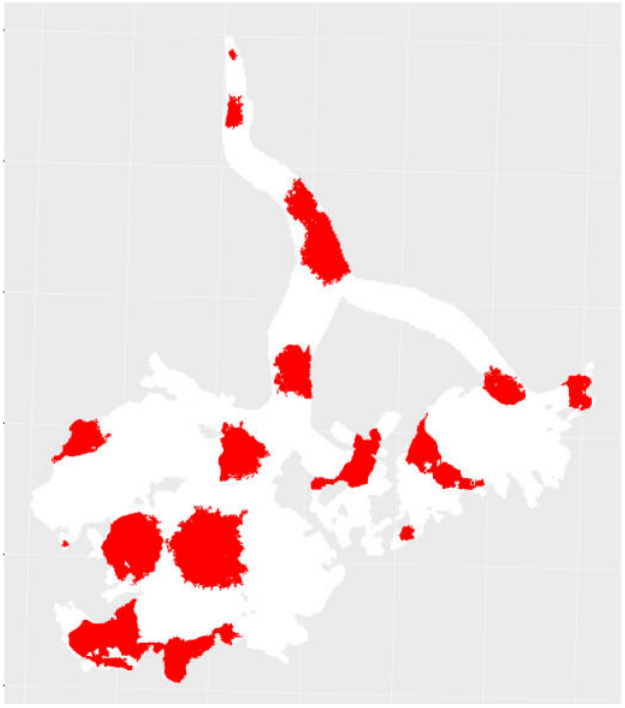

Figure 2.16: Artificial spatially correlated gaps. Correlated artifical gaps (red) with correlation range of ~500 m, evenly distributed in the Mer de Glace Glacier elevation range and covering 20% of the area.

2.4.2 Spatial propagation of correlated uncertainties in ice velocity and ice thickness

In-review article as co-author featured in this section: Kochtitzky, W. et al. (in review), *Frontal ablation: the unquantified mass loss of marine-terminating glaciers, 2000-2020*, Nature Communications.[5]

With the increasing availability of global-scale and spatially resolved ice velocity (Gardner et al., 2019; Millan et al., 2022), ice thickness (Farinotti et al., 2019a), elevation change estimates (Hugonnet et al., 2021), and the recent delineation of decadal glacier terminus positions (Kochtitzky and Copland, 2022), frontal ablation can now be estimated for all glaciers. In the study of Kochtitzky et al. (in review), we extended the spatial statistics framework presented for DEMs (Hugonnet et al., accepted) to the estimation of frontal ablation of all Northern Hemisphere marine-terminating glaciers. The objective was to estimate the influence of the spatial correlation of ice velocity and ice thickness estimates on the estimated frontal ablation during the two decades of 2000–2009 and 2010–2019.

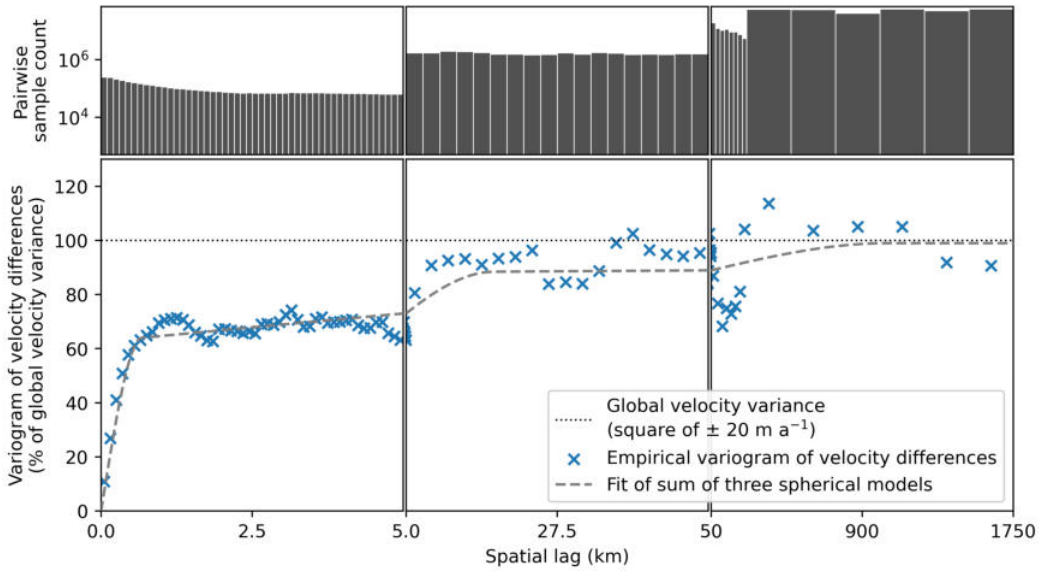

Figure 2.17: Spatial correlation of ice velocity errors. From Kochtitzky et al. (in review). Empirical and modelled variogram of velocity estimates, expressed as a percentage of the global velocity variance. The empirical variogram is estimated from the differences between ITS-LIVE and MEaSUREs or RETREAT velocities compared at the same locations and for the same yearly periods. The sample count describes the number of pairwise flux gate comparisons used to estimate the variogram at each spatial lag (i.e. distance between observations). The modelled variogram is a sum of three spherical models optimized by least-squares.

[5]Contribution: in the study of Kochtitzky et al. (in review), I contributed methods for the uncertainty analysis of ice thickness and ice velocity, including the debiasing of ice thickness modelled estimates, the estimation of spatial correlations of errors in ice velocity and ice thickness and their propagation to frontal ablation estimates from the scale of pixel to glacier, and glacier to regions and all Northern Hemisphere.

We quantified the spatial correlation of velocity and ice thickness uncertainties by estimating global-scale empirical variograms using the difference between independent sources of estimates at the same flux gates of resolution 25 m. We performed the spatial correlation analysis at distances covering several orders of magnitude (from 25 m to 1,000 km), thereby accounting for potential biases at glacier and regional scales through long-range correlations.

We first compared ITS-LIVE (Gardner et al., 2019) velocities with MEaSUREs (Joughin et al., 2010) and RETREAT (Friedl et al., 2021) velocity observations on peripheral glaciers of Greenland and found fully correlated (100%) variance at short distances (<50 m), and correlated variances at 40-100% within 700 m (Fig. 2.17). We attribute these short-range correlations to effects stemming from the resolution of optical imagery and image matching. Velocity estimates remain correlated at 15-40% within 25 km and 0-15% within 1,000 km, highlighting moderate glacier and regional scale errors likely due to seasonal differences between acquisitions when estimating yearly velocity. Beyond 1,000 km, the velocity estimates are fully decorrelated.

We then compared all available ice thickness measurements of GlaThiDa 3.0 (Welty et al., 2020) to recent model estimates of ice thickness (Farinotti et al., 2019b; Millan et al., 2022). We chose the later estimates (Millan et al., 2022) due to their smaller dispersion in polar regions. We however found strong biases of these model estimates with GlaThiDa, which were too thick even once ice thickness was adjusted for elevation changes (Hugonnet et al., 2021) to the same date as the measurements (Fig. 2.18). We identified a linear relation between the model systematic errors and the modelled ice thickness, and debiased the modelled estimates using this relation. We then estimated that the ice thickness variance was correlated at 80-100% within 2 km, corresponding to the effects of short-scale modelling errors (Fig. 2.19). Ice thickness variance remains correlated between 50-80% within 150 km, and between 0-50% within 1,000 km, implying large-scale biases in modelled ice thicknesses that are likely owed to the regional-scale temporal inconsistency of glacier outlines, velocity and topography used in ice thickness modelling. After 1,000 km, ice thickness estimates are fully decorrelated.

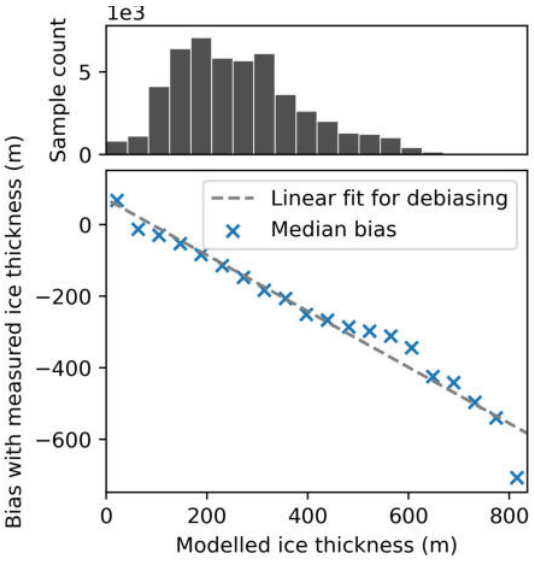

Figure 2.18: Debiasing of modelled ice thickness estimates. From Kochtitzky et al. (in review). Bias between modelled and measured ice thicknesses after adjustment of surface elevations. The bias is empirically estimated by binning the difference of measurement and model estimates within 20 intervals (every 40 m) of modelled ice thickness. The sample count of each bin represents the number of flux gate points where measured and modelled ice thickness were compared. The bias dependency to modelled ice thickness is constrained by a linear function optimized by least-squares. The bias is later removed by subtracting the value of this function at each location.

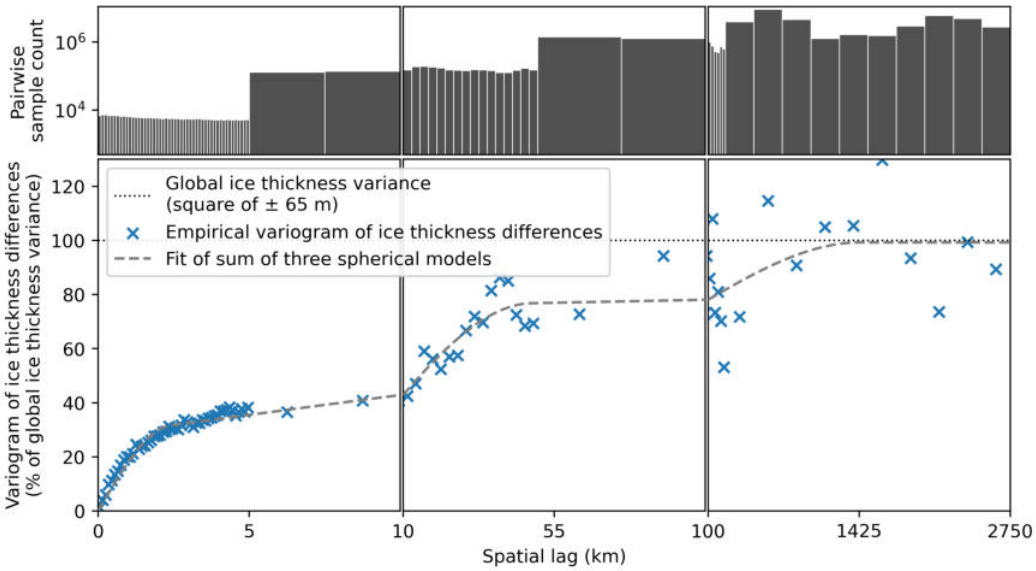

Figure 2.19: Spatial correlation of ice thickness errors. From Kochtitzky et al. (in review). Same as Fig. 2.17 for ice thickness. The empirical variogram is estimated from the differences between measured and debiased modelled ice thicknesses compared at the same locations, and adjusted to the same year with elevation changes.

Finally, we combined the spatial correlations of velocity and ice thickness to propagate the uncertainty on frontal ablation at all scales (glacier, region, Northern Hemisphere). This propagation was computed through a specific theoretical approximation for the variables used in computing frontal ablation. For glaciers distinct from the ice sheets, at the scale of the Northern Hemisphere, we estimated a frontal ablation rate of 49 ± 8 Gt yr^{-1} (95% confidence level) for 2000–2009 and 53 ± 5 Gt yr^{-1} for 2010–2019. The larger error of the earlier period arises from a lower quality of ice velocity estimates. Taking the later period as an example, using an assumption of uncorrelated uncertainties yields an uncertainty of ± 0.2 Gt yr^{-1}, against ± 90 Gt yr^{-1} with an assumption of fully correlated uncertainties. Our middle ground of ~± 5 Gt yr^{-1} corresponds much better to the expected magnitude of global uncertainty from the qualitative assessments of velocity and ice thickness errors.

Our estimates of spatial correlations in ice velocity and ice thickness errors are not only valuable for uncertainty propagation applied to frontal ablation. More generally, they also serve to characterize the structure of error in the measured or modelled estimates. They hold the potential to quantify the spatiotemporal differences in accuracy and precision between different instruments (for measured estimates) or different model approaches (for modelled estimates). Inter-comparison exercises are currently lacking of such metrics, for example that of working groups that aim at reconciling glacier models (Hock et al., 2019a; Marzeion et al., 2020; Farinotti et al., 2021) and ice sheet observations (IMBIE team, 2018; IMBIE Team, 2020).

Chapter 3

Spatiotemporal estimation of glacier surface elevation

Contents

3.1 The opening of the ASTER archive

3.1.1 An optical goldmine plagued by instrument noise

The instrument ASTER, boarding the satellite Terra, started acquiring imagery in March 2000 for all of Earth's land surfaces at latitudes lower than 83 degrees (Abrams, 2000). It still functions nowadays, despite an original life expectancy of 6 years. ASTER has been acquiring stereoscopic images at a resolution of 15 m in the visible and near-infrared that allows to generate DEMs by stereo-photogrammetry (Mikhail et al., 2001). For a long period of time, ASTER constituted the only near-global DEM available to all users at no charge (Tachikawa et al., 2011; Abrams et al., 2020). Of particular relevance to glaciology, planned acquisitions were made to prioritize the monitoring of about 15,000 valley glaciers through the Global Land Ice Monitoring from Space (GLIMS) project (Raup et al., 2007) and optimize gain settings for bright areas (Raup et al., 2000). Those efforts largely enabled the first complete glacier inventory (Pfeffer et al., 2014; RGI Consortium, 2017).

Several issues impeded the use of ASTER imagery, however. Errors associated with attitude fluctuations (Teshima and Iwasaki, 2008) and radiometric corrections (Abrams et al., 2002; Tsuchida et al., 2020) hamper ASTER acquisitions. In April 2008, the short-wave infrared sensors stopped functioning, which impacted many applications and notably the distinction between snow, ice and cloud cover. Additionally, the generated DEMs were plagued by errors in image geometry that appeared to stem from sensor motion (Girod et al., 2017). Those errors include not only along-track undulations, which are common to several sensors as illustrated in Chapter 2, but also substantial cross-track errors (Fig. 3.1). Those are at the origin of granular noise in the DEMs due to degraded cross-track parallax during photogrammetry calculations.

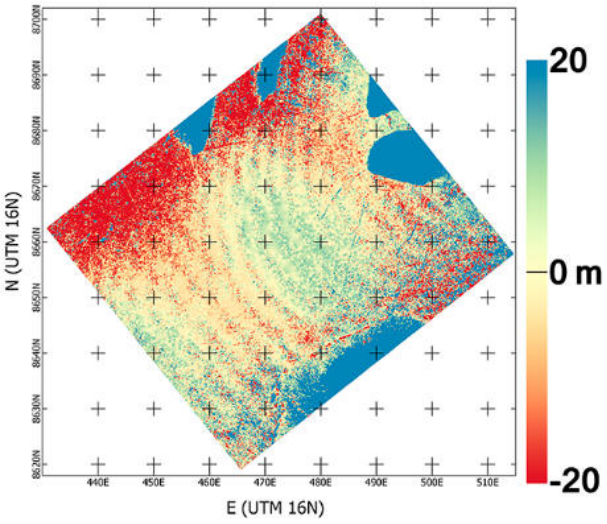

Figure 3.1: Patterns of errors in ASTER DEMs. From Girod et al. (2017). Difference between an uncorrected ASTER DEM and a artifical flat sea ice surface of 0 m. Along-track direction is northeast–southwest, perpendicular to cross-track.

3.1.2 The benefits of open, modern stereo-photogrammetry

The consequence of these errors on the usability of the ASTER DEMs was questioned by early studies in glaciology (Kääb, 2008), volcanology (Stevens et al., 2004) or geomorphology (Nefeslioglu et al., 2012). At that time, most studies relied on the AST14DMO DEM

product, generated by the Sensor Information Laboratory Corporation ASTER DEM/Ortho (SILCAST), and distributed directly by NASA (NASA/JAXA, 2007). While this DEM product provided sufficient quality for some applications or to create a gap-free mosaic DEM in the ASTER global digital elevation model (GDEM) effort (Tachikawa et al., 2011), it proved delicate to use reliably for elevation change applications. In glaciology, several studies provided estimation of elevation changes despite the noises in the AST14DMO product, which was facilitated in regions of strong glacier thinning such as Patagonia or Alaska (Willis et al., 2012; Melkonian et al., 2014), but with poor constraints on the influence the noises might have on the errors of the estimates.

In the mid-2010s, the rise of open tools for modern stereophotogrammetry, such as NASA's Ames Stereo Pipeline (ASP; Shean et al., 2016; Beyer et al., 2018) or MicMac (Rupnik et al., 2017), enabled user-specific generation of DEMs from unprocessed ASTER optical data (NASA/JAXA, 2001). In addition to the radiometric corrections enabled by on-flight calibration data (Girod et al., 2017; Tsuchida et al., 2020), the use of rational polynomial coefficients (RPCs) models (Tao and Hu, 2001), as well as cross-track corrections (Girod et al., 2017) derived from imagery metadata, substantially improved the quality of ASTER DEMs. This improvement relative to the AST14DMO product is exacerbated in low-texture areas comprising glacier surfaces, where the AST14DMO DEMs shows noise of several dozen meters (Fig. 3.2). These advances brought by modern photogrammetry thus largely benefited glaciological applications.

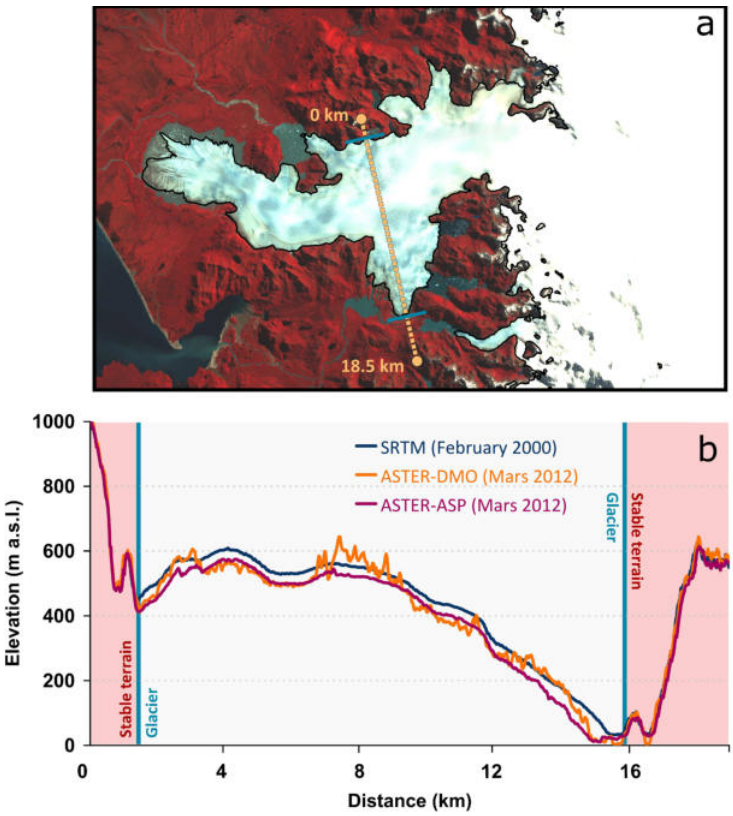

Figure 3.2: Comparison of SRTM, AST14DMO and ASTER ASP DEMs. From Dussaillant et al. (2018). **a-b,** Comparison along a transverse profile of San Quintin Glacier, Northern Patagonian Icefield shown in **(a)**. This profile illustrates the occurrence of numerous artifacts over the glacier surface in the AST14DMO DEM. Conversely, the ASTER-ASP DEM is smoother and follows nicely the undulations of the SRTM DEM with an offset due to glacier thinning between 2000 and 2012.

3.1.3 In the steps of earlier work on glacier volume changes

Despite the improvement in the quality of ASTER DEMs, the spread of their error in measurement (typically evaluated at ±5–10 m for a 30 m x 30 m pixel) largely impeded their use to detect elevation changes. To mitigate this, several studies harnessed the high temporal density provided by ASTER or other sources of DEMs to estimate per-pixel linear elevation trends through time (Willis et al., 2012; Nuimura et al., 2012), typically using ordinary or weighted least-squared for a period close to the first and last DEMs available. Another advantage of using this method to study elevation changes over the typical sequential DEM analysis (Surazakov and Aizen, 2006; Kääb, 2008; Berthier et al., 2010) is that it reduces spatial gaps that can arise from cloud cover, shade or incomplete overlap between the sensor swath and the study site.

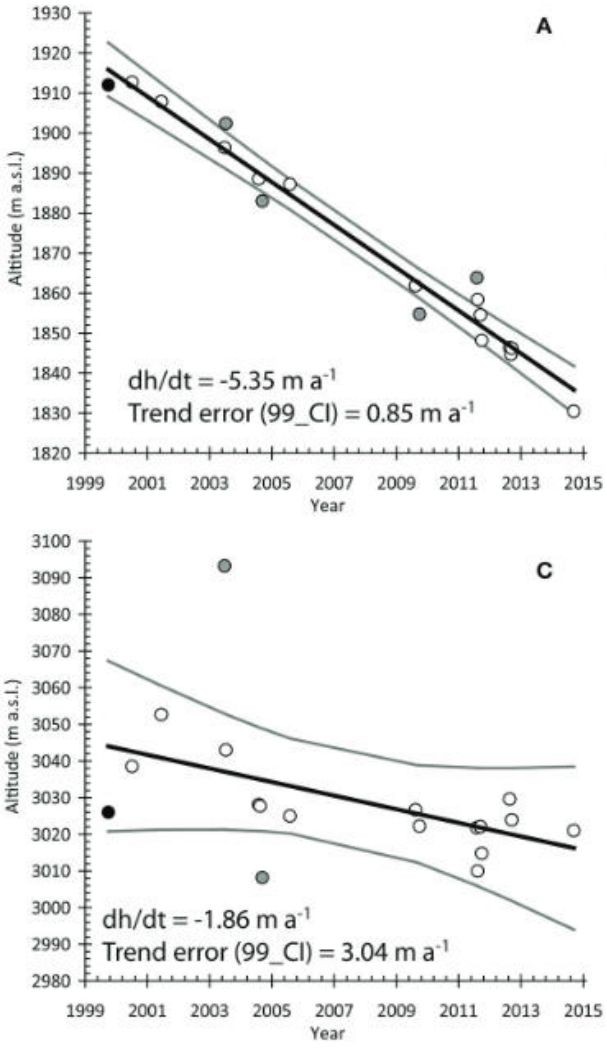

Figure 3.3: Linear elevation fits for ASTER DEMs. From Berthier et al. (2016). Fits of ASTER elevations for a pixel on **(A)** the ablation and **(C)** accumulation area of the Mer de Glace Glacier, France. The gray dots denote outliers, lying outside the 99% confidence interval (gray lines), excluded from subsequent analysis.

By combining trend fitting methods with the improved quality of the DEMs generated by modern photogrammetry (Beyer et al., 2018) and DEM coregistration techniques (Nuth and Kääb, 2011), a recent study showed that ASTER DEMs provided elevation change estimates consistent with independent validation data for periods of about a decade (Berthier et al., 2016). A filtering of large outliers that hamper least-square fitting is often required (Fig. 3.3), and the quality of fit largely depends on the amount of DEMs and their season of acquisition. The above approach was extended at the scale of a large glacierized regions (Brun et al., 2017), which also showed consistent estimates to independent data and previous estimates (Kääb et al., 2012). In this chapter, we build on the work of these previous studies and aim to identify and address several limitations to increase the robustness of glacier elevation change estimates.

3.2 Published article: *Heterogeneous changes in western North American glaciers linked to decadal variability in zonal wind strength*

Published article as second author featured in this section: Menounos, B. et al. (2019), *Heterogeneous changes in western North American glaciers linked to decadal variability in zonal wind strength*, Geophysical Research Letters.[1]

In the study of Menounos et al. (2019), we present a regional estimate of glacier mass change in western North America for the period 2000–2018. This region encompasses glaciers along the Pacific Coast from the Sierra Nevada in the South up to Nahanni in the North, and excluding Alaska. Our study provides resolved elevation changes for nearly all glaciers in the region. In recent assessments, contemporary glacier mass change of western North America was generally estimated by extrapolation of a few in-situ measurements. Notably, an earlier global assessment estimated a strongly negative mass change which does not overlap within uncertainties with our new estimate (Gardner et al., 2013), highlighting the value of large-scale, resolved observations. For British Columbia, our analysis provides a temporal extension to the analysis of Schiefer et al. (2007) that estimated glacier mass changes for the period of 1985–1999.

Our study expands on the study of Brun et al. (2017) by cumulating DEMs from a multitude of sensors including notably WorldView segments generated in high latitudes through the ArcticDEM effort (Howat et al., 2019), but also in British Columbia using the Surface Extraction from TIN based Search-space Minimization (SETSM) algorithm (Noh and Howat, 2017) and using ASP in the continental United States (Shean et al., 2016). Substantial improvements were made to massively process and analyze ASTER DEMs into elevation trends by utilizing GDAL's Python bindings and developing parallel processing routines. We additionally generated and analyzed a large validation dataset of very high-resolution DEMs including lidar acquired in British Columbia by Brian Menounos and colleagues (UNBC), as well as Pléiades and SPOT6-7 DEMs (Berthier et al., 2014). We performed a refined validation analysis by matching the trend analysis to the period of acquisition for each site of the high-resolution dataset. The increased temporal density of our DEMs led to a partitioning of the temporal trend analysis into two subperiods 2000–2008 and 2009–2018 of 9 years, that each yielded statistically significant mass change trends. We thereby uncovered substantial shifts in trends between those two subperiods, and we performed an analysis to study its relation to decadal climatic changes.

[1] Contribution: in the study of Menounos et al. (2019), I developed the code to perform the processing of all satellite and aerial data including ASTER, WorldView, SPOT and lidar DEMs, and the statistical analysis to yield glacier estimates. Some DEMs were pre-processed by co-authors. I analyzed the results and improved the uncertainty analysis alongside Brian Menounos, who wrote the initial draft and performed the climate data analysis. More details on co-author contributions in the "Acknowledgments".

AGU100 ADVANCING EARTH AND SPACE SCIENCE

Geophysical Research Letters

RESEARCH LETTER
10.1029/2018GL080942

Key Points:
- We provide a comprehensive assessment of mass change for western North American (WNA) glaciers excluding those in Alaska
- WNA glaciers lost 117 +/- 42 gigatons (Gt) of mass over the period 2000-2018 and could account for 0.32 +/- 0.11 mm of sea level rise
- Regional changes in glacier mass are partly explained by decadal scale changes in atmospheric circulation

Supporting Information:
- Supporting Information S1

Correspondence to:
B. Menounos,
menounos@unbc.ca

Citation:
Menounos, B., Hugonnet, R., Shean, D., Gardner, A., Howat, I., Berthier, E., et al. (2019). Heterogeneous changes in western North American glaciers linked to decadal variability in zonal wind strength. *Geophysical Research Letters*, *46*, 200–209. https://doi.org/10.1029/2018GL080942

Received 15 OCT 2018
Accepted 7 DEC 2018
Accepted article online 13 DEC 2018
Published online 15 JAN 2019

Heterogeneous Changes in Western North American Glaciers Linked to Decadal Variability in Zonal Wind Strength

B. Menounos[1], R. Hugonnet[1,2], D. Shean[3], A. Gardner[4], I. Howat[5], E. Berthier[2], B. Pelto[1], C. Tennant[1], J. Shea[1], Myoung-Jong Noh[5], F. Brun[6], and A. Dehecq[4]

[1]Natural Resources and Environmental Studies Institute and Geography, University of Northern British Columbia, Prince George, British Columbia, Canada, [2]LEGOS, Université de Toulouse, CNES, CNRS, IRD, UPS, Toulouse, France, [3]Department of Civil and Environmental Engineering, University of Washington, Seattle, WA, USA, [4]Jet Propulsion Laboratory, California Institute of Technology, Pasadena, CA, USA, [5]School of Earth Sciences and Byrd Polar and Climate Center, The Ohio State University, Columbus, OH, USA, [6]Université Grenoble Alpes, CNRS, IRD, Grenoble INP, IGE, Grenoble, France

Abstract Western North American (WNA) glaciers outside of Alaska cover 14,384 km^2 of mountainous terrain. No comprehensive analysis of recent mass change exists for this region. We generated over 15,000 multisensor digital elevation models from spaceborne optical imagery to provide an assessment of mass change for WNA over the period 2000–2018. These glaciers lost 117 ± 42 gigatons (Gt) of mass, which accounts for up to 0.32 ± 0.11 mm of sea level rise over the full period of study. We observe a fourfold increase in mass loss rates between 2000–2009 [−2.9 ± 3.1 Gt yr^{-1}] and 2009–2018 [−12.3 ± 4.6 Gt yr^{-1}], and we attribute this change to a shift in regional meteorological conditions driven by the location and strength of upper level zonal wind. Our results document decadal-scale climate variability over WNA that will likely modulate glacier mass change in the future.

Plain Language Summary Glaciers in western North America provide important thermal and flow buffering to streams when seasonal snowpack is depleted. We used spaceborne optical satellite imagery to produce thousands of digital elevation models to assess recent mass loss for glaciers in western North America outside of Alaska. Our analysis shows that glacier loss over the period 2009–2018 increased fourfold relative to the period 2000–2009. This mass change over the last 18 years is partly explained by changes in atmospheric circulation. Our results can be used for future modeling studies to understand the fate of glaciers under future climate change scenarios.

1. Introduction

Anthropogenic warming is expected to drive continued mass loss from alpine glaciers throughout the remainder of this century (Marzeion et al., 2017). Relative to other alpine environments, glaciers in western North America (WNA) are expected to play a minor role in future sea level rise (Levermann et al., 2013; Marzeion et al., 2018; Radić et al., 2014) given their small, cumulative volume (Huss & Farinotti, 2012). These ice masses, however, represent important freshwater reservoirs that provide late-summer meltwater runoff when seasonal snowpacks have been depleted (Frans et al., 2018; Moore et al., 2009) or during years characterized by drought (Jost et al., 2012). Water managers require up-to-date assessments of how these ice masses have and will likely change in the coming decades.

A global assessment of glacier mass change by Gardner et al. (2013) included an estimate of WNA glacier mass loss of 14 ± 3 Gt yr^{-1} for the period 2003–2009 based on the extrapolation of sparse in situ surface mass balance (SMB) measurements (Cogley, 2009). Other approaches to estimate glacier mass change, such as satellite laser altimetry and satellite gravimetry employed by Gardner et al. (2013) for other glacierized regions, have so far proven unsuccessful for WNA due to sparse repeat-track spacing at lower latitudes and challenges associated with deconvolving competing mass change signals (groundwater, seasonal snow, reservoir volumes and glacio-isostatic adjustment). Such methods perform particularly poorly for lower-latitude mountain ranges with disperse glacier coverage, such as those that characterize WNA (Gardner et al., 2013; Jacob et al., 2012).

Repeat mapping of surface elevation through stereophotogrammetry provides an additional approach to measure glacier thickness change on a regional scale that can circumvent spatial and temporal biases imposed by using SMB observations to estimate regional mass change. Geodetic surveys exist for many

Geophysical Research Letters 10.1029/2018GL080942

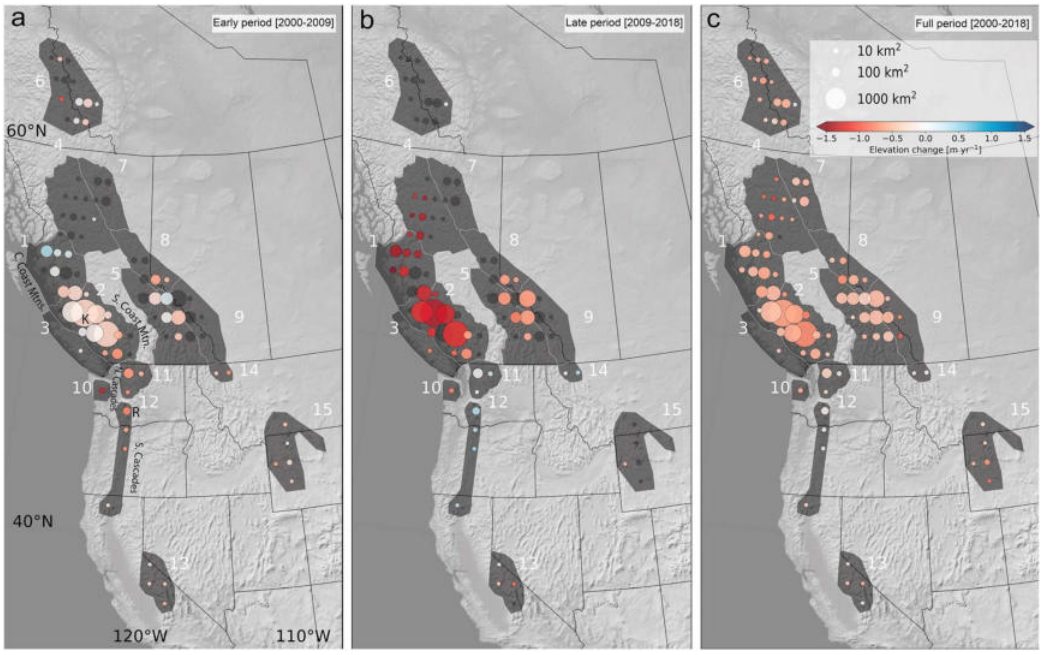

Figure 1. Gridded (1 × 1°) glacier elevation change (m yr^{-1}) for western North America. Circle diameters are scaled to area represented by grid point. Grid points with less than 30% of sampled ice are shown as dark gray. (a) early period (2000–2009), (b) late (2009–2018), (c) full (2000–2018). Numbers refer to subregions (Table 1) and letters "K" (region 03) and "R" (region 12) respectively denote approximate location of Klinaklini Glacier and Mount Rainier (Figure 2).

glacierized regions of WNA (e.g., Basagic & Fountain, 2011; Schiefer et al., 2007), but no study samples all of these regions in a systematic fashion. Novel methods to infer elevation change from medium resolution satellite imagery (Brun et al., 2017) coupled with automated processing of both medium and very high resolution optical satellite imagery (Noh & Howat, 2017; Shean et al., 2016) provide new opportunities to improve global estimates of glacier mass change.

The primary motivation of our paper is to provide the first, regionally complete estimate of glacier mass change for WNA for the period 2000–2018. We then use these data to (i) quantify the contribution of WNA glaciers to sea level rise over the last 18 years, (ii) determine the reliability and representativeness of existing WNA in situ SMB records, and (iii) assess the climatic drivers that affect mass change at the subregional scale.

2. Materials and Methods

Here we use the term WNA to define glaciers of Region 2 from the Randolph Glacier Inventory (RGI-6.0), which is the most comprehensive digital ice coverage map for WNA (RGI Consortium, 2017). Glaciers cover 14,384 km^2 of mountainous terrain in WNA with 88% of glacier coverage in British Columbia and Alberta, 7% in the conterminous United States (CONUS), and 5% in the Yukon and Northwest Territories (Figure 1 and Table 1). To provide regional comparisons of mass change, we subdivided glacierized terrain into 15 regions (Figure 1 and Table 1). In British Columbia, we use the same regions as those described in previous work (Clarke et al., 2015; Schiefer et al., 2007).

The primary data set we use to assess glacier mass change over the last 18 years consists of digital elevation models (DEMs) obtained from the Advanced Spaceborne Thermal Emission and Reflection Radiometer (ASTER) visible and near infrared instrument. The multispectral sensor collects both nadir and aft visible imagery with a native ground sample distance of 15 m and a swath width of ~60 km (Abrams, 2000; Raup et al., 2000). Our workflow for ASTER DEM generation (see supporting information S1) processes all ASTER scenes for 1 × 1° tiles that contain a minimum glacier area of 5 km^2. In British Columbia and Alberta, glacier extents in RGI-6.0 originate from Landsat imagery acquired between 2004 and 2006 (Bolch et al., 2010), whereas ice extents from Yukon, Northwest Territories, and CONUS originate from multiple sources with varied

Geophysical Research Letters 10.1029/2018GL080942

Table 1
Elevation Change and Mass Budget of Western North American Glaciers (2000–2018)

Region	Area[a] (km^2)	Mass balance[b] (kg m^{-2} yr^{-1})			Mass budget (Gt yr^{-1})
		early[c]	late	full	full
Central Coast (1)[d]	1,580	−42 ± 221	−1,067 ± 418	−424 ± 163	−0.669 ± 0.258
Southern Coast (2)	7,180	−215 ± 190	−1,027 ± 258	−517 ± 140	−3.709 ± 1.006
Vancouver Island (3)	12	−205 ± 171	−681 ± 206	−309 ± 120	−0.004 ± 0.001
Northern Interior (4)	253	75 ± 298	−1,143 ± 510	−608 ± 222	−0.154 ± 0.056
Southern Interior (5)	1,946	−175 ± 232	−647 ± 352	−353 ± 185	−0.686 ± 0.360
Nahanni (6)	649	−220 ± 250	−419 ± 444	−407 ± 192	−0.264 ± 0.124
Northern Rockies (7)	415	−148 ± 271	−724 ± 506	−362 ± 233	−0.150 ± 0.097
Central Rockies (8)	422	−483 ± 284	−671 ± 370	−474 ± 202	−0.200 ± 0.086
Southern Rockies (9)	1,350	−200 ± 240	−614 ± 376	−394 ± 205	−0.533 ± 0.277
Olympics (10)	30	−1,113 ± 259	−696 ± 235	−474 ± 144	−0.014 ± 0.004
North Cascades (11)	250	−567 ± 184	46 ± 106	−245 ± 87	−0.061 ± 0.022
South Cascades (12)	153	−632 ± 147	346 ± 112	−46 ± 61	−0.007 ± 0.009
Sierra Nevada (13)	11	−234 ± 231	−448 ± 326	−318 ± 141	−0.004 ± 0.002
Glacier Natl. Park (14)	29	−522 ± 310	235 ± 268	−41 ± 158	−0.001 ± 0.005
Wind River (15)	60	−202 ± 249	−652 ± 571	−503 ± 187	−0.030 ± 0.011
Total (WNA)[e]	14,341	−203 ± 214	−858 ± 320	−452 ± 162	−6.49 ± 2.32

[a]Glacierized area. [b]Mass change (kg m^{-2} yr^{-1}) converted to mass using a density 850 kg m^{-3}. [c]Full, early, and late, respectively, refer to periods 2000–2009, 2009–2018, and 2000–2018. [d]Numbers refer to regions defined on Figure 1. [e]Area-weighted averages and uncertainties for mass balance.

acquisition dates (Fountain et al., 2017; Kienholz et al., 2015; Pfeffer et al., 2014). For the CONUS regions, all glacier outlines of the RGI-6.0 covering less than 0.1 km^2 were removed, which excludes less than 0.5% of all WNA ice cover from our analysis.

For DEM generation we used two open-source software packages for the mass production of DEMs from satellite stereoscopic imagery: the National Aeronautics and Space Administration Ames Stereo Pipeline (ASP) (Beyer et al., 2018; Shean et al., 2016) and the Ohio State University's Surface Extraction from TIN (triangulated irregular network)-based Search-space Minimization (SETSM; Noh & Howat, 2015, 2017). We used ASP to generate 15,500 DEMs with 30-m posting from ASTER stereoscopic imagery acquired between 2000 and 2018. We supplemented the ASTER DEMs with 693 higher-resolution (2 to 8 m) DEMs generated from submeter resolution DigitalGlobe WorldView-1, WorldView-2, WorldView-3, and GeoEye-1, and three DEMs generated from Pléiades satellite imagery (e.g., Berthier et al., 2014). WorldView/GeoEye data for CONUS were processed using ASP, while those over Canada were processed using SETSM. These non-ASTER DEMs, though temporally limited, increased repeat coverage for accumulation areas where ASTER DEMs often contain data gaps due to lack of surface texture at lower spatial and radiometric resolution. Their inclusion also increased sample count for trend fitting compared to the ASTER record.

Unlike many conventional geodetic mass balance studies that difference elevation data over glaciers between two epochs (e.g., Gardner et al., 2013; Schiefer et al., 2007), we evaluate per pixel linear trends for overlapping DEMs over the last 18 years (e.g., Willis et al., 2012). Our method builds upon the techniques described for glacier mass change in the French Alps (Berthier et al., 2016) and high-mountain Asia (Brun et al., 2017). We calculate the temporal trend in elevation (dh/dt) over stable and ice-covered terrain, the latter defined as those regions that lie within polygons of the RGI-6.0 glacier inventory. Time-variable glacier outlines are not available, so we use constant glacier area outlines for the full 18-year period (supporting information S1).

Individual DEMs were resampled to 30 m and coregistered over all stable, subaerial terrain excluding ice cover, and lakes (supporting information S1) using the Nuth and Kääb (2011) approach and the Global DEM (GDEMv2; Tachikawa et al., 2011) as a reference. Once DEMs are coregistered, we perform linear weighted least squares regression for a given map coordinate$_{\{x,\,y\}}$ with elevation $z_{\{t1,\,t2,\,\ldots,\,tn\}}$, where the subscript x,y refers to the local Universal Transverse Mercator projection easting and northing of a given DEM of time t. This method provides an estimate of elevation change (dh/dt) at coordinate$_{\{x,\,y\}}$ with associated error taken to be the confidence interval of the regression about the linear fit (supporting information S1). To

Geophysical Research Letters 10.1029/2018GL080942

calculate volumetric change (dV/dt) for a given elevation band, we use hypsometric extrapolation where volume change is the summed product of average dh/dt for a given elevation band and its corresponding area. We use a density of 850 ± 60 kg m^{-3} to convert dV/dt to mass change (Huss, 2013). Global sea level equivalence is calculated using a density for water of 1,000 kg m^{-3} and an ocean surface area of 3.6×10^{14} m^2 (Amante, 2009).

Our uncertainty analysis consists of both random and systematic errors. Random errors are dominated by DEM quality (precision) and coregistration success; it can be approximated by the standard deviation (σ_z) of elevation change from stable surfaces corrected for spatial autocorrelation (Rolstad et al., 2009). Any seasonal elevation variability (e.g., snow cover and vegetation) is also included in this metric. Full details describing the propagation of errors, including systematic errors, are provided elsewhere (supporting information S1).

To calculate changes in rates of mass change at the decadal scale, we split the elevation data set into two epochs of equal duration [1 June 2000 to 15 September 2009 and 1 June 2009 to 15 September 2018] hereafter referred to as early [2000–2009] and late [2009–2018]. We did not consider changes in rates on timescales less than a decade because of relatively high errors in the individual ASTER DEMs and potentially insufficient temporal sampling.

We also analyzed geopotential height (500 hPa), temperature (700 hPa), precipitation, and wind (zonal, meridional, and speed) from ERA5 (Hersbach & Dee, 2016) for the two study epochs to evaluate climatological drivers for observed glacier mass change. The ERA5 is a global reanalysis product that consists of 107 vertical levels on a 31-km grid, assimilates the greatest number of surface- and satellite-based observations of any reanalysis product, and currently extends from January 2000 to August 2018. Temperature at 700 hPa is approximately 3,100 m above sea level, and so approximates air temperatures above the elevation of most glaciers in WNA. Interannual to interdecadal climate variability is known to affect mass change of WNA glaciers (Bitz & Battisti, 1999; Hodge et al., 1998; Moore et al., 2009; Watson et al., 2006), so we also evaluated whether decadal change in glacier mass were explained by any major shifts in ocean-atmospheric phenomena known to affect climate in WNA (supporting information S1).

3. Results

The DEMs cover over 99.5% of the WNA glacierized terrain, with statistically significant elevation change for 82% of those surveyed areas. Coverage for the early [2000–2009], late [2009–2018], and full periods [2000–2018] over glacierized terrain respectively averages 45% (10 DEMs per pixel), 45% (8 DEMs per pixel), and 80% (13 DEMs per pixel). Fortunately, the most heavily glacierized subregions of our study domain contain a suitable number of DEMs to minimize uncertainties for all three periods during the 1 × 1° tile aggregation. High random and systematic errors exist for some subregions (e.g., Olympic Mountains, Table 1) with limited available stable terrain for coregistration. We observe the highest uncertainty in the Interior Ranges and Canadian Rocky Mountains (Table 1) due to reduced temporal coverage (average of nine DEM samples per pixel). While some subregions, such as the Sierra Nevada, North Cascades, and South Cascades, have greater sample depth (26 DEMs per pixel on average), they still yield mass change estimates with moderate uncertainties due in part to the high errors caused by uncertainties in mapped glacier extent. Temporal subdivision increases the uncertainty in our mass change estimates due to the reduced sample size of each epoch relative to the full 2000–2018 period of study (supporting information S1).

We also calculated mass change using sequential DEM differencing of independent high-resolution data for 175 glaciers in British Columbia (Figure S1 and Table S1). Comparison of these changes over common periods of time suggests that our ASTER-based elevation trends (Figure S5) represent unbiased estimates of mass change for glaciers larger than 0.5 km^2 (supporting information S1).

WNA experienced spatially variable glacier elevation change over the period 2000–2018 (Figure 1). When elevation change is aggregated for subregions, small glaciers in the northern interior ranges of British Columbia thinned most, whereas our trend analysis is unable to detect elevation change that is statistically different from zero for glaciers within the South Cascades and Glacier National Park over the last 18 years (Figure 1 and Table 1). Large glaciers sourced from icefields in the southern Coast Mountains experienced high rates of thinning ($>$ 10 m yr^{-1}) at low elevations (Figure 2). When averaged over all regions, WNA glaciers lost

Geophysical Research Letters 10.1029/2018GL080942

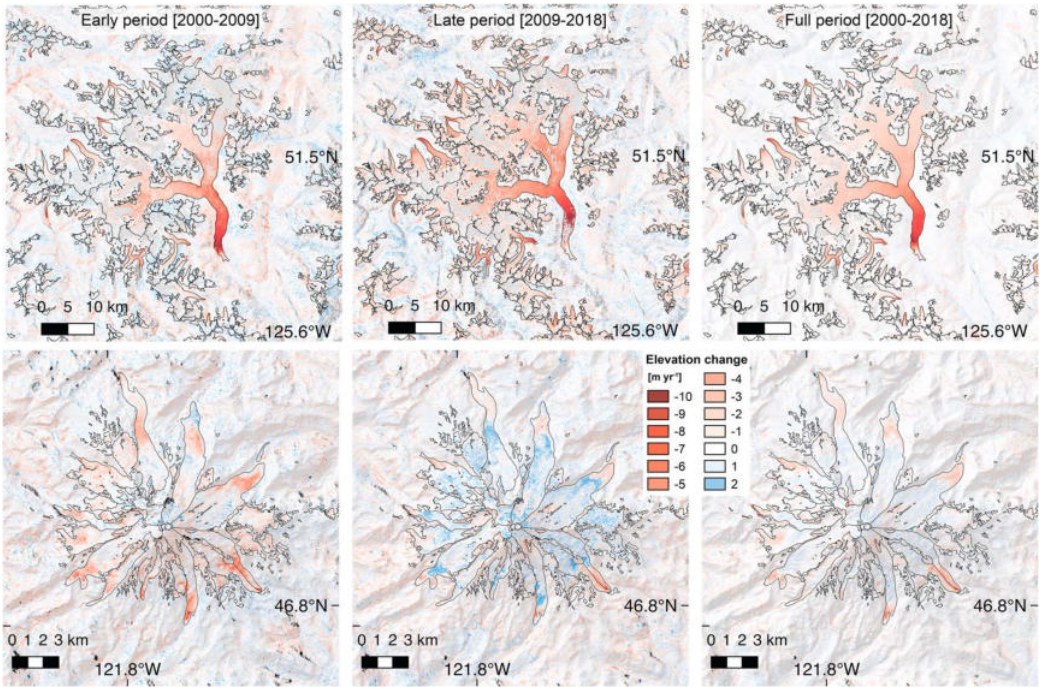

Figure 2. (top row) Elevation trend (m yr^{-1}) for Klinaklini Glacier (southern Coast Mountains) for early (top left), late (top middle), and full (top right). (bottom row) Same as upper row except for Mount Rainier (South Cascades). Gray areas denote no data.

-6.5 ± 2.3 Gt yr^{-1} during the period 2000–2018 (Table 1). Ninety-eight percent of this mass change originated from Canadian glaciers with ice loss in the southern Coast Mountains accounting for 58% of the total mass loss.

Our results show a fourfold increase in rates of mass loss between the early (-2.9 ± 3.1 Gt yr^{-1}) and late periods (-12.3 ± 4.6 Gt yr^{-1}), with notable regional differences (Figure 1). A prominent dipole in rates of mass change exists between the British Columbia central Coast [50–55°N] and the Cascade mountains [42–47°N] of the United States (Figure 1). During the early epoch, mass change was less negative for glaciers in the southern latitudes of British Columbia, whereas glaciers in the Cascade Mountains experienced high rates of mass loss (Table 1). This pattern reversed during the late period when glacier mass loss from the southern Coast Mountains increased by a factor of 4.8. Glaciers in the south Cascades showed slight mass gain with no detectable mass change in the north Cascades (Figure 2 and Table 1).

The ERA5 fields reveal changes in wind speed, temperature, and precipitation between the early and late periods (Figure 3). The north-south dipole in mass change along the U.S.-Canada border (Figure 1) coincide with a shift in the average location of the midlatitude jet, here defined as the maximum velocity for upper-level (250 hPa) winds. Regional composites of monthly averaged column-integrated moisture flux (kg·m^{-1}·s^{-1}), temperature (K) at 700 hPa, and precipitation (m yr^{-1}) over the early and late periods likewise reveal latitudinal differences in those meteorological conditions that influence SMB. Regional composites of geopotential height in the Northern Hemisphere also show a zone of lower than normal pressure across the latitude band [42–47°N] with an area of higher than normal pressure across most of British Columbia (supporting information S1). These differences in geopotential height are maximized for the winter season (October–May), but they also occur during summer (June–September). During the last decade wet conditions coincided with areas of lower-than-average geopotential height in the Pacific Northwest whereas the central Coast Mountains experienced warm, dry conditions (Figure 3).

An examination of the relation between meteorological conditions and glacier mass change at time scales finer than a decade is not possible given the number of DEMs required for statistically significant elevation trend analysis. Cumulative departures of monthly precipitation anomalies for the 31-km ERA5 grid cell near Mount Rainier in the North Cascades (Figure 2), however, reveals that the period 2000–2007 was

Geophysical Research Letters 10.1029/2018GL080942

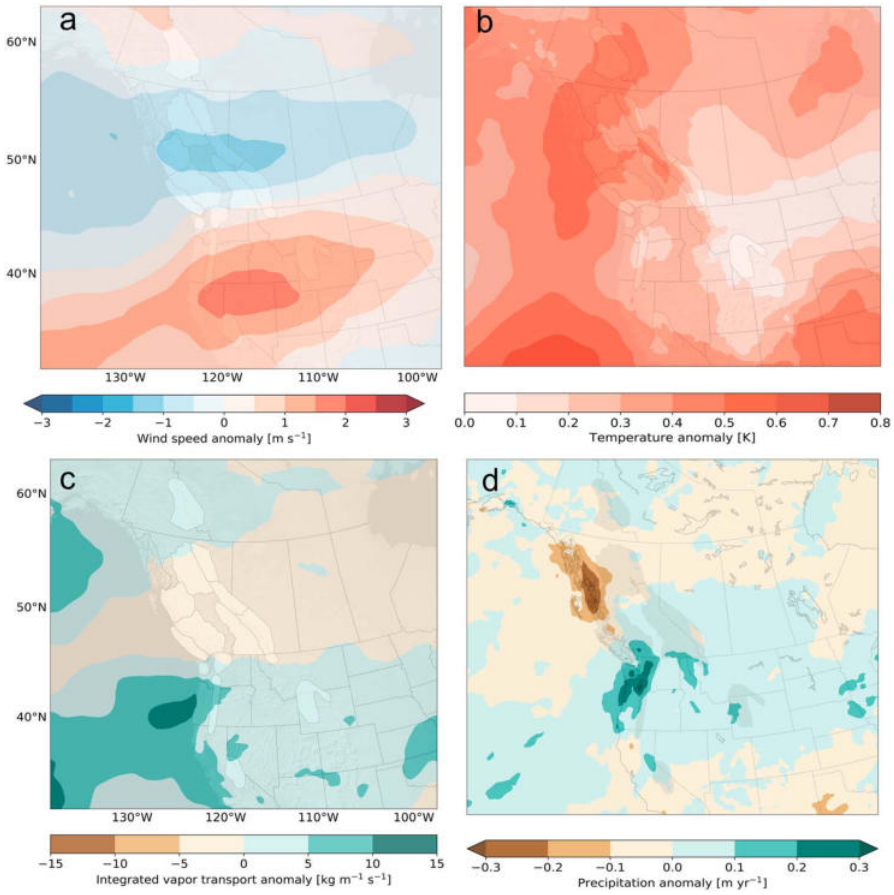

Figure 3. Anomalies ([2009–2017 mean] minus [2000–2009 mean]) of monthly fields from ERA5. (a) Zonal wind (250 hPa; m s^{-1}). (b) Temperature (700 hPa; K). (c) Column integrated vapor transport (kg m^{-1} s^{-1}). (d) Precipitation (m yr^{-1}).

characterized by drier than average conditions. An increase in precipitation commenced after 2011 for that location whereas a decrease in precipitation occurred over the central Coast Mountains after 2012.

Previous estimates of geodetic mass change for WNA glaciers at the subregional scale are primarily limited to British Columbia and Alberta (Schiefer et al., 2007). Our estimates and those from Schiefer et al. (2007) show a complex pattern of mass change (Figure 4), with most of these subregions showing mass loss for the period 1985–1999. Rates of mass loss slowed from 2000 to 2009 and then increased from 2009 to 2018 (Figure 4). The southern Coast Mountains alone contain nearly half of the total ice cover of WNA, and the rate of mass loss over the last 9 years was -7.4 ± 1.9 Gt yr^{-1}, about 20% faster than the period 1985–1999.

4. Discussion and Implications of Our Study

Our study provides a comprehensive assessment of glacier mass change (-6.5 ± 2.3 Gt yr^{-1}) for nearly all glacierized terrain in WNA over the period 2000–2018. Our estimated rate of WNA mass change for the early period (-2.9 ± 3.1 Gt yr^{-1}) is considerably less negative than the rate (-14 ± 3 Gt yr^{-1}) previously reported for the period 2003–2009 (Gardner et al., 2013).

In situ observations of SMB are invaluable given their temporal continuity and value in understanding climatic drivers of mass change (Hodge et al., 1998), but their use may bias regional estimates of mass change (Gardner et al., 2013). Our analysis (supporting information S1) shows that glaciological measurements of mass change are in broad agreement with geodetic estimates at the local scale, but they do not effectively sample large ice masses that dominate the regional signal of mass change from WNA, namely, large icefields in the southern Coast Mountains. Using available SMB measurements for 14 glaciers in WNA (supporting

Geophysical Research Letters 10.1029/2018GL080942

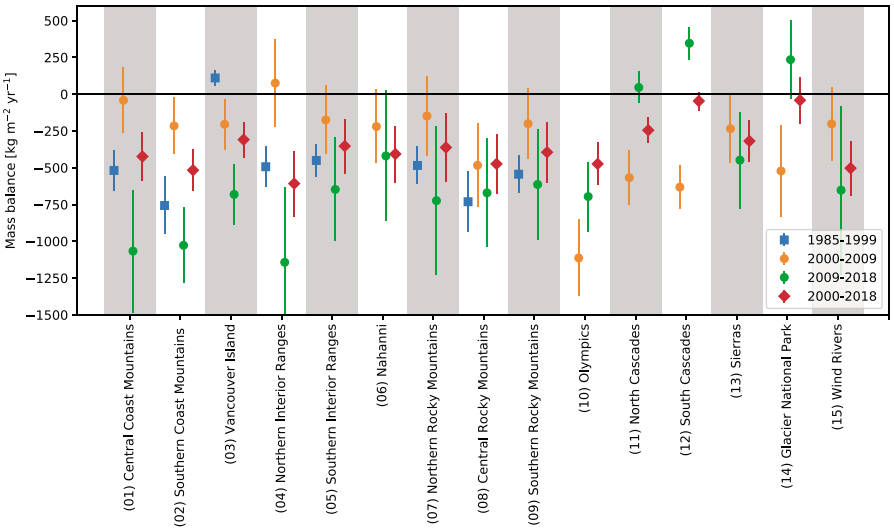

Figure 4. Estimated mass balance and uncertainties ($\pm 1\sigma$) for different subregions of western North American for periods 2000–2009, 2009–2018, 2000–2018, and for the period 1985–1999 (Schiefer et al., 2007).

information S1), we calculate an average mass change of -874 ± 100 kg m^{-2} yr^{-1} over the period 2000–2017. When multiplied by the total glacierized area of WNA, this value yields an annual mass loss of 13.6 ± 4.3 Gt yr^{-1}, close to the value (14 ± 3 Gt yr^{-1}) calculated by Gardner et al. (2013) using a similar approach. These values are twice as large as those based on our trend analysis. This discrepancy suggests that glaciers chosen for long-term monitoring programs are losing mass more rapidly than the region as a whole. Our findings accord with a study by Fountain et al. (2009), who concluded that South Cascade Glacier, chosen for long-term in situ SMB observations, lost three times more mass than glaciers in the north Cascade Mountains (subregion 11 of Table 1).

Cumulative mass loss from WNA glaciers over the period 2000–2018 could potentially account for 0.32 ± 11-mm global sea level rise equivalent, about 0.6% of observed SLR over the period 1993–2017 (Nerem et al., 2018). Our estimate is an upper limit as it assumes that meltwater from glacier mass loss was directly conveyed to the ocean and not stored in intermediate locations (e.g., proglacial lakes formed over the last 18 years). While surface storage of this water might be small, it could contribute to aquifer recharge (Liljedahl et al., 2017).

One of the most surprising findings of our study is the dipole pattern of mass change between glaciers in the British Columbia central Coast [50–55°N] and the Cascade mountains [42–47°N] of the United States (Figure 1). Positive anomalies in zonal winds (250 hPa) over the Cascade Mountains imply a strengthening and southward shift in the jet stream between the early and late periods that would increase the frequency of mid-latitude cyclones with attendant increases in precipitation. A change in meteorological conditions that favor changes in glacier mass are clearly revealed in the composite anomaly maps, especially for the central, southern Coast and Cascade glaciers (Figure 3). Glaciers of the southern Coast Mountains descend to lower elevations than those that flank high Cascade volcanoes. The partitioning of precipitation into either rain or snow may also explain why some of the Cascade glaciers gained mass during the recent period while Coast Mountain glaciers continued to experience strong thinning and mass loss. Future work employing surface mass and energy balance modeling at the glacier scale can be used to test this hypothesis.

The spatial distribution of subregional mass change is partly linked to regional changes in atmospheric circulation that affect accumulation and ablation. Others have noted the importance of zonal wind on controlling glacier mass balance (Marshall et al., 2011; Shea & Marshall, 2007), and some studies attribute a decline in zonal wind strength to explain the long-term (1950–2005) decline in winter snow water equivalent (Luce et al., 2013). In our study, anomalies in zonal wind covary with many of the meteorological fields known to control glacier mass balance, namely, temperature and precipitation. Orographically enhanced precipitation in WNA is also favored when strong zonal flow delivers moist air masses that originate over the Pacific Ocean

Geophysical Research Letters 10.1029/2018GL080942

(Jarosch et al., 2012; Neiman et al., 2008). Regions of weak zonal wind also coincide with lower-than-average geopotential height over last 18 years.

It remains uncertain whether mass change observed over the last 18 years is related to natural climate variability known to affect glacier mass balance in WNA (Bitz & Battisti, 1999; Hodge et al., 1998; Moore & Demuth, 2001), stochastic variability, or whether these recent changes are related to anthropogenic climate change. We note no obvious relation between major climate indices and decadal changes in zonal wind strength or pressure at the subregional scale (supporting information S1). Using an ensemble of 25 global climate models, however, Luce et al. (2013) show that under a high emission scenario (RCP8.5), zonal wind (700 hPa) strength significantly decreases over the Cascade and Coast Mountains by the end of this century. Zonal winds weaken most over the central and southern Coast Mountains (50–55°N) but strengthen over southern latitudes of California (Luce et al., 2013). Based on the results of our study, weaker zonal winds would tend to favor stronger mass loss for glaciers in the Cascade and Coast Mountains.

Glaciers in both the CONUS and western Canada are expected to undergo continued mass loss throughout this century, even under moderate emission scenarios (Clarke et al., 2015; Frans et al., 2018; Huss & Hock, 2018). These changes will reduce or eliminate the thermal- and flow-buffering capacity provided by glacier runoff for many watersheds, with implications for downstream ecosystems and water resources. If the last 18 years provide a suitable analogue for the next 30–50 years, future glacier change will be modulated by decadal-scale climate variability. Like seasonal snow cover, improvement in understanding and forecasting climate variability at decadal time scales will be important to help guide estimates of glacier mass change for water management. Projections of future glacier mass change for both the CONUS (Frans et al., 2018) and western Canada (Clarke et al., 2015), like other regions, depend on well-distributed observations of glacier area and mass change, and our results can be used to improve modeling efforts that seek to understand the fate of glaciers under future climate scenarios.

Acknowledgments
This research was supported by grants from National Sciences and Engineering Research Council of Canada, the Canadian Foundation for Innovation, the Canadian Research Chairs Program, the Tula Foundation (Hakai Institute) and Global Water Futures (Water Mountain Futures), BC Hydro, and the Columbia Basin Trust. Gardner and Dehecq were supported by funding from the NASA Cryosphere and MEaSUREs Programs. Berthier acknowledges support from the French Space Agency (CNES) through the TOSCA program. The Pléiades stereo pairs were provided by the Pléiades Glacier Observatory initiative (CNES). SPOT 5 HRS DEMs were made available by the International Polar Year SPIRIT project (CNES). Shean acknowledges support from the National Park Service (NPS), United States Geological Survey (USGS), and National Aeronautics and Space Administration (NASA). Resources supporting the CONUS DEM production were provided by the NASA High-End Computing (HEC) Program through the NASA Advanced Supercomputing (NAS) Division at Ames Research Center. Menounos thanks NASA JPL for partial financial support during his sabbatical. DEM generation was supported by high-performance computer facilities at UNBC, Legos, Ohio State and the National Science Foundation. Howat and Noh were funded by the U.S. National Science Foundation Polar Cyberinfrastructure (PLR) program grant 1542736. WV DEMs for Canada were produced using an allocation from NSF Extreme Science and Engineering Discovery Environment (XSEDE). We acknowledge the agencies (World Monitoring Glacier Survey, the United States Geological Survey, and Natural Resources of Canada) and key individuals (Mike Demuth, Mark Ednie, Andrew Fountain, Ed Josberger, Bob Krimmel, Shad O'Neel, Mauri Pelto, Jon Riedel, Erin Whorton, and Gordon Young) for their efforts to establish and maintain monitoring programs for WNA glaciers. Data used in this contribution are available from http://www.unbc.ca/research/supplementary-data-unbc-publications. We thank an anonymous referee and Laura Thomson for providing detailed reviews that improved our manuscript. Finally, we wish to dedicate this study to the memory of Graham Cogley who passed away during the writing of this manuscript. Menounos, Gardner, Berthier, and Shean collectively designed the study; Hugonnet and Menounos processed the ASTER DEMs and completed the trend and uncertainty analysis; and Menounos wrote the initial draft of the paper. Pelto, Tennant, and Shea compiled and

References

Abrams, M. (2000). The Advanced Spaceborne Thermal Emission and Radiometer (ASTER): Data products for the high spatial resolution imager on NASA's Terra platform. *International Journal of Remote Sensing*, *21*(5), 847–859. https://doi.org/10.1080/014311600210326

Amante, C. (2009). *ETOPO1 1 arc-minute global relief model: procedures, data sources and analysis*. Washington, DC: National Ocean and Atmospheric Administration. Retrieved from http://www.ngdc.noaa.gov/mgg/global/global.htm

Basagic, H. J., & Fountain, A. G. (2011). Quantifying 20th century glacier change in the Sierra Nevada, California. *Arctic, Antarctic, and Alpine Research*, *43*(3), 317–330. https://doi.org/10.1657/1938-4246-43.3.317

Berthier, E., Cabot, V., Vincent, C., & Six, D. (2016). Decadal region-wide and glacier-wide mass balances derived from multi-temporal ASTER satellite digital elevation models. Validation over the Mont-Blanc area. *Frontiers of Earth Science*, *4*. https://doi.org/10.3389/feart.2016.00063

Berthier, E., Vincent, C., Magnússon, E., Gunnlaugsson, Á., Pitte, P., Le Meur, E., et al. (2014). Glacier topography and elevation changes derived from Pléiades sub-meter stereo images. *The Cryosphere*, *8*(6), 2275–2291. https://doi.org/10.5194/tc-8-2275-2014

Beyer, R. A., Alexandrov, O., & McMichael, S. (2018). The Ames Stereo Pipeline: NASA's open source software for deriving and processing terrain data. *Life Support & Biosphere Science: International Journal of Earth Space*, *56*, 221.

Bitz, C. M., & Battisti, D. S. (1999). Interannual to decadal variability in climate and the glacier mass balance in Washington, Western Canada, and Alaska. *Journal of Climate*, *12*(11), 3181–3196. https://doi.org/10.1175/1520-0442(1999)012<3181:ITDVIC>2.0.CO;2

Bolch, T., Menounos, B., & Wheate, R. (2010). Landsat-based inventory of glaciers in western Canada, 1985–2005. *Remote Sensing of Environment*, *114*(1), 127–137. https://doi.org/10.1016/j.rse.2009.08.015

Brun, F., Berthier, E., Wagnon, P., Kääb, A., & Treichler, D. (2017). A spatially resolved estimate of High Mountain Asia glacier mass balances, 2000-2016. *Nature Geoscience*, *10*(9), 668–673. https://doi.org/10.1038/ngeo2999

Clark, A., Fagre, D., Peitzsch, E., Reardon, B., & Harper, J. (2017). Glaciological measurements and mass balances from Sperry Glacier, Montana, USA, years 2005-2015. *Earth System Science Data*, *9*(1), 47–61. https://doi.org/10.5194/essd-9-47-2017

Clarke, G. K. C., Jarosch, A. H., Anslow, F. S., Radić, V., & Menounos, B. (2015). Projected deglaciation of western Canada in the twenty-first century. *Nature Geoscience*, *8*(5), 372–377. https://doi.org/10.1038/ngeo2407

Cogley, G., Adams, W., Ecclestone, M., Jung-Rothenhäusler, F., & Ommanney, C. S. L. (1996). Mass balance of White Glacier, Axel Heiberg Island, NWT, Canada, 1960–91. *Journal of Glaciology*, *42*(142), 548–563. https://doi.org/10.1017/S0022143000003531

Cogley, J. G. (2009). Geodetic and direct mass-balance measurements: Comparison and joint analysis. *Annals of Glaciology*, *50*(50), 96–100. https://doi.org/10.3189/172756409787769744

Demuth, M., & Keller, R. (2006). An assessment of the mass balance of Peyto Glacier (1966–1995) and its relation to recent and past-century climatic variability. Peyto Glacier: One century of. *Science*, *8*, 83–132.

Fountain, A. G., Glenn, B., & Basagic, H. J. (2017). The geography of glaciers and perennial snowfields in the American West. *Arctic, Antarctic, and Alpine Research*, *49*(3), 391–410. https://doi.org/10.1657/AAAR0017-003

Fountain, A. G., Hoffman, M. J., Granshaw, F., & Riedel, J. (2009). The "benchmark glacier" concept—Does it work? Lessons from the North Cascade Range, USA. *Annals of Glaciology*, *50*(50), 163–168. https://doi.org/10.3189/172756409787769690

Frans, C., Istanbulluoglu, E., Lettenmaier, D. P., Fountain, A. G., & Riedel, J. (2018). Glacier recession and the response of summer streamflow in the Pacific Northwest United States, 1960-2099. *Water Resources Research*, *54*, 772. https://doi.org/10.1029/2017WR021764

Gardner, A. S., Moholdt, G., Cogley, J. G., Wouters, B., Arendt, A. A., Wahr, J., et al. (2013). A reconciled estimate of glacier contributions to sea level rise: 2003 to 2009. *Science*, *340*(6134), 852–857. https://doi.org/10.1126/science.1234532

Geophysical Research Letters 10.1029/2018GL080942

analyzed in situ data. Shean tasked, acquired, and processed WV imagery for the conterminous United States, while Gardner, Howat, Menounos and Noh acquired and processed WV scenes from western Canada. Brun and Dehecq developed code used in our analysis. All authors discussed and commented on the manuscript. Author contributions and competing interests: none.

Granshaw, F. D., & Fountain, A. G. (2006). Glacier change (1958–1998) in the North Cascades National Park Complex, Washington, USA. *Journal of Glaciology*, *52*(177), 251–256. https://doi.org/10.3189/172756506781828782

Hersbach, H., & Dee, D. (2016). ERA5 reanalysis is in production. *ECMWF Newsletter*, *147*, 7.

Hodge, S. M., Trabant, D. C., Krimmel, R. M., Heinrichs, T. A., March, R. S., & Josberger, E. G. (1998). Climate variations and changes in mass of three glaciers in western North America. *Journal of Climate*, *11*(9), 2161–2179. https://doi.org/10.1175/1520-0442(1998)011<2161:CVACIM>2.0.CO;2

Hopkinson, C., & Demuth, M. (2006). Using airborne lidar to assess the influence of glacier downwasting on water resources in the Canadian Rocky Mountains. *Canadian Journal of Remote Sensing*, *32*(2), 212–222. https://doi.org/10.5589/m06-012

Huss, M. (2013). Density assumptions for converting geodetic glacier volume change to mass change. *The Cryosphere*, *7*(3), 877–887. https://doi.org/10.5194/tc-7-877-2013

Huss, M., & Farinotti, D. (2012). Distributed ice thickness and volume of all glaciers around the globe. *Journal of Geophysical Research*, *117*(F4), F04010. https://doi.org/10.1029/2012JF002523

Huss, M., & Hock, R. (2018). Global-scale hydrological response to future glacier mass loss. *Nature Climate Change*, *8*(2), 135–140. https://doi.org/10.1038/s41558-017-0049-x

Jacob, T., Wahr, J., Pfeffer, W. T., & Swenson, S. (2012). Recent contributions of glaciers and ice caps to sea level rise. *Nature*, *482*(7386), 514–518. https://doi.org/10.1038/nature10847

Jarosch, A. H., Anslow, F. S., & Clarke, G. K. C. (2012). High-resolution precipitation and temperature downscaling for glacier models. *Climate Dynamics*, *38*(1–2), 391–409.

Josberger, E., Bidlake, W., March, R., & Kennedy, B. (2007). Glacier mass-balance fluctuations in the Pacific Northwest and Alaska, USA. *Annals of Glaciology*, *46*(1), 291–296. https://doi.org/10.3189/172756407782871314

Jost, G., Moore, R. D., Menounos, B., & Wheate, R. (2012). Quantifying the contribution of glacier runoff to streamflow in the upper Columbia River Basin, Canada. *Hydrology and Earth System Sciences*, *16*(3), 849–860. https://doi.org/10.5194/hess-16-849-2012

Kienholz, C., Herreid, S., Rich, J. L., Arendt, A. A., Hock, R., & Burgess, E. W. (2015). Derivation and analysis of a complete modern-date glacier inventory for Alaska and Northwest Canada. *Journal of Glaciology*, *61*(227), 403–420. https://doi.org/10.3189/2015JoG14J230

Korona, J., Berthier, E., Bernard, M., Rémy, F., & Thouvenot, E. (2009). SPIRIT. SPOT 5 stereoscopic survey of polar ice: Reference images and topographies during the fourth international polar year (2007–2009). ISPRS journal of photogrammetry and remote sensing: Official publication of the International Society for Photogrammetry and. *Remote Sensing*, *64*(2), 204–212.

Krimmel, R. (1999). Analysis of difference between direct and geodetic mass balance measurements at South Cascade glacier, Washington. *Geografiska Annaler. Series A, Physical Geography*, *81*(4), 653–658. https://doi.org/10.1111/j.0435-3676.1999.00093.x

Krimmel, R. M. (1997). Water, ice, meteorological, and speed measurements at South Cascade Glacier, Washington, 1996 balance year. *U.S. Geological Survey*. https://doi.org/10.3133/wri994049

Levermann, A., Clark, P. U., Marzeion, B., Milne, G. A., Pollard, D., Radic, V., & Robinson, A. (2013). The multimillennial sea-level commitment of global warming. *Proceedings of the National Academy of Sciences of the United States of America*, *110*(34), 13745–13750. https://doi.org/10.1073/pnas.1219414110

Liljedahl, A. K., Gädeke, A., O'Neel, S., Gatesman, T. A., & Douglas, T. A. (2017). Glacierized headwater streams as aquifer recharge corridors, subarctic Alaska. *Geophysical Research Letters*, *44*, 6876–6885. https://doi.org/10.1002/2017GL073834

Luce, C. H., Abatzoglou, J. T., & Holden, Z. A. (2013). The missing mountain water: Slower westerlies decrease orographic enhancement in the Pacific Northwest USA. *Science*, *342*(6164), 1360–1364. https://doi.org/10.1126/science.1242335

Marshall, S. J., White, E. C., Demuth, M. N., Bolch, T., Wheate, R., Menounos, B., et al. (2011). Glacier water resources on the eastern slopes of the Canadian Rocky Mountains. *Canadian Water Resources Journal/Revue Canadienne Des Ressources Hydriques*, *36*(2), 109–134. https://doi.org/10.4296/cwrj3602823

Marzeion, B., Champollion, N., Haeberli, W., Langley, K., Leclercq, P., & Paul, F. (2017). Observation-based estimates of global glacier mass change and its contribution to sea-level change. *Surveys in Geophysics*, *38*(1), 105–130. https://doi.org/10.1007/s10712-016-9394-y

Marzeion, B., Kaser, G., Maussion, F., & Champollion, N. (2018). Limited influence of climate change mitigation on short-term glacier mass loss. *Nature Climate Change*, *8*(4), 305–308. https://doi.org/10.1038/s41558-018-0093-1

Meier, M., & Tangborn, W. (1965). Net budget and flow of South Cascade Glacier, Washington. *Journal of Glaciology*, *5*(41), 547–566. https://doi.org/10.1017/S0022143000018608

Moore, R. D., & Demuth, M. N. (2001). Mass balance and streamflow variability at Place Glacier, Canada, in relation to recent climate fluctuations. *Hydrological Processes*, *15*(18), 3473–3486. https://doi.org/10.1002/hyp.1030

Moore, R. D., Fleming, S. W., Menounos, B., Wheate, R., Fountain, A., Stahl, K., et al. (2009). Glacier change in western North America: Influences on hydrology, geomorphic hazards and water quality. *Hydrological Processes*, *23*(1), 42–61. https://doi.org/10.1002/hyp.7162

Neiman, P. J., Ralph, F. M., Wick, G. A., Lundquist, J. D., & Dettinger, M. D. (2008). Meteorological characteristics and overland precipitation impacts of atmospheric rivers affecting the west coast of North America based on eight years of SSM/I satellite observations. *Journal of Hydrometeorology*, *9*(1), 22–47. https://doi.org/10.1175/2007JHM855.1

Nerem, R. S., Beckley, B. D., Fasullo, J. T., Hamlington, B. D., Masters, D., & Mitchum, G. T. (2018). Climate-change–driven accelerated sea-level rise detected in the altimeter era. *Proceedings of the National Academy of Sciences of the United States of America*, *115*(9), 2022–2025. https://doi.org/10.1073/pnas.1717312115

Noh, M. J., & Howat, I. M. (2017). The surface extraction from TIN based search-space minimization (SETSM) algorithm. *ISPRS Journal of Photogrammetry and Remote Sensing: Official Publication of the International Society for Photogrammetry and Remote Sensing*, *129*, 55–76.

Noh, M.-J., & Howat, I. M. (2015). Automated stereo-photogrammetric DEM generation at high latitudes: Surface extraction with TIN-based search-space minimization (SETSM) validation and demonstration over glaciated regions. *GIScience and Remote Sensing*, *52*(2), 198–217. https://doi.org/10.1080/15481603.2015.1008621

Nuth, C., & Kääb, A. (2011). Co-registration and bias corrections of satellite elevation data sets for quantifying glacier thickness change. *The Cryosphere*, *5*(1), 271–290. https://doi.org/10.5194/tc-5-271-2011

Pelto, M. (1996). Changes in glacier and alpine runoff in the North Cascade Range, Washington, USA 1985–1993. *Hydrological Processes*, *10*(9), 1173–1180. https://doi.org/10.1002/(SICI)1099-1085(199609)10:9<1173::AID-HYP368>3.0.CO;2-V

Pelto, M., & Brown, C. (2012). Mass balance loss of mount baker, Washington glaciers 1990–2010. *Hydrological Processes*, *26*(17), 2601–2607. https://doi.org/10.1002/hyp.9453

Pelto, M., & Riedel, J. (2001). Spatial and temporal variations in annual balance of North Cascade glaciers, Washington 1984–2000. *Hydrological Processes*, *15*(18), 3461–3472. https://doi.org/10.1002/hyp.1042

Pfeffer, W. T., Arendt, A. A., Bliss, A., Bolch, T., Cogley, J. G., Gardner, A. S., et al., & The Randolph Consortium (2014). The Randolph Glacier Inventory: A globally complete inventory of glaciers. *Journal of Glaciology*, *60*(221), 537–552. https://doi.org/10.3189/2014JoG13J176

Radić, V., Bliss, A., Cody Beedlow, A., Hock, R., Miles, E., & Graham Cogley, J. (2014). Regional and global projections of twenty-first century glacier mass changes in response to climate scenarios from global climate models. *Climate Dynamics*, *42*(1–2), 37–58.

Raup, B. H., Kieffer, H. H., Hare, T. M., & Kargel, J. S. (2000). Generation of data acquisition requests for the ASTER satellite instrument for monitoring a globally distributed target: Glaciers. *IEEE Transactions on Geoscience and Remote Sensing: A Publication of the IEEE Geoscience and Remote Sensing Society*, *38*(2), 1105–1112.

RGI Consortium (2017). Randolph Glacier Inventory—A dataset of global glacier outlines: Version 6.0: Technical report, Global Land Ice Measurements from Space, Colorado, USA. Digital Media. DOI: [Data set]. https://doi.org/10.7265/N5-RGI-60

Roberti, G., Friele, P., van Wyk de Vries, B., Ward, B., Clague, J. J., Perotti, L., & Giardino, M. (2017). Rheological evolution of the Mount Meager 2010 debris avalanche, southwestern British Columbia. *Geosphere*, *13*(2), 369–390.

Rolstad, C., Haug, T., & Denby, B. (2009). Spatially integrated geodetic glacier mass balance and its uncertainty based on geostatistical analysis: Application to the western Svartisen ice cap, Norway. *Journal of Glaciology*, *55*(192), 666–680. https://doi.org/10.3189/002214309789470950

Schiefer, E., Menounos, B., & Wheate, R. (2007). Recent volume loss of British Columbian glaciers, Canada. *Geophysical Research Letters*, *34*, L16503. https://doi.org/10.1029/2007GL030780

Shea, J. M., & Marshall, S. J. (2007). Atmospheric flow indices, regional climate, and glacier mass balance in the Canadian Rocky mountains. *International Journal of Climatology*, *27*(2), 233–247. https://doi.org/10.1002/joc.1398

Shean, D. E., Alexandrov, O., Moratto, Z. M., Smith, B. E., Joughin, I. R., Porter, C., & Morin, P. (2016). An automated, open-source pipeline for mass production of digital elevation models (DEMs) from very-high-resolution commercial stereo satellite imagery. *ISPRS Journal of Photogrammetry and Remote Sensing: Official Publication of the International Society for Photogrammetry and Remote Sensing*, *116*, 101–117.

Tachikawa, T., Hato, M., Kaku, M., & Iwasaki, A. (2011). Characteristics of ASTER GDEM version 2. In 2011 *IEEE International Geoscience and Remote Sensing Symposium* (pp. 3657–3660).

Tennant, C., & Menounos, B. (2013). Glacier change of the Columbia Icefield, Canadian Rocky Mountains, 1919–2009. *Journal of Glaciology*, *59*(216), 671–686. https://doi.org/10.3189/2013JoG12J135

Tennant, C., Menounos, B., Ainslie, B., Shea, J., & Jackson, P. (2012). Comparison of modeled and geodetically-derived glacier mass balance for Tiedemann and Klinaklini glaciers, southern Coast Mountains, British Columbia, Canada. *Global and Planetary Change*, *82–83*, 74–85.

VanLooy, J., & Forster, R. (2008). Glacial changes of five Southwest British Columbia icefields, Canada, mid-1980s to 1999. *Journal of Glaciology*, *54*(186), 469–478. https://doi.org/10.3189/002214308785836931

Watson, E., Luckman, B. H., & Yu, B. (2006). Long-term relationships between reconstructed seasonal mass balance at Peyto glacier, Canada, and Pacific sea surface temperatures. *Holocene*, *16*(6), 783–790. https://doi.org/10.1191/0959683606hol973ft

Willis, M. J., Melkonian, A. K., Pritchard, M. E., & Rivera, A. (2012). Ice loss from the Southern Patagonian Ice Field, South America, between 2000 and 2012. *Geophysical Research Letters*, *39*, L17501. https://doi.org/10.1029/2012GL053136

Young, G. J. (1981). The mass balance of Peyto glacier, Alberta, Canada, 1965 TO 1978. *Arctic and Alpine Research*, *13*(3), 307–318. https://doi.org/10.2307/1551037

Zemp, M., Nussbaumer, S., Gartner-Roer, I., Huber, J., Machguth, H., Paul, F., & Hoelzle, M. (2017). Global Glacier Change Bulletin (no. 2). World Glacier Monitoring Service, Switzerland.

Zemp, M., Thibert, E., Huss, M., Stumm, D., Rolstad Denby, C., Nuth, C., et al. (2013). Reanalysing glacier mass balance measurement series. *The Cryosphere*, *7*(4), 1227–1245. https://doi.org/10.5194/tc-7-1227-2013

3.3 Limitations in glacier volume change estimation from satellite imagery

3.3.1 Spatial variability of precision in photogrammetric-based geodetic elevation changes

Published article as co-author featured in this section: Dussaillant, I. et al. (2019), *Two decades of glacier mass loss along the Andes*, Nature Geoscience.[2]

Despite the recent improvements in regional glacier assessments from satellite imagery (Brun et al., 2017; Menounos et al., 2019), several limitations remain. In the study of Dussaillant et al. (2019), we tackled a first limitation that concerns the filtering of outliers and the spatial interpolation of data gaps. Outliers are common in digital elevation models (Höhle and Höhle, 2009). For photogrammetric DEMs, they generally stem from artefacts that can arise from cloud cover or lack of texture. For interferometric DEMs, outliers can originate from layover, shadowing, or signal scattering. On stable terrain, the filtering of these outliers is straightforward if an independent, quality-controlled reference DEM is available (e.g., by removing elevations with a difference to the reference DEM larger than a certain threshold, possibly based on the dispersion of the elevation differences to the reference). Such filtering methods are unfeasible on moving terrain, however, where the signal of elevation changes from moving surfaces is entangled with that of artefacts from the instrument or processing (e.g. Fig. 3.2).

Moreover, data gaps occur in the DEMs when the estimated elevations are discarded due to their low quality during processing. For photogrammetry, data gaps are especially common in textureless surfaces or in areas shadowed by steep slopes. Both affect glacier surfaces and are particularly limiting to resolve bright accumulation areas. With moderate resolution stereo imagery such as ASTER, there are relatively few data gaps in alpine regions where surfaces are fragmented by rugged topography and blackened by debris, including High Mountain Asia (Brun et al., 2017) or western North America (Menounos et al., 2019). But data gaps are substantial in regions with large icefields such as Patagonia (Dussaillant et al., 2019), and for ice caps that comprise most of the glacierized surfaces in the polar regions. The outliers and data gaps in DEMs thus call for outlier filtering and interpolation methods to analyze elevation changes.

In the study of Dussaillant et al. (2019), we identified a bias owed to an outlier filter used by previous geodetic studies during interpolation (Brun et al., 2017; Braun et al., 2019). This filter was used in combination with the global hypsometric method (McNabb et al., 2019) where data gaps are interpolated by the mean elevation change of glaciers in the region for a given 50–100 m elevation band. To remove outliers on moving terrain, the outlier filter

[2]Contribution: in the study of Dussaillant et al. (2019), I developed new code to automatically retrieve and sort ASTER L1A data. I also developed computationally-efficient code to process ASP-generated ASTER DEMs into elevation change trends, and aggregate estimates from pixel-scale to glacier- and regional-scale, largely inspired by routines originally developed by Fanny Brun. Additionally, I provided input to Ines Dussaillant to perform supplemental analyses, notably regarding outlier filtering methods.

excluded elevation changes values outside 3 times the Normalized Median Absolute Deviation (NMAD) in the elevation band. For regions with a high variability of elevation changes among glaciers, this method erroneously excluded the most negative and positive elevation changes, replacing them by the regional average (Fig. 3.8). Because of the non-symmetrical distribution of elevation changes in the region, this filtering ultimately biased the final estimate. For example, the mass change of the Southern Patagonian Icefield from TanDEM-X data is estimated at -1.01 m yr^{-1} (Braun et al., 2019) with a 3 NMAD filter, and -1.20 m yr^{-1} without filter (Dussaillant et al., 2019), which is not captured by the reported uncertainties of <0.01 m yr^{-1} (Braun et al., 2019).

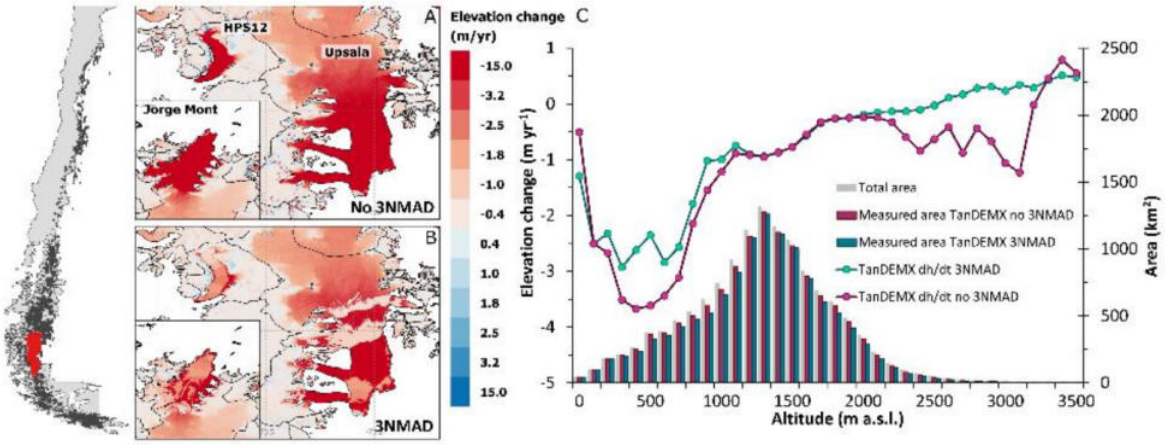

Figure 3.8: Influence of the NMAD filter in hypsometric glacier elevation change interpolation. From Dussaillant et al. (2019). Example at the Southern Patagonian Icefield. TanDEM-X elevation changes of Braun et al. (2019) are used due to their nearly-complete coverage. **(A)** TanDEM-X elevation changes for Jorge Mont, HPS12 and Upsala glaciers without filter. **(B)** TanDEM-X elevation changes using a 3 NMAD filter for each 100 m elevation band of the SPI. **(C)** TanDEM-X hypsometric elevation changes for the entire icefield, without filter (purple) and with a 3 NMAD filter (blue).

Additionally, to reduce the need of a filter during interpolation of glacier elevation change in Dussaillant et al. (2019), we introduced a temporal filtering method that directly applies to the DEMs. We tested this method on the extreme case of the tongue of glacier HPS12 of the Southern Patagonian Icefield (Fig. 3.8) where we identified the most negative known glacier elevation change trend of -50 m yr^{-1}, translating to 1 km of thinning in 20 years. Our temporal filter harnesses the temporal density of the ASTER acquisitions. Starting chronologically with the quality-controlled SRTM elevation of February 2000 as reference, we exclude the temporally-closest ASTER elevation if that observation is separated by a higher trend than 50 m yr^{-1}. If the elevation is kept, it becomes the new reference for the next filtering step. The maximum value of thinning was adjusted per region to improve the filter. This method helped to reduce the effect of outliers. Yet, it remains limited due its simplicity and the inherent variability in the precision of elevation observations due to terrain- and sensor-related variables described in Chapter 2. In the next main article of this chapter, we tackle these issues to include the spatial variability in precision, i.e. heteroscedasticity of elevation, into a refined temporal filter for outliers and an improved hypsometric interpolation.

3.3.2 Improving the temporal resolution of geodetic elevation change estimations

Published article as co-author featured in this section: Davaze, L. et al. (2020), *Region-wide annual glacier surface mass balance for the European Alps from 2000 to 2016*, Frontiers in Earth Science.[3]

The precision of geodetic mass change estimates directly depends on the length of the study period. Indeed, the uncertainties of a DEM are anchored to a certain point in time and, when propagated into uncertainties of yearly rates of elevation change, decrease linearly with the period length. As such, shorter periods are usually tainted by larger uncertainties when using DEMs of similar precision. Additionally, the conversion from volume to mass changes for a period shorter than 5 years entails large uncertainties due to unknown states of accumulated firn and its compaction (Huss, 2013). Geodetic volume changes alone are therefore limited to estimate interannual glacier mass changes.

In the work of Davaze et al. (2020), we aim to capture the interannual variability of glacier mass changes by remote sensing. To this end, we utilized an approach based on observation of end-of-summer snowline altitude. The end-of-summer snowline altitude is a known proxy of the equilibrium-line altitude for glacier where superimposed ice is negligible (Lliboutry, 1965), and its position has been described as a predictor of annual glacier mass changes (Braithwaite, 1984). We estimated the annual end-of-summer snowlines altitude from optical images including Landsat, Sentinel-2 and ASTER. Using an approach developed by Rabatel et al. (2005), we calibrated their variability to the long-term geodetic mass change of each glacier, independently estimated from ASTER DEMs with a methodology similar to that of Menounos et al. (2019). We applied this methodology at the scale of the European Alps, and we found that the standardized mass changes from our per-glacier estimations were consistent with that of in situ measurements available for 23 glaciers (Fig. 3.9).

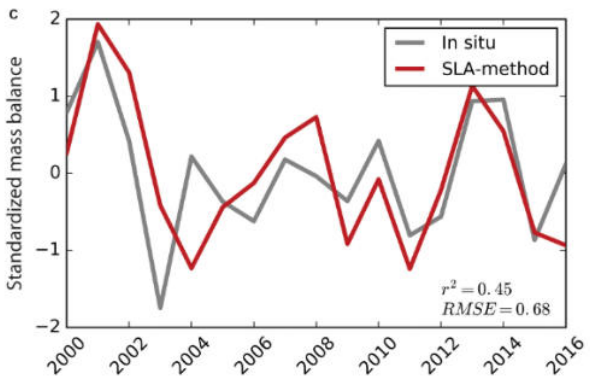

Figure 3.9: End-of-summer snowline as a proxy for interannual mass balance variability. From Davaze et al. (2020). Mean standardized interannual variability of in situ and end-of-summer snowline estimates for 23 glaciers of the European Alps.

Remotely-sensed snowline methods are especially valuable to shed light on interannual mass balance variability in regions of scarce in situ measurements, such as in Central Asia (Barandun et al., 2021). Snowline methods act as a proxy, however, for which it is complex to assess the sources and mechanisms leading to errors that propagate to the final estimations.

[3]Contribution: in the study of Davaze et al. (2020), I retrieved, processed and analyzed all ASTER DEMs covering the European Alps to provide glacier mass balance estimates for the period 2000–2016.

Moreover, the geodetic estimates used to calibrate the magnitude of the mass change over longer period contribute largely to the uncertainties. A critical limitation of using geodetic estimates for calibration is that they generally suffer from inconsistent temporal coverage owed to uncontrolled acquisition dates. Recent studies have further complexified the definition of temporal coverage by employing linear temporal fitting to improve spatial coverage and mitigate precision issues (Brun et al., 2017; Menounos et al., 2019), as they rely on the aggregation of pixel-wise elevation change estimates that are based on different year and season of DEM acquisition for every location. These estimations rarely corrected for possible seasonal or yearly biases due to this inconsistent temporal coverage and, when they do so, generally rely on modelling (Belart et al., 2017). In the next main article of this chapter, we tackle these issues by introducing a temporal fitting method based on the covariance of the data through Gaussian Processes. This approach mitigates the effects of varying seasonal and yearly acquisitions to allow a more robust estimation for any period with associated propagation of errors.

3.3.3 The spatiotemporal inconsistency of uncertainty analyses

The recent increase in large-scale DEM availability both from ASTER and TanDEM-X imagery has led to a multitude of large-scale glacier volume change assessments (Brun et al., 2017; Braun et al., 2019; Zemp et al., 2019; Shean et al., 2020; Sommer et al., 2020). With these new estimations available, the issue of inter-comparability quickly arose. Many estimations differ substantially, both in their central estimate and their reported uncertainty range, and often refer to unclear time periods. This issue was largely echoed by the IPCC Special Report on the Ocean and Cryosphere in a Changing Climate (Hock et al., 2019b) in their effort to provide a reconciled glacier mass change estimate.

Table 3.2: Estimates of two assessements of glacier mass change in the Andes. The estimate of Braun et al. (2019) refers to 2000–2011/15 and the estimate of Dussaillant et al. (2019) refers to 2000–2015.

Study	Andes-wide	Southern Patagonian Icefield
Dussaillant et al. (2019)	-0.69 ± 0.17 m w.e. yr^{-1}	-0.90 ± 0.29 m w.e. yr^{-1}
Braun et al. (2019)	-0.58 ± 0.07 m w.e. yr^{-1}	-0.86 ± 0.08 m w.e. yr^{-1}

The most critical aspect of the inter-comparability of estimates is their statistical significance, i.e. the reported uncertainty. For example, the two recent studies of Dussaillant et al. (2019) and Braun et al. (2019) provide uncertainty estimates for specific-mass change that differ by a factor of 2–5 (Table 3.2), and even more for mean elevation change rates (factor of 5–50). Surprisingly, however, these studies all rely on the same methods for their uncertainty analysis, could it be for spatial correlations of elevation changes (Rolstad et al., 2009), gap-filling (Berthier et al., 2016) or volume-to-mass conversion (Huss, 2013). Additionally, their underlying DEMs all have an average vertical precision of the same order of magnitude ($\pm$3–10 m), and a similar spatial resolution (12–30 m).

Where do these large differences come from, then? Mainly, they arise from the spatiotemporal scale at which the uncertainty propagation methods have been applied. For demonstration purposes, let us consider the example of the uncertainty in volume-to-mass conversion of $\pm 60\,\mathrm{kg\,m^{-3}}$ (Huss, 2013) that is multiplied to the mean elevation change during propagation. Some studies apply this uncertainty at the glacier scale, and then propagate them independently between glaciers, or sometimes at the subregional scale and propagate them independently between subregions (e.g. Braun et al., 2019). Others apply them as if fully correlated for all glaciers in the region (e.g. Dussaillant et al., 2019). Some apply them for 5-year periods and propagate the contributions of those periods independently in time, while others apply them for 20-year periods as if fully correlated. Ultimately, these different assumptions make uncertainty estimates vary by several orders of magnitude for an individual uncertainty source (for volume-to-mass conversion, by a factor larger than 100 between the former and latter spatial assumptions applied in the Andes).

The final uncertainties of different assessments fall within the same range of magnitude only because of a few sources that were consistently applied at the same scale (e.g. 5% uncertainty on the glacier area applied at the regional scale for the whole period), and which have been hiding the large discrepancies between other sources. Another issue that prevented these discrepancies to come to light is that assumptions of spatiotemporal scale or uncertainty propagation are generally given little importance during the scientific writing and review of these studies. Eventually, those aspects are largely omitted in the published methods, which makes reproducibility difficult to understand the origin of differences.

In the study of Menounos et al. (2019) and Dussaillant et al. (2019), we introduced an additional, empirical source of uncertainty estimated from a triangulation exercise inspired by Brun et al. (2017) on the DEM temporal coverage at the tile scale to help reconcile the discrepancies between the glacier scale and the regional scale, and account for varying temporal coverage (see Fig. B3). This simple empirical method helps yield larger, more realistic uncertainties but fails to estimate the error at all spatial and temporal scales and mixes sources of uncertainties (measurement precision, interpolation, and seasonal biases). To tackle this, in the next main article of this chapter, we introduce a spatiotemporal approach expanding on our work in Chapter 2. This approach estimates and propagates elevation uncertainties based on spatial correlations with varying time lags to the closest DEM observation, estimated from the difference between our elevation time series and high-precision ICESat measurements. Beforehand, however, we need to develop the tools necessary to produce, correct and analyze a large amount of DEMs globally.

3.4 Development of open tools for large-scale DEM bias-correction and spatiotemporal analysis

3.4.1 *pymmaster:* an open package for generating and correcting ASTER DEMs

In-prep article as co-author featured in this section: Nuth, C., McNaab, R., Girod, L., and Hugonnet, R. (in prep.), *The ASTER DEM legacy: precise elevation extraction for change detection.*[4]

In the study of Nuth et al. (in prep.), we build on the work of Girod et al. (2017) on MicMac for ASTER (MMASTER) to further improve the quality of ASTER DEMs. During his doctoral thesis, Luc Girod (Department of Geosciences, University of Oslo) focused notably on photogrammetry with historical and modern stereo-imagery, including notably ASTER DEMs (Girod, 2018). In a recent continuation of this work on ASTER, we made several advances described below, and directly integrated into the open package *pymmaster* of Girod et al. (2017) (available at `https://github.com/luc-girod/MMASTER-workflows` with documentation at `https://mmaster-workflows.readthedocs.io/`) and which is based on both Python and bash routines from MicMac (Rupnik et al., 2017).

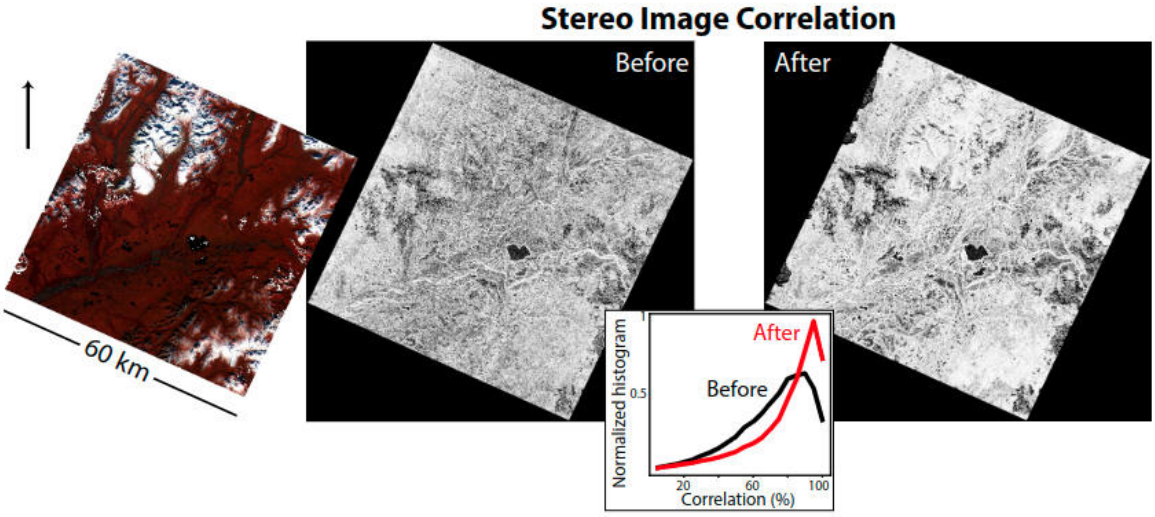

Figure 3.10: Improvement in stereo-correlation from ASTER cross-track correction. From Nuth et al. (in prep.). Example of an ASTER scene taken in northwestern Alaska. Maps shows values of stereo-correlation from 0% (black) to 100% (white). Inset shows normalized histogram of correlation values (0-100%). The cross-track corrections significantly improve the quality of stereo-correlation, and thus the resulting DEMs.

[4]Contribution: in the study of Nuth et al. (in prep.), I analyzed a case study of nearly simultaneous SPOT-5 and ASTER DEMs at the Northern Patagonian Icefield to assess the robustness of cross- and along-track corrections. I processed about 500,000 ASTER DEMs near glaciers globally by optimizing the routines of *pymmaster* for mass processing, and analyzed the metadata of correction parameters worldwide.

The first step forward of Nuth et al. (in prep.) consists of correcting the parallax in the back-looking image due to cross-track ASTER biases (Fig. 3.1). This procedure requires only the nadir and back-looking image, and is therefore independent of an external reference DEM. Because this correction is made directly in image geometry, before the DEM is generated, it directly improves the quality of the generated DEM, mirrored by the improvement in stereo-correlation (Fig. 3.10).

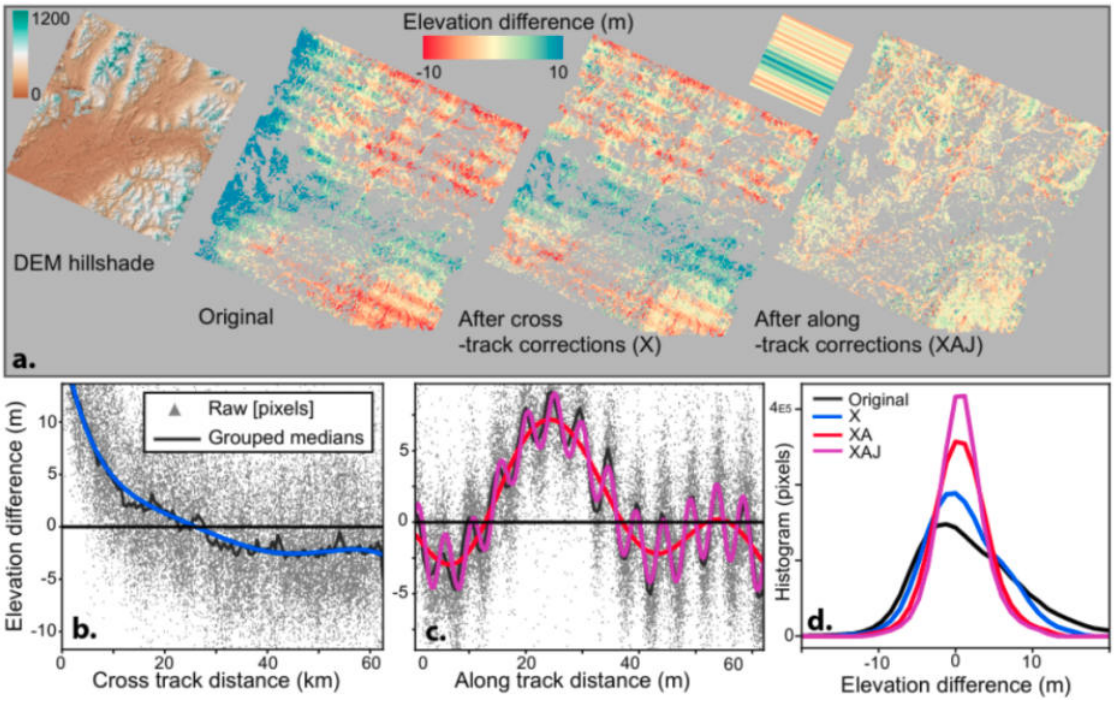

Figure 3.11: Cross- and along-track corrections of ASTER DEMs. From Nuth et al. (in prep.). **a-d,** Corrections steps of MMASTER shown on **(a)** elevation differences maps, **(b)** cross-track distance with polynomial fit, **(c)** along-track distance with sum of sinusoids fit and **(d)** histograms of elevation differences. X stands for cross-track, XA for cross- and along-track low frequency undulations and XAJ for cross- and along-track with both low frequency undulations and jitter (i.e. high-frequency undulations). The map of along-track correction is shown in a small inset on panel **(a)**, between elevation differences after cross- and along-track corrections.

A second improvement of Nuth et al. (in prep.) relates to the along-track undulations in ASTER DEMs. Unfortunately, those cannot be corrected solely from the ASTER imagery and metadata because they have not been linked to any measured sensor motion, and because they occur in the same direction utilized by the photogrammetric calculations to generate the DEM (Girod et al., 2017). Previous studies used a polynomial or sum of sinuoids fit in the along-track direction with an independent DEM to correct these undulations (Girod et al., 2017; Brun et al., 2017; Deschamps-Berger et al., 2020). When using these methods, however, imperfect fitting and edge artefacts are created in the DEMs. To mitigate these effects, we introduce a fitting method based on a sum of sinusoids that accounts for the varying along-track angle of the satellite swath within the scene (Fig. 3.11). Additionally, we stitch the arbitrarily split ASTER granules of 60 km x 60 km into longer, 3-granule strips of 180 km x 180 km to improve the quality of the sinusoid fit and reduce edge effects.

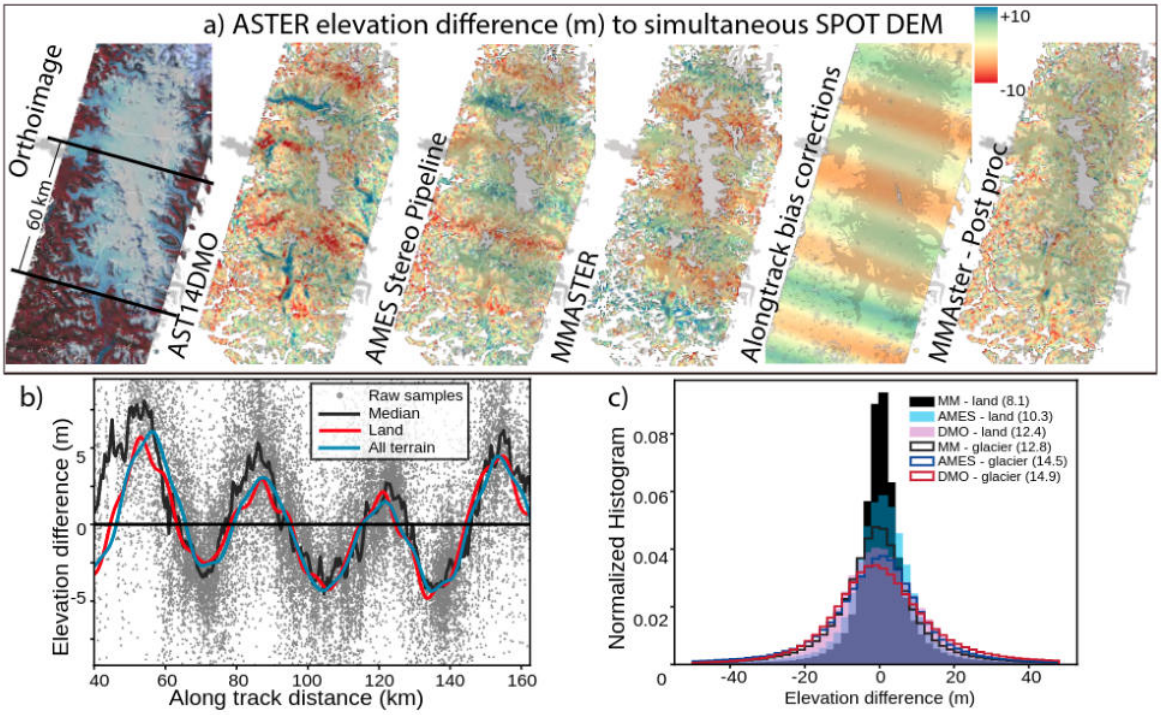

Figure 3.12: ASTER DEMs from MMASTER, AST14DMO and ASP for the Northern Patagonian Icefield case study. From Nuth et al. (in prep.). **a-c,** Elevation differences between simultaneous ASTER and SPOT DEMs shown with **(a)** elevation difference maps, **(b)** along-track distance for the MMASTER DEM only and with **(c)** histograms for AST14DMO, ASP and MMASTER (NMAD value between parentheses). Glacier and stable terrain are shown separately on **(b)** and **(c)**.

We test the robustness of the correction to the amount of stable terrain by applying MMASTER corrections to the case study of nearly simultaneous ASTER and SPOT acquisitions at the Northern Patagonian Icefield, for which stable terrain is limited (Fig. 3.12). We find a good consistency between the corrections applied to stable and glacier terrain. Additionally, we compare the MMASTER DEM with the AST14DMO product (NASA/JAXA, 2007) and an ASTER DEM generated by ASP (Beyer et al., 2018), and show the improvement of the MMASTER processing. We notice, however, that the jitter, i.e. higher frequency undulations, are not well resolved for the Northern Patagonian Icefield case study (Fig. 3.12b) compared to when a large amount of stable terrain is available (Fig. 3.11c). This limitation echoes our previously raised argument on the need to account for uncorrected correlated noise in uncertainty analysis, which was largely addressed in Chapter 2. With the omnipresence of along-track undulations in DEMs including SRTM, SPOT, Pléiades, the robust methods developed in MMASTER based on optimizing a sum of sinusoids by basin-hopping (Wales and Doye, 1997) hold the potential to help correct many types of DEMs. For ASTER, the mass processing and correction of DEMs performed in the next main article of this chapter brings about the means to analyze the spatial consistency of these error patterns. Amongst others, we identified a latitudinal dependency in the magnitude of cross-track biases, and further analysis is still ongoing.

3.4.2 *pyddem:* an open package for estimating DEM time series

To work with DEM time series, gridded data with more than 2 dimensions need to be manipulated. The raster format previously covered by our package *geoutils* is not well-suited for these operations. For multi-dimensional arrays, the commonly used format in geosciences is the Network Common Data Form (netCDF). In recent years, several open tools have been developed to facilitate the manipulation of the multi-dimensional arrays stored in netCDFs, which notably include *xarray* in Python (Hoyer and Hamman, 2017). While the netCDF format supports georeferencing, the handling of georeferenced calculations for these multi-dimensional arrays, such as reprojection or interfacing with georeferenced vectors, is only partially covered by bourgeoning tools (Snow et al., 2022). This problem of georeferencing is generally circumvented by most applications by using concatenable grids in a single georeference (e.g., latitude and longitude grids in global climate modelling). For observational assessments that are both large-scale and spatially resolved, grids based on a single georeference raise the issue of area-deforming projections. At high resolution, Earth's ellipsoidal surface projected onto a two-dimensional grid entails aerial deformations that are not negligible. As such, local projections such as Universal Transverse Mercator (UTM) zones have to be used locally which requires georeferenced software support.

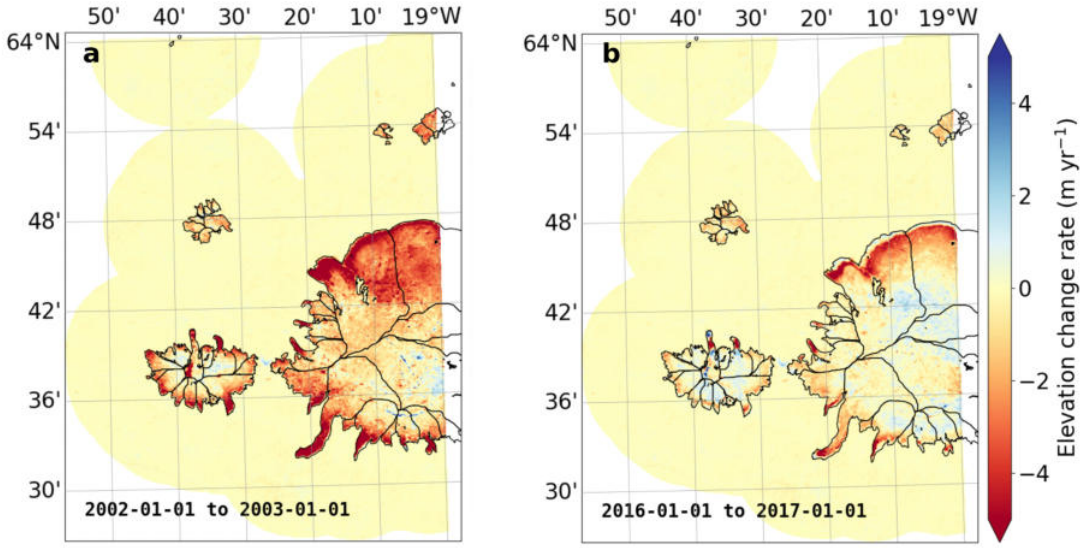

Figure 3.13: Elevation time series with *pyddem*. Example of Gaussian Process-based elevation time series for Mýrsdaljökull and Eyjafjallajökull Ice Caps, Iceland based on ASTER and ArcticDEM DEMs. The slowdown of icelandic glacier and retreat at the margin between the two periods can be observed.

To address this, along with Robert McNaab (School of Geography and Environmental Sciences, Ulster University), we developed Python routines to facilitate the interface between multidimensional georeferenced arrays and georeferenced raster data. We used GDAL's

Python bindings (GDAL/OGR contributors, 2022) in combination with netCDF's Python bindings to translate the metadata between georeferenced formats for our specific use cases of spatiotemporal elevation data. We combined these routines with machine learning packages such as *scikit-learn* (Pedregosa et al., 2011) to enable different temporal fitting methods. We vectorized our computations by combining *numpy* and *numba* (Lam et al., 2015; Harris et al., 2020) to improve the efficiency of big matrices operations, and integrated chunk processing and parallelization to scale with big data both in terms of memory usage and processing speed, by partially relying on routines from *dask* (Rocklin, 2015). Finally, we developed a processing chain relying on the dataframe structures of *pandas* (McKinney, 2010). This chain performs the spatiotemporal integration of elevation change from the spatial scale of a pixel and temporal scale of monthly estimates into glacier, regions over specific time periods, while propagating all uncertainties. All of these routines were organized in our DEM time series package *pyddem* (available at `https://github.com/iamdonovan/pyddem` with documentation at `https://pyddem.readthedocs.io/`).

Amongst others, our package *pyddem* provides the means to perform Gaussian Process regression (Williams and Rasmussen, 2006) for the temporal prediction of glacier elevation. This allows to create resolved time series of surface elevation which can be extracted for any date or converted to elevation changes between any period (Fig. 3.13). The underlying methods are detailed in the published article below.

3.5 Published article: *Accelerated global glacier mass loss in the early twenty-first century*

Published article as first author featured in this section: Hugonnet, R. et al. (2021), *Accelerated global glacier mass loss in the early twenty-first century*, Nature.[5]

In Hugonnet et al. (2021), we expand on previous studies (Brun et al., 2017; Menounos et al., 2019; Dussaillant et al., 2019; Shean et al., 2020) by utilizing nearly all openly available optical or laser, planetary-scale elevation datasets. We generate and bias-correct ASTER DEMs from 30 TB of imagery intersecting glaciers worldwide, corresponding to about 500,000 ASTER stereo pairs of 60 km x 60 km. This required one year on all 576 core processing units (CPUs) of the high-performing computer (HPC) at University of Northern British Columbia (UNBC), Canada. It necessitated specific optimization of the MMASTER workflow regarding embarassingly parallel tasks, file compression, and node input-output operations. These optimizations eventually yielded a processing about 8 times more efficient per CPU than on local machines with default parameters. We processed about 70 TB of ArcticDEM and REMA DEM segments into longer, sequentially co-registered strips. Those required two months of computation optimized in parallel on 64 CPUs of the HPC of the Laboratoire d'Etudes en Géophysique et Océanographie Spatiales (LEGOS), France. Finally, our analysis of DEM time series required six months of computation on 64 cores for all runs. We additionally retrieved and analyzed all ICESat and IceBridge laser data intersecting glaciers, as well as several high-resolution datasets including notably lidar data from UNBC and SwissTopo.

Using all this additional data, we expanded on the limitations raised above using the open tools *pymmaster* and *pydddem* we developed, as well as an early pre-*xdem* version of the spatial statistics tools presented in Chapter 2. We addressed the issue of spatial variability in photogrammetric precision by modelling the elevation error as a function of slope and quality of stereo-correlation. As MicMac does not perform a forced removal of elevations with low quality of stereo-correlation as does ASP, we kept those elevations to better resolve the accumulation areas of glaciers within quantified error ranges. We included this error range into new spatial and temporal filters based on weighted linear regression. Using Gaussian Processes, we refined this weighted filtering and then produced time series of surface elevation. Those mitigate temporal inconsistencies of other trend methods by capturing nonlinearity and seasonality in the temporal sampling, and by propagating elevation errors in time. Finally, we addressed the issue of spatiotemporal inconsistency of uncertainty applications by performing a spatial correlation analysis on ICESat data. With the spatiotemporal structure of error characterized, which accounts for both errors due to uncorrected ASTER instrument noise and those due to temporal interpolation, we propagated uncertainties across spatial scales. We ultimately present and analyze a globally complete and spatiotemporally resolved estimate of glacier mass change for the period of 2000–2019.

[5]Contribution: the study of Hugonnet et al. (2021) is my own work. I developed the code and performed the analysis of all data, with support from Robert McNabb for DEM time series, and at the exception of the ERA5 data which was analyzed by Brian Menounos. I wrote the initial draft and realized all figures. I provided a repository for full reproduction of the analysis, tables, figures and dataset manipulation at `https://github.com/rhugonnet/ww_tvol_study`. More details in the "Acknowledgments".

Article

Accelerated global glacier mass loss in the early twenty-first century

https://doi.org/10.1038/s41586-021-03436-z

Received: 3 July 2020

Accepted: 9 March 2021

Published online: 28 April 2021

Check for updates

Romain Hugonnet[1,2,3]✉, Robert McNabb[4,5], Etienne Berthier[1], Brian Menounos[6,7], Christopher Nuth[5,8], Luc Girod[5], Daniel Farinotti[2,3], Matthias Huss[2,3,9], Ines Dussaillant[1,10], Fanny Brun[11] & Andreas Kääb[5]

Glaciers distinct from the Greenland and Antarctic ice sheets are shrinking rapidly, altering regional hydrology[1], raising global sea level[2] and elevating natural hazards[3]. Yet, owing to the scarcity of constrained mass loss observations, glacier evolution during the satellite era is known only partially, as a geographic and temporal patchwork[4,5]. Here we reveal the accelerated, albeit contrasting, patterns of glacier mass loss during the early twenty-first century. Using largely untapped satellite archives, we chart surface elevation changes at a high spatiotemporal resolution over all of Earth's glaciers. We extensively validate our estimates against independent, high-precision measurements and present a globally complete and consistent estimate of glacier mass change. We show that during 2000–2019, glaciers lost a mass of 267 ± 16 gigatonnes per year, equivalent to 21 ± 3 per cent of the observed sea-level rise[6]. We identify a mass loss acceleration of 48 ± 16 gigatonnes per year per decade, explaining 6 to 19 per cent of the observed acceleration of sea-level rise. Particularly, thinning rates of glaciers outside ice sheet peripheries doubled over the past two decades. Glaciers currently lose more mass, and at similar or larger acceleration rates, than the Greenland or Antarctic ice sheets taken separately[7–9]. By uncovering the patterns of mass change in many regions, we find contrasting glacier fluctuations that agree with the decadal variability in precipitation and temperature. These include a North Atlantic anomaly of decelerated mass loss, a strongly accelerated loss from northwestern American glaciers, and the apparent end of the Karakoram anomaly of mass gain[10]. We anticipate our highly resolved estimates to advance the understanding of drivers that govern the distribution of glacier change, and to extend our capabilities of predicting these changes at all scales. Predictions robustly benchmarked against observations are critically needed to design adaptive policies for the local- and regional-scale management of water resources and cryospheric risks, as well as for the global-scale mitigation of sea-level rise.

About 200 million people live on land that is predicted to fall below the high-tide lines of rising sea levels by the end of the century[11], whereas more than one billion could face water shortage and food insecurity within the next three decades[4]. Glaciers distinct from the ice sheets hold a prominent role in these outcomes as the largest estimated contributor to twenty-first century sea-level rise after thermal expansion[2], and as one of the most climate-sensitive constituents of the world's natural water towers[12,13]. Current glacier retreat temporarily mitigates water stress on populations reliant on ice reserves by increasing river runoff[1], but this short-lived effect will eventually decline[14]. Understanding present-day and future glacier mass change is thus crucial to avoid water-scarcity-induced sociopolitical instability[15], to predict the alteration of coastal areas due to sea-level rise[4], and to assess the impacts on ecosystems[16] and cryosphere-related hazards[3].

Nevertheless, glacier mass change stands out as one of the least-constrained elements of the global water cycle, identified as a critical research gap in the Special Report on the Ocean and Cryosphere in a Changing Climate (SROCC) of the Intergovernmental Panel on Climate Change (IPCC)[4]. Observational limits stem from the fragmented expanse of glacierized surfaces around the globe. Largely inaccessible, only a few hundred of the more than 200,000 glaciers are monitored in situ[17]. Notwithstanding recent progress in glacier monitoring from space[18], global-scale remote-sensing-based studies have been so far limited by (i) the coarse spatial resolution of satellite gravimetry, which

[1]LEGOS, Université de Toulouse, CNES, CNRS, IRD, UPS, Toulouse, France. [2]Laboratory of Hydraulics, Hydrology and Glaciology (VAW), ETH Zürich, Zürich, Switzerland. [3]Swiss Federal Institute for Forest, Snow and Landscape Research (WSL), Birmensdorf, Switzerland. [4]School of Geography and Environmental Sciences, Ulster University, Coleraine, UK. [5]Department of Geosciences, University of Oslo, Oslo, Norway. [6]Geography Earth and Environmental Sciences, University of Northern British Columbia, Prince George, British Columbia, Canada. [7]Hakai Institute, Campbell River, British Columbia, Canada. [8]The Norwegian Defense Research Establishment, Kjeller, Norway. [9]Department of Geosciences, University of Fribourg, Fribourg, Switzerland. [10]Department of Geography, University of Zurich, Zurich, Switzerland. [11]IGE, Université Grenoble Alpes, CNRS, IRD, Grenoble INP, Grenoble, France. ✉e-mail: romain.hugonnet@gmail.com

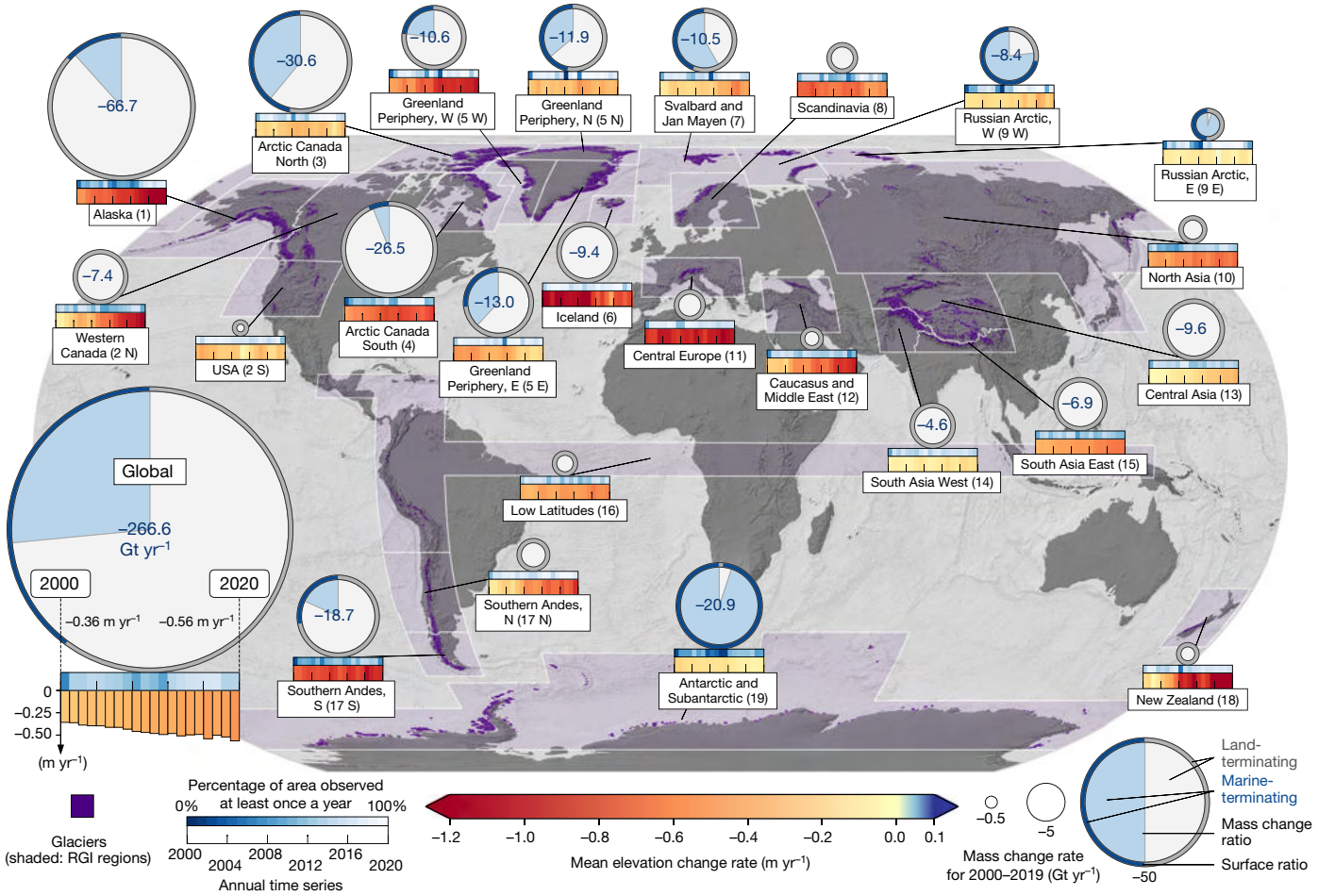

Fig. 1 | Regional glacier mass changes and their temporal evolution from 2000 to 2019. Regional and global mass change rates with time series of mean surface elevation change rates for glaciers (indigo) of the 19 first-order RGI 6.0[22] regions (white-delimited indigo polygons; region numbers indicated in parentheses), shown on top of a world hillshade[36]. Regions 2, 5, 9, 17 are further divided (N, S, E and W indicating north, south, east and west, respectively) to illustrate contrasting temporal patterns. Mass change rates are represented by the area of the disk delimiting the inside wedge, which separates the mass change contribution of land-terminating (light grey) and marine-terminating (light blue) glaciers. Mass change rates larger than 4 Gt yr^{-1} are printed in blue inside the disk (in units of Gt yr^{-1}). The outside ring discerns between land (grey) and marine-terminating (blue) glacier area. Annual time series of mean elevation change (in m yr^{-1}) and regional data coverage are displayed on time friezes at the bottom of the disks.

is unable to reliably disentangle glacier mass change signals from those of the ice sheets, solid Earth and hydrology in many regions[5,19,20]; (ii) the sparse repeat sampling of satellite altimetry that operated over short timespans[5,10]; and (iii) the uneven coverage of optical and radar surface elevation change estimations that account at most for 10% of the world's glaciers[21].

Spatiotemporally resolved estimation

In this study, we leverage large-scale and openly available satellite and airborne elevation datasets as a means of estimation, reference or validation of Earth's surface elevation over all glaciers and their vicinity between 1 January 2000 and 31 December 2019 (Extended Data Fig. 1). For observational coverage, we rely mostly on NASA's 20-year-long archive of stereo images from the Advanced Spaceborne Thermal Emission and Reflection Radiometer (ASTER). We use modern photogrammetry techniques and specifically developed statistical methods to generate and bias-correct nearly half a million Digital Elevation Models (DEMs) at 30 m horizontal resolution. In total, our repeat DEMs cover more than 20 times Earth's land area (Extended Data Fig. 2).

Changes in glacier elevation based on DEMs are traditionally quantified by differencing pairs of acquisitions from two distinct epochs. To harness the full potential of the repeat temporal coverage provided by the archives, we introduce an approach to producing continuous elevation time series interpolated from all available DEMs (see Methods, Extended Data Fig. 3). This technique allows us to mitigate the strong effects of seasonality while preserving longer, nonlinear glacier elevation changes through time. In total, we independently compute surface elevation time series for about half a billion pixels at a horizontal resolution of 100 m, covering 97.4% of inventoried glacier areas[22], with an average of 39 independent observations per pixel between 2000 and 2019 (Extended Data Table 2). Using glacier-wide hypsometric gap-filling methods, we then extend our estimated elevation changes to nearly 99.9% of glacier areas.

We perform an extensive validation by intersecting our elevation time series with 25 million high-precision measurements from NASA's Ice, Cloud, and land Elevation Satellite (ICESat) and Operation IceBridge campaigns over glaciers, spanning 2003 to 2019. We thereby confirm the absence of temporal and spatial biases in our elevation change estimates (see Methods, Extended Data Fig. 4). We further utilize ICESat data to constrain the spatiotemporal correlations that are either structural to our interpolated elevation time series or that emerge owing to latent, uncorrected ASTER instrument noise, and we propagate our elevation uncertainties into volume change uncertainties accordingly. We validate the reliability of our uncertainty estimates down to the scale of individual glaciers by comparison with

Table 1 | Separating mass losses of glaciers and ice sheets

	Reference	Mass change rate (Gt yr^{-1})					
		2000–2004	2005–2009	2010–2014	2015–2018[a]	2000–2018[a]	2003–2018[a]
Glaciers	This study	−227 ± 25	−257 ± 22	−284 ± 23	−292 ± 24	−264 ± 16	−272 ± 16
Greenland Ice Sheet	IMBIE[7] minus this study (Greenland Periphery)	−94 ± 65	−206 ± 56	−267 ± 57	−152 ± 64	−181 ± 31	−205 ± 32
	Smith et al.[9]						−200 ± 24
Antarctic Ice Sheet	IMBIE[8] minus this study (Antarctic and Subantarctic)	−36 ± 118	−93 ± 104	−214 ± 94	−157 ± 87	−121 ± 104	−143 ± 104
	Smith et al.[9]						−118 ± 48

Mass losses from glaciers, the GIS and AIS with 95% confidence intervals. Half of the peripheral glacier component estimated in this study is removed from the ensemble estimates of the ice sheet mass balance inter-comparison exercise (IMBIE)[78]; see Methods.
[a]The end date for the AIS IMBIE estimate is June 2017.

independent, high-precision DEM differences for 588 glaciers around the globe (Extended Data Fig. 5).

Integration of elevation changes over each of the 217,175 inventoried glaciers yields volume change, which is subsequently converted to water-equivalent mass change[23]. Our analysis includes 200,000 km^2 of glaciers located near the coast of Greenland (Greenland Periphery) and in the Antarctic seas (Antarctic and Subantarctic), referred to as peripheral glaciers, that are distinct from the Greenland Ice Sheet (GIS) and the Antarctic Ice Sheet (AIS). We aggregate our estimates over the 19 first-order regions of the Randolph Glacier Inventory 6.0 (RGI 6.0)[22] (Fig. 1), and report estimates for periods exceeding five years owing to larger uncertainties at shorter timescales (Extended Data Table 1). Uncertainties, provided at the 95% confidence level (two standard deviations), depend primarily on observational coverage. When converting from volume to mass change, our estimates are largely hampered by a poor knowledge of density conversion[23], which constitutes the dominant uncertainty component of our glacier mass change assessment.

Global contribution to sea-level rise

From 2000 to 2019, global glacier mass loss totalled 267 ± 16 Gt yr^{-1} (Extended Data Table 1), a mass loss 47% larger than that of the GIS, and more than twice that of the AIS[7–9] (Table 1). Assuming that all meltwater ultimately reached the ocean, the contribution to sea-level rise was 0.74 ± 0.04 mm yr^{-1} or 21 ± 3% of the observed rise[24]. Global glacier mass loss rapidly accelerated (see Methods) at a rate of 48 ± 16 Gt yr^{-1} per decade (62 ± 8 Gt yr^{-1} per decade excluding peripheral glaciers), corresponding to a thinning rate acceleration of 0.10 ± 0.02 m yr^{-1} per decade (0.16 ± 0.02 m yr^{-1} per decade). While thinning rates increased steadily, mass loss acceleration slightly attenuated in time owing to the decreasing extent of glacier surfaces caused by glacier retreat. Excluding peripheral glaciers, thinning rates nearly doubled, from 0.36 ± 0.21 m yr^{-1} in 2000 to 0.69 ± 0.15 m yr^{-1} in 2019. Observational studies have been unable to discern significant (95% confidence interval does not overlap zero) accelerated glacier mass loss[19,21], with the exception of a recent gravimetric study[20] that estimated an acceleration of 50 ± 40 Gt yr^{-1} per decade excluding peripheral glaciers. Despite its large uncertainties, this estimate is in agreement with our results. The observed acceleration of mass loss for glaciers exceeds that of the GIS[7] and is similar to that of the AIS[8]. For the AIS, gravimetric observations indicate a decelerating mass loss since the mid-2010s[25]. We thereby infer that acceleration of sea-level rise since 2000, which is often attributed to the accelerated loss from both the GIS and AIS, also substantially originates from glaciers. Observed sea-level trends[24] place the glacier contribution at 6–19% of the acceleration in global sea-level rise, with a mean estimate at 9%. The large spread of this contribution primarily arises from uncertainties in the observed acceleration of sea-level rise[24].

Marine-terminating glaciers collectively represent 40% of Earth's total glacierized area, yet only contribute 26% to the global mass loss (Fig. 1). This smaller contribution to sea-level rise is uniform for all maritime regions, except where losses of marine-terminating glaciers are dominated by recent large surge events (for example, Svalbard and Jan Mayen; Extended Data Fig. 6). The delayed and asynchronous response of tidewater glaciers to changes in climate[26] may partly explain why most marine-terminating glaciers show reduced mass loss. Despite differing mass loss rates, relative acceleration of land- and marine-terminating glaciers within each maritime region are similar (Extended Data Table 3). Notable exceptions exist for glaciers in the Antarctic and Subantarctic, where few land-terminating glaciers are present, and in regions of strong surge-driven mass losses.

Regionally contrasting mass changes

Seven glacierized regions account for 83% of the global mass loss (Extended Data Table 1): Alaska (25%); the Greenland Periphery (13%); Arctic Canada North and South (10% each); Antarctic and Subantarctic, High Mountain Asia (composed of Central Asia, South Asia West and South Asia East) and the Southern Andes (8% each). From 2000 to 2019, specific-mass change (that is, mass change divided by area) strongly varied in latitudinal belts (Fig. 2). The large, northernmost Arctic regions composed of Arctic Canada North, northern Greenland Periphery, Svalbard and Jan Mayen, and the Russian Arctic, all showed moderate specific-mass change rates, averaging −0.28 ± 0.04 metres water equivalent (w.e.) per year. Further South in the Arctic (at latitudes encompassing Alaska, Arctic Canada South, southern Greenland Periphery, Iceland and Scandinavia) specific-mass change rates were consistently more negative, at a near-triple value of −0.74 ± 0.10 m w.e. yr^{-1}, reaching the world's most negative regional rate over these two decades of −0.88 ± 0.13 m w.e. yr^{-1} in Iceland. Non-polar regions also experienced substantial mass loss (−0.69 ± 0.11 m w.e. yr^{-1} on average) with the exception of High Mountain Asia (−0.22 ± 0.05 m w.e. yr^{-1}). The Antarctic and Subantarctic exhibited the least-negative specific-mass change rate of −0.17 ± 0.04 m w.e. yr^{-1}.

Our regional mass change estimates closely match those of a recent gravimetric study[19] in remote polar regions (Arctic Canada, Svalbard and Jan Mayen, and the Russian Arctic) in which gravimetric uncertainties are considered small owing to weak competing signals[27] (Fig. 3). We note, however, the large discrepancies between the latter gravimetric study[19] and a more recent one[20] in both Iceland and the Russian Arctic. We find good agreement with the dense in situ measurements of Central Europe, Scandinavia and New Zealand[5]. In High Mountain Asia and the Southern Andes, where gravimetric and glaciological records are less constrained, our mass change estimates of −0.21 ± 0.05 m w.e. yr^{-1} and −0.67 ± 0.15 m w.e. yr^{-1}, respectively, are slightly more negative than the −0.19 ± 0.06 m w.e. yr^{-1} and −0.64 ± 0.04 m w.e. yr^{-1} reported by recent

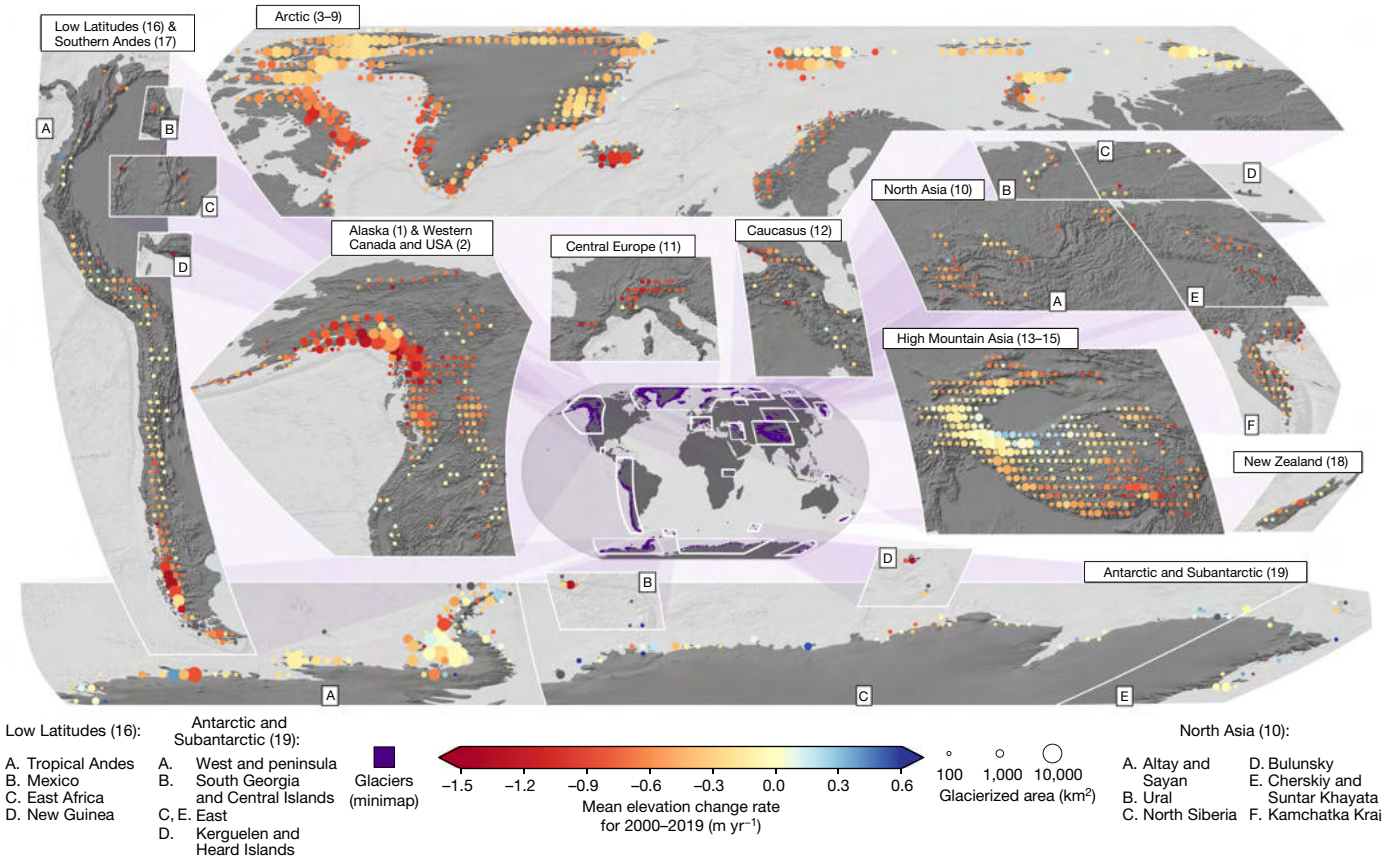

Fig. 2 | Spatial distribution of glacier elevation change between 2000 and 2019. Glacier mean elevation change rate is aggregated for tiles of 1° × 1° below 60° latitude, 2° × 1° between 60° and 74° latitude and 2° × 2° above 74° latitude, thus representing similar surface areas of approximately 10,000 km². Disks scale with the glacierized area of each tile and are coloured according to the mean elevation change rate (coloured in grey if less than 50% of the surface is covered by observations or if the 95% confidence interval is larger than 1 m yr⁻¹; only applies to 0.4% of the glacierized area) shown on top of a world hillshade[36]. Tiles with glacierized areas less than or equal to 10 km² are displayed at the same minimum size.

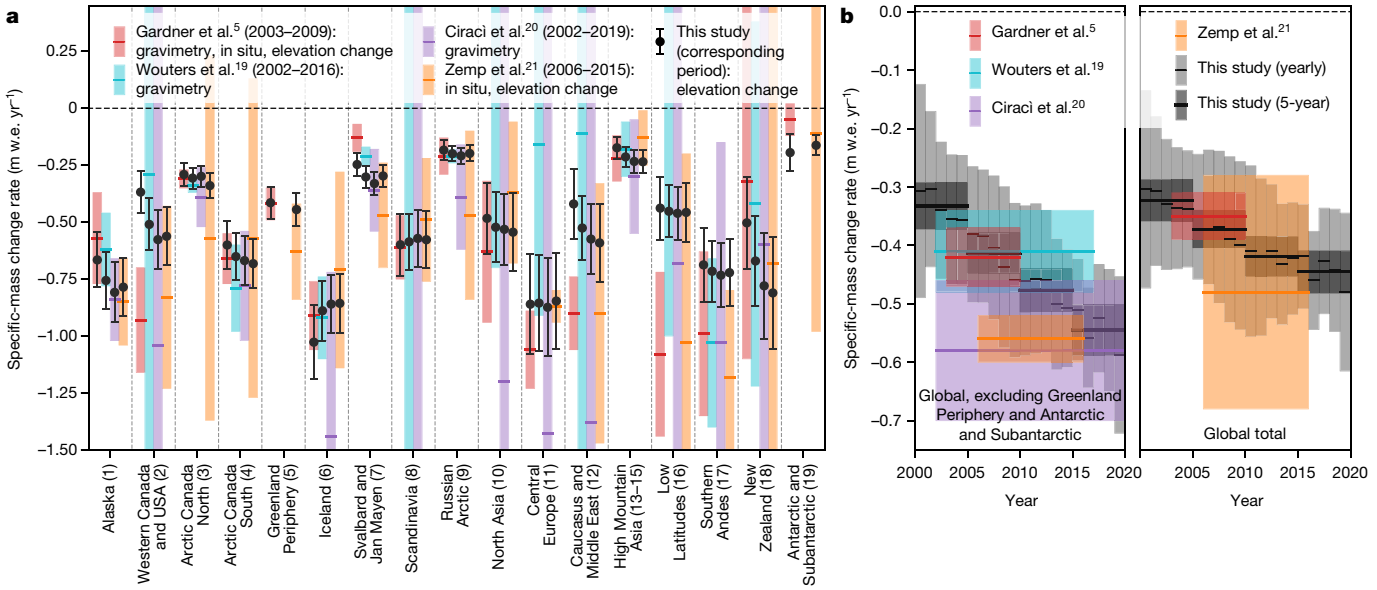

Fig. 3 | Comparison to previous global estimates. Regional and global specific-mass change rates with 95% confidence intervals. **a**, Estimates from earlier studies[5,19–21] (coloured) and from this study (black) over the corresponding time periods. **b**, Global estimates from earlier studies, and annual and 5-year rates from this study. Annual rates from earlier studies are not shown owing to large uncertainties. Uncertainties from this study are conservative, in particular for regions with most negative specific rates (see Methods).

Article

DEM-based studies[28,29]. For glaciers located in the tropics (Low Latitudes), our estimate of −0.43 ± 0.12 m w.e. yr^{-1} is about twice as negative as that of a recent interferometric radar study[29], −0.23 ± 0.08 m w.e. yr^{-1}, a difference that plausibly originates from biases associated with the penetration of radar signals into ice and firn[30].

Drivers of temporal variabilities

While global glacier mass loss distinctly accelerated, the loss from glaciers peripheral to the GIS and AIS slightly decelerated, from 65 ± 16 Gt yr^{-1} in 2000–2004 to 43 ± 13 Gt yr^{-1} in 2015–2019 (Extended Data Table 1). Variability within the ice sheet peripheries was strong, however (Figs. 2, 4a). The peculiar surface elevation change patterns that we capture for glaciers fringing Greenland, particularly notable around the eastern Greenland sub-regions of mass gain in 2015–2019 (Extended Data Fig. 7), mirror those observed by satellite radar altimetry for the outer parts of the GIS[31]. Similarly, the elevation change rate patterns of Antarctica's scattered peripheral glaciers largely agree with mass changes reported for the AIS[8]. Western Antarctic peripheral glaciers substantially thinned (−0.23 ± 0.06 m yr^{-1}) while those of East Antarctica slowly thickened (0.04 ± 0.05 m yr^{-1}). Ice masses surrounding the Antarctic Peninsula, representing 63% of the glacier area in the Antarctic and Subantarctic, experienced moderate, decelerating thinning (−0.19 ± 0.05 m yr^{-1}), in line with recent gravimetric surveys of the entire peninsula[25].

Only two regions of the world beyond the ice sheet peripheries experienced slowdown of glacier thinning. The record thinning rates of Icelandic glaciers during 2000–2004 (1.21 ± 0.18 m yr^{-1}) were nearly halved during 2015–2019 (0.77 ± 0.13 m yr^{-1}), which coincides with the decelerated thinning of Scandinavian glaciers. Both are well corroborated by in situ observations[21]. Taken together, the slowdown in mass loss from these two regions, in addition to the one of peripheral glaciers of the southeast Greenland Periphery[32], define a regional pattern that we refer to as the North Atlantic anomaly.

Elsewhere on Earth, glacier thinning accelerated. The combined mass loss of these regions with increased loss escalated from 148 ± 19 Gt yr^{-1} in 2000–2004 to 247 ± 20 Gt yr^{-1} in 2015–2019. Two-thirds of this increase derives from three regions: Alaska (38%), High Mountain Asia (19%) and Western Canada and USA (9%). Glaciers in the latter region experienced a fourfold increase in thinning rates. Most notably, glaciers in northwestern America (Alaska, Western Canada and USA) are responsible for nearly 50% of the accelerated mass loss. The widespread and strong increase of thinning of glaciers in High Mountain Asia brought a large sub-region of sustained thickening in central–western Asia down to a generalized thinning in the late 2010s (Extended Data Fig. 7), suggesting the end of the so-called Karakoram anomaly[10]. Smaller glacierized regions also underwent strong, sometimes drastic acceleration of thinning. New Zealand, for example, shows a record thinning rate of 1.52 ± 0.50 m yr^{-1} in 2015–2019, which is a nearly sevenfold increase compared to 2000–2004.

Analysis of climate data reveals that many of the regional patterns of mass change uncovered by our resolved estimates are consistent with large-scale, decadal changes in annual precipitation and temperature (Fig. 4b, c). Strong dipoles that reflect concordant spatial patterns between precipitation change and mass change are observed notably in northwestern America, the southern Greenland Periphery and the Southern Andes. The southern Andean dipole is consistent with the mega-drought[33] of the 2010s that drove increased glacier mass loss in the Central Andes. In the Coast Mountains of western Canada and in southeast Alaska, glaciers were severely deprived of precipitation, which instead benefited neighbouring regions of central Alaska and continental USA, correspondingly showing either stable or reduced mass loss. The North Atlantic anomaly coincided with the cool, wet conditions of the last decade. Weaker dipoles can also be observed within the European Alps or Scandinavia. In both regions, glacier thinning slightly accelerated in the northeast and decelerated in the southwest.

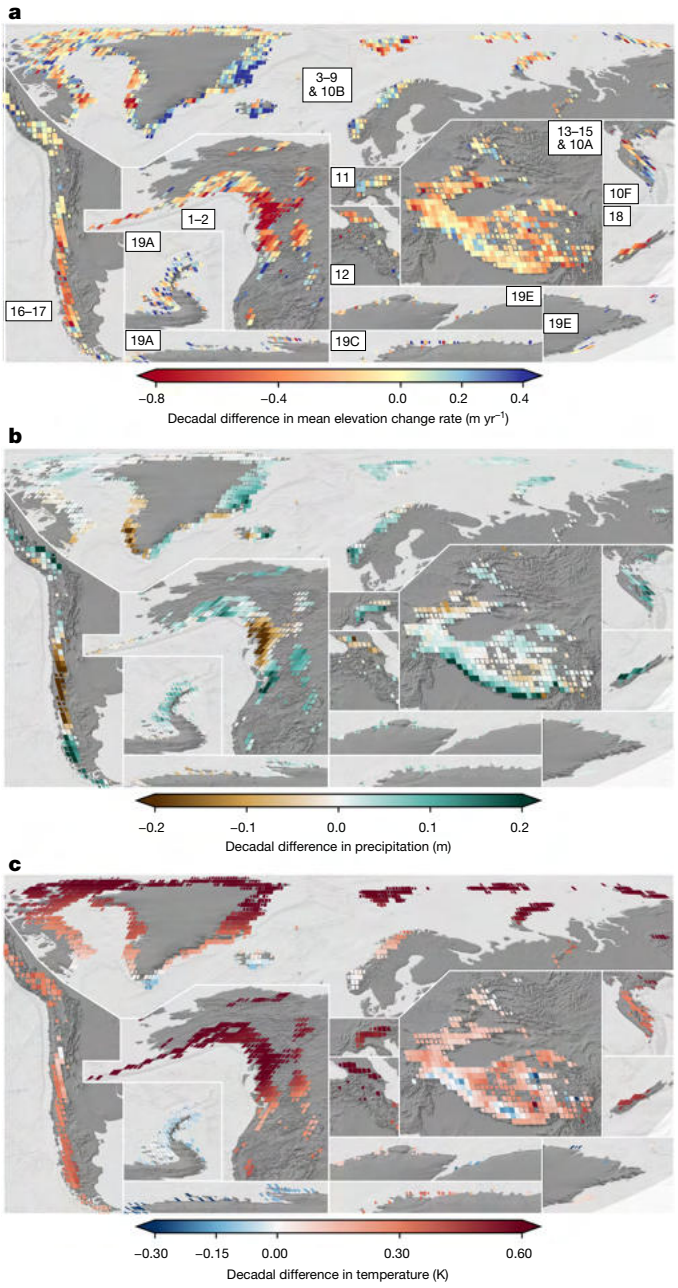

Fig. 4 | Decadal patterns of glacier thinning are consistent with decadal variations in precipitation and temperature. a–**c**, Difference between 2010–2019 and 2000–2009 for the mean elevation change rates from this study (**a**) and the mean annual precipitation (**b**), and mean annual temperature (**c**) from ERA5. The region inset numbering corresponds to Fig. 2. Tiles are 1° × 1°, with size inversely scaled to uncertainties in the mean elevation change difference shown on top of a world hillshade[36]. The minimum tile area is 10% for a 95% confidence interval larger than 1 m yr^{-1}, and tiles are displayed at full size for a 95% confidence interval smaller than 0.4 m yr^{-1}.

Although decadal changes in precipitation explain some of the observed regional anomalies, the global acceleration of glacier mass loss mirrors the global warming of the atmosphere. Aggregated globally over glacierized terrain, we observe modest trends in precipitation during the period 2000–2019 (0.002 m yr^{-1}, +6.2% in 20 years), whereas we detect a strong increase in air temperature (0.030 K yr^{-1}). Combined with our estimate of accelerated mass change, this warming trend yields

an observational global glacier mass balance sensitivity to temperature of −0.27 m w.e. yr^{-1} K^{-1}, in agreement with modelling-based estimates[34]. Previous studies[35] have indicated large multi-decadal variation in rates of glacier mass change across the 20th century, implying that some of the acceleration that we observe could fall within the range of natural variability. Nonetheless, the strong concordance to the increase in global surface temperatures suggests, indirectly, a considerable response to anthropogenic forcing. Together, the contrasting patterns and global-scale sensitivities consistent with meteorological conditions support the notion of a long-term, temperature-driven acceleration in glacier mass loss[13] that is still subject to regional and sub-decadal precipitation-driven fluctuations of large magnitude.

Two decades of observational wealth

Benefiting from the nearly complete spatial coverage afforded by ASTER stereo imagery, our global estimate of recent glacier mass change (−275 ± 17 Gt yr^{-1} for the 2006–2015 IPCC SROCC reference period) shows strongly reduced uncertainties compared to the latest IPCC report[4] (−278 ± 226 Gt yr^{-1}) and a recent global study[21] (−335 ± 144 Gt yr^{-1}). We resolve the time-varying nature of this mass change signal for nearly all of Earth's glaciers, which reveals a significantly accelerated mass loss globally. Decadal rates of glacier mass change remain, however, strongly modulated by regional climatic conditions. We capture the magnitude of such fluctuations, most contrasting for North Atlantic and northwestern American glaciers that evolved in opposing directions. At the end of the 2010s, the North Atlantic anomaly brought a whole sub-region of the eastern Greenland Periphery close to balance, whereas the strong increase in thinning rates of High Mountain Asian glaciers probably marks the end of the Karakoram anomaly.

From the spatiotemporally resolved nature of our assessment, multiple possibilities arise to harness observations of the satellite era. Such resolved estimates are not only instrumental for glaciers, but also hold the potential to constrain recent ice sheet mass balance, in particular for the outlet glaciers that are prone to the highest long-term sea-level rise. The improved ability to deconvolve glacier signals from gravimetric observations might foster the detection of nearly two decades of changes in terrestrial water storage. In time, we expect our observational baseline to help drive the development of the next generation of global glaciological and hydrological models, and to ultimately result in more reliable projections at all scales[14]. In light of the rapid, ongoing change of the cryosphere, the increasingly reliable projections made possible by accurate, global-scale observations are critical for the design of adaptation strategies, with impacts ranging from further sea-level rise[4,11] to changes in water management for some of the most vulnerable regions on Earth[12,15].

Online content

Any methods, additional references, Nature Research reporting summaries, source data, extended data, supplementary information, acknowledgements, peer review information; details of author contributions and competing interests; and statements of data and code availability are available at https://doi.org/10.1038/s41586-021-03436-z.

1. Pritchard, H. D. Asia's shrinking glaciers protect large populations from drought stress. *Nature* **569**, 649–654 (2019).
2. WCRP Global Sea Level Budget Group. Global sea-level budget 1993–present. *Earth Syst. Sci. Data* **10**, 1551–1590 (2018).
3. Stoffel, M. & Huggel, C. Effects of climate change on mass movements in mountain environments. *Prog. Phys. Geogr.* **36**, 421–439 (2012).
4. IPCC. *IPCC Special Report on the Ocean and Cryosphere in a Changing Climate* (eds Pörtner, H. O. et al.) (IPCC, 2019).
5. Gardner, A. et al. A reconciled estimate of glacier contributions to sea level rise: 2003 to 2009. *Science* **340**, 852–857 (2013).
6. Nerem, R. S. et al. Climate-change-driven accelerated sea-level rise detected in the altimeter era. *Proc. Natl Acad. Sci. USA* **115**, 2022–2025 (2018).
7. IMBIE Team. Mass balance of the Greenland Ice Sheet from 1992 to 2018. *Nature* **579**, 233–239 (2020).
8. IMBIE team. Mass balance of the Antarctic Ice Sheet from 1992 to 2017. *Nature* **558**, 219–222 (2018).
9. Smith, B. et al. Pervasive ice sheet mass loss reflects competing ocean and atmosphere processes. *Science* **368**, 1239–1242 (2020).
10. Kääb, A., Berthier, E., Nuth, C., Gardelle, J. & Arnaud, Y. Contrasting patterns of early twenty-first-century glacier mass change in the Himalayas. *Nature* **488**, 495–498 (2012).
11. Kulp, S. A. & Strauss, B. H. New elevation data triple estimates of global vulnerability to sea-level rise and coastal flooding. *Nat. Commun.* **10**, 4844 (2019); author correction **10**, 5752 (2019).
12. Immerzeel, W. W. et al. Importance and vulnerability of the world's water towers. *Nature* **577**, 364–369 (2020).
13. Marzeion, B., Cogley, J. G., Richter, K. & Parkes, D. Attribution of global glacier mass loss to anthropogenic and natural causes. *Science* **345**, 919–921 (2014).
14. Huss, M. & Hock, R. Global-scale hydrological response to future glacier mass loss. *Nat. Clim. Chang.* **8**, 135–140 (2018).
15. IPCC. *Climate Change 2014: Impacts, Adaptation, and Vulnerability. Part B: Regional Aspects* (Cambridge University Press, 2014).
16. Cauvy-Fraunié, S. & Dangles, O. A global synthesis of biodiversity responses to glacier retreat. *Nat. Ecol. Evol.* **3**, 1675–1685 (2019).
17. World Glacier Monitoring Service (WGMS). *Fluctuations of Glaciers Database* https://wgms.ch/data_databaseversions/ (2019).
18. Bamber, J. L., Westaway, R. M., Marzeion, B. & Wouters, B. The land ice contribution to sea level during the satellite era. *Environ. Res. Lett.* **13**, 063008 (2018); corrigendum **13**, 099502 (2018).
19. Wouters, B., Gardner, A. S. & Moholdt, G. Global glacier mass loss during the GRACE satellite mission (2002–2016). *Front. Earth Sci.* **7**, 96 (2019).
20. Ciracì, E., Velicogna, I. & Swenson, S. Continuity of the mass loss of the world's glaciers and ice caps from the GRACE and GRACE Follow-On missions. *Geophys. Res. Lett.* **47**, 226 (2020).
21. Zemp, M. et al. Global glacier mass changes and their contributions to sea-level rise from 1961 to 2016. *Nature* **568**, 382–386 (2019).
22. RGI Consortium. *Randolph Glacier Inventory – A Dataset of Global Glacier Outlines*. Technical Report https://www.glims.org/RGI/00_rgi60_TechnicalNote.pdf (Global Land Ice Measurements from Space, 2017).
23. Huss, M. Density assumptions for converting geodetic glacier volume change to mass change. *Cryosphere* **7**, 877–887 (2013).
24. Ablain, M. et al. Uncertainty in satellite estimates of global mean sea-level changes, trend and acceleration. *Earth Syst. Sci. Data* **11**, 1189–1202 (2019).
25. Velicogna, I. et al. Continuity of ice sheet mass loss in Greenland and Antarctica from the GRACE and GRACE Follow-On missions. *Geophys. Res. Lett.* **47**, L11501 (2020).
26. Larsen, C. F. et al. Surface melt dominates Alaska glacier mass balance. *Geophys. Res. Lett.* **42**, 5902–5908 (2015).
27. Blazquez, A. et al. Exploring the uncertainty in GRACE estimates of the mass redistributions at the Earth surface: implications for the global water and sea level budgets. *Geophys. J. Int.* **215**, 415–430 (2018).
28. Shean, D. E. et al. A systematic, regional assessment of High Mountain Asia glacier mass balance. *Front. Earth Sci.* **7**, 363 (2020).
29. Braun, M. H. et al. Constraining glacier elevation and mass changes in South America. *Nat. Clim. Chang.* (2019).
30. Dehecq, A. et al. Elevation changes inferred from TanDEM-X data over the Mont-Blanc area: impact of the X-band interferometric bias. *IEEE J. Sel. Top. Appl. Earth Obs. Remote Sens.* **9**, 3870–3882 (2016).
31. Sandberg Sørensen, L. et al. 25 years of elevation changes of the Greenland Ice Sheet from ERS, Envisat, and CryoSat-2 radar altimetry. *Earth Planet. Sci. Lett.* **495**, 234–241 (2018).
32. Bevis, M. et al. Accelerating changes in ice mass within Greenland, and the ice sheet's sensitivity to atmospheric forcing. *Proc. Natl Acad. Sci. USA* **116**, 1934–1939 (2019).
33. Garreaud, R. D. et al. The Central Chile Mega Drought (2010–2018): a climate dynamics perspective. *Int. J. Climatol.* **40**, 421–439 (2020).
34. Raper, S. C. B. & Braithwaite, R. J. Low sea level rise projections from mountain glaciers and icecaps under global warming. *Nature* **439**, 311–313 (2006).
35. Parkes, D. & Marzeion, B. Twentieth-century contribution to sea-level rise from uncharted glaciers. *Nature* **563**, 551–554 (2018).
36. Becker, J. J. et al. Global bathymetry and elevation data at 30 arc seconds resolution: SRTM30_PLUS. *Mar. Geod.* **32**, 355–371 (2009).

Article

Methods

We summarize the workflow used to process elevation datasets into estimates of glacier mass change for the period of 1 January 2000 to 31 December 2019 (Extended Data Fig. 1).

Glacier inventories

We used the Randolph Glacier Inventory 6.0 (RGI 6.0)[22] outlines for all regions except for Caucasus Middle East (region 12). Owing to the high number of uncharted ('nominal') glaciers in that region, we updated our inventory with the latest Global Land Ice Measurements from Space (GLIMS) outlines available[37]. This increased the number of glacier outlines in region 12 from 1,888 to 3,516, representing an increase in total area from 1,307 km^2 to 1,336 km^2. In Svalbard and Jan Mayen (region 7), we manually updated glacier outlines to account for advances resulting from major surges[38–40], increasing mapped areas by 228 km^2 (Extended Data Fig. 6). In the Greenland Periphery (region 5), we did not analyse the 955 glaciers strongly connected to the ice sheet (RGI 6.0 connectivity level 2) with an area of 40,354 km^2, because these are generally included within the ice sheet by studies on the GIS[7,9]. Our updated inventory numbers 217,175 glaciers covering a total area of 705,997 km^2. For the purpose of co-registering and bias-correcting DEMs, we masked ice-covered terrain using the RGI 6.0 for glaciers, the Greenland Ice Mapping Project[41] for the GIS, and Bedmap2[42] for the AIS.

Digital elevation models

We retrieved all ASTER[43], ArcticDEM[44] and Reference Elevation Model of Antarctica (REMA)[45] data intersecting glaciers worldwide (Extended Data Fig. 2), totalling more than 100 TB of data. Because of the non-negligible effects of radar penetration into snow and ice[30], we excluded radar elevation datasets from our analysis except for the TanDEM-X 90 m global DEM[46] (TanDEM-X). We used TanDEM-X as a globally homogeneous reference[47] for co-registration[48] and bias correction over ice-free terrain, keeping only elevations with an error smaller than 0.5 m in the provided TanDEM-X height error map. For all DEMs bilinearly resampled to 30 m, co-registration was performed only if more than 100 valid elevation differences (slope >3°, absolute elevation difference <200 m) were available at each iterative step.

From 440,548 ASTER L1A stereo images[43] (each covering 60 km × 60 km), we generated, co-registered and bias-corrected 154,656 ASTER DEM strips (30 m resolution; 180 km × 60 km strip size) using improved techniques of MicMac for ASTER[49,50]. Improvements were made by adjusting the back-looking image for cross-track biases before stereo calculations, by accounting for the curved along-track angle of the satellite Terra, and by stitching the arbitrarily split 60 km × 60 km archive granules into longer strips. The latter operation mitigates edge effects and increases the amount of ice-free terrain available for improved basin-hopping optimizations[51] of along-track undulations and satellite jitter parameters. Further details on the processing of ASTER DEMs are available in Supplementary Information.

From 97,649 release 7 ArcticDEM[44] DEMs at 2 m resolution and 13,790 release 1.1 REMA[45] DEMs at 2 m and 8 m resolution, we stitched and co-registered 40,391 ArcticDEM and 3,456 REMA longer strips to TanDEM-X. Our stitching of the original DEM segments, generated by the Polar Geospatial Center using the Surface Extraction with TIN-based search-space minimization algorithm[52], was performed by a sequential pairwise co-registration between same-day acquisitions over all available terrain. This procedure was necessary to increase the amount of ice-free terrain in the final DEM strip for co-registration to TanDEM-X. We allowed for a maximum standard deviation of co-registered elevation differences of 10 m before stopping the sequential co-registration iteration and starting a new strip, instead of the 1-m root-mean-square error originally used[44,45].

Elevation time series

Following co-registration, we excluded all DEMs for which the root-mean-square error of the elevation difference with TanDEM-X on ice-free terrain was larger than 20 m. Using all remaining DEMs, we created three-dimensional arrays (time t, space x and y) of elevation $h(t, x, y)$, divided into 2,106 tiles of 1° × 1° containing glaciers and downsampled to 100 m to decrease computing time.

To filter and interpolate our DEMs into elevation time series, we empirically characterized the spatial and temporal variance of elevation observations. For this, two global-scale statistical modelling steps relying on a large sampling of the data were performed. One was used to assess the vertical precision of elevation observations and the other to assess their pairwise dependency with varying time lags (Extended Data Fig. 3a, b).

Concomitantly to the variance modelling process described further below, a multi-step outlier filtering was performed to iteratively improve the quality of the DEMs (Extended Data Fig. 1), which itself affects the empirical estimation of the variances. The filtering algorithms consist of a spatial filter, removing elevations outside a topographical maximum and minimum from the TanDEM-X elevations in the pixel surroundings, and a temporal filter propagated from the TanDEM-X elevation at a given pixel through a maximum possible glacier elevation change rate (Extended Data Fig. 3c). These maxima were first conditioned by extreme values (for example, the maximum observed absolute glacier elevation change rate of 50 m yr^{-1} on HPS12 glacier, Southern Patagonian Icefield[53]). Later, those were refined by estimating a linear glacier elevation change rate in the surroundings through weighted least squares[54].

In our first global-scale statistical modelling step, we identified a heteroscedasticity in elevation measurements (that is, non-uniform variance; Extended Data Fig. 3a). We determined that the elevation measurement error σ_h varied with the terrain slope[55,56] α, the quality of stereo-correlation[49,57] q and the individual performance of each DEM's co-registration[48] $\sigma_c(t, x, y)$. To empirically quantify this elevation variance, we used ice-free terrain, where no changes in elevation are expected through time, as a proxy for ice-covered terrain. We randomly sampled up to 10,000 ice-free pixels without replacement for each bin of a studied category of terrain (for example, slope) in each 1° × 1° tile and computed the difference to TanDEM-X. We used the median as a robust estimator of the mean and the square of the normalized median absolute deviation (NMAD) as a robust estimator of the variance to mitigate the effects of elevation outliers[58]. We found that the empirical variances for the slope σ_α^2 and the quality of stereo-correlation σ_q^2 were consistent among regions, and used them to condition a model at the global scale to account for the measurement error independently for each elevation observation $h(t, x, y)$:

$$\sigma_h^2(t, x, y) = \sigma_c^2(t, x, y) + \sigma_\alpha^2(\alpha, q) + \sigma_q^2(q). \quad (1)$$

In our second step of global-scale statistical modelling, we determined the temporal covariance of glacier elevation change (Extended Data Fig. 3b), which serves as our best unbiased estimator to interpolate elevation observations into continuous time series through Gaussian process[59] (GP) regressions. To empirically quantify this temporal covariance, we sampled median temporal variograms by the time lag between pairwise elevation observations Δt of ice-covered pixels. We found that the covariance structure could be estimated by the sum of a pairwise linear (PL) kernel, a periodic (exponential sine squared, ESS) kernel, a local (radial basis function, RBF) kernel, and the product of a pairwise linear and local (rational quadratic, RQ) kernel. This sum decomposes the differences of elevation observations with varying time lags into: an underlying linear trend (the PL), a seasonality (the ESS), a proximity at short time lags (the RBF) and a nonlinear trend (the RQ times PL). Empirical covariances showed little variability

between regions. We thus conditioned the parameters of the kernels (periodicity ϕ_p and variance σ_p^2 for the ESS; length scale Δt_l and variance σ_l^2 for the RBF; length scale Δt_{nl}, variance σ_{nl}^2 and scale mixture α_{nl} for the RQ) at the global scale on the basis of our empirical variograms, whereas the PL kernel was determined directly from the observations of each pixel (x, y), and thereby described the temporal covariance as:

$$\sigma_h^2(x, y, \Delta t) = \mathrm{PL}(x, y, \Delta t) + \mathrm{ESS}(\phi_p, \sigma_p^2, \Delta t) + \mathrm{RBF}(\Delta t_l, \sigma_l^2, \Delta t) + \mathrm{RQ}(\Delta t_{nl}, \sigma_{nl}^2, \alpha_{nl}, \Delta t)\mathrm{PL}(x, y, \Delta t) + \sigma_h^2(t, x, y). \quad (2)$$

By applying GP regression, we iteratively removed observations outside the 20σ, 12σ, 9σ, 6σ and 4σ credible intervals (Extended Data Fig. 3d). Within the same process, elevation time series were then derived at a monthly time step independently for each of the 400 million pixels (x, y) falling on or within 10 km of an inventoried glacier[22] (Extended Data Fig. 3e). Further details on the variance estimation, filtering and time series methods are available in Supplementary Information and build on refs. [60–63].

Validation of elevation time series

We retrieved all ICESat (GLAH14[64]) and IceBridge (IODEM3[65] and ILAKS1B[66]) laser and optical elevations intersecting glaciers worldwide from the National Snow and Ice Data Center. IceBridge data are dominated by 1,220,494 Ames Stereo Pipeline[67] photogrammetric 0.5–2 m resolution DEMs[65] with a typical footprint of 500 m × 500 m that we down-sampled to a resolution of 50 m to limit repeat spatial sampling when comparing to the 100 m resolution of our elevation time series. We linearly interpolated our GP elevation time series in space and time to match the date and centre of each ICESat footprint or IceBridge pixel[68] (Extended Data Fig. 4a–c).

We found that regional and seasonal vertical shifts (typically below 2 m) of surface elevation exist, and attribute these differences to snow cover in the TanDEM-X global DEM[46] and the presence of seasonally varying snow cover in ASTER, ArcticDEM and REMA DEMs. At the global scale, these shifts do not affect our annual estimates once differenced into elevation changes, verified by the absence of elevation change bias over glaciers (0.001 ± 0.011 m yr^{-1}). We additionally demonstrated that the uncertainties in our elevation time series (credible interval of the GP regression) are conservative (that is, too large by a factor of about two). We reached the same conclusions at the scale of individual RGI 6.0 regions, and also performed these verifications with several additional relevant variables (Extended Data Fig. 4d). In particular, the absence of a bias with glacier elevation denotes our ability to adequately resolve low-texture glacier surfaces in the accumulation area, including flat, high-latitude ice caps. Further details on the validation of the elevation time series are available in Supplementary Information and build on ref. [69].

Integration of elevation into volume changes

We differenced all elevations h into elevation change according to their value of h on 1 January 2000. We integrated the elevation change dh into volume change dV independently for each glacier and time step using a weighted version of the mean local hypsometric method[70] with 100-m elevation bins. Weights were derived from the GP elevation change uncertainties, thus ensuring that pixels with a lower vertical precision in a given elevation bin have a smaller impact on the mean elevation change of that bin. Pixels with a 20-year elevation change larger than five times the NMAD from the median elevation change of the elevation bin were removed[53]. If no valid elevation estimate existed within a given bin, the elevation change was linearly interpolated from adjacent bins, or extrapolated from the closest bins. For retreating lake- and ocean-terminating glaciers, we excluded any loss below water level, because DEMs refer to the water surface and not the poorly known bathymetry in the deglaciated terrain. We note that these losses do not contribute to sea-level rise.

Uncertainty analysis of volume changes

We propagated our uncertainties in elevation change into uncertainties in volume change by assuming that the uncertainty in the mean elevation change $\sigma_{\overline{dh}}$ and the uncertainty in the glacier area σ_A are independent:

$$\sigma_{dV}^2 = (\sigma_{\overline{dh}} A)^2 + (\sigma_A \overline{dh})^2. \quad (3)$$

The uncertainty in the mean elevation change $\sigma_{\overline{dh}}$ is highly subject to spatial correlations due to instrument resolution (spatial scale of 0–150 m), uncorrected ASTER instrument noise[50] (0–20 km) and the interpolated nature of our elevation time series (0–500 km). The latter spatial correlation term arises from the fact that neighbouring pixels of a given region share similar temporal data gaps, and are hence likely to have similar interpolation biases that correspond to long-range correlations. To empirically quantify these three sources of spatial correlations, we drew spatial variograms of elevation differences between ICESat and our GP elevation time series[71] at each ICESat acquisition date. We found that the spatial correlations greatly varied with the time lag Δt to the closest ASTER, ArcticDEM or REMA observation. For each time lag, we estimated the partial sill s_k (correlated variance) by fitting a sum of seven spherical variogram models $S(d, s_k, r_k)$, with d the spatial lag, at ranges r_k (correlation lengths) of 0.15 km, 2 km, 5 km, 20 km, 50 km, 200 km and 500 km (Extended Data Fig. 5a, b). To propagate these spatial correlations when integrating glacier volumes, we computed the time lag to the closest ASTER, ArcticDEM or REMA observation for each time step of our elevation time series and for each glacier pixel to estimate s_1 to s_6. We then used the GP elevation change uncertainties of each glacier pixel to derive s_0. Finally, we propagated the pixel-wise uncertainties in elevation change into the uncertainty in the mean elevation change $\sigma_{\overline{dh}}$ by circular integration of the sum of variograms[72] over the glacier area A (Extended Data Fig. 5c):

$$\sigma_{\overline{dh}}^2 = \frac{1}{A} \sum_{k=0}^{6} \sigma_{\overline{dh}_k}^2, \quad (4)$$

where $\sigma_{\overline{dh}_k}^2$ is the integrated variance component correlated with range r_k:

$$\sigma_{\overline{dh}_k}^2 = \int_A [s_k - S(d, s_k, r_k)] \mathrm{d}A. \quad (5)$$

The reliability of the sum of short-range correlations used to account for uncorrected ASTER instrument noise (0–20 km) was further verified by applying empirical methods to ice-free terrain[73], and found to yield larger and more realistic uncertainty estimates than the single-range variograms of 0.2–1 km used in previous studies[28,53,54,74–76]. Our maximum correlation length of 500 km accords with known spatial correlations of mass balance estimates[77]. Further details on the spatial correlation methods are available in Supplementary Information and build on refs. [78–83].

For each glacier, we estimated an uncertainty in the area σ_A based on a buffer[84] of 15 m corresponding to the typical resolution of the optical imagery used to derive these outlines[37,85–87]. These uncertainties vary from about 0.1% of the area for large icefields (>1,000 km^2) to 50% of the area and above for small isolated glaciers (<0.1 km^2).

Validation of volume changes

We retrieved high-resolution DEMs from LiDAR[74,88], Pléiades[54,89], Satellite Pour l'Observation de la Terre[90,91] and aerial photographs[92,93] acquired in Alaska, Western North America, Central Europe and High Mountain Asia between 2000 and 2019. We derived precise volume change estimates during specific periods for 588 glaciers covering 3,300 km^2 and compared these to our volume time series extracted over the same glaciers and periods. We found no statistically significant bias

of mean elevation change (0.03 ± 0.03 m yr^{-1}; Extended Data Fig. 5d). We then validated that our uncertainties, derived from spatially integrated variograms calibrated on ICESat measurements, matched the empirical errors deduced from the comparison (~92% of 95% uncertainty ranges intersect the high-precision volume changes; Extended Data Fig. 5d–f). On average, our 5-year uncertainties at the 95% confidence level are lower than 0.5 m yr^{-1} for glaciers larger than 1 km^2 and conservative for smaller glaciers. We thus validated the reliability of our improved uncertainty approaches for volume change estimation down to the scale of individual glaciers.

Aggregation to regions

We summed volume changes of glaciers per region. To propagate correlated uncertainties among glaciers of the same region, we extended the spatial statistics approach used at the glacier scale. For each time step, glacier-wide correlated uncertainties were propagated again to yield an uncertainty in the mean regional elevation change $\sigma_{\overline{\mathrm{d}h_R}}$. Having been integrated once over a spatial support (from pixel to glacier), the glacier-wide uncertainties can be propagated again (from glacier to regions) directly by a double sum of covariances based on the same describing variograms, following Krige's relation[71]:

$$\sigma^2_{\overline{\mathrm{d}h_R}} = \frac{1}{A_\mathrm{R}^2} \sum_i \sum_j \sum_{k=0}^{6} \left[\sigma_{\overline{\mathrm{d}h_{k,i}}} \sigma_{\overline{\mathrm{d}h_{k,j}}} - S\left(G_i - G_j, \sigma_{\overline{\mathrm{d}h_{k,i}}} \sigma_{\overline{\mathrm{d}h_{k,j}}}, r_k\right) \right] A_i A_j , \quad (6)$$

where i, j are indexes for glaciers in the region, $\sigma_{\overline{\mathrm{d}h_{k,i}}}$ is the uncertainty in the mean elevation change $\sigma_{\overline{\mathrm{d}h_k}}$ with range r_k and sill s_k for glacier i, $G_i - G_j$ is the pairwise distance (spatial lag d) between glaciers i and j on the basis of their outline centroids, and A_R is the sum of areas A_i of glaciers i in the region.

Conversion to mass changes

We converted volume change into mass change by using a density conversion factor[23] of 850 kg m^{-3} and an uncertainty of 60 kg m^{-3}. This density conversion uncertainty was applied at the scale of RGI 6.0 regions, as if correlated for all glaciers in the entire region—an assumption that yields more conservative estimates than earlier studies[29,54]. We made this conservative assumption owing to the limited knowledge of spatiotemporal correlations in density conversion. Consequently, our mass change uncertainties might be too large, in particular for regions with the most negative specific-mass change rates (Fig. 3, Extended Data Fig. 5g, h).

Aggregation to global

We summed our regional volume and mass change estimates into global volume and mass change. Assuming independence of the uncertainty in volume and mass changes between RGI 6.0 regions, we summed regional uncertainties quadratically. We report uncertainties in mass change for periods shorter than five years solely for the global or near-global estimates (for example, Fig. 3b) by assuming that the aggregation of largely independent regions leaves limited temporal autocorrelation of density conversion factors. We compare our regional and global mass changes results with global and regional studies listed by the latest IPCC assessment[4] as well as additional recent studies[28,53,94–96] (Supplementary Table 4).

Time-evolving glacier areas

We accounted for temporal changes in glacier areas when deriving regional or global time series of specific (area-scaled) mass balances or mean elevation change (specific-volume change). We assumed a linear change through time, calibrated on time-evolving glacier outlines of each RGI 6.0 region[21]. Over the 20-year study period, these time-evolving glacier areas correspond to a nearly 10% decrease of glacier areas around the globe—a non-negligible change when assessing mean elevation change rates. To account for this, we added an additional uncertainty in the time-evolving glacier area at each time step of 1% of the regional area at that time step.

Observed sea-level rise

We derived global mean sea-level trends from a recent study[24] with time series extended to match our period of study of 2000–2019, yielding an estimate of sea-level rise of 3.56 ± 0.4 mm yr^{-1} with an acceleration of 0.15 ± 0.08 mm yr^{-2}. For conversion, we assumed that 361.8 Gt of water-equivalent mass loss amounted to 1 mm of sea-level rise.

Acceleration

Glacier mass change acceleration and its uncertainties were derived from weighted least squares on the 5-year elevation and mass change rates (that is, 2000–2004, 2005–2009, 2010–2014 and 2015–2019), propagating their related uncertainties as independent. Although shorter timescales and smaller spatial domains are affected by temporal autocorrelation, we assumed the 5-year estimates at the global or near-global scale (that is, excluding peripheral glaciers) as temporally uncorrelated. This assumption is supported by timescales described for density conversion factors[23], by the validation of our elevation time series with ICESat and IceBridge, and relies on the billions of globally distributed surface elevation observations, leading to large independent and repeat sampling over 5-year periods (Extended Data Table 2).

Distinction between glaciers and ice sheets

When comparing our results to ice sheet studies, we avoided double-counting contributions from peripheral glaciers by subtracting part of our own estimate for RGI 6.0 regions 5 and 19 to ice sheet estimates from IMBIE[7,8]. Because IMBIE estimates are a weighted mean of three ensemble estimates where half includes peripheral glaciers, the other half does not (gravimetric studies include peripheral glaciers, altimetric studies exclude peripheral glaciers, and input–output studies do both), we assumed that subtracting half of our estimates for the peripheral glaciers was most adequate. Notably, applying this subtraction leads to better agreement of GIS and AIS estimates between IMBIE and a recent study[9] over the period 2003–2018 (Table 1).

Temperature and precipitation analysis

We analysed ERA5 precipitation and temperature[97] at both annual and seasonal scales. For the latter scale, we considered only winter precipitation and summer temperature. We found similar decadal patterns at both annual and seasonal scales, and thus present annual changes (Fig. 4) to avoid the latitudinal ambiguity of glaciological definitions of seasons. Temperature change was extracted at 700 hPa (about 3,100 m above sea level) to minimize variations in air temperature affected by differences in land surface class at the 0.125° nominal resolution of the ERA5 reanalysis. To estimate trends of annual precipitation and temperature over 2000–2019, we derived ordinary least-squares trends for each ERA5 grid cell containing glaciers. We then area-weighted the global trend by the glacierized area of each grid cell. We detected a small increase in precipitation at the global scale (4.0% in 20 years) and over glaciers (6.2% in 20 years), coherent with the amplification of the global water cycle in a warming world near the Clausius–Clapeyron rate[98]. The sensitivity of mass change to air temperature was computed by dividing the specific-mass change acceleration by the temperature increase over glacierized terrain for the period 2000–2019.

Data availability

Global, regional, tile and per-glacier elevation and mass change time series, elevation change maps for 5-, 10- and 20-year periods at 100 m resolution, and tables in this article are publicly available at https://doi.org/10.6096/13. Source data are provided with this paper.

Code availability

The code developed for the global processing and analysis of all data, and to generate figures and tables in this article, is publicly available at https://github.com/rhugonnet/ww_tvol_study. Code concomitantly developed for processing ASTER data is available as the Python package pymmaster at https://github.com/luc-girod/MMASTER-workflows (with supporting documentation at https://mmaster-workflows.readthedocs.io) and for processing DEM time series as the Python package pyddem at https://github.com/iamdonovan/pyddem (with supporting documentation at https://pyddem.readthedocs.io).

37. Tielidze, L. G. & Wheate, R. D. The Greater Caucasus glacier inventory (Russia, Georgia and Azerbaijan). *Cryosphere* **12**, 81–94 (2018).
38. Dunse, T. et al. Glacier-surge mechanisms promoted by a hydro-thermodynamic feedback to summer melt. *Cryosphere* **9**, 197–215 (2015).
39. McMillan, M. et al. Rapid dynamic activation of a marine-based Arctic ice cap: ice cap dynamic activation. *Geophys. Res. Lett.* **41**, 8902–8909 (2014).
40. Nuth, C. et al. Dynamic vulnerability revealed in the collapse of an Arctic tidewater glacier. *Sci. Rep.* **9**, 5541 (2019).
41. Howat, I. M., Negrete, A. & Smith, B. E. The Greenland Ice Mapping Project (GIMP) land classification and surface elevation data sets. *Cryosphere* **8**, 1509–1518 (2014).
42. Fretwell, P. et al. Bedmap2: improved ice bed, surface and thickness datasets for Antarctica. *Cryosphere* **7**, 375–393 (2013).
43. NASA/METI/AIST/Japan Spacesystems & U.S./Japan ASTER Science Team. *ASTER Level 1A Data Set – Reconstructed, Unprocessed Instrument Data*. 2001, NASA EOSDIS Land Processes DAAC, 2001); https://doi.org/10.5067/ASTER/AST_L1A.003.
44. Porter, C. et al. *ArcticDEM* (Harvard Dataverse, 2018); https://dataverse.harvard.edu/dataset.xhtml?persistentId=doi:10.7910/DVN/OHHUKH.
45. Howat, I. M., Porter, C., Smith, B. E., Noh, M.-J. & Morin, P. The reference elevation model of Antarctica. *Cryosphere* **13**, 665–674 (2019).
46. Rizzoli, P. et al. Generation and performance assessment of the global TanDEM-X digital elevation model. *ISPRS J. Photogramm. Remote Sens.* **132**, 119–139 (2017).
47. Vassilaki, D. I. & Stamos, A. A. TanDEM-X DEM: comparative performance review employing LIDAR data and DSMs. ISPRS J. *Photogramm. Remote Sens.* **160**, 33–50 (2020).
48. Nuth, C. & Kääb, A. Co-registration and bias corrections of satellite elevation data sets for quantifying glacier thickness change. *Cryosphere* **5**, 271–290 (2011).
49. Rupnik, E., Daakir, M. & Pierrot Deseilligny, M. MicMac – a free, open-source solution for photogrammetry. *Open Geospat. Data Softw. Stand.* **2**, 14 (2017).
50. Girod, L., Nuth, C., Kääb, A., McNabb, R. & Galland, O. MMASTER: improved ASTER DEMs for elevation change monitoring. *Remote Sens.* **9**, 704 (2017).
51. Wales, D. J. & Doye, J. P. K. Global optimization by basin-hopping and the lowest energy structures of Lennard–Jones clusters containing up to 110 atoms. *J. Phys. Chem. A* **101**, 5111–5116 (1997).
52. Noh, M.-J. & Howat, I. M. The surface extraction from TIN based Search-space Minimization (SETSM) algorithm. *ISPRS J. Photogramm. Remote Sens.* **129**, 55–76 (2017).
53. Dussaillant, I. et al. Two decades of glacier mass loss along the Andes. *Nat. Geosci.* **12**, 802–808 (2019); author correction **13**, 711 (2020).
54. Brun, F., Berthier, E., Wagnon, P., Kääb, A. & Treichler, D. A spatially resolved estimate of High Mountain Asia glacier mass balances, 2000–2016. *Nat. Geosci.* **10**, 668–673 (2017); author correction **11**, 543 (2018).
55. Toutin, T. Three-dimensional topographic mapping with ASTER stereo data in rugged topography. *IEEE Trans. Geosci. Remote Sens.* **40**, 2241–2247 (2002).
56. Lacroix, P. Landslides triggered by the Gorkha earthquake in the Langtang valley, volumes and initiation processes. *Earth Planets Space* **68**, 1–10 (2016).
57. Shean, D. E. et al. An automated, open-source pipeline for mass production of digital elevation models (DEMs) from very-high-resolution commercial stereo satellite imagery. *ISPRS J. Photogramm. Remote Sens.* **116**, 101–117 (2016).
58. Höhle, J. & Höhle, M. Accuracy assessment of digital elevation models by means of robust statistical methods. *ISPRS J. Photogramm. Remote Sens.* **64**, 398–406 (2009).
59. Williams, C. K. I. & Rasmussen, C. E. *Gaussian Processes for Machine Learning* Vol. 2 (MIT Press, 2006).
60. Schiefer, E., Menounos, B. & Wheate, R. Recent volume loss of British Columbian glaciers, Canada. *Geophys. Res. Lett.* (2007).
61. Nuimura, T., Fujita, K., Yamaguchi, S. & Sharma, R. R. Elevation changes of glaciers revealed by multitemporal digital elevation models calibrated by GPS survey in the Khumbu region, Nepal Himalaya, 1992–2008. *J. Glaciol.* **58**, 648–656 (2012).
62. Willis, M. J., Melkonian, A. K., Pritchard, M. E. & Rivera, A. Ice loss from the Southern Patagonian Ice Field, South America, between 2000 and 2012. *Geophys. Res. Lett.* **39**, L17501 (2012).
63. Pedregosa, F. et al. Scikit-learn: machine learning in Python. *J. Mach. Learn. Res.* **12**, 2825–2830 (2011).
64. Zwally, H. J., Schutz, R., Hancock, D. & Dimarzio, J. *GLAS/ICESat L2 Global Land Surface Altimetry Data (HDF5), Version 34* (NASA Snow and Ice Data Center, 2014); https://nsidc.org/data/GLAH14.
65. Alexandrov, O., McMichael, S. & Beyer., R. A. *IceBridge DMS L3 Ames Stereo Pipeline Photogrammetric DEM, Version 1* (accessed 1 June 2019); https://nsidc.org/data/IODEM3/versions/1.
66. Larsen, C. *IceBridge UAF Lidar Scanner L1B Geolocated Surface Elevation Triplets, Version 1* (accessed 20 February 2020); https://nsidc.org/data/ILAKS1B/versions/1.
67. Beyer, R. A., Alexandrov, O. & McMichael, S. The Ames Stereo Pipeline: NASA's open source software for deriving and processing terrain data. *Earth Space Sci.* **5**, 537–548 (2018).
68. Harding, D. J. ICESat waveform measurements of within-footprint topographic relief and vegetation vertical structure. *Geophys. Res. Lett.* **32**, L21S10 (2005).
69. Gardelle, J., Berthier, E. & Arnaud, Y. Impact of resolution and radar penetration on glacier elevation changes computed from DEM differencing. *J. Glaciol.* **58**, 419–422 (2012).
70. McNabb, R., Nuth, C., Kääb, A. & Girod, L. Sensitivity of glacier volume change estimation to DEM void interpolation. *Cryosphere* **13**, 895–910 (2019).
71. Cressie, N. A. C. *Statistics for Spatial Data* **Vol. 4**, 613–617 (Wiley, 1993).
72. Rolstad, C., Haug, T. & Denby, B. Spatially integrated geodetic glacier mass balance and its uncertainty based on geostatistical analysis: application to the western Svartisen ice cap, Norway. *J. Glaciol.* **55**, 666–680 (2009).
73. Dehecq, A. et al. Automated processing of declassified KH-9 Hexagon satellite images for global elevation change analysis since the 1970s. *Front. Earth Sci.* **8**, 566802 (2020).
74. Menounos, B. et al. Heterogeneous changes in western North American glaciers linked to decadal variability in zonal wind strength. *Geophys. Res. Lett.* **46**, 200–209 (2018).
75. Howat, I. M., Smith, B. E., Joughin, I. & Scambos, T. A. Rates of southeast Greenland ice volume loss from combined ICESat and ASTER observations. *Geophys. Res. Lett.* **35**, L17505 (2008).
76. Wang, D. & Kääb, A. Modeling glacier elevation change from DEM time series. *Remote Sens.* **7**, 10117–10142 (2015).
77. Cogley, J. G. & Adams, W. P. Mass balance of glaciers other than the ice sheets. *J. Glaciol.* **44**, 315–325 (1998).
78. Journel, A. G. & Huijbregts, C. J. *Mining Geostatistics* Vol. 600 (Academic Press, 1978).
79. Webster, R. & Oliver, M. A. *Geostatistics for Environmental Scientists* (John Wiley & Sons, 2007).
80. Gräler, B., Pebesma, E. & Heuvelink, G. Spatio-temporal interpolation using gstat. *R J.* **8**, 204 (2016).
81. Mälicke, M. & Schneider, H. D. *Scikit-GStat 0.2.6: A Scipy Flavored Geostatistical Analysis Toolbox Written in Python* (2019); https://zenodo.org/record/3531816#.YFsJ737Le00.
82. Dussaillant, I., Berthier, E. & Brun, F. Geodetic mass balance of the Northern Patagonian Icefield from 2000 to 2012 using two independent methods. *Front. Earth Sci.* **6**, 8 (2018).
83. Berthier, E., Scambos, T. A. & Shuman, C. A. Mass loss of Larsen B tributary glaciers (Antarctic Peninsula) unabated since 2002. *Geophys. Res. Lett.* **39**, L13501 (2012).
84. Granshaw, F. D. & Fountain, A. G. Glacier change (1958–1998) in the North Cascades National Park Complex, Washington, USA. *J. Glaciol.* **52**, 251–256 (2006).
85. Pfeffer, W. et al. The Randolph Glacier Inventory: a globally complete inventory of glaciers. *J. Glaciol.* **60**, 537–552 (2014).
86. Rastner, P. et al. The first complete inventory of the local glaciers and ice caps on Greenland. *Cryosphere* **6**, 1483–1495 (2012).
87. Bolch, T., Menounos, B. & Wheate, R. Landsat-based inventory of glaciers in western Canada, 1985–2005. *Remote Sens. Environ.* **114**, 127–137 (2010).
88. Pelto, B. M., Menounos, B. & Marshall, S. J. Multi-year evaluation of airborne geodetic surveys to estimate seasonal mass balance, Columbia and Rocky Mountains, Canada. *Cryosphere* **13**, 1709–1727 (2019).
89. Wagnon, P. et al. Seasonal and annual mass balances of Mera and Pokalde glaciers (Nepal Himalaya) since 2007. *Cryosphere* **7**, 1769–1786 (2013).
90. Berthier, E., Schiefer, E., Clarke, G. K. C., Menounos, B. & Rémy, F. Contribution of Alaskan glaciers to sea-level rise derived from satellite imagery. *Nat. Geosci.* **3**, 92–95 (2010).
91. Berthier, E., Cabot, V., Vincent, C. & Six, D. Decadal region-wide and glacier-wide mass balances derived from multi-temporal ASTER Satellite Digital Elevation Models. Validation over the Mont-Blanc area. *Front. Earth Sci.* **4**, 63 (2016).
92. Glacier Monitoring Switzerland. *Swiss Glacier Volume Change, Release 2018* (2018); https://doi.glamos.ch/data/volumechange/volumechange_2018_r2018.html.
93. Bauder, A., Funk, M. & Huss, M. Ice-volume changes of selected glaciers in the Swiss Alps since the end of the 19th century. *Ann. Glaciol.* **46**, 145–149 (2007).
94. Davaze, L., Rabatel, A., Dufour, A., Hugonnet, R. & Arnaud, Y. Region-wide annual glacier surface mass balance for the European Alps from 2000 to 2016. *Front. Earth Sci.* **8**, 149 (2020).
95. Schuler, T. V. et al. Reconciling Svalbard Glacier mass balance. *Front. Earth Sci.* **8**, 523646 (2020).
96. Aðalgeirsdóttir, G. et al. Glacier Changes in Iceland From ~1890 to 2019. *Front. Earth Sci.* **8**, 520 (2020).
97. Hersbach, H. & Dee, D. ERA5 reanalysis is in production. *ECMWF Newsl.* **147**, 5–6 (2016).
98. Skliris, N., Zika, J. D., Nurser, G., Josey, S. A. & Marsh, R. Global water cycle amplifying at less than the Clausius–Clapeyron rate. *Sci. Rep.* **6**, 38752 (2016).
99. Sakakibara, D., Sugiyama, S., Sawagaki, T., Marinsek, S. & Skvarca, P. Rapid retreat, acceleration and thinning of Glaciar Upsala, Southern Patagonia Icefield, initiated in 2008. *Ann. Glaciol.* **54**, 131–138 (2013).
100. Farr, T. G. et al. The Shuttle Radar Topography Mission. *Rev. Geophys.* **45**, RG2004 (2007).

Acknowledgements We thank C. Porter for discussions on ArcticDEM and REMA DEMs, B. Meyssignac for comments on sea-level rise and A. Dehecq for input on the presentation of the manuscript. The GLIMS initiative (in particular J. Kargel and B. Raup) allowed the population of a vast archive of ASTER stereo images over glaciers. Hakai Institute and the University of Northern British Columbia provided computational resources for processing ASTER stereo imagery. SPOT6/7 data were obtained from GEOSUD (ANR-10-EQPX-20, programme 'Investissements d'Avenir'). ArcticDEM DEMs were provided by the Polar Geospatial Center under NSF-OPP awards 1043681, 1559691 and 1542736 and REMA DEMs were provided by the Byrd Polar and Climate Research Center and the Polar Geospatial Center under NSF-OPP awards 1543501, 1810976, 1542736, 1559691, 1043681, 1541332, 0753663, 1548562, 1238993 and NASA award NNX10AN61G. Computer time was provided through a Blue Waters Innovation Initiative. DEMs were produced using data from DigitalGlobe, Inc. R.H. acknowledges a fellowship from the University of Toulouse. E.B. acknowledges support from the French Space Agency (CNES) through ISIS and TOSCA programmes. R.M., C.N., L.G. and

A.K. acknowledge support by ESA through Glaciers_cci and EE10 (4000109873/14/I-NB, 4000127593/19/I-NS, 4000127656/19/NL/FF/gp), and by the European Research Council under the European Union's Seventh Framework Programme (FP/2007-2013)/ERC grant agreement number 320816. B.M. acknowledges funding from the National Sciences and Engineering Research Council of Canada, the Canada Research Chairs Program, the Tula Foundation and Global Water Futures. R.H., D.F. and M.H. acknowledge funding from the Swiss National Science Foundation, grant number 184634.

Author contributions E.B. and R.H. designed the study with contributions from D.F., M.H. and B.M. L.G., C.N., R.M. and A.K. developed ASTER bias-correction methods. R.H. and R.M. developed glacier elevation GP methods. R.H. implemented spatial statistics methods with inputs from F.B. B.M. assembled and analysed ERA5 data. R.H. performed the processing and analysis of all data with main inputs from E.B., as well as R.M., B.M., D.F., M.H., I.D. and F.B. All authors interpreted the results. R.H. led the writing of the paper and all other co-authors contributed.

Competing interests The authors declare no competing interests.

Additional information

Supplementary information The online version contains supplementary material available at https://doi.org/10.1038/s41586-021-03436-z.

Correspondence and requests for materials should be addressed to R.H.

Peer review information *Nature* thanks Beata Csatho, Thomas Frederikse, Michael Willis and the other, anonymous, reviewer(s) for their contribution to the peer review of this work. Peer reviewer reports are available.

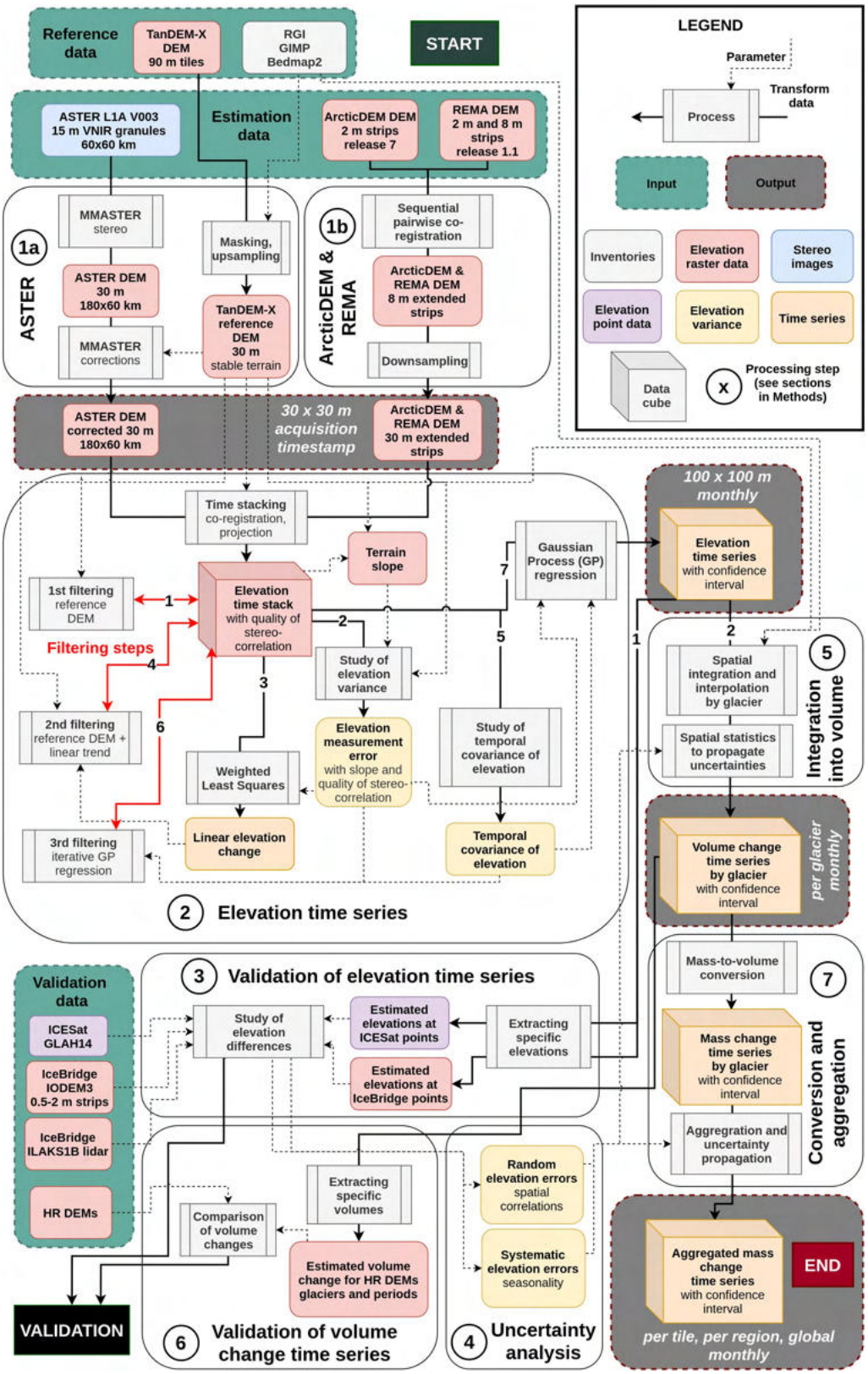

Extended Data Fig. 1 | Flow chart of the methodology. Flow diagram describing the processing steps from satellite imagery to global glacier mass change time series. Processing steps correspond to sections in Methods.

Article

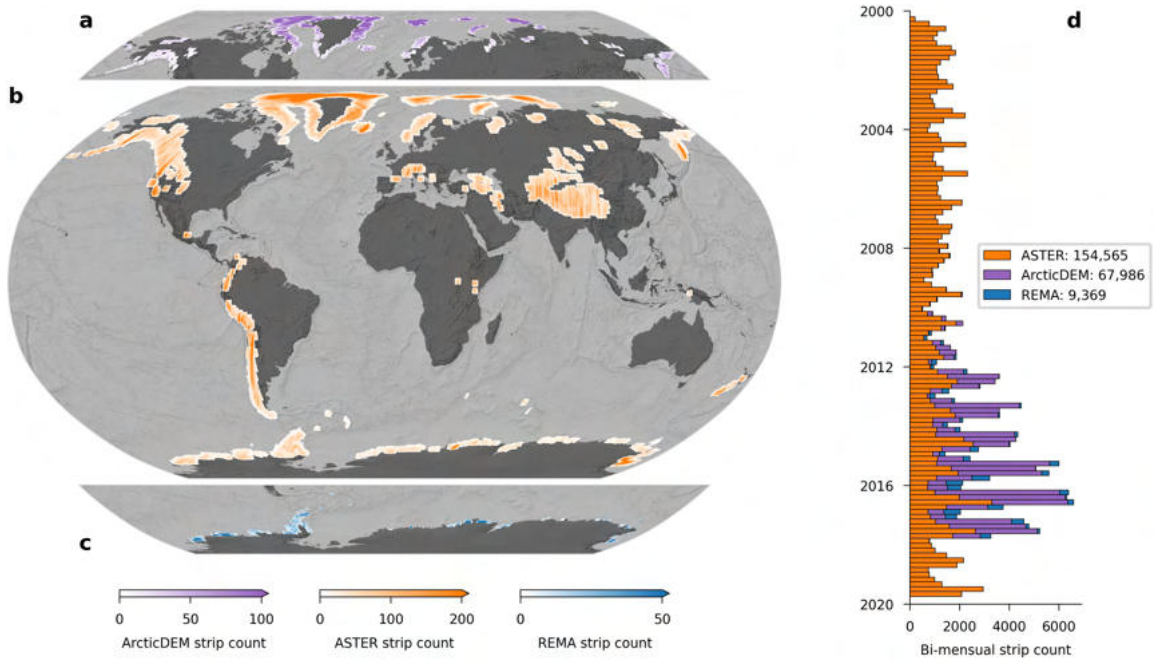

Extended Data Fig. 2 | Spatial and temporal coverage of ASTER, ArcticDEM and REMA DEMs. a–**c**, Spatial distribution of DEMs as a strip count for ArcticDEM strips above 50° N (**a**), ASTER DEM strips (**b**) and REMA strips below 50° S (**c**), shown on top of a world hillshade[36]. 67,986 ArcticDEM and 9,369 REMA strips are counted before co-registration to TanDEM-X. This later reduces their number to 40,391 and 3,456, respectively, owing to the limited stable terrain in polar regions. **d**, Temporal distribution of the strip count as a bi-mensual histogram from January 2000 to December 2019. We note that ArcticDEM and REMA strip footprints (15 km × 50 km) are generally much smaller than ASTER DEM strip footprints (180 km × 60 km).

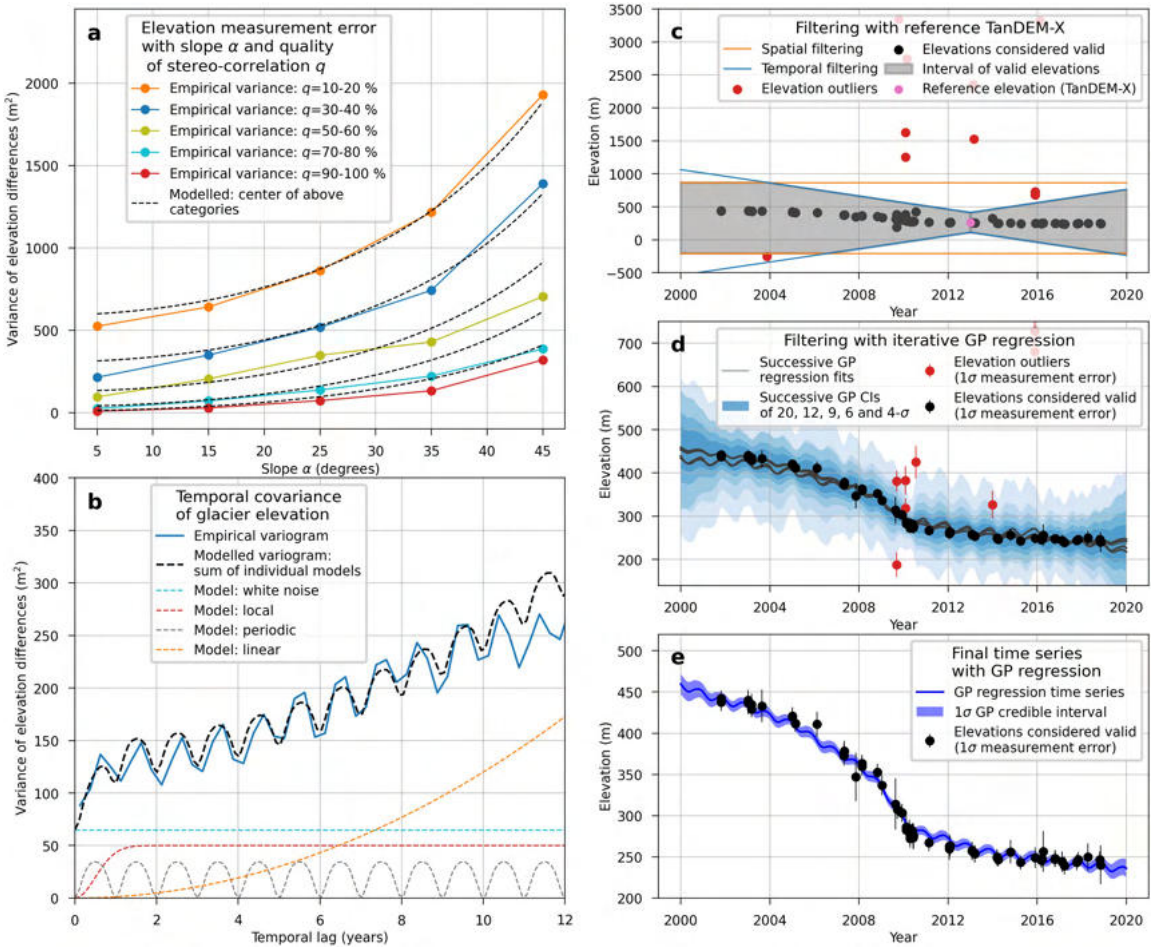

Extended Data Fig. 3 | Elevation time series estimation. a–**e**, Empirical and modelled elevation measurement error (**a**) and temporal covariance of glacier elevation (**b**) estimated globally. These are used to condition the filtering (**c**, **d**) and elevation time series estimation (**e**) of elevation observations, illustrated here for a 100 m × 100 m pixel on the ablation area of Upsala, where a strong nonlinear elevation loss occurred[99]. **a**, Squared measurement error, estimated by the squared NMAD of elevation differences to TanDEM-X on stable terrain as a function of terrain slope and of quality of stereo-correlation. We express the quality of stereo-correlation as a percentage ranging from 0% for poor correlations to 100% for good correlations. **b**, Variance between pairwise glacier elevations in time, or temporal variogram. The empirical temporal variogram is derived from the aggregated median of variances binned by time lags of 0.25 yr. Here, pixels were selected on glacierized terrain showing a linear trend of elevation change (estimated from weighted least squares) between −1.5 and −1.0 m yr^{-1}. The median of the linear trend at these locations (−1.2 m yr^{-1}) was directly used to derive the linear model (orange), which has a quadratic variance. The other models are calibrated so that their sum (dashed black line) matches the empirical variogram. **c**, Spatial and temporal filtering by conditioning a maximum linear elevation change rate from the neighbouring TanDEM-X elevations (see Supplementary Information for further details). **d**, Filtering by successive GP regression fits for credible intervals of size 20σ, 12σ, 9σ, 6σ and 4σ. **e**, Elevation time series of final GP regression after the removal of outliers.

Article

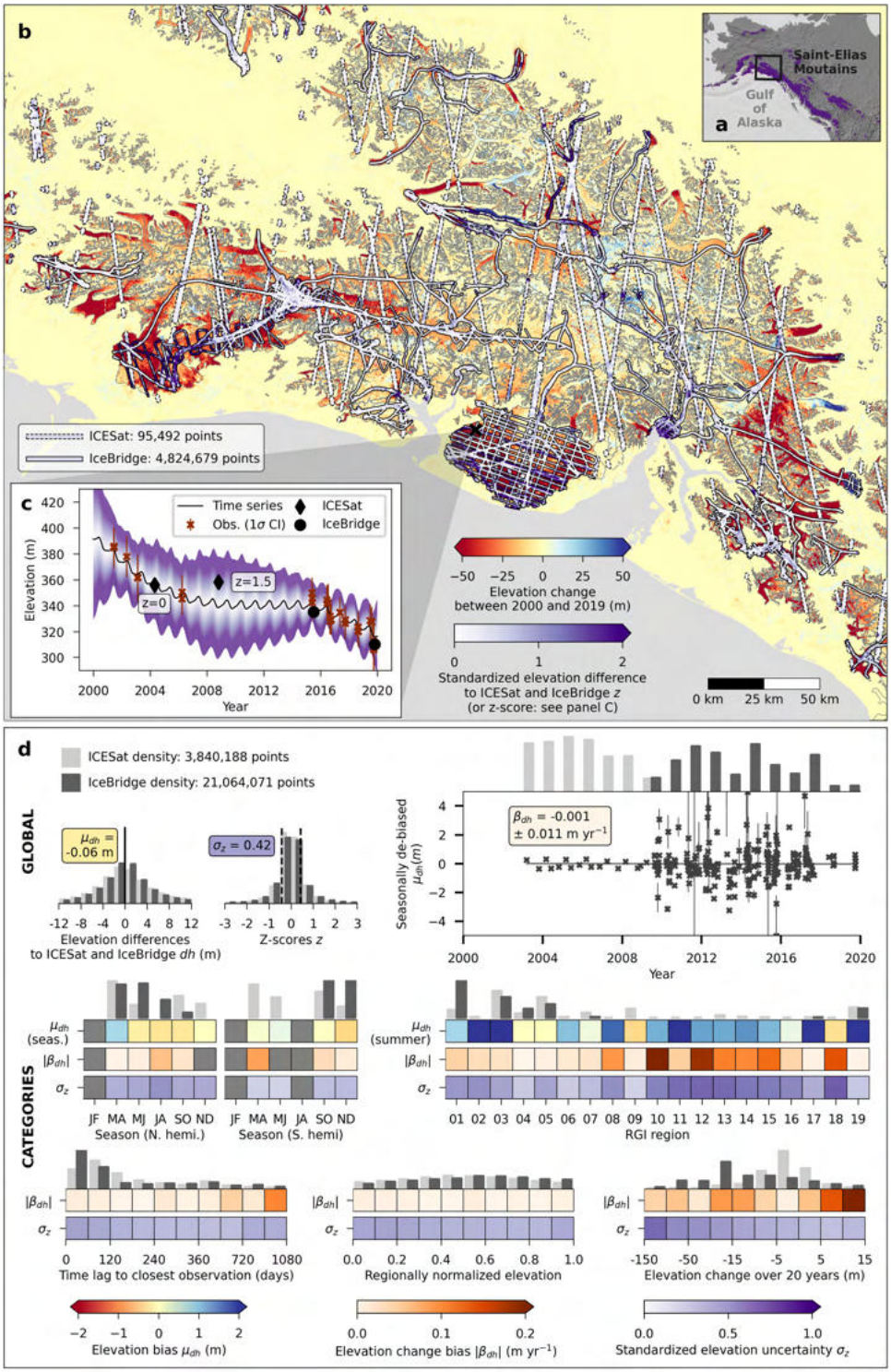

Extended Data Fig. 4 | Validation of elevation time series and uncertainties to ICESat and IceBridge. a–**d**, ICESat[64] and IceBridge[65,66] measurements compared to our surface elevation time series over glacierized terrain in the Saint-Elias Mountains, Alaska (**a**–**c**) and at the global scale (**d**). **b**, Absolute *z*-scores (white to purple) are shown on top of the 2000–2019 surface elevation change. *z*-scores correspond to elevation differences to ICESat (dashed outlines) or IceBridge (solid outlines), standardized by our time series uncertainty. **c**, Time series for a 100 m × 100 m pixel extracted on the tongue of Agassiz Glacier with neighbouring ICESat and IceBridge elevation differences for demonstration purposes. **d**, Summary of global validation statistics for categories of time, season, region, elevation, observation time lag and total elevation change, with density distributions of measurements for ICESat (light grey) and IceBridge (dark grey). Mean elevation differences, subject to snow-cover biases, are shown only by region (summer mean) and by two-month seasonal component (difference to the annual mean) for each hemisphere.

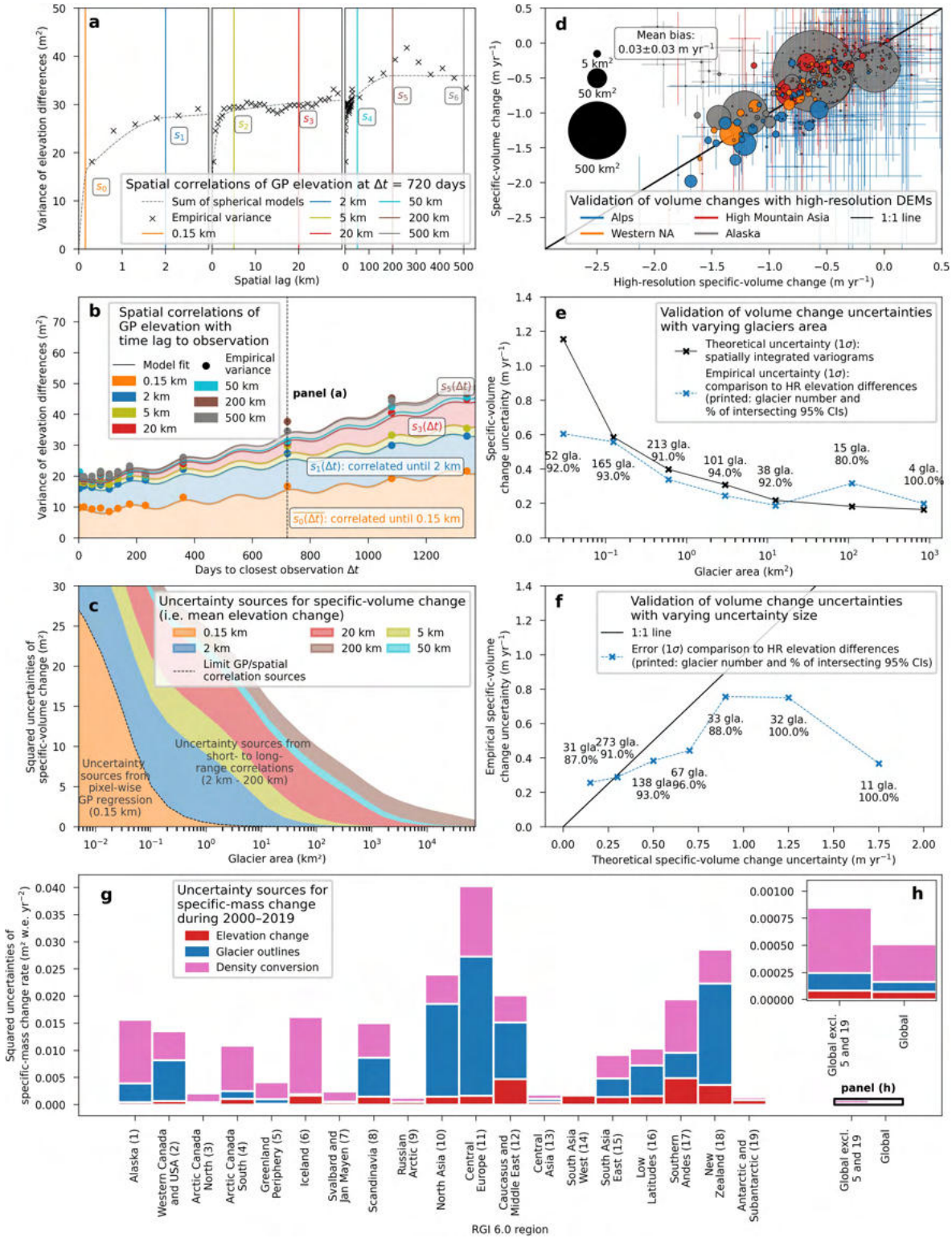

Extended Data Fig. 5 | See next page for caption.

Article

Extended Data Fig. 5 | Uncertainty analysis of volume changes and validation using high-resolution DEMs. a–**h**, Spatial correlation of elevations between the GP time series and ICESat with the time lag to the closest ASTER, ArcticDEM or REMA observation (**a**, **b**), propagation of correlations into specific-volume change uncertainties (**c**), validation of volume change estimates and uncertainties to high-resolution volume changes extracted over the same 588 glaciers and periods (**d**–**f**) and contribution from all uncertainty sources to the 2000–2019 specific-mass change estimates (**g**, **h**). **a**, An empirical spatial variogram is shown and fitted with a sum of spherical models at correlation lengths of 0.15, 2, 5, 20, 50, 200 and 500 km for elevation differences sampled at 720 days (2 years) from the closest observation. **b**, Spatially correlated variances as a function of the time lag to the closest observation. The model for the variance used during uncertainty propagation is shown in plain lines (sum of quadratic and squared sinusoidal functions optimized by least squares). **c**, Propagation of elevation change uncertainties to volume change uncertainties with varying glacier area. As this computation is specific to the time lag of each pixel to the closest observation, for each glacier, at each time step, **c** refers to an example. The spatial correlations are computed for a time lag to the closest observation, representing the average of our study, of 0–1 yr for 50% of observations, 1–2 yr for 20% of observations, 2–3 yr for 20% of observations and 3–4 yr for 10% of observations. We assume a mean pixel-wise uncertainty of 10 m and simplify by considering only the first step of integration over a continuous glacierized area (equation (5)). This assumption leads to slightly larger contributions from short-range correlations than with further propagation to the second propagation step between discontinuous glaciers (equation (6)). Uncertainties are largely dominated by short- to long-range spatial correlations. **d**, Comparison of specific-volume changes per glacier with 1σ uncertainties. The mean of differences in estimates over all glaciers does not statistically differ from zero. **e**, **f**, Theoretical and empirical 1σ uncertainties, and their evolution with glacier size. The theoretical uncertainty is the mean of per-glacier uncertainties derived from spatially integrated variograms and the empirical uncertainty is the NMAD of the difference between high-resolution and GP estimates. **g**, **h**, Propagation of uncertainty sources to specific-mass changes for each RGI 6.0 region, and all glaciers with and without the Greenland Periphery and the Antarctic and Subantarctic, which are magnified in **h**. Uncertainties are largely dominated by the volume-to-mass conversion uncertainties globally, and by uncertainties in glacier outlines for regions with a relevant share of small glaciers.

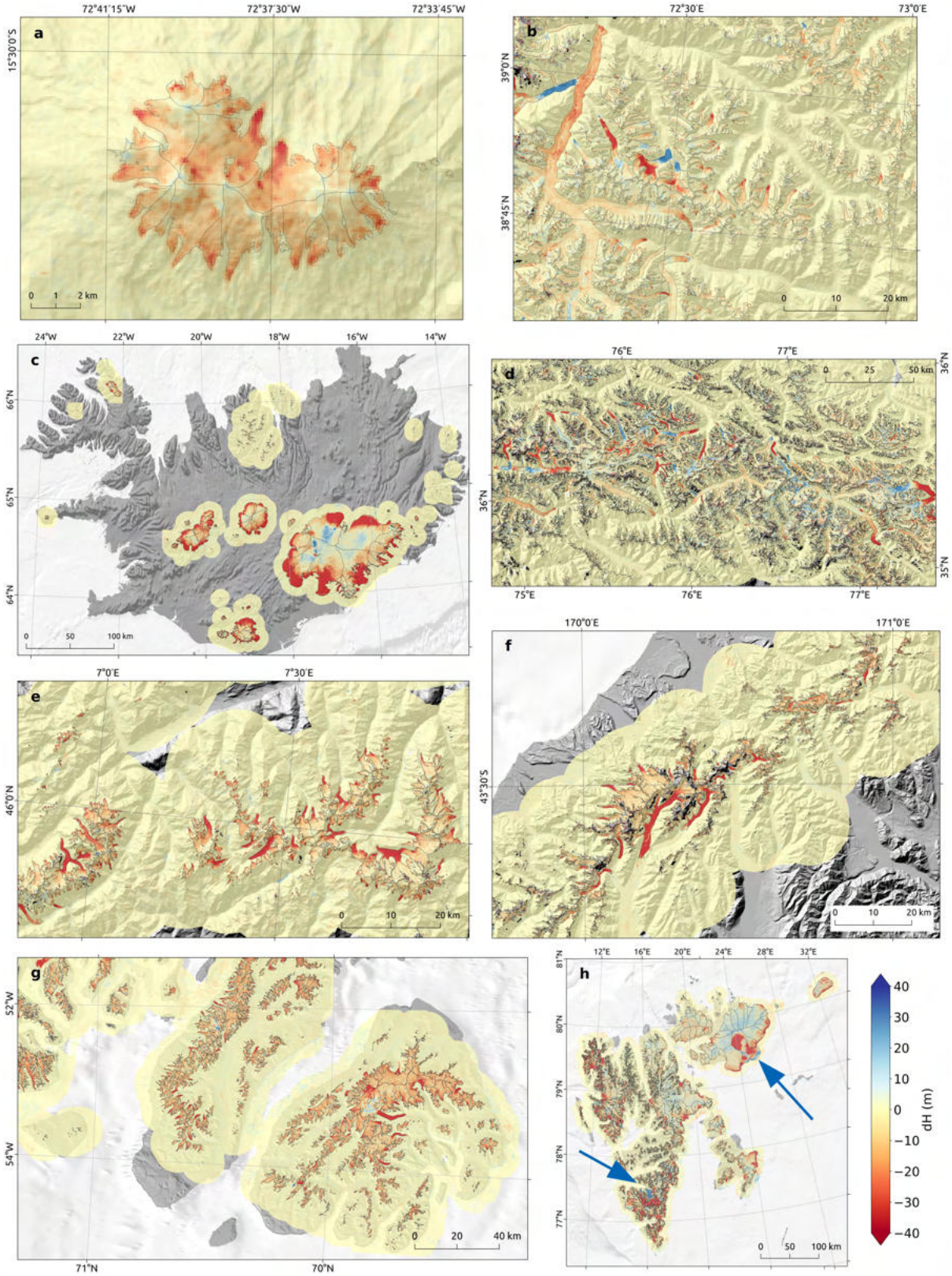

Extended Data Fig. 6 | Two decades of elevation change over various regions. a–**h**, Elevation change of glaciers between 2000 and 2019 in Coropuna, Peru (**a**), Pamir Mountains (**b**), Iceland (**c**), Karakoram Mountains (**d**), European Alps (**e**), Southern Alps, New Zealand (**f**), West Greenland (note the rotated orientation of map) (**g**) and Svalbard (**h**). Except for Svalbard, glacier outlines displayed are from the RGI 6.0. In the background is shown a hillshade derived from several sources[36,46,100]. In Svalbard, outlines have been updated to include the massive surges of Austfonna Basin 3[38,39] in the northeast and Nathorstbreen in the southwest[40], indicated by blue arrows.

Article

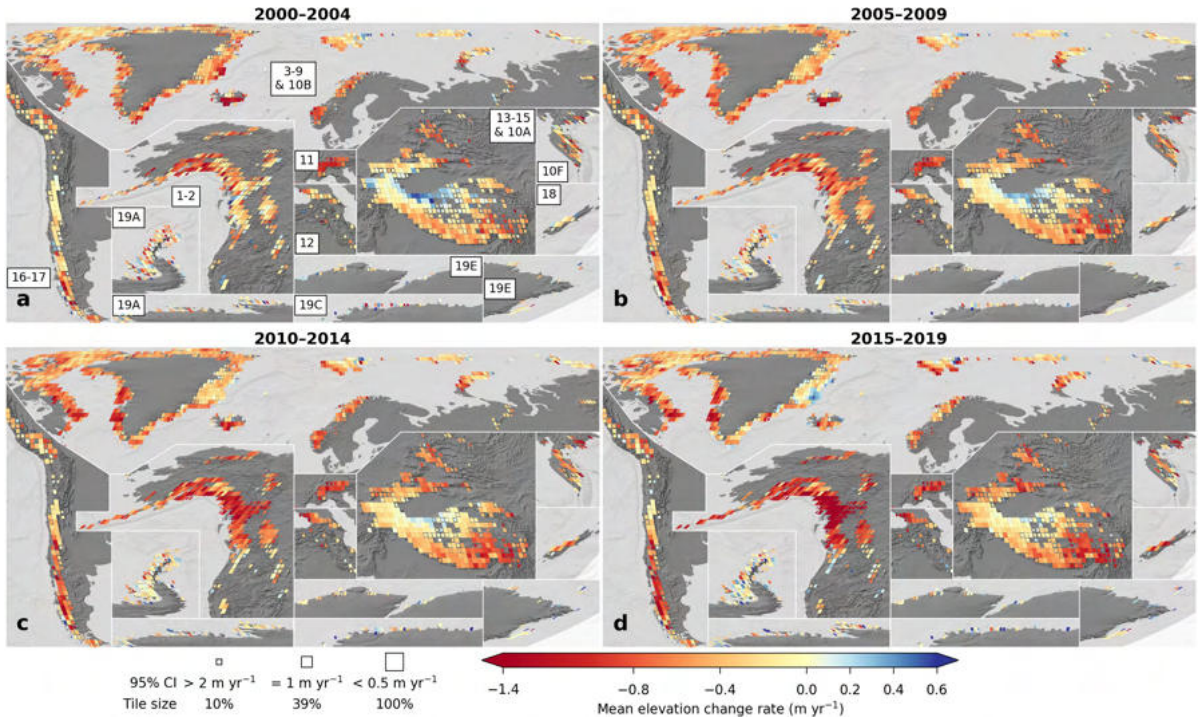

Extended Data Fig. 7 | Global evolution of 5-year thinning rates. a–**d**, Mean elevation change rates aggregated by tiles of 1° × 1° for the periods 2000–2004 (**a**), 2005–2009 (**b**), 2010–2014 (**c**) and 2015–2019 (**d**). The tile area is inversely scaled to the squared 95% confidence interval of the mean elevation change in the tile, and tiles are coloured with mean elevation change rates, on top of a world hillshade[36]. The minimum tile area is 10% for a 95% confidence interval larger than 2 m yr^{-1} and tiles are displayed at full size for a 95% confidence interval smaller than 0.5 m yr^{-1}. Region labelling refers to that of Fig. 2. The acceleration of thinning brings the Karakoram anomaly to its apparent end.

Extended Data Table 1 | Regional rates of glacier elevation and mass change from 2000 to 2019

Region	Area (km²)	2000–2004 / 2005–2009 / 2010–2014 / 2015–2019		2000–2019	
		Mean elevation change rate (m yr⁻¹)	Mass change rate (Gt yr⁻¹)	Mean elevation change rate (m yr⁻¹)	Mass change rate (Gt yr⁻¹)
1 Alaska	86,725	-0.65/-0.80/-0.98/-1.24 ± 0.12/0.11/0.12/0.11	-49.5/-59.4/-70.5/-87.2 ± 11.4/11.7/12.9/14.4	-0.91 ± 0.08	-66.7 ± 10.9
2 Western Canada and USA	14,524	-0.25/-0.47/-0.76/-1.05 ± 0.10/0.10/0.15/0.21	-3.1/-5.8/-9.1/-12.3 ± 1.4/1.5/2.2/3.0	-0.62 ± 0.11	-7.6 ± 1.7
3 Arctic Canada North	105,111	-0.27/-0.38/-0.40/-0.33 ± 0.09/0.06/0.05/0.06	-24.0/-34.2/-35.2/-28.9 ± 8.3/6.9/6.4/6.7	-0.34 ± 0.03	-30.6 ± 4.8
4 Arctic Canada South	40,888	-0.63/-0.73/-0.84/-0.87 ± 0.15/0.09/0.08/0.10	-22.0/-25.1/-29.0/-29.9 ± 6.1/4.7/4.8/5.5	-0.77 ± 0.06	-26.5 ± 4.3
5 Greenland Periphery	89,717	-0.49/-0.49/-0.57/-0.47 ± 0.07/0.05/0.05/0.05	-36.6/-35.2/-39.2/-31.0 ± 7.3/6.0/6.6/5.4	-0.5 ± 0.04	-35.5 ± 5.8
6 Iceland	11,060	-1.21/-1.17/-0.97/-0.77 ± 0.18/0.12/0.12/0.13	-11.3/-10.7/-8.7/-6.7 ± 2.3/1.8/1.6/1.5	-1.03 ± 0.06	-9.4 ± 1.4
7 Svalbard and Jan Mayen	34,187	-0.26/-0.28/-0.38/-0.56 ± 0.09/0.06/0.06/0.08	-7.5/-8.1/-10.8/-15.8 ± 2.8/2.1/2.3/3.1	-0.37 ± 0.03	-10.5 ± 1.7
8 Scandinavia	2,949	-0.77/-0.67/-0.72/-0.56 ± 0.18/0.14/0.14/0.17	-1.9/-1.7/-1.7/-1.3 ± 0.5/0.4/0.4/0.5	-0.68 ± 0.11	-1.7 ± 0.4
9 Russian Arctic	51,592	-0.19/-0.22/-0.24/-0.30 ± 0.10/0.05/0.05/0.06	-8.4/-9.6/-10.6/-13.1 ± 4.5/2.7/2.7/3.2	-0.24 ± 0.03	-10.4 ± 1.9
10 North Asia	2,410	-0.51/-0.59/-0.65/-0.70 ± 0.21/0.19/0.20/0.23	-1.1/-1.2/-1.3/-1.4 ± 0.5/0.4/0.5/0.5	-0.61 ± 0.16	-1.3 ± 0.4
11 Central Europe	2,092	-0.97/-0.99/-1.00/-1.11 ± 0.27/0.23/0.23/0.26	-1.7/-1.7/-1.6/-1.7 ± 0.5/0.5/0.4/0.5	-1.02 ± 0.21	-1.7 ± 0.4
12 Caucasus and Middle East	1,336	-0.31/-0.57/-0.73/-0.96 ± 0.28/0.20/0.24/0.33	-0.3/-0.6/-0.8/-1.0 ± 0.3/0.2/0.3/0.4	-0.64 ± 0.16	-0.7 ± 0.2
13 Central Asia	49,303	-0.06/-0.19/-0.30/-0.40 ± 0.09/0.07/0.08/0.10	-2.6/-7.7/-12.2/-16.0 ± 3.7/2.9/3.6/4.6	-0.23 ± 0.04	-9.6 ± 2.1
14 South Asia West	33,568	-0.10/-0.15/-0.18/-0.23 ± 0.17/0.11/0.10/0.14	-2.9/-4.2/-4.9/-6.2 ± 5.0/3.3/3.0/4.0	-0.16 ± 0.06	-4.6 ± 1.7
15 South Asia East	14,734	-0.46/-0.53/-0.59/-0.67 ± 0.16/0.13/0.14/0.17	-5.8/-6.6/-7.2/-8.0 ± 2.1/1.9/1.9/2.3	-0.56 ± 0.08	-6.9 ± 1.4
16 Low Latitudes	2,341	-0.47/-0.52/-0.54/-0.62 ± 0.21/0.18/0.21/0.23	-0.9/-0.9/-0.9/-1.0 ± 0.4/0.4/0.4/0.4	-0.53 ± 0.11	-0.9 ± 0.2
17 Southern Andes	29,429	-0.73/-0.82/-0.85/-0.98 ± 0.29/0.17/0.17/0.27	-18.1/-20.2/-20.8/-23.7 ± 7.7/5.1/5.1/7.3	-0.84 ± 0.12	-20.7 ± 4.1
18 New Zealand	1,162	-0.22/-0.72/-1.01/-1.52 ± 0.31/0.32/0.34/0.50	-0.2/-0.6/-0.8/-1.1 ± 0.3/0.3/0.3/0.4	-0.85 ± 0.23	-0.7 ± 0.2
19 Antarctic and Subantarctic	132,867	-0.26/-0.22/-0.18/-0.11 ± 0.12/0.12/0.12/0.12	-28.7/-23.7/-19.5/-11.6 ± 14.0/13.3/13.2/12.2	-0.2 ± 0.04	-20.9 ± 4.9
Total, excl. regions 5 and 19	**483,412**	**-0.39/-0.49/-0.56/-0.64 ± 0.04/0.03/0.03/0.04**	**-161/-198/-226/-255 ± 19/17/17/20**	**-0.52 ± 0.02**	**-210 ± 14**
Global total	**705,997**	**-0.38/-0.44/-0.49/-0.52 ± 0.04/0.03/0.03/0.03**	**-227/-257/-285/-298 ± 25/22/23/24**	**-0.46 ± 0.02**	**-267 ± 16**

Regional and global mean elevation change and mass change rates over 2000–2019 and 5-year subperiods of 2000–2019. The mean elevation change is the volume change divided by time-evolving regional glacier areas (see Methods)[21]. Areas reported are those of the RGI 6.0 inventory[22], except for region 12 (Caucasus Middle East), which was updated with more recent outlines[37]. Periods are inclusive and refer to calendar years of 1 January–31 December. Uncertainties correspond to 95% confidence intervals. In Greenland, glaciers highly connected to the ice sheet (RGI 6.0 connectivity level 2) are not reported.

Article

Extended Data Table 2 | Regional data coverage of elevation time series from 2000 to 2019

Region	Area of nominal glaciers and glaciers without any coverage (% of regional area)	Spatial coverage over glacierized terrain (% of regional area)	Average elevation observations per pixel (after filtering)	
			2000–2004 / 2005–2009 / 2010–2014 / 2015–2019	2000–2019
1 Alaska	0.02	99.03	3.9/4.4/6.9/13.4	28.6
2 Western Canada and USA	0.28	98.23	6.0/8.6/5.2/8.5	28.3
3 Arctic Canada North	0	99.95	11.6/8.9/15.3/19.4	55.3
4 Arctic Canada South	0	99.86	4.0/5.8/8.1/10.4	28.3
5 Greenland Periphery	0.02	99.48	13.4/11.2/18.8/22.7	66.1
6 Iceland	0	100	13.5/13.9/26.6/12.5	66.4
7 Svalbard and Jan Mayen	0	99.99	8.7/6.5/10.6/22.4	48.2
8 Scandinavia	0.01	99.88	6.5/4.4/8.1/8.0	27
9 Russian Arctic	0	100	5.2/5.2/19.3/22.3	51.9
10 North Asia	3.67	95.62	5.8/10.1/11.9/9.7	37.5
11 Central Europe	0.5	97.66	11.2/10.4/12.6/12.7	46.8
12 Caucasus and Middle East	0.73	91.69	8.9/7.2/7.4/5.8	29.3
13 Central Asia	0.07	97.13	8.4/10.4/7.9/8.5	35.2
14 South Asia West	0.18	94.77	8.0/10.6/11.1/10.8	40.5
15 South Asia East	0.18	92.51	6.6/8.7/6.4/6.5	28.2
16 Low Latitudes	0.12	95.57	9.2/8.8/8.5/8.7	35.2
17 Southern Andes	0.41	92.54	4.6/5.8/8.3/8.7	27.4
18 New Zealand	2.31	84.27	12.6/9.8/15.5/26.4	64.2
19 Antarctic and Subantarctic	0.4	92.4	3.0/2.8/4.3/5.3	15.4
Total, excl. regions 5 and 19	**0.09**	**98.3**	**7.3/7.4/11.4/14.6**	**40.8**
Global total	**0.14**	**97.34**	**7.3/7.0/11.0/13.9**	**39.2**

Spatial and temporal coverage of our elevation time series after the three steps of elevation outlier filtering. Nominal glaciers correspond to uncharted glaciers inventoried in the RGI 6.0 with only an estimated surface area, present notably in region 10 (North Asia), where they contribute to 3.0% of the region's total glacier area. Those are accounted for in our volume change estimates by applying the mean elevation change of the region to their reported area. Glaciers without any coverage correspond to glaciers having no valid, post-filtering elevation change observation within their outline. This generally occurs when repeat spatial sampling is poor (less than three observations in 20 years) for small glaciers located in steep slopes.

Extended Data Table 3 | Regional rates of land- and marine-terminating glaciers in maritime regions

	2000–2004 / 2005–2009 / 2010–2014 / 2015–2019 / **2000–2019**					
	Marine-terminating			*Land-terminating*		
Maritime region	**Area (km²)**	**Mean elevation change rate (m yr⁻¹)**	**Increase 2000–2004 to 2015–2019**	**Area (km²)**	**Mean elevation change rate (m yr⁻¹)**	**Increase 2000–2004 to 2015–2019**
1 Alaska	11,650	-0.60/-0.69/-0.86/-1.03/**-0.79** ± 0.22/0.21/0.20/0.14/**0.06**	72%	75,075	-0.66/-0.82/-1.00/-1.27/**-0.93** ± 0.12/0.11/0.12/0.12/**0.08**	92%
3 Arctic Canada North	49,111	-0.25/-0.33/-0.32/-0.25/**-0.29** ± 0.12/0.08/0.07/0.09/**0.03**	0%	56,000	-0.29/-0.43/-0.46/-0.40/**-0.39** ± 0.08/0.06/0.05/0.06/**0.03**	38%
4 Arctic Canada South	3,030	-0.53/-0.58/-0.71/-0.69/**-0.63** ± 0.28/0.19/0.16/0.21/**0.08**	30%	37,859	-0.64/-0.74/-0.85/-0.89/**-0.78** ± 0.15/0.09/0.08/0.10/**0.06**	39%
5 Greenland Periphery	31,106	-0.44/-0.45/-0.56/-0.46/**-0.48** ± 0.12/0.06/0.07/0.07/**0.04**	5%	58,611	-0.51/-0.51/-0.57/-0.48/**-0.52** ± 0.07/0.06/0.06/0.06/**0.05**	-6%
7 Svalbard and Jan Mayen	15,108	-0.25/-0.36/-0.53/-0.81/**-0.48** ± 0.13/0.09/0.10/0.12/**0.04**	224%	19,079	-0.27/-0.22/-0.26/-0.36/**-0.27** ± 0.10/0.07/0.07/0.08/**0.03**	33%
9 Russian Arctic	33,434	-0.23/-0.26/-0.31/-0.38/**-0.30** ± 0.11/0.06/0.06/0.07/**0.03**	65%	18,158	-0.11/-0.14/-0.13/-0.16/**-0.13** ± 0.13/0.07/0.07/0.09/**0.04**	45%
17 Southern Andes	7,057	-0.48/-0.55/-0.59/-0.69/**-0.58** ± 0.48/0.27/0.25/0.39/**0.13**	44%	22,372	-0.81/-0.90/-0.93/-1.07/**-0.93** ± 0.27/0.17/0.18/0.26/**0.14**	32%
19 Antarctic and Subantarctic	131,192	-0.26/-0.21/-0.18/-0.10/**-0.19** ± 0.12/0.12/0.12/0.12/**0.04**	-62%	1,676	-0.66/-0.75/-0.85/-0.97/**-0.80** ± 0.44/0.32/0.34/0.39/**0.14**	47%
Total, excl. regions 5 and 19	119,390	-0.30/-0.37/-0.42/-0.47/**-0.39** ± 0.07/0.05/0.04/0.05/**0.02**	57%	228,542	-0.50/-0.62/-0.70/-0.80/**-0.66** ± 0.06/0.05/0.05/0.05/**0.03**	60%
Total	281,687	-0.30/-0.31/-0.33/-0.30/**-0.31** ± 0.07/0.06/0.06/0.06/**0.02**	0%	288,829	-0.51/-0.60/-0.68/-0.74/**-0.63** ± 0.05/0.04/0.04/0.04/**0.03**	45%

Uncertainties correspond to 95% confidence intervals. For marine-terminating glaciers, subaqueous losses are not included (see Methods).

3.6 Extension to other types of surface elevation applications

3.6.1 Supervised Master thesis: *Global cartography of radar penetration in glaciers from the Shuttle Radar Topographic Mission*

Master thesis as supervisor featured in this section: Menthon, M. (2020), *Global cartography of radar penetration in glaciers from the Shuttle Radar Topographic Mission*.[6]

The elevation time series produced in Hugonnet et al. (2021) are useful for other applications than glacier mass change estimation. A closely related application is the estimation of penetration of radar signals in firn and ice. Many planetary-scale DEMs, including notably SRTM and TanDEM-X, rely on radar measurements. While those have the benefit to function at night and with cloud cover, complex patterns of penetration that depend on the seasonal and interannual variation of firn and ice surfaces are entangled in the measurements, raising the question of what surface is observed. Radar penetration has indeed been the focus of specific research for two decades (Dall et al., 2001; Rignot et al., 2001), with estimations of penetration that generally rely on independent surface elevation measurements acquired simultaneously. Benefiting from spatially homogeneous surface elevations measured from altimetry, estimates of penetration have flourished for the Antarctic and Greenland ice sheets (Zhao and Floricioiu, 2017; Abdullahi et al., 2019; Fischer et al., 2020; Rott et al., 2021). Due to the scarcity of simultaneous measurements over glaciers, however, penetration estimates have been more difficult to produce. Those originally relied on acquisitions performed years apart (Berthier et al., 2006). More recently, the increasing availability of DEMs enabled analysis of acquisitions taken months apart (Dehecq et al., 2016; Lambrecht et al., 2018) and even days apart (Li et al., 2021). While these improvements are shedding light on the impact radar penetration has on surface elevation estimation of firn and ice, large-scale estimation for glaciers remains hardly feasible.

In the thesis of Menthon (2020), we focused on DEMs produced from the C- and X-band of the SRTM. The C-band has a complete coverage of latitudes lower than 60 degrees and produced the first near-global topography of the Earth in February 2000, while the X-band has a smaller swath coverage of the same flight plan. We used the recent NASADEM (NASA JPL, 2020) product based on a reprocessing of the SRTM C-band with additional corrections and auxiliary data such as radar backscatter made available. We also retrieved the SRTM X-band product available from the German Space Agency. After co-registration on stable terrain (Nuth and Kääb, 2011) on a $1° \times 1°$ tiling, we compared the SRTM C- and X-bands to the estimated elevation on 15 February 2000 from the ASTER time series (Fig. 3.25). ASTER acquisitions started as soon as March 2000, with smaller repeat coverage until the end of 2001, and are thus typically extrapolated before the first measurement for a period of a few months to a few years. We performed this analysis for all $100\,\text{m} \times 100\,\text{m}$ pixels of low-latitude glaciers and aggregated the results globally (Fig. 3.26).

[6]Contribution: in Maxence Menthon's thesis, I provided scientific and technical supervision, with co-supervision by Etienne Berthier. I produced code tutorials to provide Maxence Menthon with starting tools to analyze the different DEM datasets, and helped scale his final processing chain developed on case studies to the global scale.

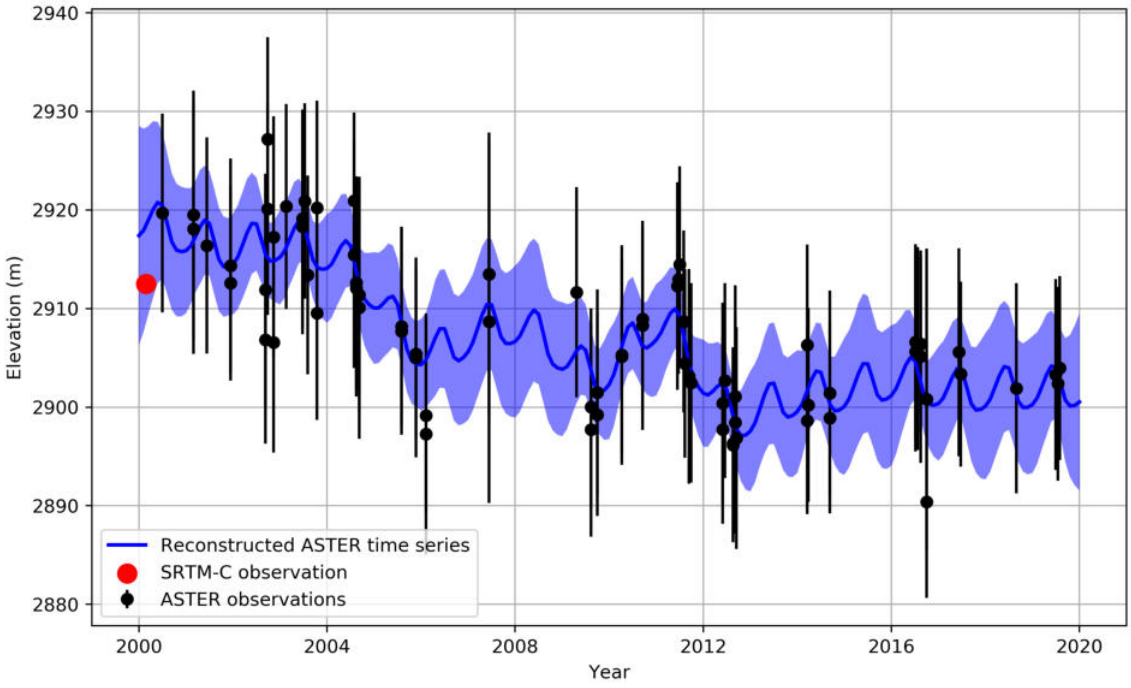

Figure 3.25: Example of SRTM-C band penetration estimated from ASTER time series. Time series of ASTER elevation from Hugonnet et al. (2021) for a 100 m x 100 m pixel of the accumulation area of the Mer de Glace Glacier, France. The C-band SRTM elevation has approximately an 8 m of penetration at this location.

We found a widespread C-band penetration of 4–9 m on average for Northern hemisphere glacierized regions consistent with previous estimates (Berthier et al., 2006; Dehecq et al., 2016). Those coincide with the expected glacier surface conditions in mid-February of dry firn accumulated during winter, exacerbating signal penetration. For the Southern hemisphere, we estimated low penetration values of 0–2 m with high regional variability in the Tropics (Fig. 3.26), that match the wetter surface conditions of the austral summer. For Northern hemisphere regions, taking an arbitrary 10-year study period that uses the SRTM C-band as an early DEM, and using another unbiased late DEM, the magnitude of this penetration would underestimate the current regional glacier mass loss by 90–150%.

We analyzed the hypsometric distribution of our estimates (Fig. 3.27). In the Northern hemisphere, penetration does not only occur in high but also lower elevations, likely owing to thick firn layers. For the Southern hemisphere, we surprisingly identified elevation biases in ablation areas. These differences cannot be due to radar penetration due to the wet snow conditions. While those could stem from the extrapolation of ASTER data, they do not coincide with the accelerating trend identified in Hugonnet et al. (2021) which would imply a positive bias. We therefore speculate that these elevation biases are due to the presence of liquid water at the surface that aggravate surface decorrelation, as previously identified in Li et al. (2021).

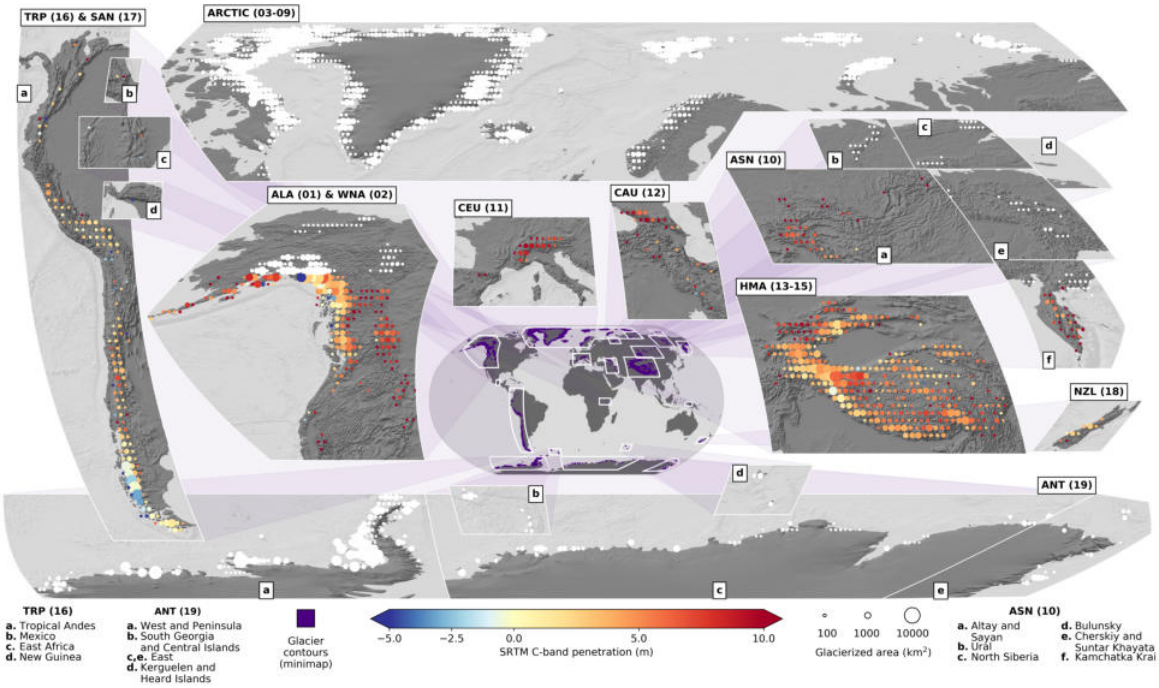

Figure 3.26: Penetration of SRTM C-band in low-latitude glaciers. The mean penetration of the entire glacierized surface is estimated per tile. White disks correspond to glacierized areas not covered by the SRTM. See more legends details on Fig. 3.15.

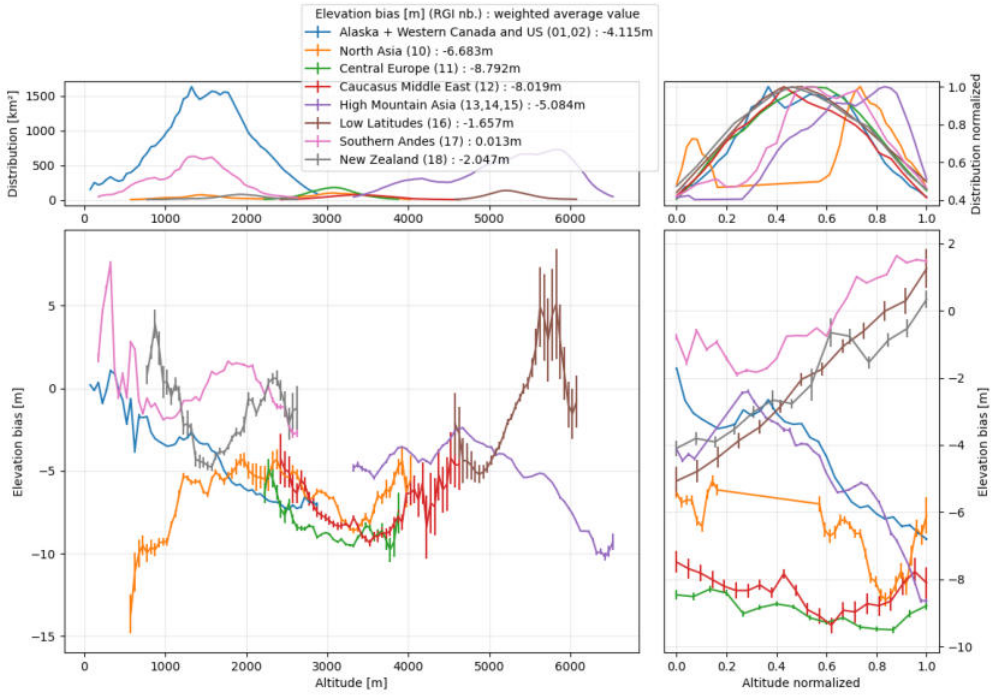

Figure 3.27: Regional hypsometry of C-band penetration in glaciers. Elevation bias estimated from SRTM C-band minus ASTER elevations (i.e. negative values correspond to penetration).

The thesis of Menthon (2020) holds promising results to assess the penetration of C- and X-band in the SRTM for all low-latitude glaciers. Additional analyses focusing on understanding the relationship of the backscatter provided by NASADEM, and the surface conditions in February 2000 from reanalyses are still ongoing. We expect our recently developed tools in *xdem* to help correct the undulations in the X-band SRTM DEMs (Fig. A1b) using tools inspired from *pymmaster*. We also aim to constrain uncertainties of the temporal extrapolation using the spatiotemporal statistics approach developed in Hugonnet et al. (2021), to ultimately provide a robust assessment of radar penetration. The thesis of Menthon (2020) provides valuable estimates for SRTM, but these methods could be similarly applied to other radar instruments such as TanDEM-X. This contemporary archive indeed provides temporally closer acquisition dates to those of ASTER DEMs, a more varied seasonal and repeat sampling, as well as coverage of polar regions and ice sheet margins. An analysis of TanDEM-X DEMs globally would thus substantially improve our means to estimate, and eventually correct, radar penetration into ice and snow.

3.6.2 Supervised Master thesis: *Large-scale snow depth mapping from moderate resolution satellite imagery*

Master thesis as supervisor featured in this section: Xiong, Z. (2021), *Large-scale snow depth mapping from moderate resolution satellite imagery*.[7]

In the estimation of changes in surface elevation, another closely related application to glacier surface changes is that of snow depth estimation. Snow depth is a climate variable essential to water resource management and avalanche hazard forecasting. Yet, quantifying snow depth at large scales remains challenging due to its high spatial variability and the sparse number of available observations. Those observations are generally based on in-situ measurements in populated regions (Jonas et al., 2009; Schöner et al., 2019; Matiu et al., 2021), and sometimes complemented with dedicated and costly airborne campaigns from unmanned aircraft vehicles or terrestrial laser scanning (Nolan et al., 2015; Eberhard et al., 2021). Such high-resolution observations only exist for a few regions and were generally acquired after the 2010s, and have been recently complemented by high-resolution satellite photogrammetry (Marti et al., 2016; Deschamps-Berger et al., 2020). A recent study based on Sentinel-2 provided large-scale snow depth estimates of the Northern Hemisphere, which amount to nearly all snow covered surfaces globally (~98%). Yet, this estimate is limited to post-2017 and to a coarse spatial resolution of 1 km x 1 km (Lievens et al., 2019). Moderate-resolution satellite photogrammetry such as ASTER imagery has been discarded owing to their lesser precision and sources of error from instrument noise. The recent improvements in the correction and constraint of these errors might render the exploitation of the ASTER archive feasible and unlock two decades of snow depth estimation.

[7]Contribution: in Zhouyi Xiong's thesis, I provided scientific and technical supervision, with co-supervision by Daniel Farinotti. I produced code tutorials to provide Zhouyi Xiong with starting tools to analyze available ASTER DEMs, and helped scale her final processing chain developed on a case study to the scale of the European Alps.

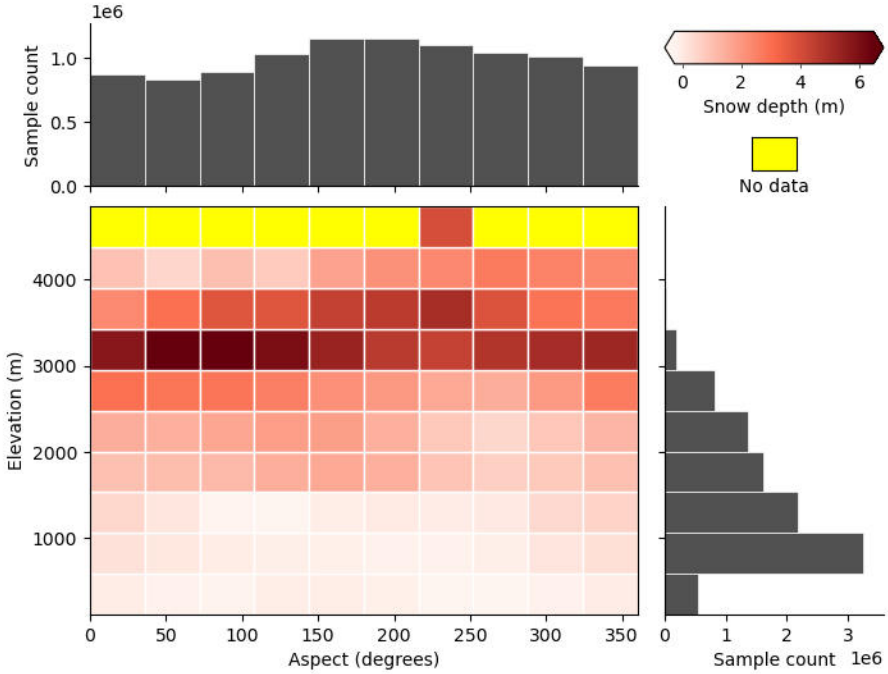

Figure 3.28: Snow depth with elevation and aspect. Median of 2000–2019 winter snow depths estimated in the European Alps for elevation and aspect bins. South correspond to 180 degree aspect. Snow depth increases with elevation, and for north faces. Above 3500 m, terrain is mostly ice-covered and thus only steep slopes, mostly snow-free, are resolved hence the decrease in snow depth.

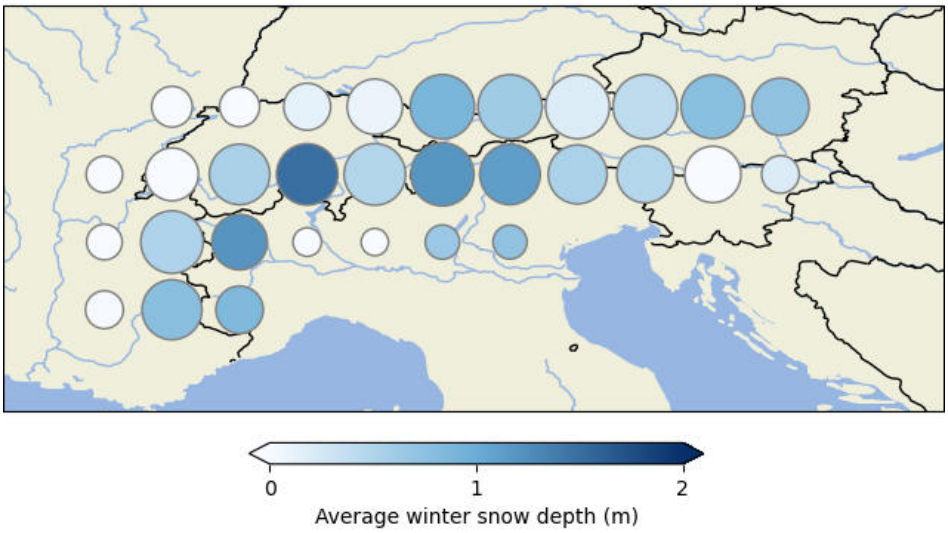

Figure 3.29: Average 2000–2019 winter snow depth in the European Alps. The spatial average is performed on 100 km x 100 km tiles. Disk sizes scale with the number of pixels measured which exclude glacierized, forested and snow-free terrain.

In the thesis of Xiong (2021), we explored the potential of ASTER DEMs to assess snow depth in the European Alps. The first step towards an estimation of snow depth is the production of an end-of-summer, snow-free DEM. Unfortunately, the quality-controlled DEM products available globally, such as TanDEM-X global DEM (Rizzoli et al., 2017), are a mosaic of many acquisitions that mixes snow-covered and snow-free elevations. We thus produced our own snow-free DEM by aligning and merging all ASTER DEMs acquired in summer during 2000–2019. To simplify the temporal aspect of the work, we performed the same merging seasonally to produce average DEMs of winter, spring and fall for 2000–2019, i.e. a 20-year average climatology of seasonal snow depth. To this end, we vertically aligned all DEMs exclusively on low elevation stable terrain (<500 m), which mitigates the effects of snow depth at higher elevations. This effect is generally omitted in glaciological applications (Fig. C5). We then excluded glacierized and forested terrain from our analysis, as well as snow-free terrain using the 2000-2019, seasonal average of monthly MODIS snow-cover fraction (Hall and Riggs, 2021). This masking significantly reduces the sampled area of the European Alps, as forests cover most of the lower elevation ranges (1,000–2,500 m), and glaciers the upper ones (3,000 m–4,800 m).

We analyzed the reliability of our estimated snow depths by studying their relation to topographical variables. We did this by computing the median of snow depth in bins of elevation, slope, and aspect for the entire European Alps. The binning mitigates the lesser pixel-wise precision of ASTER DEMs by inferring from a larger sample size. We found a strong snow depth dependency with elevation (Fig. 3.28) that matches the trends measured from previous high-resolution catchment surveys in the Alps and Pyrenees (Grünewald et al., 2014). We measured a consistent elevation trend when subdividing arbitrarily in catchments of a 100 km x 100 km tiling, which validated the spatial homogeneity of the ASTER-based snow depth estimates. We identified a dependency to aspect independent of elevation (Fig. 3.28), owed to the lesser solar exposure of northern faces, of magnitude consistent with estimations of (Zheng et al., 2016) in Sierra Nevada. We found biases in high slopes, however, that might originate from photogrammetric blunders. Overall, we estimated an average of 0.5 m of 2000-2019 winter snow depth on all winter snow-covered terrain (Fig. 3.29).

This exploratory thesis showed that ASTER DEMs could be utilized to estimate snow depth at large scales. While it is yet unclear what would be the spatiotemporal precision of the underlying estimations (e.g., statistical significance for a 10 km x 10 km catchment every 5 years, or for larger areas and longer periods?), these results at the scale of the European Alps show a promising avenue. Performing a comparison with the dense field measurements available in the European Alps is discouraged due to their high local variability. We thus envision an intercomparison with ICESat and ICESat-2 data (Abdalati et al., 2010), and the use of advanced statistical analyses to help characterize the precision of these estimations at different spatial and temporal scales.

3.7 The potential of precise glacier mass changes for the glaciological and hydrological community

3.7.1 Resolved calibration of global glacier models

In-review article as co-author featured in this section: Rounce, D.R. et al. (in review), *Global glacier change in the 21st century: every tenth of a degree temperature increase matters*, Science.[8]

The availability of glacier volume change estimates at the scale of individual glaciers globally is redefining the way mass balance models are addressed and calibrated. Thus far, global mass balance models have indeed been relying on sparse in situ data, or regional mass change estimates for calibration (Huss and Hock, 2015; Hock et al., 2019a; Marzeion et al., 2020; Edwards et al., 2021). This calibration implied large sources of uncertainties and, in some occasions, negative biases propagated from the calibration data (Gardner et al., 2013; Zemp et al., 2019). Most critically, this calibration was performed by imposing the same mass change to all glaciers in the region, thereby allowing less liberty to the calibration parameters of individual glaciers, and increasing the risk of local biases when predicting glacier- or catchment-scale mass changes.

In the study of Rounce et al. (in review), we calibrated nearly every glacier worldwide based on the 20-year estimates of Hugonnet et al. (2021) using a Bayesian calibration scheme developed in (Rounce et al., 2020) to account for parameter uncertainty and prevent overfitting. To improve the calibration, we quality-controlled the data of Hugonnet et al. (2021), keeping only data with more than 80% coverage and 1σ uncertainty smaller than 1 m w.e. yr^{-1} which represents 96% of glacier areas and 87% of the number of glaciers (Fig. 3.30). Additionally, we refined mass balance predictions by integrating as-yet unaccounted frontal ablation and debris thicknesses processes, calibrated on recent associated estimates (Rounce et al., 2021; Kochtitzky et al., in review). Our projections are grouped based on mean global temperature increases by the end of the 21st century compared to pre-industrial levels by aggregating Representative Concentration Pathways (RCPs) and Shared Socioeconomic Pathways (SSPs) accordingly in order to provide policy-relevant scenarios. This simplification is taken due to the linear relationship that exists between glacier mass change and temperature change (Edwards et al., 2021).

Globally, our projections of sea-level rise for the period 2015-2100 in Rounce et al. (in review) are larger than previous predictions, despite two factors that reduce sea-level contributions: our mass change calibration and our new sea-level correction. We indeed calibrated on the estimates of Hugonnet et al. (2021) which are less negative than extrapolated in-situ measurements (Gardner et al., 2013; WGMS, 2019) or previous global estimates (Zemp et al., 2019) for the period 2000–2019. We additionally implemented a correction for the mass loss of ice that is below sea level, unaccounted by previous studies (Marzeion et al., 2020; Edwards

[8]Contribution: in the study of Rounce et al. (in review), I provided early estimates of the Hugonnet et al. (2021) study along with quality-control analysis of the dataset and discussions on uncertainty analysis.

et al., 2021), which reduces by about ~15% our projected sea-level rise. For RCP2.6 projections, our projections are 11% and 19% larger than that of Marzeion et al. (2020) and Edwards et al. (2021), respectively. Neglecting the loss of ice below sea level, our projections of glacier contribution to sea-level rise would be 10–33% greater than these consensus estimates for all emission scenarios. We attribute these differences to the improved representation of physical processes in our model, and possibly the accelerated trend in mass loss in (Hugonnet et al., 2021). As projected mass losses of glaciers are linearly related to global temperature increases, we identified that only scenarios with warming lower than +2°C would prevent widespread deglaciation of low latitude regions (Fig. 3.31).

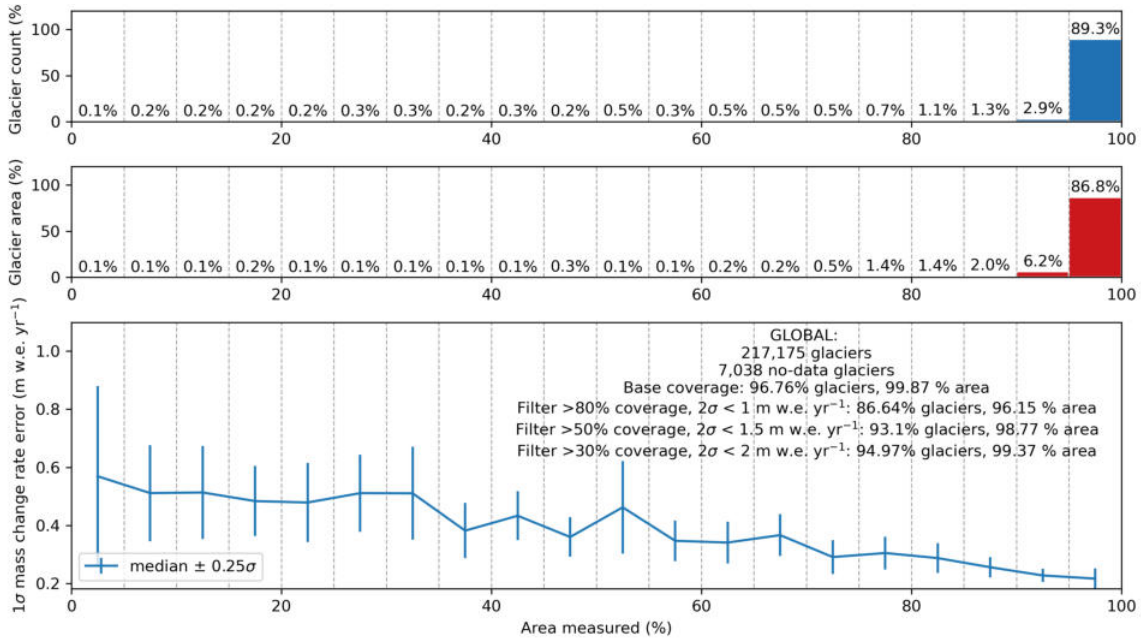

Figure 3.30: Coverage and uncertainties of glacier estimates. Uncertainty of glacier mass change estimates of Hugonnet et al. (2021) aggregated by percentage of glacier area measured. The top two panels show histograms of glaciers in each bin, per number of glacier and per glacierized area. The first filtering choice listed was kept for the study of Rounce et al. (in review) to ensure highest quality estimates. Glaciers without observations were calibrated on the regional average.

While our modelling improvements are valuable to yield robust predictions of glacier mass changes, there is still untapped potential from the increased wealth of observations (e.g. Hugonnet et al., 2021; Geyman et al., 2022). Firstly, global glacier models were historically calibrated on mass change to match the units of in situ measurements. Yet, recent improvements in large-scale estimation yield precise volume changes, rather than mass changes. A conversion to mass changes is convenient to provide a usable water-equivalent change, but this common practice might not be optimal. Volume-to-mass conversion factors are indeed largely based on modelling due to the scarcity of firn density profile measurements (Huss, 2013). It thus seems preferable that volume-to-mass conversion be integrated within models, and that the calibration of models evolve to use volume changes as input, instead of relying on simplified conversions computed in observational assessments.

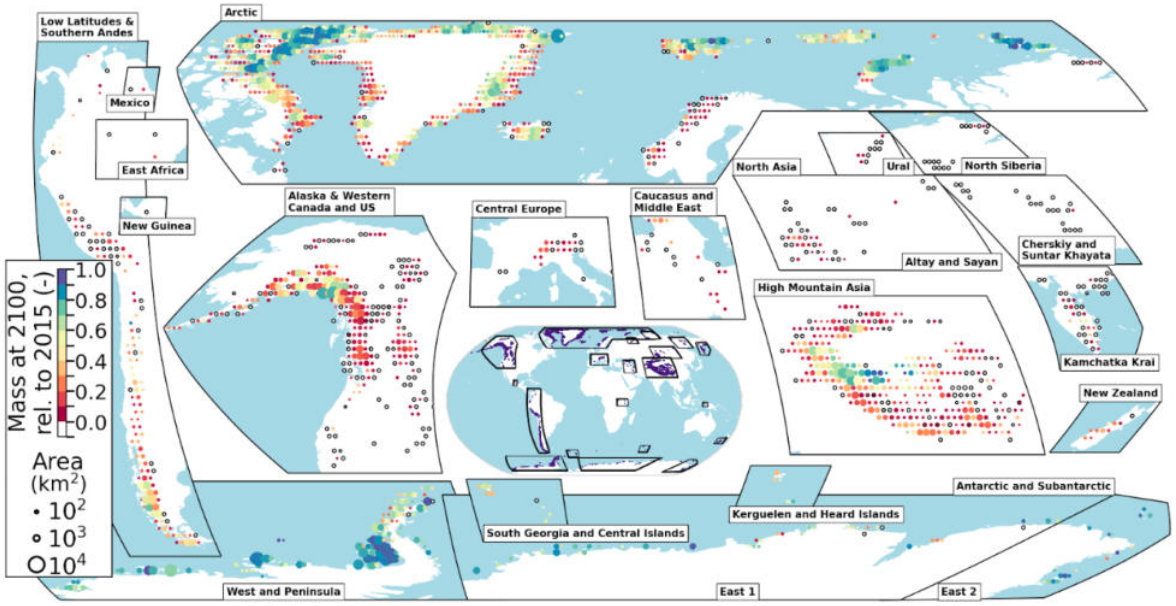

Figure 3.31: Spatial distribution of glacier mass remaining by 2100 for the +2°C scenario. From Rounce et al. (in review). Multi-scenario median glacier mass remaining by 2100 (relative to 2015) for the +2°C (above pre-industrial levels) global mean temperature change scenario. This includes all RCP and SSPs within a 0.5°C tolerance. Tiles are aggregated by 1°x1° below 60° latitude, 2°x1° between 60° and 74° latitude and 2°x2° above 74° latitude to represent approximately 10,000 km2 each. Circles are scaled based on simulated glacierized area in 2015 and are colored by normalized mass remaining. Regions that have experienced complete deglaciation by 2100 are shown in white and outlined in black.

Secondly, the increasing availability and temporal coverage of glacier elevation change estimation is now providing statistically significant elevation changes resolved in space, and sometimes continuous in time (Zemp et al., 2019; Hugonnet et al., 2021). In global glacier models, a commonly used spatial simplification uses a one-dimensional, hypsometrical representation of glacier (Huss and Hock, 2015). Besides, calibration is also often performed on a single period rather than accounting for observed trends in time. Current global models consequently do not benefit from the wealth of observational data. To address this, those could evolve towards a two- or three-dimensional calibration in space and time, despite rendering these models more computationally expensive.

Finally, the spatial propagation of predicted errors of glacier models does not yet include error assessment based on spatiotemporal statistics. Model uncertainties are mostly based on the sensitivity analysis of physical processes, and the spread of RCP and SSP scenarios (Marzeion et al., 2020). Those methods might omit systematic errors from biases in process modelling and, with the increasing resolution expected of predictions (Rounce et al., in review), are not well suited to propagate random errors between spatial and temporal scales. Spatiotemporal statistics could be used to shed light on biases and correlations in the structure of error of glacier predictions and ensure the robustness of uncertainties in model prediction at all scales.

3.7.2 Refining density conversion of glacier volume changes

In-prep article as co-author featured in this section: Huss, M. et al. (in prep), *Converting geodetic ice volume to mass change: a global-scale assessment*.[9]

Water-equivalent glacier mass change can only be estimated from volume changes after density conversion. On a first intuition, converting from glacier volume changes to mass changes appears as simple as using the density of ice of around $917\,\mathrm{kg\,m^{-3}}$. Yet this problem is much more complex. To illustrate this, let us consider the idealized case of a glacier in a balanced state during a short period (e.g., during spring or fall), where ablation is balanced by accumulation. We define the density conversion factor ρ as the fraction of mass change dM by volume change dV:

$$\rho = \frac{dM}{dV}. \tag{3.1}$$

We assume that the volume change is measured between two dates: a first date just after a heavy snowfall resulting in the accretion of a thick and light snow layer on top of the glacier, and a second date where this layer has compacted into firn. The mass change dM is around zero during the period, while the volume change dV is negative due to the volume reduction from the compaction. And thus the density conversion factor is about zero, according to Eq. 3.1. Changing our first assumption, we now assume that the glacier was imbalanced and gaining mass, and that the volume loss due to compaction counter-balances the mass gain in terms of volume change, yielding a total volume change of zero. Then, from Eq. 3.1, we have ρ equals either plus or minus infinity. In summary, the density conversion factor ρ can take any value.

To address this, Huss (2013) investigated the use of a periodic average density conversion factor ρ to describe volume-to-mass conversion. Huss (2013) relied on a glacier mass balance model coupled to a firn compaction model (Heritage et al., 2009) and calibrated on ice density profiles compiled from ice cores over the world (e.g. Oerter et al., 1982; Nuth et al., 2010; Zdanowicz et al., 2013). These models were used on both idealized glacier geometries and Swiss glaciers with homogenized time series of in situ measurements (Huss et al., 2009). Huss (2013) identified a high variability of density conversion factors for short periods and, using idealized climate forcings, showed that those are also more delicate to constrain when glacier are in balance with climate. Based on these quantitative results, and in a context of global glacier retreat, Huss (2013) recommended an average density conversion factor of $\sim 850\,\mathrm{kg\,m^{-3}}$ with a 1σ uncertainty of $\pm 60\,\mathrm{kg\,m^{-3}}$ for periods lasting at least 5 years. This value, systematically smaller than that of ice density, is explained by the partial removal of low-density firn layers in addition to ice, owing to the skrinking extent of glacier surfaces. Since then, these recommended values have become common usage in glacier volume change assessments.

[9] Contribution: in the study of Huss et al. (in prep.), I provided glacier mass change estimates of Hugonnet et al. (2021) for calibration of individual glaciers and performed statistical analysis of the density conversion factors estimated yearly for all 200,000 glaciers during 2000–2019.

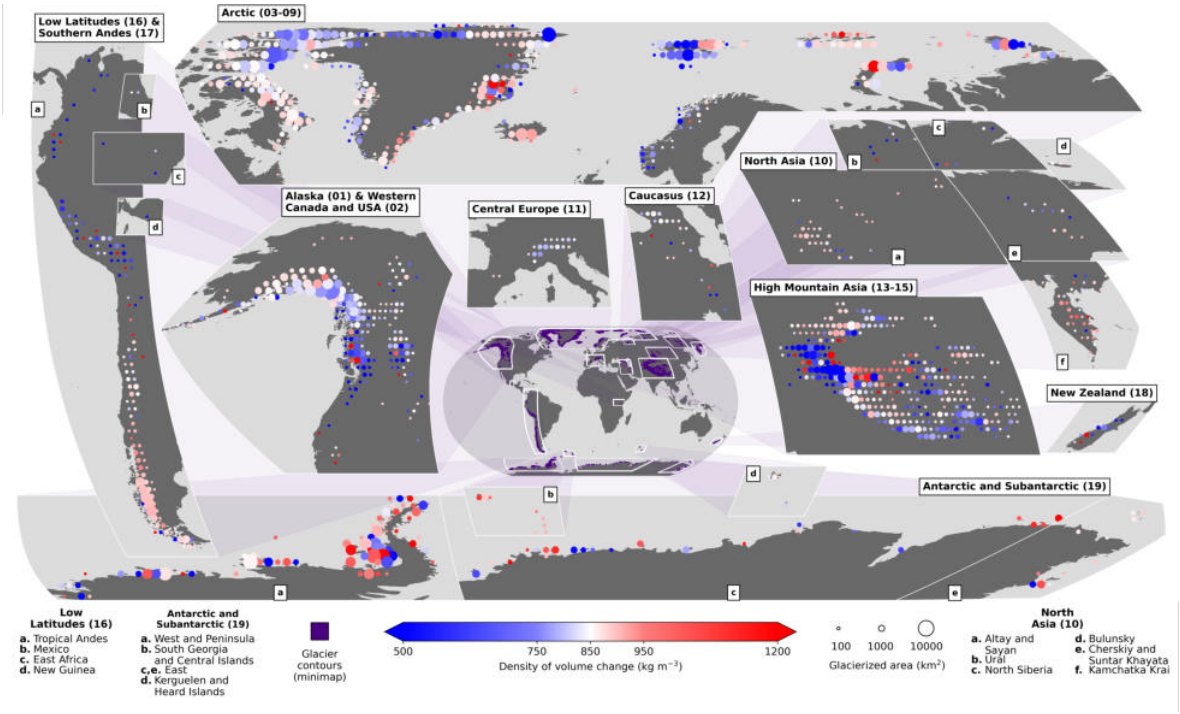

Figure 3.32: Global density of glacier volume change from 2000–2019. From Huss et al. (in prep.). Same layout as Fig. 3.15. Density conversion factors are aggregated within tiles by volume change-weighting, as volume changes correspond to the spatial support of density conversion factors.

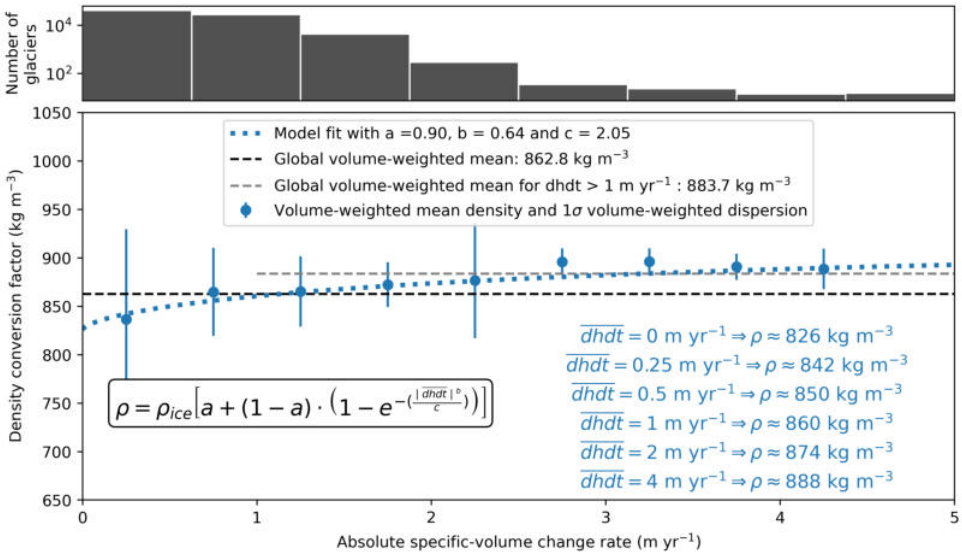

Figure 3.33: Influence of the thinning rate on the density conversion factor. From Huss et al. (in prep.). Volume change-weighted median and dispersion of the 2000–2019 density conversion factors for bins of absolute specific-volume change rates for all glaciers globally. An exponential model fit is derived for the binned statistics by weighted least-squares. Density conversion factors increase with specific-volume change rates, converging towards ice density.

With the recent increase in precision and coverage of glacier volume changes, density conversion factors have become the largest uncertainty source of mass change estimations (Hugonnet et al., 2021), and thus the next limiting factor. In the work on Huss et al. (in prep.), we combined the global glacier model GloGEM (Huss and Hock, 2015) with a firn densification model similar to that of Huss (2013). We initialized mass balances for roughly all 200,000 individual glaciers globally using the mass change estimates of Hugonnet et al. (2021). We used ERA5 reanalysis data (Hersbach et al., 2020) to drive the model in estimating volume changes with firn densification processes, and ultimately derived a density conversion factor for every glacier and any period over the last two decades (Fig. 3.32). Our assessment thereby accounts for local changes in climate, as well as the observed changes of each individual glacier, that translate into shifts in the firn properties.

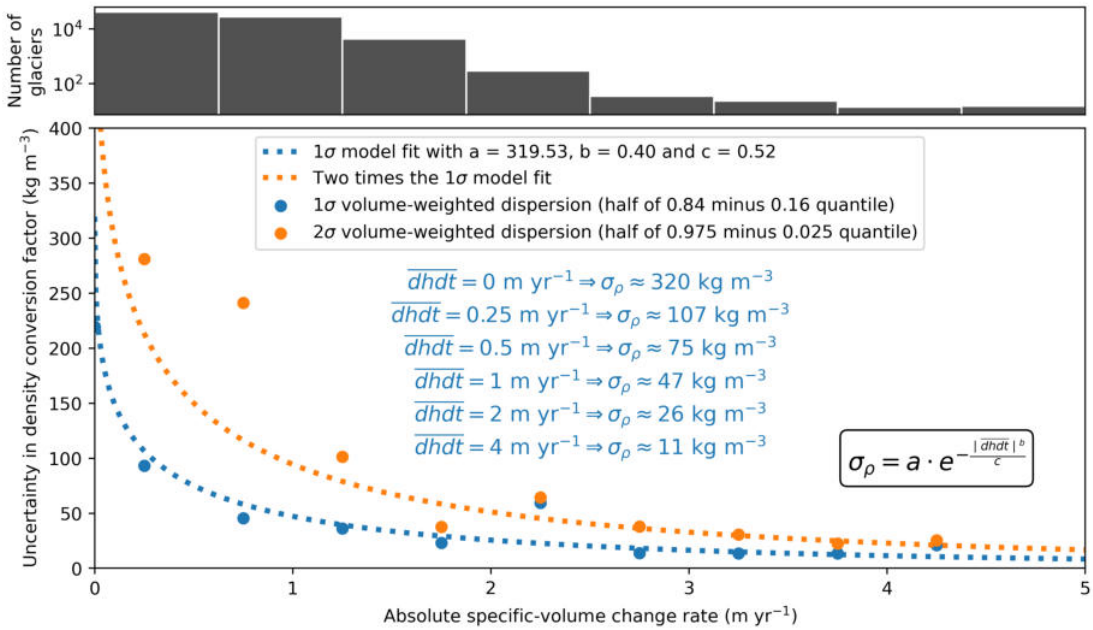

Figure 3.34: Influence of the thinning rate on density conversion uncertainties. From Huss et al. (in prep.). 1σ and 2σ dispersions of the 2000–2019 density conversion factors for bins of absolute specific-volume change rates, i.e. mean elevation change rates, for all glaciers globally. An exponential model fit is derived for the binned statistics by weighted least-squares. Density conversion uncertainties decrease strongly with increasing specific-volume change rates, converging towards zero.

We analyzed the estimated density factors globally. As density conversion factors are spatially integrated on a volume, their spatial aggregation is volume change-weighted in contrast to the typical area-weighting of elevation changes. The mean density factor of 20-year volume change was estimated at ~863 kg m^{-3}, matching the previous estimate of Huss (2013). We identified that density factors are on average lower with specific-volume change (i.e. mean elevation change) rates that are closer to zero (Fig. 3.33), and closer to 917 kg m^{-3} with large volume changes. This finding echoes with the intuition that, over a fixed period, more ice is proportionally removed than firn with a higher thinning rate. Additionally, we found that uncertainties in density conversion varied strongly with volume change rates, with 1σ

uncertainties larger than $\pm 100\,\mathrm{kg\,m^{-3}}$ for specific-volume changes smaller than $0.25\,\mathrm{m\,yr^{-1}}$, and uncertainties smaller than $\pm 50\,\mathrm{kg\,m^{-3}}$ for those larger than $1\,\mathrm{m\,yr^{-1}}$ (Fig. 3.34). We also identified a strong dependency of the uncertainty on the length of the study period.

Additionally, we performed an analysis of spatial correlation and identified that density conversion factors are correlated over a range of ~500 km, which corresponds to the patterns visible on Fig. 3.32. This implies that the density conversion factors are not independent between glacier of a region, but similar over very large distances. Consequently, studies that propagate density uncertainties as uncorrelated between glaciers or small glacierized subregions (e.g. Braun et al., 2019) potentially strongly underestimate density uncertainties, while studies that propagate those as fully correlated in RGI regions such as Hugonnet et al. (2021) moderately overestimate uncertainties. As such, these considerations of spatial correlation of density factors require the attention of the community to better grasp the limitations of past estimates and provide robust estimates in the future.

3.7.3 Deconvolution of glacier signals in terrestrial water storage change

Published article as co-author featured in this section: An, L. et al. (2021), *Divergent causes of terrestrial water storage decline between drylands and humid regions globally*, Geophysical Research Letters.[10]

Terrestrial water storage (TWS) is an important climate variable to monitor the global water and energy budget, and is defined as the summation of all water on the land surface and in the subsurface (Girotto and Rodell, 2019). This includes water stored in canopies, snow and ice, rivers, lakes and reservoirs, wetlands, soil and in the ground. TWS is thus inherently linked to droughts, floods and sea-level rise, and notably plays a key role in determining water resource availability.

TWS is difficult to measure at the global scale, however. A recent global study provided an interpretation of global estimates of TWS change based on gravimetric observations of GRACE since 2002 (Rodell et al., 2018). Another recent study identified a strong decline of TWS in endorheic basins (Wang et al., 2018), i.e. basins that do not flow to the sea, estimated at about half of the glacier mass loss during this period. These losses further exacerbate water stress in these regions, as well as global sea-level rise. Furthermore, TWS is expected to continue declining, which will potentially double the global land area and population subject to extreme-to-exceptional droughts by the late twenty-first century (Pokhrel et al., 2021). In global studies such as Rodell et al. (2018), the interpretation of TWS changes remains largely qualitative due to two main challenges. The first challenge is the coarse resolution of GRACE data, and the second is the entanglement of all mass change signals from the biosphere, hydrosphere, cryosphere, and solid Earth.

[10]Contribution: in the study of An et al. (2021), I integrated glacier mass change estimates of Hugonnet et al. (2021) and their uncertainties for specific global regions with different aridity levels during the period 2002–2016.

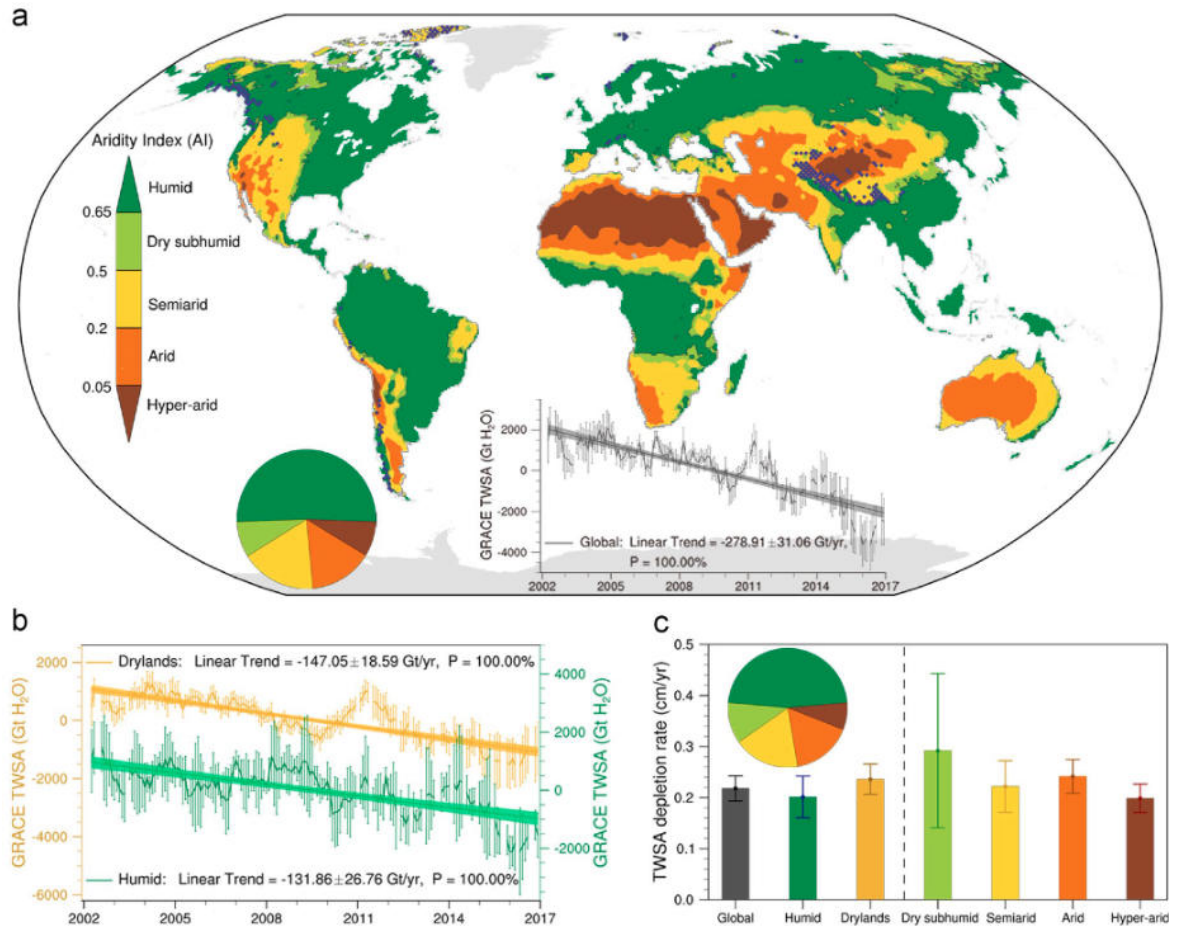

Figure 3.35: Terrestrial water storage trends over different climate zones from GRACE observations, 2002–2016. From An et al. (2021). **a,** Map of climate zones based on the long-term Aridity Index (1961—1990). Blue dots show glacierized regions. The inset pie chart illustrates the proportions of global land area for each climate zone. The inset time series illustrates monthly deseasonalized TWS anomalies in global landmass, with error bars and shading denoting 95% confidence intervals of monthly anomalies and the best-fit linear trend, respectively. **b,** Same as the inset time series in **(a)**, but for monthly deseasonalized TWS anomalies in drylands (yellow) and humid regions (green). **c,** TWS decline rates (in cm yr^{-1}) for each climate zone. Error bars show 95% confidence intervals. The inset pie chart illustrates the relative contributions of each climate zone to the global TWS change (in Gt yr^{-1}).

In An et al. (2021), we aim to provide quantitative estimates of TWS changes globally with relevance to the impacts of droughts and water stress. To address the first challenge, we defined regions with different levels of aridity worldwide (Feng and Fu, 2013). This enabled us to aggregate GRACE data for all locations of a certain aridity level, losing in resolution but also reducing uncertainties to provide statistically significant global trends (Fig. 3.35). For the second challenge, we partitioned TWS change into its different contributors from independent estimations of the most resolved components. We used our estimation of global glacier mass changes (Hugonnet et al., 2021). Their increased resolution and precision unlocks the potential to use glaciers to better constrain other TWS components, rather than the opposite which was done in gravimetric glacier studies (Wouters et al., 2019; Ciracì et al., 2020). We

used a reconstruction from a global statistical hydrological model trained on GRACE data and meteorological datasets to derive precipitation-induced TWS change (Humphrey and Gudmundsson, 2019). We also used a state-of-the-art hydrological model that accounts for human interference such as groundwater abstraction and reservoir regulation (Müller Schmied et al., 2021) to estimate human-induced change. Finally, we combined these to partition TWS change into three main contributors: precipitation-induced changes, glacier mass changes, and human-induced changes (Fig. 3.36).

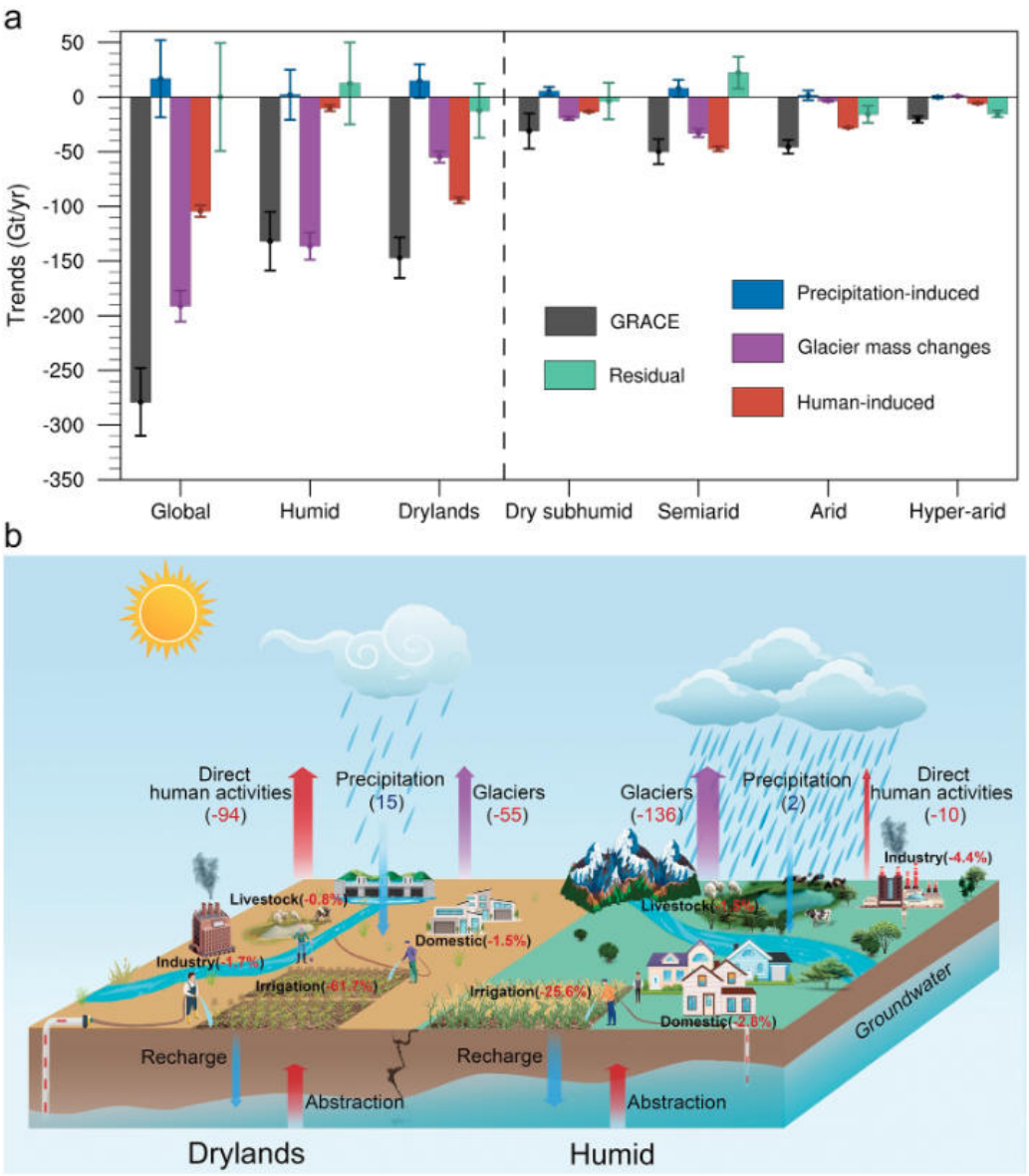

Figure 3.36: Quantitative attribution of terrestrial water storage trends in each climate zone during 2002–2016. From An et al. (2021). **a,** Contributions of each driver to zonal TWS trends. **b,** Schematic diagram summarizing the contributions of major drivers to the net TWS trends in global drylands and humid regions. Contributions of direct human activities, precipitation, and glacier mass changes are in Gt yr^{-1}, whereas sectoral water consumptions are in percentage.

We found that the sum of our three contributors explains nearly all TWS changes measured by GRACE data. Precipitation-induced changes have limited and transitory impacts (<20%), while glacier mass losses explain the TWS changes (~103%) in humid regions and human-induced changes dominate the TWS decline in drylands (~64%). In drylands, TWS losses appear enduring and widespread owing to human activities, and are attributed largely to unsustainable groundwater abstraction (Fig. 3.36). Our findings quantified that arid regions, already vulnerable, will be at an increased risk of water scarcity, stressing the need for dryland water conservation efforts globally. Improved quantifications are necessary to better resolve the local variations in these trends, and isolate where efforts are most needed. By combining our estimates of Hugonnet et al. (2021) and GRACE data with downscaling techniques, TWS changes could potentially be resolved at finer scales in glacierized regions.

3.7.4 The relation between glacier thinning and ice-dammed outburst floods

Published and in review articles as co-author featured in this section: Veh, G. et al. (2022), *Trends, breaks, and biases in the frequency of reported glacier lake outburst floods*, Earth's Future and Veh, G. et al. (in review), *Smaller and earlier outbursts from ice-dammed lakes with ongoing glacier decay*, Nature.[11]

Glacier lake outburst floods (GLOFs) are floods that emerge from lakes storing meltwater behind a glacier or moraine dam, or in overdeepened parts of exposed glacier beds. Hundreds of GLOFs have been recorded in the past century, claiming more than 10,000 fatalities and devastating farmland, livestock, and infrastructure (Carrivick and Tweed, 2016). Several studies have argued that, under atmospheric warming, the annual number of GLOFs might increase (Bolch et al., 2012; Harrison et al., 2018; Shugar et al., 2020). Thousands of lakes have indeed been forming in the foreland of retreating glaciers (Shugar et al., 2020), and reported outbursts are deemed to be on the rise, especially since the beginning of the 20th century (Harrison et al., 2018). Additionally, the demographic increase in mountainous regions, as well as the growing economic activities such as hydropower generation, forestry, and mining, call for a better understanding of GLOFs to mitigate their potential impacts.

In Veh et al. (2022), we collated a new global GLOF inventory recording more than 2,000 events based on catalogues of national authorities, regional inventories (e.g. Haeberli, 1983; Bhambri et al., 2019), as well as ~700 other sources that includes stream gages analyses, air- and space-borne imagery, stratigraphy, tree rings, news outlets, social media accounts and unpublished works. Due to the difference in reporting activities, we investigated the presence of bias in this new inventory by specific statistical analyses. Temporal biases might be due to historical changes in data recording and instrumentation, with events missing systematically in databases (Veh et al., 2019). Geographical biases might originate from societal differences in monitoring, for instance mith more event recorded in regions that have long traditions in mountaineering, glacier research, and more inhabitants and infrastructure near glaciers (Harrison et al., 2018).

[11] Contribution: in the studies of Veh et al. (2022) and Veh et al. (in review), I discussed the biases in the GLOF inventory collated by Georg Veh and I extracted thinning time series for specific glacier lake dams.

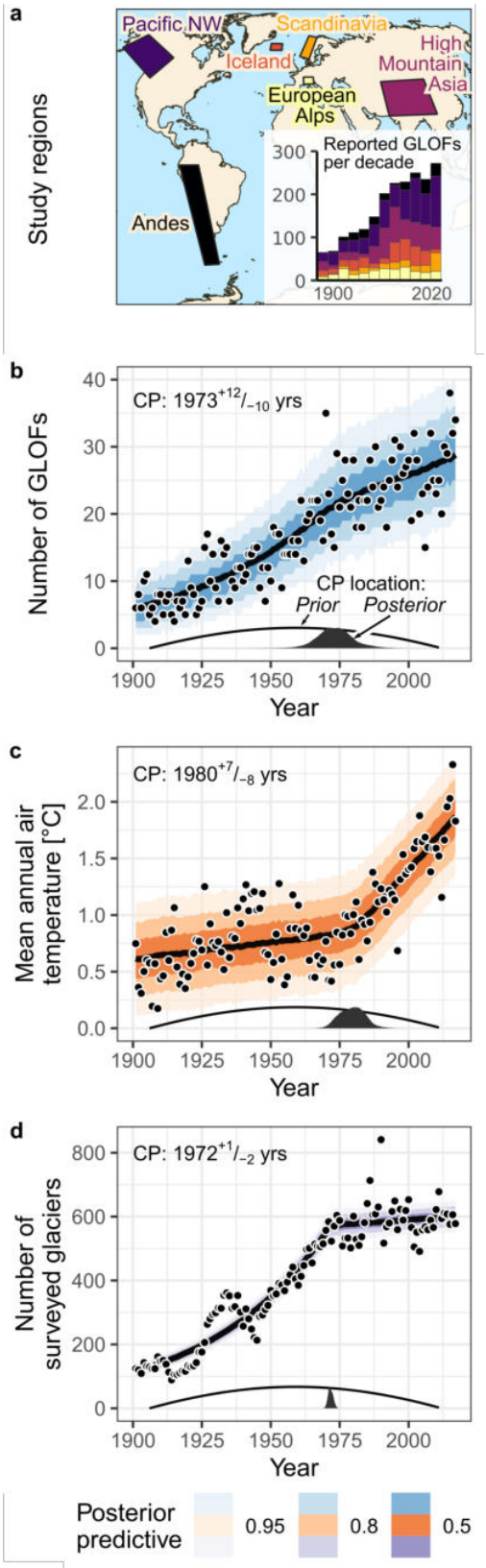

Figure 3.37: Comparing the annual number of reported GLOFs with annual air temperatures and research activity in the period 1901—2017. From Veh et al. (2022). **a,** Map of the six study regions. Inset shows the number of GLOFs per decade. **b,** Annual number of reported GLOFs. **c,** Mean annual air temperature averaged from all sites that produced at least one GLOF. **d,** Total number of annual glacier surveys in our study regions. In panels **(b-d)**, thick lines are the means and shades are the 50—95% posterior predictive highest density intervals from a Bayesian piecewise Poisson regression of the outcome on the y-axis versus year. Bottom black lines and probability densities are the prior and posterior location of the change-point.

We found a positive trend in the number of reported GLOFs that reduces significantly after a break in the 1970s. This break coincides with independently detected trend changes in annual air temperature and in the annual number of field-based glacier surveys (Fig. 3.37), here used as a proxy of scientific event reporting. We observed a deceleration of both the number of reported GLOFs and the number of glacier surveys, while the temperature kept rising in the past five decades. Therefore, warming alone does not explain the trends in reported GLOFs. This suggests that temperature-driven glacier lake formation, growth, and failure are weakly coupled to the number of GLOFs, or that those have been overlooked. Further analysis identifies distinct geographic and temporal biases. We predict that, on average, two to four out of five GLOFs might have gone unnoticed in the early to mid-20th century. While those findings on biases help reconcile the observed trends in reported GLOFs, it is still unclear how climate change is affecting GLOFs.

In Veh et al. (in review), we used the collated inventory to analyze the changing characteristics of ice-dammed GLOFs globally. We investigated notably the flood volume and peak discharge with possible explanatory variables. We identified that ice-dammed outburst floods with the highest magnitude have decayed, producing smaller flood volumes, but that average magnitude outbursts show little change. Ice-dammed GLOFs also happen earlier in the season, and the associated lakes are forming at higher elevations, with is largely explained by ongoing glacier retreat from atmospheric warming. Additionally, we utilized the elevation estimates of Hugonnet et al. (2021) extracted from the glacier areas damming the lakes to investigate its relationship with ice-dammed GLOF volume and peak discharge (Fig. 3.38). We found no clear relationship, suggesting either a nonlinear response of these two quantities or that glacier thinning at the dam is not an appropriate proxy to predict GLOF magnitude.

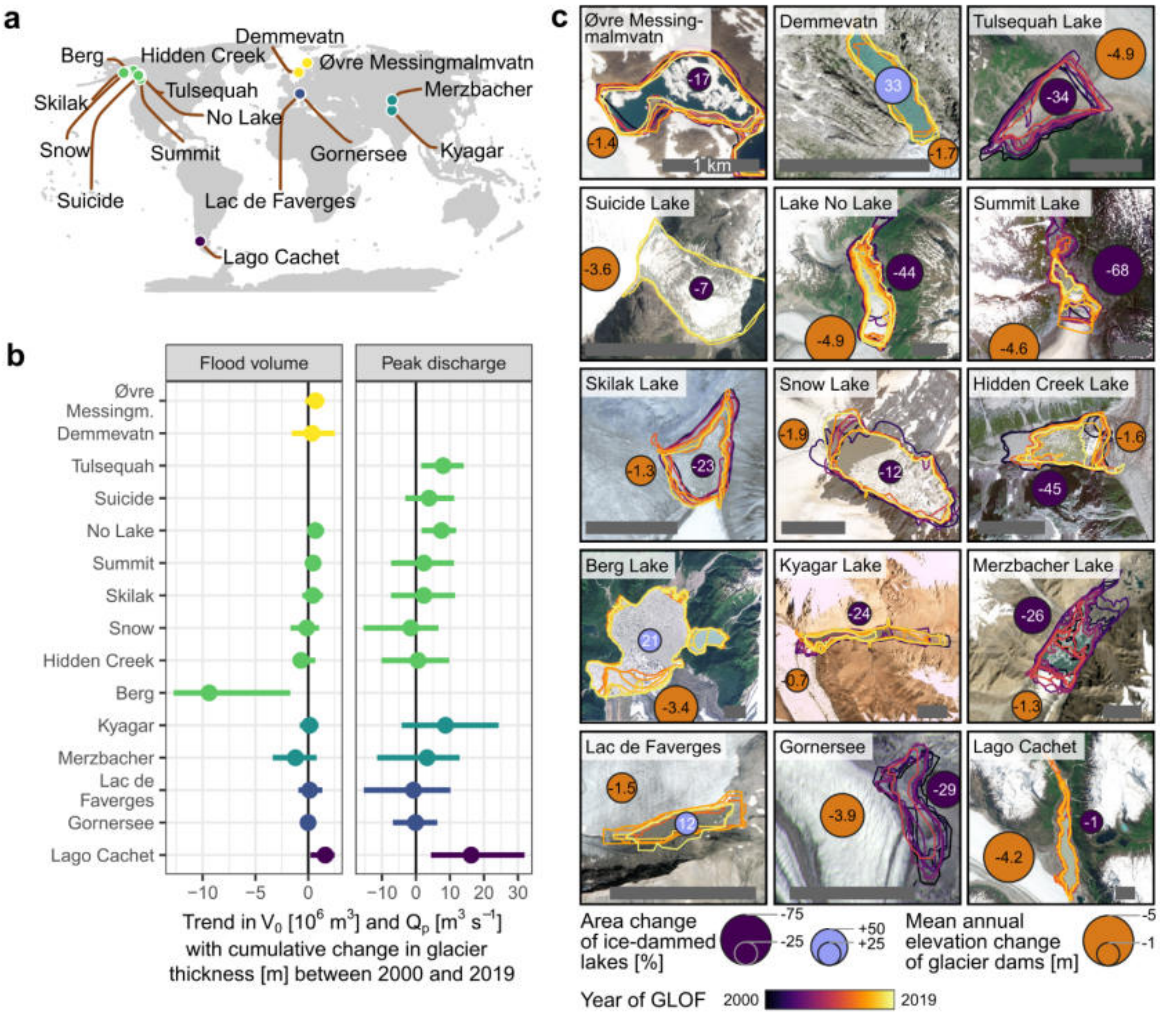

Figure 3.38: Trends in flood volume, peak discharge, and lake area against cumulative glacier elevation change between 2000 and 2019. From Veh et al. (in review). **a,** Map of 15 ice-dammed lakes that produced >5 GLOFs in that period. **b,** Posterior regression slopes of water volume V_0 (left) and peak discharge Q_p (right) versus cumulative elevation change of the glacier dam. Bubbles are median values, and horizontal lines show the 95% posterior highest density interval of the posterior trends. Colours in **(a-b)** distinguish between the study regions. **c,** Local changes in lake area and glacier elevation between 2000 and 2019. Lake areas were mapped from satellite imagery immediately prior to the outburst and colour codes of the lake outlines show the year of the GLOF. Blue bubbles show the average percent change in lake area between the first and last reported GLOF for each lake. Orange bubbles show the mean elevation change of the glacier dam. Grey horizontal scale bar is one kilometre in all panels in c. All background images obtained by Planet Labs in 2019.

Conclusions and outlook

What was done in this thesis?

In this thesis, we first studied the accuracy and precision of digital elevation models. We showed the importance of accounting for the spatial variability and spatial correlation in the structure of elevation errors. Those considerations are not only essential to robustly propagate uncertainties, but more generally to characterize the ability of digital elevation models to represent surface elevation and improve inter-comparability of reliant applications. Benefiting from the generic character of the spatial statistics methods developed, we extended their applications to other types of observational or model-based estimates, including ice velocity, ice thickness, and elevation change interpolation. Those helped improve uncertainty estimation across spatial scales, from local measurements to regional- or planetary-scale assessments.

We then tackled glacier mass change estimation. We harnessed two decades of digital elevation models obtained or generated from various sensors, relying primarily on the ASTER archive. We developed a temporal prediction method that relies on the structure of the data to mitigate existing limitations, and produced a resolved estimate of glacier surface elevation worldwide. We adapted our previous methods to characterize the spatiotemporal structure of errors and improve filtering, interpolation, and uncertainty estimation at all scales, with extensive validation on independent data. We extended our estimations from surface elevation to radar penetration and snow depth. And, by ingesting our estimates into other applications, we helped constrain glacier predictions, density conversion of volume changes, changes in terrestrial water storage and shed light on the relation to lake outburst floods.

In this endeavor, we developed open tools to help foster reproducible and consistent analyses of digital elevation models and glacier mass changes. We made our estimates accessible and paired with the documentation of our tools, to ensure that they can benefit the broad community.

What do we retain from this thesis?

Nowadays, the increasing amount and precision of available data has rendered large-scale geospatial estimations not only feasible, but relatively common. Providing central tendency estimates is generally not the limiting factor, however. A first major challenge lies in the identification and mitigation of biases that can stem from poor accuracy of the instruments or arise from errors during statistical prediction, to ensure that estimates are unbiased. A second challenge is related to the characterization of precision, inherently rooted in the spatial and temporal nature of geospatial problems, to robustly report uncertainties at different scales. Both challenges are also relevant to modelling, in particular when model-based estimates are validated against observations.

In this thesis, we showed that these challenges can be addressed robustly using spatiotemporal statistics, or more generally Gaussian processes. For the first challenge, Gaussian processes allow to perform a prediction historically coined "best unbiased estimation" in kriging by describing and utilizing the multidimensional covariance of the studied variable, as done here in the temporal prediction of glacier elevation. For the second challenge, the same approach can be used to describe errors by relying on the difference between the studied measurement and independent measurements, generally of higher precision. The spatial and temporal dimensions are embedded in geospatial assessments, yet other variable-specific dimensions might also be useful to resolve the challenges of certain applications. Ultimately, these robust techniques are crucial to the interpretation and dissemination of results, especially in fields susceptible to large uncertainties as are climate sciences.

Future research directions

Several research directions are envisioned from this work. Regarding digital elevation models, the methods developed could be applied to all existing sensors and products to provide the community with a description of their respective structure of error. Additionally, by using these structures of error as input, digital elevation model methods could become error-aware. This includes routines such as co-registration and bias-corrections, which are increasingly used and would benefit from statistically-based rather than arbitrarily-based criteria (e.g., subsampling, binning, convergence) to progress towards optimized functioning. Additionally, our framework of non-stationary spatial statistics, owing to its genericity, could be utilized for the uncertainty analysis of other geospatial estimates, be it observational or modelled.

For elevation-based estimations, our improved ASTER products could help refine the mass change estimates of the Greenland and Antarctic ice sheets. Our method of prediction from Gaussian processes could be extended to the dimension of space in addition to that of time, and potentially to other explanatory variables, to eventually harness the entirety of available surface elevation datasets simultaneously, including footprint- or swath-based altimetry. A comparative analysis of elevation time series with bias-prone instruments could produce a wealth of information on biases such as radar penetration into firn and ice, including SRTM and TanDEM-X, and shed light on how auxiliary instrument data can be used to correct them. Eventually, all debiased elevations could be combined to yield reconciled estimations, as well for glacier mass changes as for other applications such as seasonal snow depth.

Finally, our methods are not only useful for statistical estimation, but also for analysis. Spatial and temporal, or other dimensional correlations could help standardize the way glacier mass balances are analyzed, for instance to deconvolve their climatic and geomorphological responses and improve past reconstructions, or better quantify the hypsometric dependency of their climatic response in space and time. Spatiotemporal correlations are continuous approaches to the definition of spatial and temporal domains, free of arbitrary discretization, such as regional delineation or periodic demarcation, and might benefit a wide range of applications including glaciology and, more generally, Earth system science.

Conclusions et perspectives

Qu'est-ce qui a été realisé durant cette thèse ?

Dans cette thèse, nous avons d'abord étudié l'exactitude et la précision des modèles numériques de terrain. Nous avons montré l'importance de la prise en compte de la variabilité spatiale et de la corrélation spatiale dans la structure des erreurs d'altitude de surface. Ces considérations sont non seulement essentielles pour propager de manière robuste les incertitudes, mais plus généralement pour caractériser la capacité des modèles numériques de terrain à représenter l'altitude de surface et à améliorer l'inter-comparabilité des applications qui en dépendent. En profitant du caractère générique des méthodes de statistiques spatiales développées, nous avons étendu leurs applications à d'autres types d'estimations basées sur des observations ou des modèles, notamment la vitesse de la glace, l'épaisseur de la glace et l'interpolation des changements d'altitude. Ces méthodes ont permis d'améliorer l'estimation de l'incertitude à toutes les échelles spatiales, de la mesure locale à des évaluations à l'échelle régionale ou planétaire.

Nous nous sommes ensuite attaqués à l'estimation du changement de masse des glaciers. Nous avons exploité deux décennies de modèles numériques de terrain obtenus ou générés par divers capteurs, en nous appuyant principalement sur l'archive de l'instrument ASTER. Nous avons développé une méthode de prédiction temporelle qui s'appuie sur la structure des données pour atténuer les limitations existantes, et nous avons produit une estimation résolue de l'altitude de la surface des glaciers dans le monde entier. Nous avons adapté nos méthodes précédentes pour caractériser la structure spatio-temporelle des erreurs et améliorer le filtrage, l'interpolation et l'estimation de l'incertitude à toutes les échelles, avec une validation poussée à partir de données indépendantes. Nous avons étendu nos estimations de l'altitude de surface aux cas de l'estimation de la pénétration radar et de l'épaisseur de la neige. Et, en intégrant nos estimations dans d'autres applications, nous avons contribué à contraindre les prédictions d'évolution des glaciers, la conversion en densité des changements de volume, les changements dans le stockage de l'eau terrestre et à éclaircir la relation avec les vidanges de lacs glaciaires.

Dans cette entreprise, nous avons développé des outils libres d'accès pour favoriser des analyses reproductibles et cohérentes des modèles numériques de terrain et des changements de masse des glaciers. Nous avons rendu nos données d'estimations accessibles et les avons associées à une documentation de nos outils, afin de garantir qu'elles puissent bénéficier la communauté large.

Que retenons-nous de cette thèse ?

De nos jours, la quantité et la précision croissantes des données disponibles ont rendu les estimations géospatiales à grande échelle non seulement réalisables, mais relativement courantes.

Cependant, fournir des estimations de tendances centrales n'est généralement pas le facteur limitant. Un premier défi majeur réside dans l'identification et l'atténuation des biais qui peuvent naître d'une mauvaise précision des instruments ou provenir d'erreurs lors de prédictions statistiques, cela afin de s'assurer que les estimations ne sont pas biaisées. Un deuxième défi est lié à la caractérisation de la précision, intrinsèquement ancrée dans la nature spatiale et temporelle des problèmes géospatiaux, afin de rendre compte de manière robuste des incertitudes à différentes échelles. Ces deux défis sont également pertinents pour les travaux de modélisation, en particulier lorsqu'ils sont validés par rapport à des observations.

Dans cette thèse, nous avons montré que l'on peut répondre à ces défis par l'utilisation de statistiques spatio-temporelles, ou plus généralement de processus gaussiens. Pour le premier défi, les processus gaussiens permettent de réaliser une prédiction historiquement nommée "meilleure estimation non biaisée" en krigeage, qui s'effectue par la description de la covariance multidimensionnelle de la variable étudiée, comme cela est fait ici dans la prédiction temporelle de l'altitude des glaciers. Pour le second défi, la même approche peut être utilisée pour décrire les erreurs en s'appuyant sur la différence entre la mesure étudiée et des mesures indépendantes, généralement de plus grande précision. Les dimensions spatiales et temporelles sont ancrées dans les évaluations géospatiales, mais d'autres dimensions spécifiques aux variables étudiées peuvent également être utiles pour résoudre les défis de certaines applications. En fin de compte, ces techniques robustes sont cruciales pour l'interprétation et la diffusion des résultats, en particulier dans les domaines sujets à de grandes incertitudes tels que les sciences du climat.

Pistes de future recherche

Plusieurs directions de recherche sont envisagées à partir de ce travail. En ce qui concerne les modèles numériques de terrain, les méthodes développées pourraient être appliquées à tous les capteurs et produits existants afin de fournir à la communauté une description de leur structure d'erreur respective. De plus, en utilisant ces structures d'erreur en entrée, les méthodes d'analyse de modèles numériques d'altitude pourraient évoluer pour tenir compte de ces erreurs. Cela inclut des routines telles que la co-registration et les corrections de biais, qui sont de plus en plus utilisées et qui bénéficieraient de critères basés sur des statistiques plutôt qu'arbitraires (par exemple pour le sous-échantillonnage, le binning, la convergence) pour progresser vers un fonctionnement optimisé. De plus, notre approche de statistiques spatiales non stationnaires, par sa généricité, pourrait être utilisée pour l'analyse d'incertitude d'autres estimations géospatiales, que celles-ci soient observées ou modélisées.

Pour les estimations basées sur l'altitude, nos produits ASTER améliorés pourrait être utilisés pour contraindre le changement de masse des calottes glaciaires du Groenland et de l'Antarctique. Notre méthode de prédiction à partir de processus gaussiens pourrait être étendue à la dimension spatiale en plus de celle du temps, et potentiellement à d'autres variables explicatives, pour finalement exploiter de manière simultanée la totalité des données d'altitude de surface disponibles, incluant l'altimétrie d'empreinte ou de fauchée. Une anal-

yse comparative de séries temporelles d'altitude avec les instruments à biais pourrait alors produire une mine d'informations sur ces biais tels que la pénétration des radars dans le névé et la glace, notamment pour les instruments SRTM et TanDEM-X, et éclairer la façon dont les données des instruments auxiliaires peuvent être utilisées pour corriger ceux-ci. À terme, toutes les altitudes corrigées pourraient être combinées pour produire des estimation réconciliées, aussi bien pour le changements de masse des glaciers que pour d'autres applications telles que l'épaisseur saisonnière de la neige.

Enfin, nos méthodes ne sont pas seulement utiles pour l'estimation statistique, mais aussi pour l'analyse. Les corrélations spatiales et temporelles, ou celles d'autres dimensions, pourraient aider à standardiser la façon dont les bilans de masse des glaciers sont analysés, par exemple pour déconvoluer leurs réponses climatiques et géomorphologiques et améliorer les reconstructions passées, ou mieux quantifier la dépendance hypsométrique de leur réponse climatique dans l'espace et le temps. Les corrélations spatiotemporelles approchent de manière continues la définition des domaines spatiaux et temporels, libre de toute discrétisation arbitraire telles que la délimitation de régions ou le choix d'une période d'étude, et peuvent bénéficier à un large éventail d'applications, telles que la glaciologie et, plus généralement, la science du système terrestre.

Appendix A: Supplementary Information of *Uncertainty analysis of digital elevation models by spatial inference from stable terrain*

Supplementary Information of *Uncertainty analysis of digital elevation models by spatial inference from stable terrain*

Romain Hugonnet, Fanny Brun, Etienne Berthier, Amaury Dehecq, Erik Schytt Mannerfelt, Nicolas Eckert and Daniel Farinotti

I. Supplementary Data

A. Case study of the Northern Patagonian Icefield

In addition to using terrain-dependent variables (Fig. 3), we add a second case study to exemplify the use of sensor-dependent variables to constrain elevation heteroscedasticity. We use nearly simultaneous SPOT-5 and ASTER images acquired over the Northern Patagonian Icefield (NPI), South America, in March 2012 (Table S1). We generate an ASTER DEM from ASTER L1A imagery [135] using MicMac for ASTER (MMASTER) [66]. This processing merges three consecutive 60 km x 60 km granules into a 180 km x 60 km strip and mitigates the effects of cross-track biases during stereo calculations. We use the quality of stereo-correlation computed by MicMac [136] as a sensor variable for the ASTER DEM (Fig. S5). Additional results and discussion on the Northern Patagonian Icefield case study are presented in the Supplementary Section III.

B. DEMs used for the noise examples

All examples of DEM noise show elevation differences in areas that mainly comprise stable terrain, after coregistration following [77]. Fig. 1b shows elevation differences from two Pléiades DEMs acquired 10 days apart in Peru, which were generated using the Ames Stereo Pipeline (ASP) [134]. The undulations of both DEMs are intertwined.

Fig. S1a shows a difference between ASTER DEM and TanDEM-X global 90 m DEM in Yukon, Canada. The ASTER DEM was generated using MMASTER [66] with cross-track parallax adjustment and 3-granule stitching, but without cross- or along-track bias corrections [47]. These patterns of cross-track bias and along-track undulations are typical of most ASTER DEMs [66].

Fig. S1b shows a difference between the X-band SRTM DEM provided by the German Aerospace Center and the C-band SRTM elevations provided through NASADEM [137] on the Tibetan Plateau. This SRTM-C product corrects for systematic "ripple" errors based on independent elevations from the Ice, Cloud and land Elevation Satellite (ICESat). The observed undulations thus largely stem from the X-band SRTM. Co-registration is performed on a 1° x 1° tile basis (i.e. about 100 km x 100 km) which, due to the long range of X-band undulations, entails different vertical shifts among tiles.

Fig. S1c shows a difference between a WorldView-2 DEM generated by the ArcticDEM effort [138], [139] and a TanDEM-X DEM in Yukon, Canada. The presence of clouds in the Worldview-2 stereo images results in artefacts of amplitude 25–50 m in the DEM segment, also observable in the hillshade. The typical per-pixel random errors of TanDEM-X (about $\pm$ 5 m) are negligible compared to the amplitude of the observed noises, so the elevation differences are largely due to errors in the WorldView-2 DEM.

Fig. S1d shows a difference between a SPOT-6 DEM generated with ASP [134] and the Copernicus 30 m DEM in Iceland. The stripped artefacts stem from the SPOT-6 DEM.

II. Supplementary Methods

A. Spatial statistics and second-order stationarity

Spatial statistics are based on the characterization of correlations that generally depend only on the distance between observations [112], [113], [117]. To this end, spatial statistics are applied in a statistical framework governed by the assumption of second-order stationarity. That is, if the following three assumptions are fulfilled:

- the mean of the variable of interest is stationary in space, i.e. constant over sufficiently large areas within the spatial domain;
- the variance of the variable of interest is stationary in space, i.e. constant over sufficiently large areas within the spatial domain; and
- the covariance between two observations only depends on the spatial distance between them, i.e. no other factor than this distance plays a role in the spatial correlation.

B. Robust estimators for variograms

We use Dowd's estimator [146] to estimate empirical variograms. Empirical variogram estimation is a binning procedure in which the variance between pairs of observations that fall within a similar spatial lag, i.e. distance between the pair, is estimated. Variogram estimators are subject to the influence of outliers in a manner similar to that of dispersion estimators for a traditional sample. We did not use Genson's robust variogram estimator [150] due to long computation times, not well fitted to elevation data. While the Cressie-Hawkins estimator [149] was defined to be more robust than the most common Matheron estimator [148], it is still less robust than median estimators such as Dowd's [146]. However, median estimators can misrepresent sample variability in the case of

a small sample size. As DEM analysis generally contains large sample sizes, we choose to consistently rely on Dowd's estimator. Furthermore, we highlight the practical advantage of using Dowd's estimator along with the NMAD. In fact, both estimators are scaled to the dispersion of a normal distribution with a similar scaling factor. Dowd's scaling factor of 2.198 (for the variance) corresponds exactly to the square of the scaling factor of the NMAD of 1.482 (for the dispersion).

C. Pairwise sampling for grids

To improve our variogram estimation across spatial scales that span several orders of magnitude (1–10 m to 10–100 km), we delve into the problem of pairwise sampling of grid data. Historically, variograms were sampled from point measurements [112]. All pairwise combinations of point observations were used to derive an empirical variogram. For dense spatial data, however, the millions of sampled locations yield trillions of possible pairwise combinations, which are not computationally feasible. Many studies have addressed this by selecting a random subset of data, typically a few thousand random points. This method remains inefficient for large grids, as pairwise sampling of a random selection of dense data does not sample equally across all spatial scales (Fig. S13a). The resulting variogram is poorly sampled in the short and long ranges relative to the middle ranges (Fig. S13c,e).

To remedy this, we introduce an approach that samples large and dense grid data by partitioning the space between a subset defined by a central disk and successive subsets of outer rings that share the same center (Fig. S13b). The pairwise sampling is only made between the central and outer subsets, and is repeated for several random center points across the grid. Pairwise samples that are drawn twice are removed to ensure independent sampling. Through this procedure, which we implemented in *scikit-gstat* [147], the variogram is sampled more equally across spatial scales, and the computation is more efficient for short and long ranges (Fig. S13d,f). Specifically, the same number of pairs is sampled for distances separated by a factor $\sqrt{2}$, which produces rings $\mathcal{R}$ of the same successive area A:

$$\begin{aligned} A(\mathcal{R}_{r,\sqrt{2}r}) &= A(\mathcal{D}_{\sqrt{2}r}) - A(\mathcal{D}_r) \\ &= \pi\left[(\sqrt{2}r)^2 - r^2\right] = \pi r^2, \end{aligned} \tag{S1}$$

where D_r is the disk of radius r and $\mathcal{R}_{r_1,r_2}$ is the ring of inside radius r_1 and outside radius r_2. Therefore, the distances are sampled equally in logarithmic binning (Fig. S13f).

Furthermore, we estimate our empirical variograms for 100 realizations and use these realizations to empirically estimate an uncertainty. We perform the pairwise sampling of each realization without constraints from the previous one due to the complexity of the pairwise sampling procedure. This implies that pairwise differences are not fully independent among realizations. In practice, this has a minor impact due to the billions of potential pairwise samples within the grid. Given the small percentage of pairwise samples computed per realization (typically $< 1\%$), we consider that the empirical variograms estimated for each realization are largely independent. We aggregate the empirical variograms by deriving the mean variance at each spatial lag and, assuming independence of the samples, compute its uncertainty as the standard error of the mean at each lag. This is possible because every realization estimates the empirical variogram for the same binning.

D. Effective number of samples in an area

We aim to characterize the effective number of samples, that is, the number of samples that are effectively independent considering spatial correlations. The number of effective samples is a function of the area A and the variogram model γ. To this end, we take the example of a spatial average of elevation $\overline{h}$ inside a study area A:

$$\overline{h} = \frac{\sum_{i=1}^{N} h_i}{N}, \tag{S2}$$

where N is the number of pixels in the study area A, and h_i is the elevation of a given pixel i.

We define the number of effective samples N_{eff} in the area A following the classical standard error formulation:

$$\sigma^2_{\overline{h}} = \frac{\overline{\sigma_h}^2|_A}{N_{eff}}, \tag{S3}$$

where $\overline{\sigma^2_h}|_A$ is the average variance of pixels i in the area A:

$$\overline{\sigma^2_h}|_A = \frac{1}{N}\sum_i \sigma^2_{h_i}. \tag{S4}$$

To express N_{eff}, we need to determine the uncertainty in the spatial average of elevation $\sigma_{\overline{dh}}$. Once a variogram model $\gamma_h(d)$ is defined to represent the spatial correlation of the data as a function of spatial lag d, the uncertainty of h over the area A is derived from the spatial average of its covariance $Cov(A) = \overline{\sigma^2_h}|_A - \gamma_h(A)$ over the area A:

$$\sigma^2_{\overline{h}} = \overline{Cov(A)} = \frac{1}{A^2}\iint_A \left(\sigma_h(x)\sigma_h(x') - \gamma_h(x-x')\right) dx\, dx', \tag{S5}$$

where dx and dx' sweep independently over the area A. Note that Eq. S5 is the continuous, integral version of Eq. 17.

A variogram model is composed of a range, which describes a correlation length, and a partial sill, which describes a correlated variance. We assume the absence of a variogram nugget term [112] that, to our knowledge, was not identified in DEM applications. The sum of partial sills amounts to the variance, which implies that the variogram tends toward $\overline{\sigma^2_h}|_A$ with increasing spatial lag d:

$$\begin{cases} \gamma_h(d) \in \left[0, \overline{\sigma^2_h}|_A\right], \\ \lim_{d\to\inf} \gamma_h(d) = \overline{\sigma^2_h}|_A. \end{cases} \tag{S6}$$

Consequently, a variogram model can be conveniently factorized by the average variance of the process in the area A:

$$\gamma_h(d) = \overline{\sigma^2_h}|_A \gamma_1(d), \tag{S7}$$

where $\gamma_1(d)$ is the variogram with unit sill, which corresponds to the correlation function $\rho(d)$ (Eq. 17) and only takes values between 0 and 1.

The uncertainty of the average elevation h over an area A is thus directly related to the dispersion variance [154], i.e. the double integral of the variogram over the area A:

$$\overline{\gamma_1(A)} = \frac{1}{A^2} \iint_A \gamma_1(x - x')\, dx\, dx' \,. \tag{S8}$$

By combining this term with Eq. S4, we have:

$$\begin{aligned} \sigma_{\bar{h}}^2 &= \frac{1}{A^2} \iint_A \sigma_h(x)\sigma_h(x')\,(1 - \gamma_1(x - x'))\, dx\, dx' \\ &\approx \overline{\sigma_h^2}|_A \cdot \left(1 - \overline{\gamma_1(A)}\right), \end{aligned} \tag{S9}$$

where the latter approximation is only valid if the variability of σ_h is distributed homogeneously in the area A, that is, without any dependence on spatial lag $d = x - x'$.

It follows that the effective number of samples N_{eff} is only a function of spatial correlations γ_1 and the area of integration A:

$$N_{eff}(A) \approx \frac{1}{1 - \overline{\gamma_1(A)}}. \tag{S10}$$

In particular, the effective number of samples is independent of the variance of the process σ_h.

E. Theoretical approximation for spatially contiguous spatial propagation

The propagation described by Eq. 17, or its continuous version Eq. S5, allows to derive uncertainties for the distribution of any spatial sample. However, its double-sum computation scales exponentially with the number of samples, resulting in trillions of calculations with millions of samples.

To remedy this, [65] introduced an approach to approximate the integral of the variogram integral for spatially contiguous areas. The shape of the area A is simplified to a disk of equal area. The integral $\overline{\gamma_1(A)}_{A=disk}$ is then computed circularly as a single aerial integral from the center point of the disk:

$$\overline{\gamma_1(A)}_{A=disk} = \frac{2\pi}{A} \int_{r=0}^{r=\sqrt{\frac{A}{\pi}}} \gamma_z(r)\, dr \,. \tag{S11}$$

While this integral can be computed exactly, the derivation of the analytical integration is complex [65]. This is especially the case when using a sum of several variogram models. Additionally, the disk simplification yields a conservative estimate (i.e. an estimate that is larger than it should actually be) once γ_1 is converted into an uncertainty with Eqs. S3 and S10). This is because the disk's center point has the shortest distance to other points falling within the disk and, thus, the largest cumulative correlated errors (Eq. 17). This simplification has even more deviation from the exact analytical solution when the shape of the area differs substantially from that of a disk (Fig. S16).

To mitigate these issues, we introduce a new approach inspired by [65]. We hold onto the concept of using single instances of aerial integration to numerically simplify the calculation. For this, we iterate over k randomly selected "center" points x_k of a subset $\mathcal{K}$ of the N points within the area A, and compute the average of the aerial integrals for each of these subset center points $\overline{\gamma_1(A)}_{sub}$:

$$\overline{\gamma_1(A)}_{sub} = \frac{1}{A} \overline{\int_A \gamma_1(x_k - x)\, dx|_{k \in \mathcal{K}}}. \tag{S12}$$

Discretized, and combined with Eq. S9, this corresponds to Eq. 18. The random iteration over several "center" points x_k ensures that the approximation captures the spatial variability of the shape of the area A. Indeed, using a single center point omits the distribution of points beyond the longest correlation range, since those have no correlation with the center point.

We perform the integration numerically for each iteration l. The computational efficiency of the approximation is well suited to large sample sizes with $O(K \cdot N)$ for a sample size N, instead of $O(N^2)$ for Eq. 17. We find robust results using 100 "center points" k for different shapes of areas (Fig. S16).

III. Supplementary Results and Discussion for the Northern Patagonian Icefield case study

We estimate the dispersion over stable and moving terrain by binning on (i) the quality of stereo-correlation, (ii) slope, and (iii) curvature (Figs. S6 and S7), where stable terrain is defined by non-glacierized terrain. We find a strong variability of dispersion with the quality of stereo-correlation, which is independent of that with terrain slope or maximum curvature. The relative difference between the dispersion on stable and moving terrain is small ($< 30\,\%$), although the dispersion on moving terrain is systematically larger (Figs. S6 and S7). This larger dispersion probably originates from the variability introduced by the quality of the SPOT-5 stereo-correlation, which is not considered in this analysis. The higher resolution of the SPOT-5 images (Table S1) better resolves the stable terrain, yet is still limited by the lack of texture on glacierized surfaces.

IV. Supplementary Figures

This section contains Figs. S1 to S21.

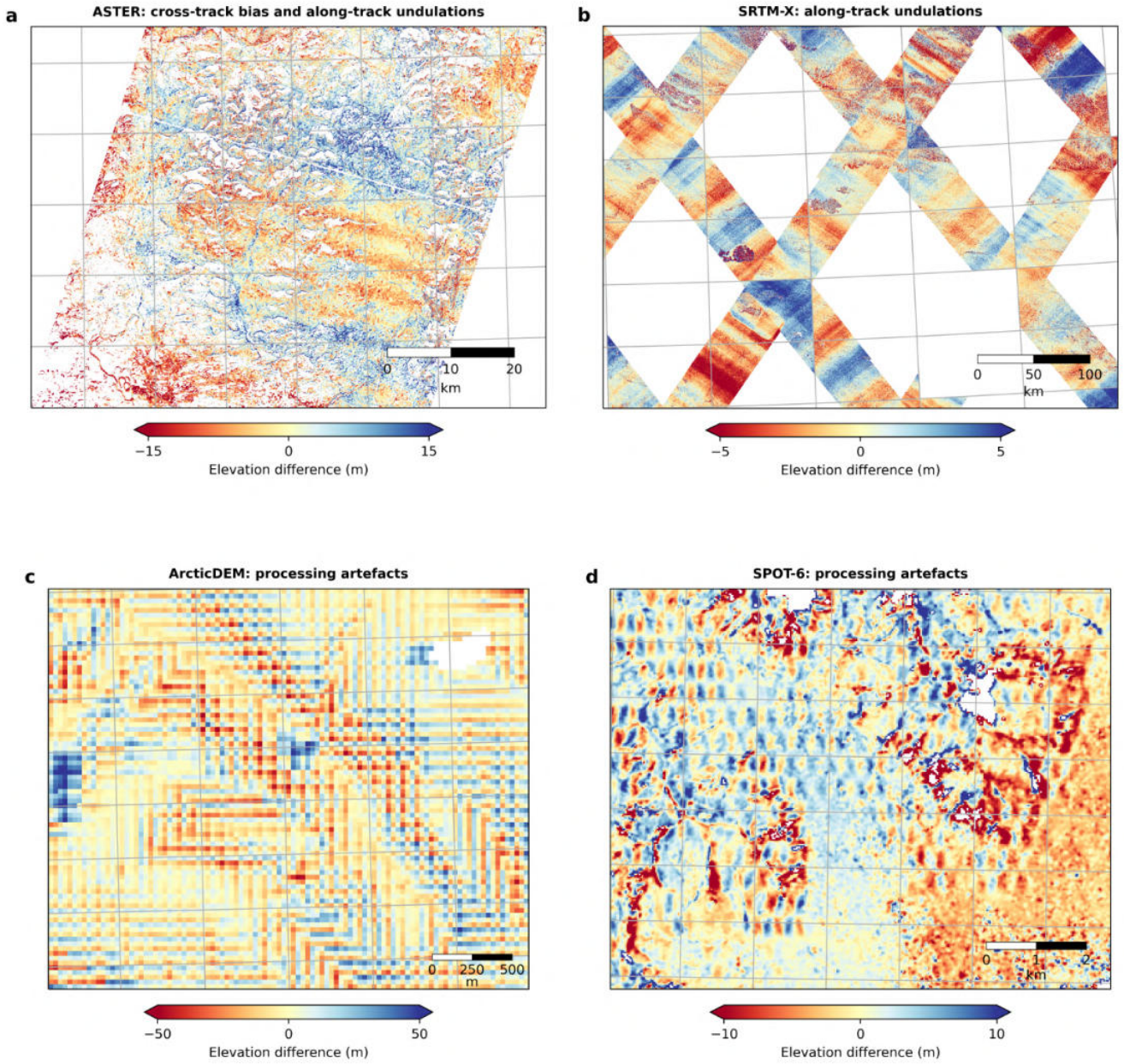

Fig. S1: Instrument undulations and processing artefacts in digital elevation models. a-d, Elevation differences between **(a)** a ASTER DEM and a TanDEM-X reference, **(b)** a SRTM X-band DEM and a NASADEM reference (i.e. SRTM C-band jitter-corrected), **(c)** a WorldView-2 DEM from ArcticDEM and a TanDEM-X reference, and **(d)**, a SPOT-6 DEM and the Copernicus 30 m DEM (i.e. gap-filled TanDEM-X). More details on DEMs are provided in Section I-B.

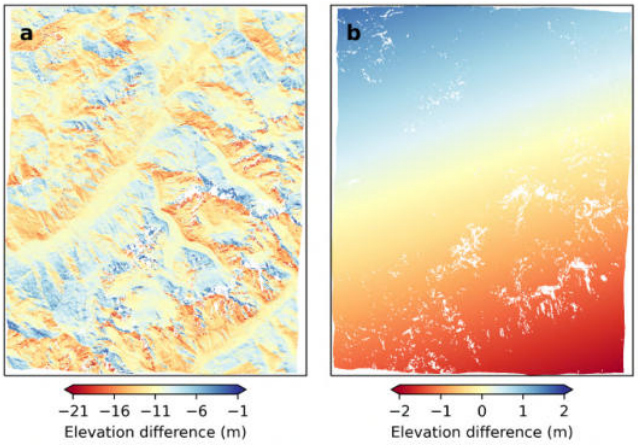

Fig. S2: Shift and tilt between the Pléiades DEM and the SPOT-6 DEM of the Mont-Blanc case study. a, Elevation differences of the 2 m east, 4 m north horizontal shift (about half a pixel) and 11 m vertical shift of the Pléiades DEM to the SPOT-6 DEM. Note that the colorbar is centered on this vertical shift. **b,** Elevation differences of the tilt between the Pléiades DEM and the SPOT-6 DEM.

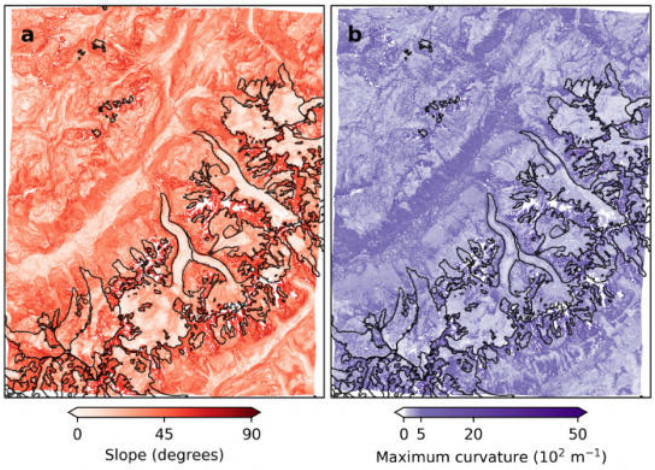

Fig. S4: Slope and maximum absolute curvature of the Mont-Blanc case study. a, Terrain slope after [143]. **b,** Maximum absolute curvature, i.e. pixel-wise maximum of the absolute profile curvature and the absolute planform curvature after [144]. Both are computed from the Pléiades DEM. Glacier outlines are shown in black.

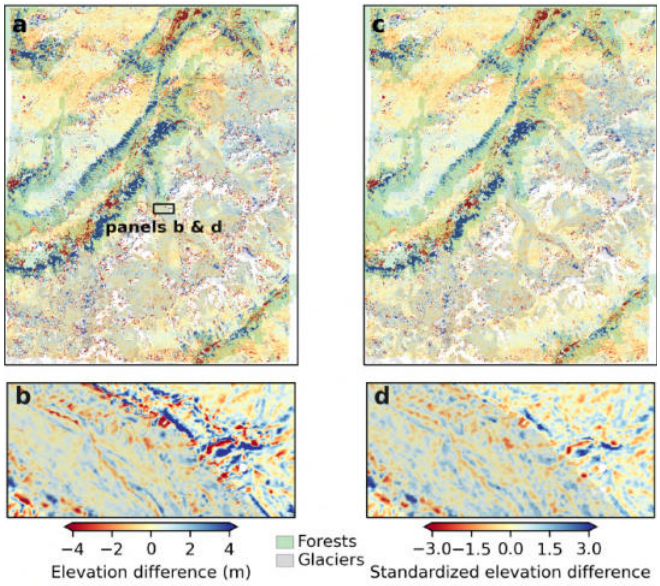

Fig. S3: Maps of elevation difference and standard score of the Mont-Blanc case study. a-d, Elevation differences after co-registration and tilt correction **(a-b)** before and **(c-d)** after standardization. Elevation differences are overlayed with glacierized terrain (gray) and forested terrain (green).

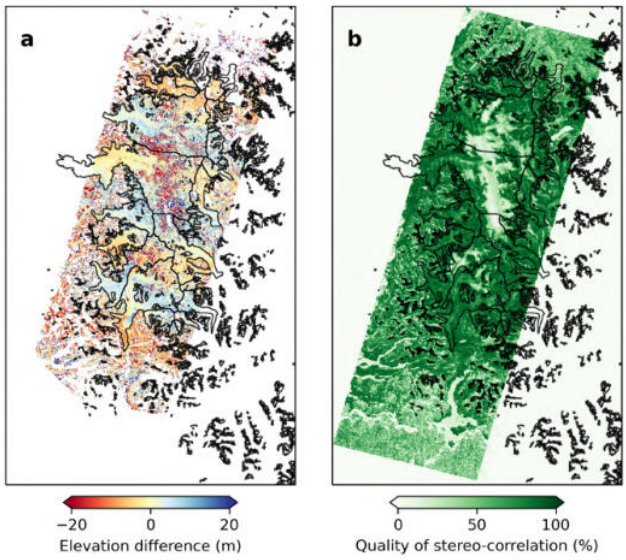

Fig. S5: Elevation differences for the Northern Patagonian Icefield case study. a, Elevation differences of the NPI case study (Supplementary Section I-A) after co-registration and tilt correction. **b,** Quality of stereo-correlation of the ASTER DEM, with low quality (values close to 0%) due to lack of texture. Glacier outlines are shown in black.

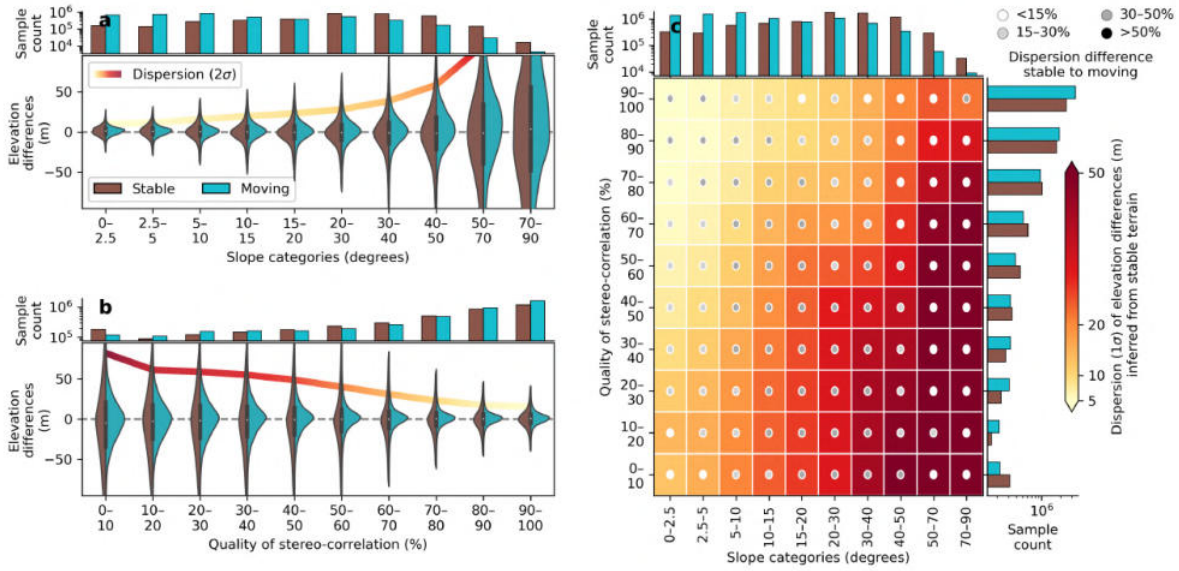

Fig. S6: Heteroscedasticity inference from stable terrain as a function of both slope and quality of stereo-correlation for the Northern Patagonian Icefield case study. a-b, Violin plots of elevation differences of the NPI case study (Supplementary Sections I-A and III) on stable and moving terrain by bins of **(a)** slope and **(b)** quality of stereo-correlation. Dispersion inferred from stable terrain is showed by a thick line with color matching other panels. Note the logarithmic scales of histograms. **c,** Heatmap of stable terrain dispersion for slope and quality of stereo-correlation. Bins with a relative dispersion difference between stable and moving terrain greater than 30% (dark gray and black dots) contain less than 12% of samples.

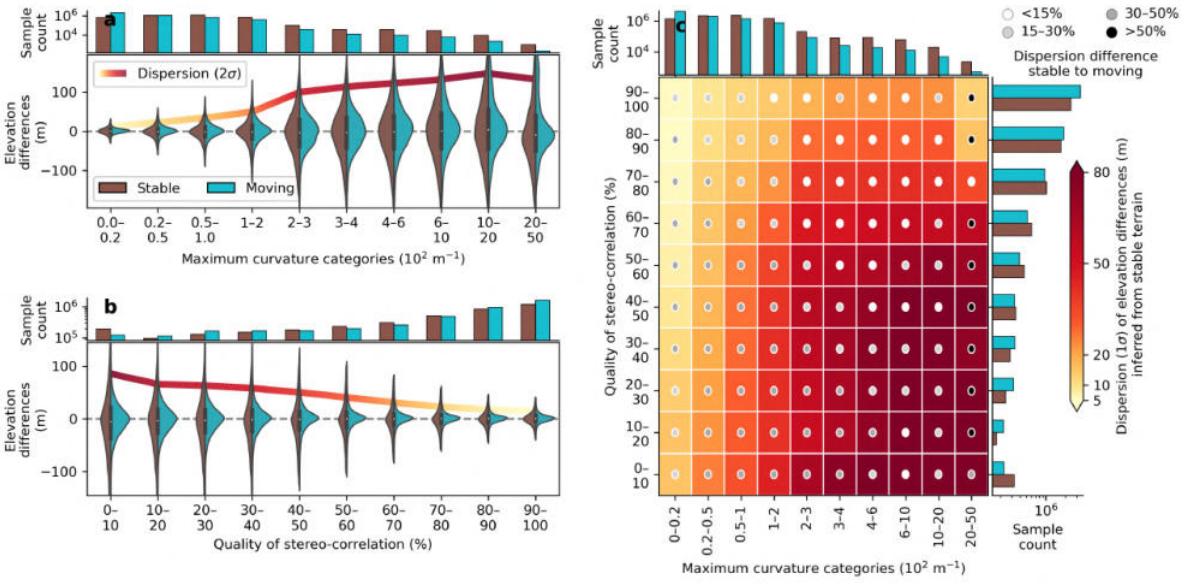

Fig. S7: Heteroscedasticity inference from stable terrain as a function of both curvature and quality of stereo-correlation for the Northern Patagonian Icefield case study. a-b, Violin plots of elevation differences of the NPI case study (Supplementary Sections I-A and III) on stable and moving terrain by bins of **(a)** curvature and **(b)** quality of stereo-correlation. Dispersion inferred from stable terrain is showed by a thick line with color matching other panels. Note the logarithmic scales of histograms. **c,** Heatmap of stable terrain dispersion for curvature and quality of stereo-correlation. Bins with a relative dispersion difference between stable and moving terrain greater than 30% (dark gray and black dots) contain less than 16% of samples.

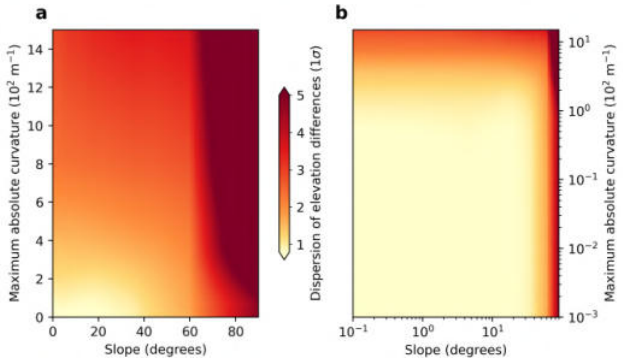

Fig. S8: Heteroscedasticity modelled as a bilinear interpolant of slope and maximum absolute curvature. a-b, Dispersion interpolated from the center bins of Fig. 3c, shown with **(a)** a linear scale and **(b)** a logarithmic scale.

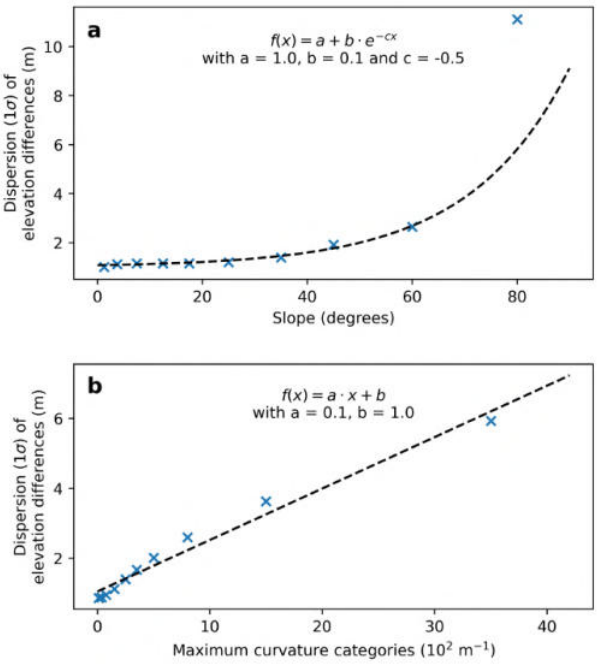

Fig. S9: Parametric modelling of elevation heteroscedasticity with slope and curvature. a, Exponential model fit between the dispersion and the slope. **b,** Linear model fit between the dispersion and the maximum absolute curvature. Both fits perform well and are more robust to smaller sample sizes than 2-dimensional binning. However, they will not capture the two-dimensional variability of the dispersion (Fig. 3).

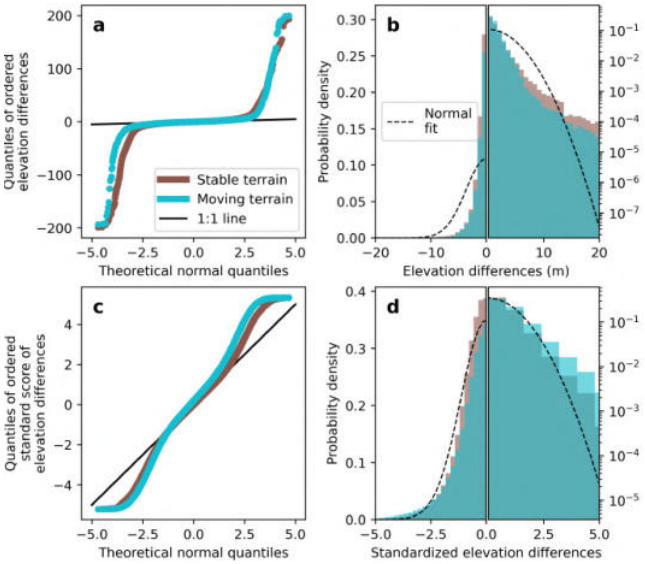

Fig. S10: Heteroscedasticity explains the departure of elevation errors from normality. a,c, Q-Q plots of elevation differences, **(a)** before and **(c)** after standardization by the heteroscedasticity of the Mont-Blanc case study with slope and maximum absolute curvature. Note the change in scale of the Y-axis. **b,d,** Normal distribution fit on probability density distribution of elevation differences **(b)** before and **(d)** after standardization. Note the logarithmic scale on the right side of the panels.

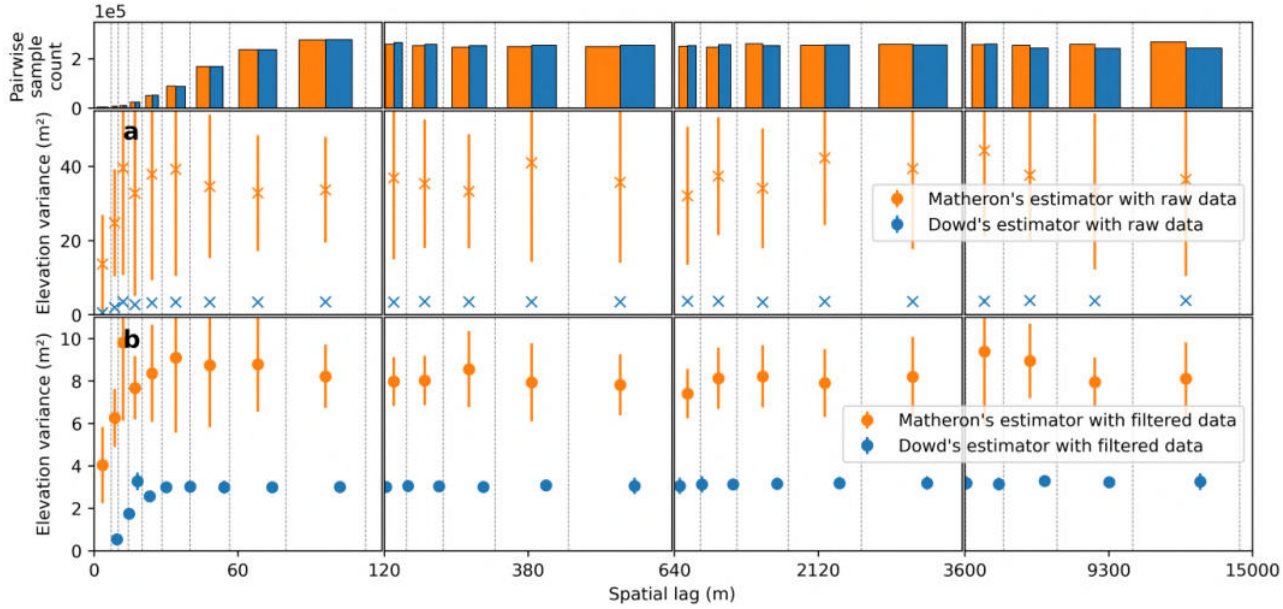

Fig. S11: Effect of estimator's robustness on variogram estimation. a-b, Empirical variogram of elevation differences for estimators by Matheron [148] and Dowd [146] **(a)** before and **(b)** after outlier filtering, with 1σ dispersion estimated by the standard deviation of 100 independent realizations. Both variograms are estimated directly on elevation differences, without standardization. **a,** A simple filtering of elevation differences greater than 500 m is performed. **b,** Elevation differences outside a 7 NMAD interval centered on the median are excluded, for each category of slope and maximum absolute curvature (Fig. 3).

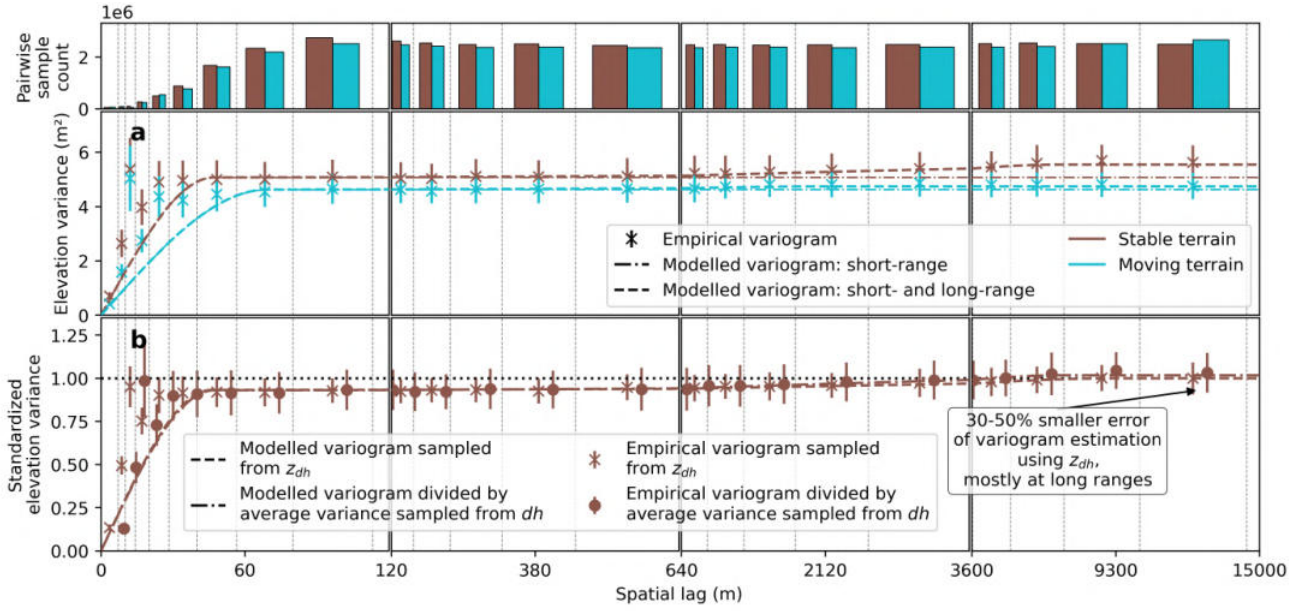

Fig. S12: Effect of standardization on variogram estimation. a, Empirical and modelled variograms of elevation differences without standardization. Variograms sampled from different terrains substantially differ, and thus standardization is required. **b,** Comparison of the empirical variogram on stable terrain sampled with standardized elevation differences (Fig. 5a) and sampled on elevation differences later divided by the average variance, as in panel **(a)**. The 1σ dispersion of the empirical variograms is shown, estimated by the standard deviation of 100 independent realizations. Both empirical variograms are estimated with Dowd's estimator [146] which reduces variability due to outliers, partly owing to heteroscedasticity. Estimating the variogram with standardized elevation differences reduces errors in variogram estimation by 30-50%.

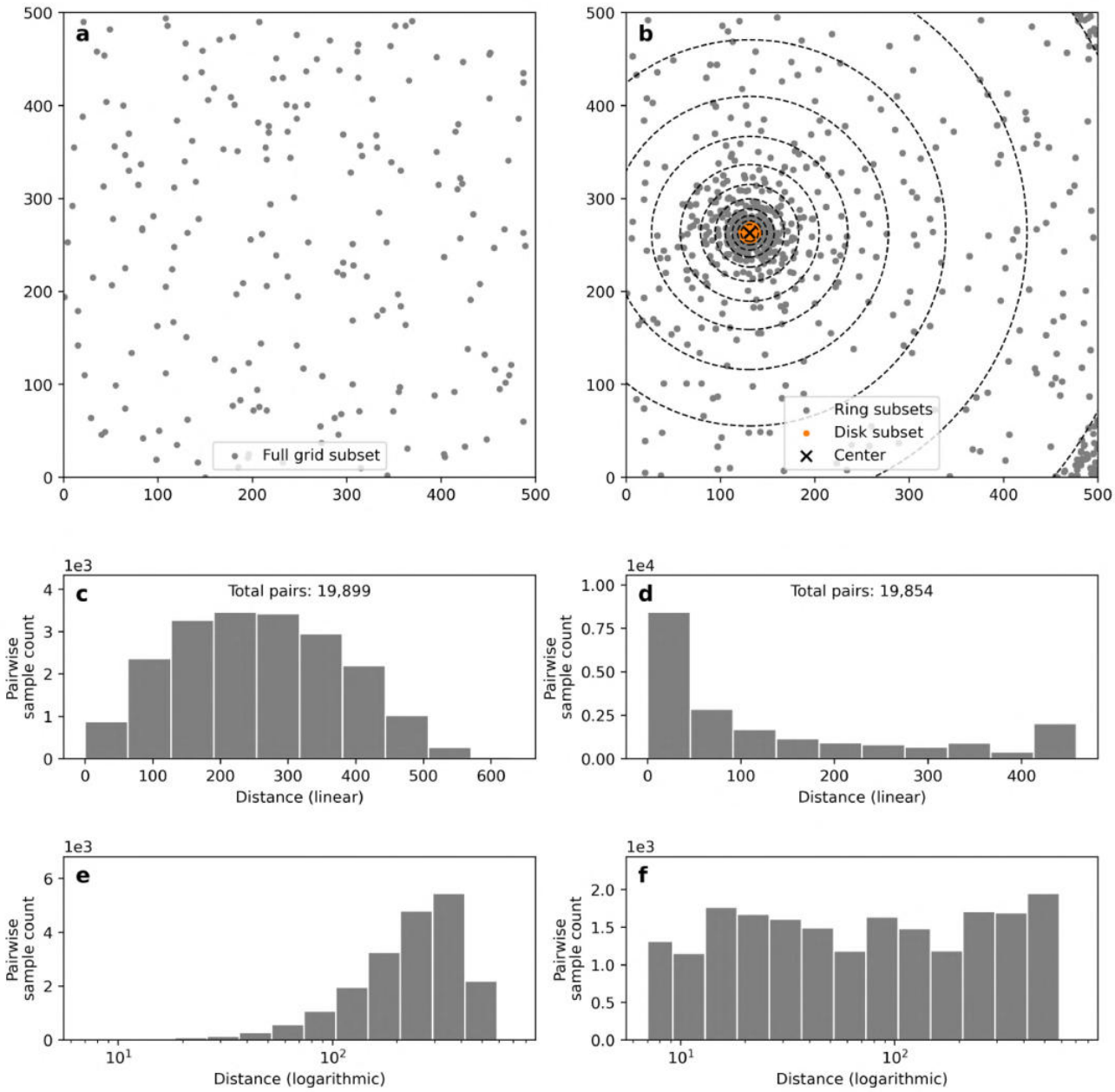

Fig. S13: Improved pairwise comparisons across spatial scales by iterative circular grid sampling. a-b, Random point sampling **(a)** within the entire grid and **(b)** between a disk and a subset of rings. **c-d,** Histogram of pairwise differences with linear distance for the sampling of pairwise differences of all points in **(a)** and between disk and ring points in **(b)**, for **(c)** and **(d)** respectively. **e-f,** Same as **(c)** and **(d)** but with distance on a logarithmic scale.

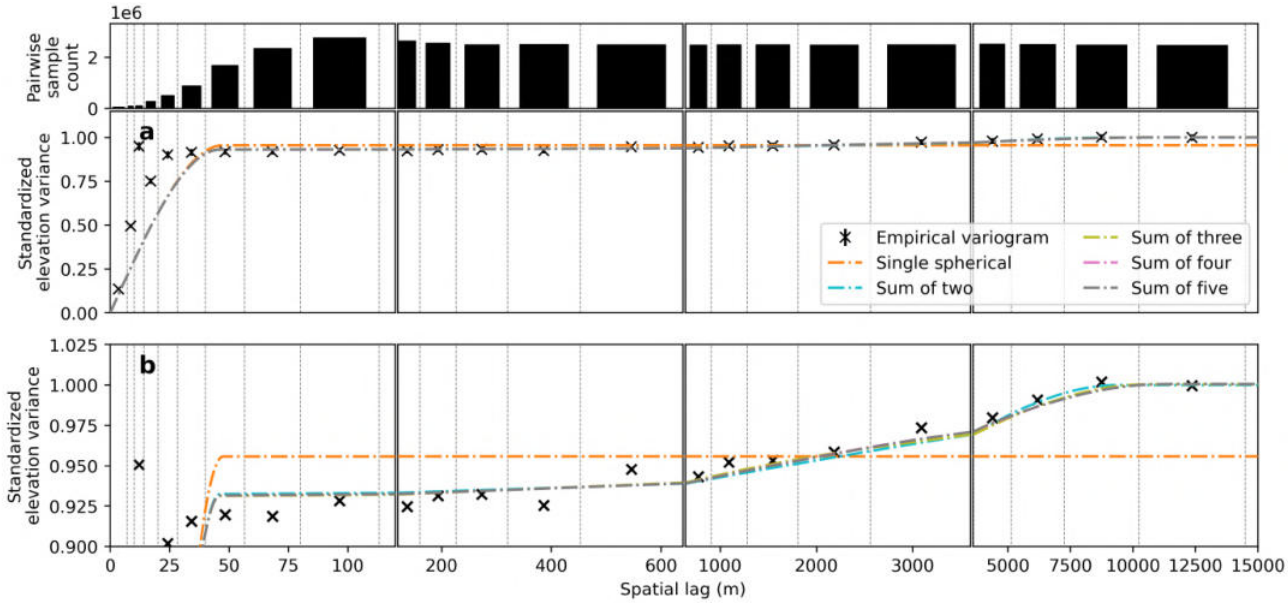

Fig. S14: Sensitivity of variogram fitting to the number of summed models. a, Empirical variogram and model fits for a sum of one to five spherical models for the Mont-Blanc case study. With a sum of two models, the second model fit has a range of 11.2 km. With a sum of three models, the third model has a range of 3.9 km. No improvement in the residual sum of squares is found when using a number of models greater than three (Table S2). **b,** Same as **(a)**, but enlarged near the variance of 1 to visualize the long-range fit.

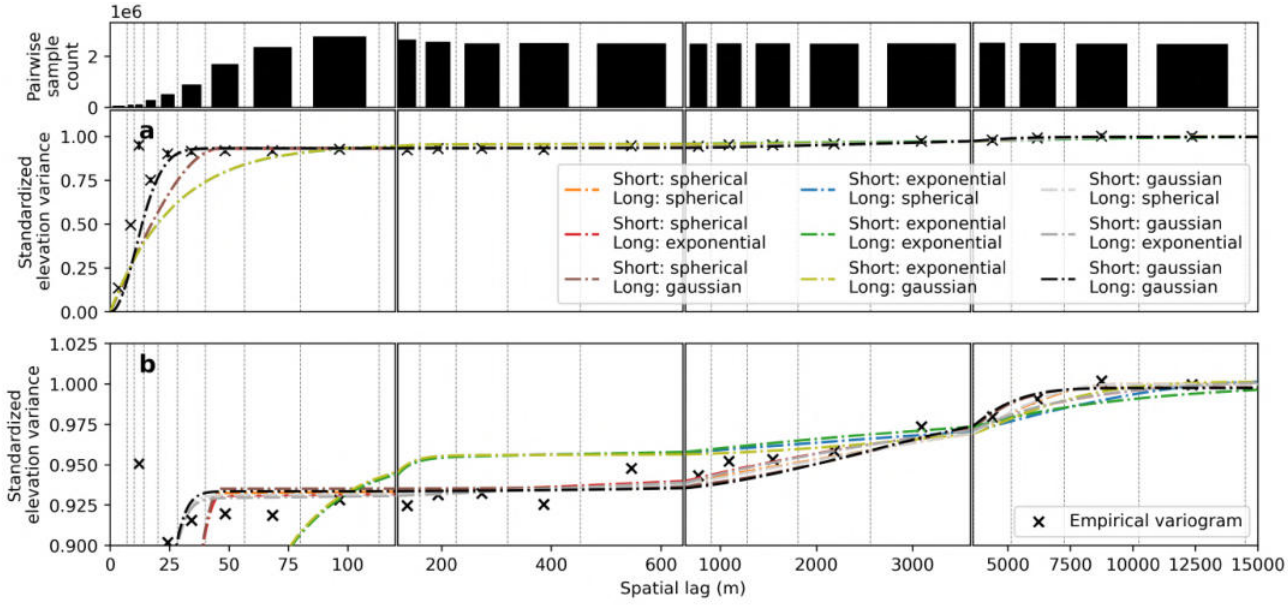

Fig. S15: Sensitivity of variogram fitting to model form. a, Empirical variogram and model fits for a sum of two models, using all possible combinations of spherical, exponential and gaussian models. The best fit at short ranges is found with a gaussian model (Table S3). The sum of residuals of squares evaluated for large lags shows that the spherical model provides a slightly better fit (Table S4). **b,** Same as **(a)**, enlarged near the variance of 1 to visualize the long-range fit.

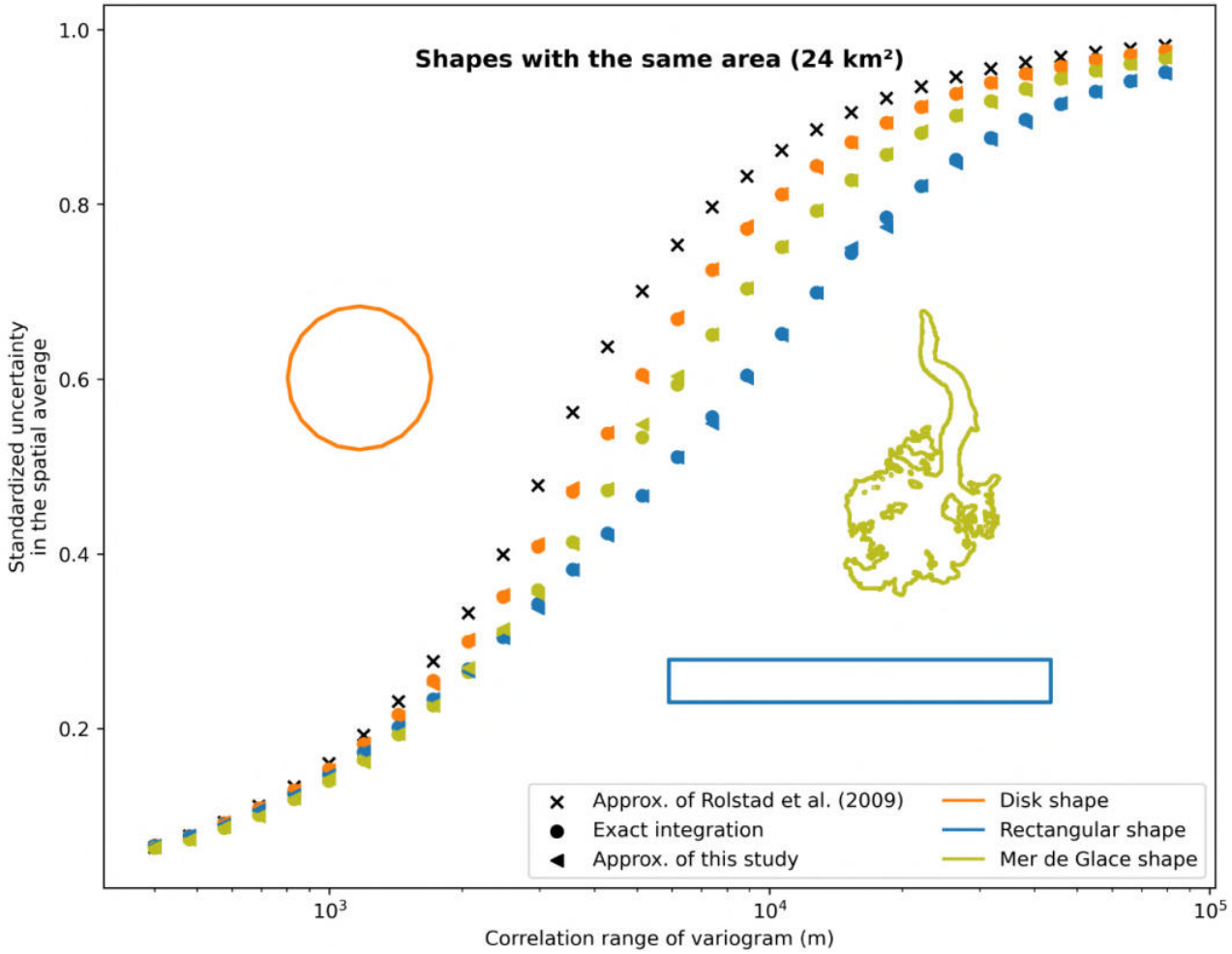

Fig. S16: Performance of theoretical approximations for spatial uncertainty propagation. Uncertainty in the spatial average based on the correlation range for a unit variance process. A spherical model is used as an example (similar results are found for all model types). The uncertainty is integrated over an area of 24 km² for a disk, a rectangle of aspect-ratio 9:1, and the Mer de Glace Glacier. The integration methods include Rolstad's approximation of Eq. S11 [65], the approximation of the present study of Eq. S12, and the exact integration of Eq. 17. The approximation of [65] yields the same result for all shapes, and is therefore only displayed in black. We use 100 random center points k for the approximation of the present study (Eq. S12), which shows good performance. To decrease the processing time for the exact solution, we perform the calculations at a grid resolution of 200 m. At the native resolution of 5 m, the exact integration of Eq. S11 requires about a trillion computations (3 TB of memory for pairwise distances).

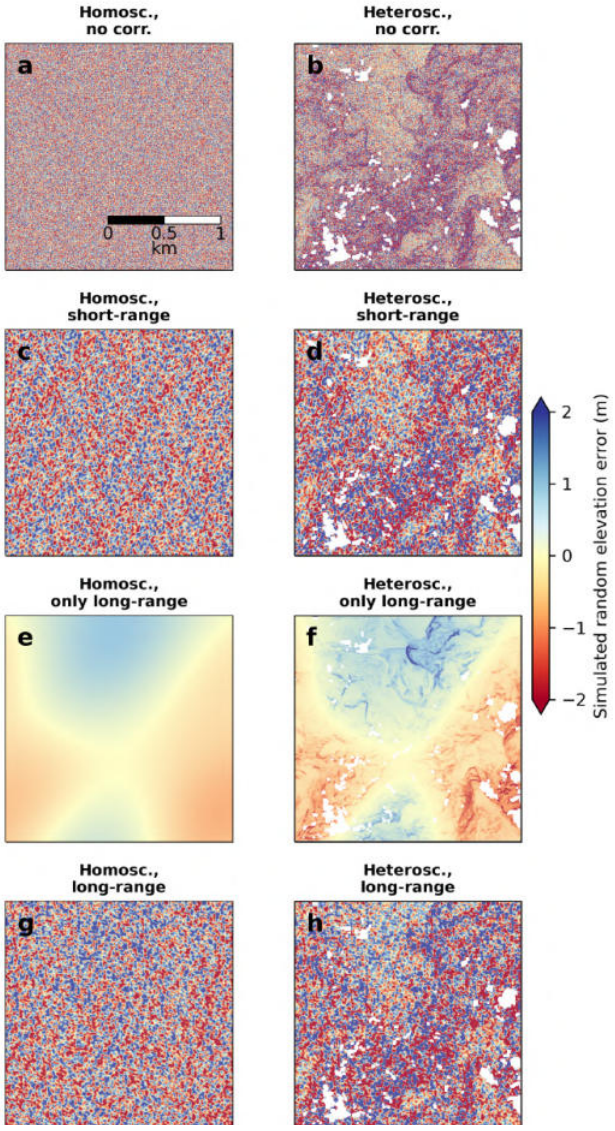

Fig. S17: Simulated elevation errors for different heteroscedasticity and spatial correlation scenarios. a-h, Single realization of a random error field around the Mont-Blanc summit for **(a,b)** a random pixel noise, **(c,d)** a short-range correlation of 30 m, **(e,f)** long-range correlations of 3.9 and 11.2 km and **(g, h)** the sum of short- and long-range correlations. The variance is computed as stationary for panels **(a,c,e,g)** using the average variance of stable terrain in the spatial subset, and non-stationary for panels **(b,d,g,h)** using the elevation heteroscedasticity with terrain slope and maximum absolute curvature.

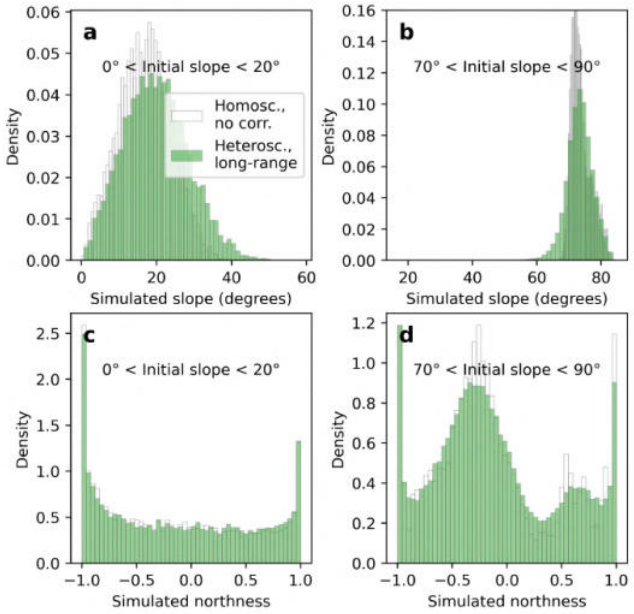

Fig. S18: Non-normality of the distributions of slope and aspect derived from simulated elevation errors. a-b, Distributions of simulated slopes for 200 realizations, aggregated for all pixels with an initial slope of **(a)** 0–20 degrees and **(b)** 70–90 degrees. **c-d,** Same for northness, the cosinus of aspect.

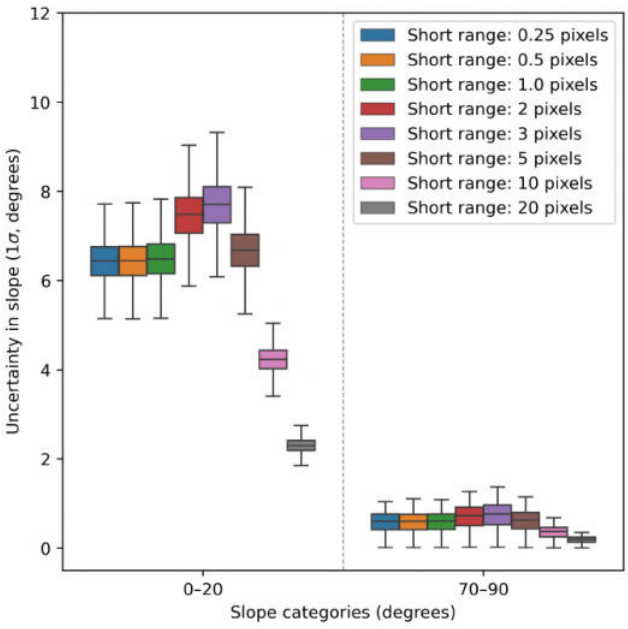

Fig. S19: Impact of varying short-range correlations near a 3x3 kernel size for slope uncertainties. Distributions of slope uncertainties for varying short-range correlation ranges from 0.25 to 20 times the pixel size. Boxes denote the interquartile range and whiskers extend to the whole distribution. Two category of slope, 0–20 degrees and 70–90 degrees, are illustrated from the Mont-Blanc case study (Fig. 6).

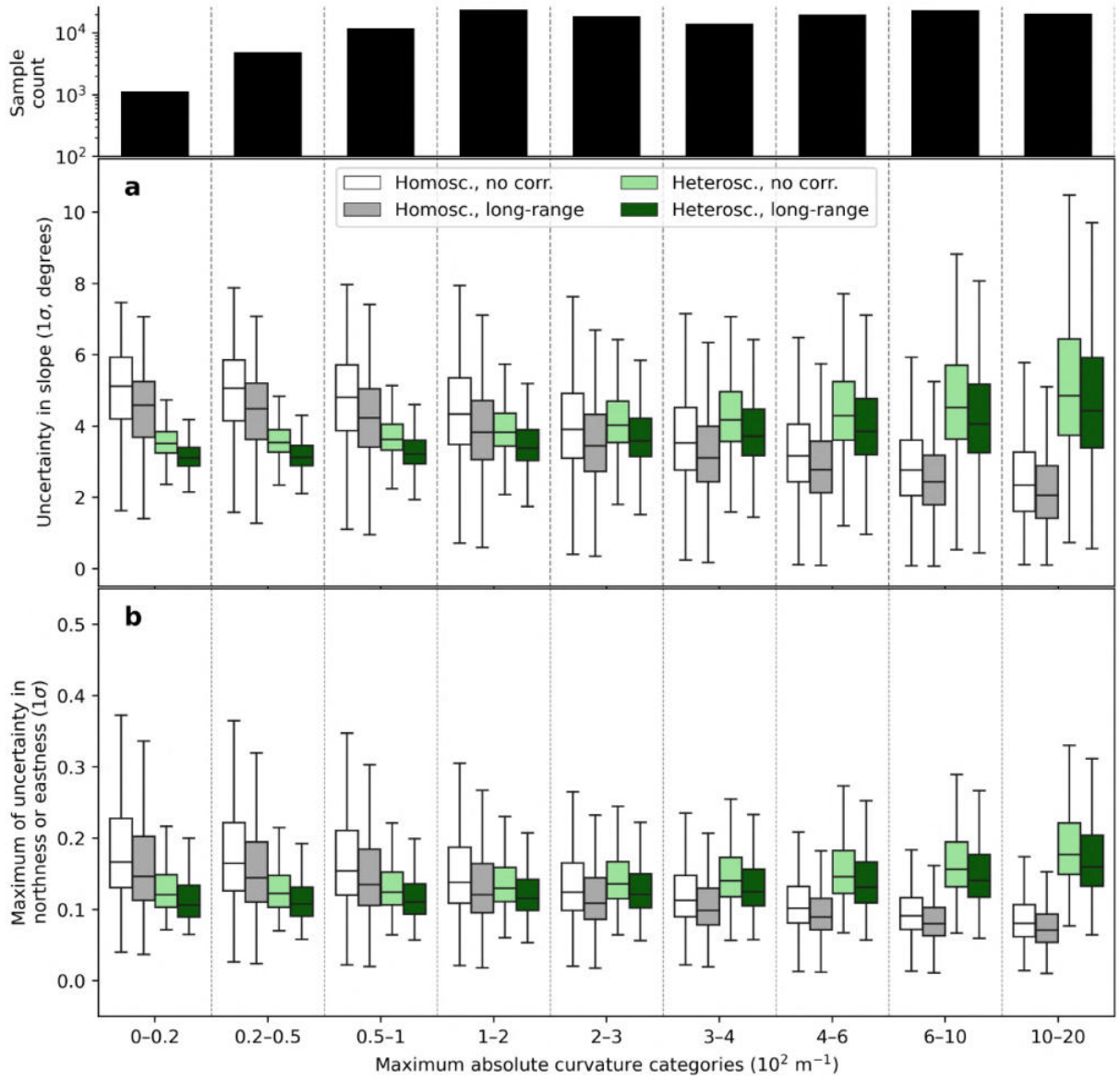

Fig. S20: Impact of maximum absolute curvature on uncertainty propagation to terrain slope and orientation. a-b, Distributions of slope and orientation uncertainties by category of maximum absolute curvature for each scenario, with boxes denoting the interquartile range and whiskers extending to the whole distribution.

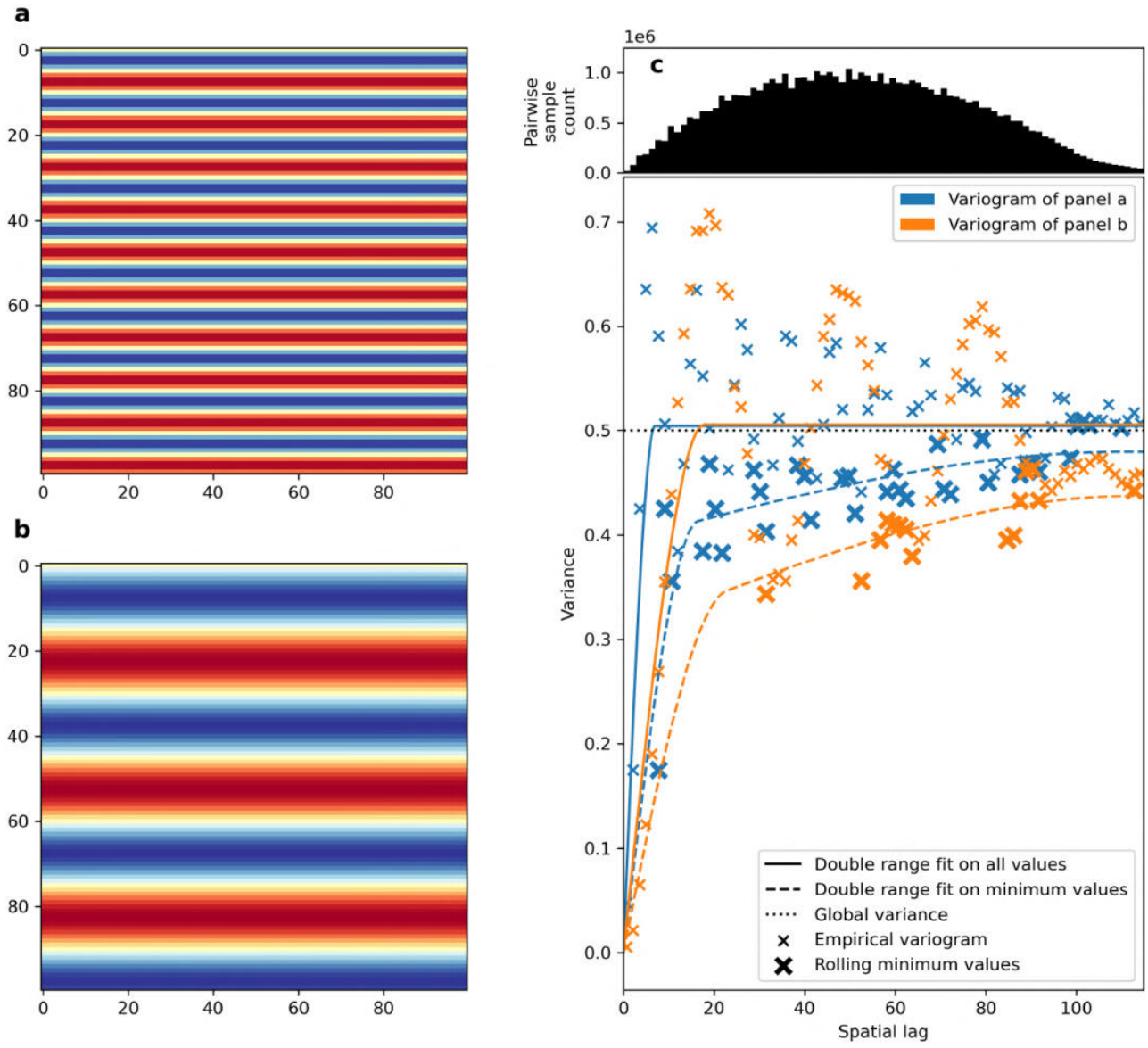

Fig. S21: Conservative variogram estimation for along-track undulations. a-b, Artificial sinusoidal undulation in the Y-axis direction, with unit amplitude and a **(a)** 10- and **(b)** 30-pixel frequency on a 100 pixel x 100 pixel grid. **c,** Empirical and modelled variogram of artificial sinusoidal undulations, using all pairs of samples. A fit with a sum of two variogram models is performed. Using all points of the empirical variogram, the fit converges to a single range variogram, which only captures the correlation range of the frequency of the undulation. Using minimum rolling values, the fit converges to two distinct correlation ranges. The first range matches the frequency of the undulation. The second range captures a longer-range correlation of swath length, here 100 pixels, owing to the fully correlated signal in the X-axis direction. The fit on minimum rolling values describes a conservative estimate of the correlation, i.e. the largest possible correlation between points.

V. Supplementary Tables

This section contains Tables S1 to S4.

TABLE S1: Nearly-simultaneous ASTER and SPOT-5 DEMs used for the Northern Patagonian Icefield case study.

Instrument	Acquisition time	Resolution of stereo-pair
ASTER	18/03/2012, 14:42 UTC-3	15 m x 15 m
SPOT-5	18/03/2012, 14:40 UTC-3	5 m x 10 m

TABLE S2: Goodness of fit for a sum of one to five spherical models. Residual sum of squares (RSS) of model fit for fits of one to five summed spherical models to the empirical variogram of the Mont-Blanc case study on stable terrain (Fig. S14). The RSS is derived for all lags, lags shorter than 1 km, and lags longer than 1 km. For a sum of two models, the second range found is 11.2 km, which substantially reduces the RSS. The addition of a third range of 3.9 km help further describe the long-range form of the empirical variogram, shown by the slight improvement in RSS for large lags. Additional models do not improve the RSS.

Number of summed spherical models	RSS for all lags	RSS for lags $\leq$ 1 km	RSS for lags $>$ 1 km
1	0.41	0.40	0.01014
2	0.39	0.39	0.00009
3	0.39	0.39	0.00005
4	0.39	0.39	0.00005
5	0.39	0.39	0.00005

TABLE S3: Goodness of fit for a sum of two model types. Residual sum of squares of model fit for two summed models. All combination of spherical, exponential and gaussian model types for short- and long-range are tested (Fig. S15). The RSS is computed for all lags. Most of the RSS arises from differences at small lags. Therefore, we use it as a criterion to select the best short-range model, here the gaussian model.

Model types	Long: spherical	Long: exponential	Long: gaussian
Short: spherical	0.39	0.39	0.39
Short: exponential	0.54	0.54	0.54
Short: gaussian	0.20	0.20	0.20

TABLE S4: Goodness of long-range fit for a sum of two model types. Same as Table S3, with residual sum of squares computed only on lags larger than 1 km. We use the RSS computed only for large lags to select the best performing models for long ranges, here the spherical model.

Model types	Long: spherical	Long: exponential	Long: gaussian
Short: spherical	0.00009	0.00009	0.00025
Short: exponential	0.00033	0.00039	0.00013
Short: gaussian	0.00011	0.00084	0.00030

Appendix B: Supplementary Information of *Heterogeneous changes in western North American glaciers linked to decadal variability in zonal wind strength*

Geophysical Research Letters

Supporting Information for

Heterogeneous changes in western North American glaciers linked to decadal variability in zonal wind strength

B. Menounos[1*], R. Hugonnet[1,2], D. Shean[3], A. Gardner[4], I. Howat[5], E. Berthier[2], B. Pelto[1], C. Tennant[1], J. Shea[1], Myoung-Jong Noh[5] , F. Brun[6], A. Dehecq[4]

[1]University of Northern British Columbia, Natural Resources and Environmental Studies Institute and Geography, Prince George BC, V2N 4Z9, Canada

[2]LEGOS, Université de Toulouse, CNES, CNRS, IRD, UPS, 31400 Toulouse, France

[3]Dept. of Civil and Environmental Engineering, University of Washington, Seattle, WA, 98195 USA

[4]Jet Propulsion Laboratory, California Institute of Technology, Pasadena, CA 91109, USA

[5]School of Earth Sciences and Byrd Polar Research Center, The Ohio State University, 1090 Carmack Road, Columbus, OH, USA

[6]Univ. Grenoble Alpes, CNRS, IRD, Grenoble INP, IGE, F-38000 Grenoble, France

Contents of this file

Introduction

Here we provide additional details that relate to the data used in our study and associated methods.

1 Data sources

We evaluate the reliability of our mass change estimates to those calculated from independent DEMs generated for glaciers and icefields across the southern latitudes of British Columbia (Fig. S1). These sites were chosen because we have access to optical imagery and airborne laser altimetry data. For several sites we also evaluated satellite-based trends in mass change against in situ mass balance observations (Fig. S1).

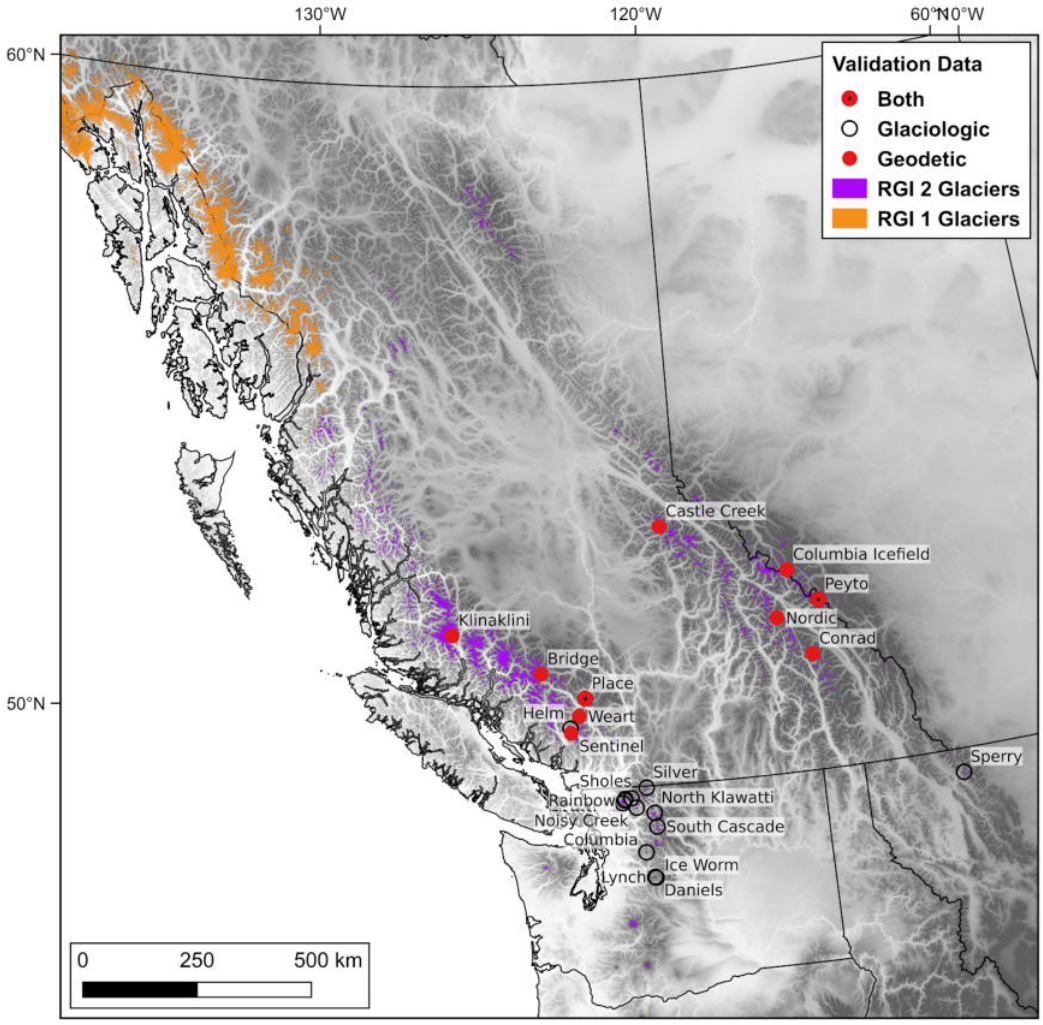

Figure S1. Sites with independent geodetic data and surface mass balance records.

1.1 Geodetic data and methods

Site[1]	*Location*	*Data sources*	*GSD*[2] *[m]*	*Number of sampled glaciers*[3]	*Area of all glaciers (area of named glacier) [km²]*
Place	South Coast Mountains	Lidar (08/2006) Lidar (09/2018)	1	7	4.9 (3.0)
Sentinel	South Coast Mountains	Lidar (08/2006) Lidar (09/2018)	1	10	22.3 (2.0)
Bridge	South Coast Mountains	Lidar (08/2006) Lidar (09/2017)	5	12	111.9 (82.9)
Weart	South Coast Mountains	Lidar (08/2006) Lidar (08/2018)	1	9	8.1 (12.8)
Klinaklini	South Coast Mountains	SPOT HRS (10/2009) Lidar (09/2017)	40	27	627.1 (469.9)
Columbia Icefield	Southern Rocky Mountains	SPOT5 (08/2009) Lidar (09/2017)	20	83 (40)[4]	213.3 (176.2)
Castle Creek	Southern Interior Ranges	ATPhoto[5] (08/2005) Lidar (11/2017)	5	3	12.0 (9.7)
Peyto	Southern Rocky Mountains	ATPhoto (08/2005) Lidar (09/2017)	5	3	12.6 (9.7)
Conrad	Southern Interior Ranges	ATPhoto (07/2005) Lidar (09/2017)	5	15	22.1 (16.9)
Nordic	Southern Interior Ranges	ATPhoto (08/2004) Lidar (09/2017)	5	6	5.6 (4.4)

Notes: 1. The site name is that of one of the main glaciers in the scene.
2. Ground Sampling Distance (m). Final resolution used is the lowest resolution of the two data sources.
3. Number of glaciers covered by the scene (> 80% area).
4. The Columbia Icefield is considered as the aggregation of 40 glaciers.
5. Aerially-triangulated imagery.

Table S1. Details of geodetic data sites used in this study.

1.1.1 Airborne laser altimetry

We performed repeat airborne laser altimeter surveys for key glaciers in western Canada (Fig. S1). The earliest surveys used an infrared (1064 nm) laser and inertial measurement unit (IMU) described elsewhere (Hopkinson & Demuth, 2006). Surveys between 2014-2015 were completed with a Riegl 580 (1060 nm) and Applanix PosAV IMU. Surveys completed between 2016-2018 used a Riegl Q780 full waveform scanner and Applanix PosAV IMU. For all post 2006 surveys, LiDAR and flight trajectory were processed with vertical and horizontal positional uncertainties better than ±15 cm (1σ). Average point density for the LiDAR surveys were typically 1-2 laser shots m^{-2} with an effective sampling diameter of 10-20 cm. We classified all of the LiDAR data into ground and non-ground laser returns, with the latter ones being subsequently gridded into 1 m bare earth Geotiffs.

1.1.2 Aerial triangulated imagery

For some glaciers in British Columbia (Table S1), we also used digital or digitally scanned aerial photography flown with dedicated IMUs. Camera positions were available from the Province of British Columbia either through aerial triangulation using established ground control points or as approximate photo centers. In either case we constructed DEMs using commercial software (Agisoft version 1.4.4) to yield 1 m DEMs.

1.1.3 SPOT DEMs

In several cases we also had access to SPOT HRS DEMs (product V2). These DEMs were acquired as part of the SPIRIT campaign (Korona et al., 2009). One of these DEMs covered most of the Heiltskuk Icefield from which Klinaklini Glacier flows (Fig. S1). Mass change from this icefield was previously studied by others (Schiefer et al., 2007; Tennant et al., 2012; VanLooy & Forster, 2008).

We used the mask available with the SPOT HRS data (40 m) to clip poor quality data from the DEM (clouds and failed elevations). We also used two targeted SPOT 5 scenes acquired in August, 2009 for the Columbia Icefield (Tennant & Menounos, 2013). These scenes were processed into a DEM (20 m) in PCI Orthoengine (ver. SPI 2017-09-06) using ground control points collected from the laser altimetry data described below. We used the same data described for the satellite DEM analysis to mask out unstable terrain.

1.2. Glaciological Data

We assembled glaciological records (SMB) from sites within RGI Region 2 (RGI02:Table S2) as validation and comparison data with ASTER-derived mass

change rate estimates. All data were obtained through the World Glacier Monitoring Service - WGMS (Zemp et al., 2017) or through personal communication. Glaciological (surface mass balance records) from RGI02 originate from the Cascade Range of Washington, and the Southern Coast Mountains of BC. In Canada, we draw upon the work of the Geologic Survey of Canada (GSC) at the Peyto Glacier in the Canadian Rockies, as well as Helm and Place glaciers in the Southern Coast Mountains (Demuth & Keller, 2006; Moore & Demuth, 2001; Young, 1981). In the North Cascades of Washington and in Glacier National Park, we draw upon the data of the United States Geological Survey (USGS: (Josberger et al., 2007; Krimmel, 1999), the North Cascades Glacier Climate Project (Pelto & Brown, 2012; Pelto, 1996) and the National Park Service (Clark et al., 2017; National Park Service et al., 2017; Pelto & Riedel, 2001).

The GSC has monitored surface mass balance of Peyto and Place glaciers since 1965, and the Helm Glacier since 1977. The GSC reports glaciological net balance (B_a) as a function of winter balance (B_w) and summer balance (B_s) until 1995 in the case of Peyto and Place, and 1989 in the case of Helm (Zemp et al., 2017). It is unclear whether current reported mass balance is calculated from annual balance (B_a) alone or still as a function of B_w and B_s. The Peyto, Place and Helm glaciers are WGMS reference glaciers (Zemp et al., 2017).

The National Park Service has monitored the Noisy Creek, North Klawatti, Silver, and Sandalee glaciers within North Cascades National Park from 1993 to present. They use a two-season stratigraphic approach to calculate mass balance as a function of glacier mass gain (B_w) and glacier mass loss (B_s). They follow the procedures of the USGS-Water Resources Division on the South Cascade Glacier (Krimmel, 1997; Meier & Tangborn, 1965). Point mass balances are direct field measurements of winter accumulation and summer melt at one location. For both winter and summer balances, the measurement points are typically located at ablation stake sites. For a single glacier there are typically four to five sites corresponding with the number of ablation stakes. Detailed methods can be found elsewhere (National Park Service et al., 2017).

The North Cascade Glacier Climate Project (NCGCP) monitors glaciers throughout the North Cascade Range of Washington. Since 1984, NCGCP has monitored B_a at 9-10 glaciers (Pelto 1996; Pelto and Riedel 2001; Pelto and Brown 2012). The Columbia, Daniels, Ice Worm, Lower Curtis, Lynch, and Rainbow Glacier have a 35-year record. The Rainbow and Columbia glaciers are WGMS reference glaciers (Zemp et al. 2017). In 1990, Easton Glacier and Sholes Glacier were added to the annual balance program and now have a 29-year record.

NCGCP measures glacier mass balance near the time of minimal mass balance at the end of the water year, using a fixed date method. Measurements are made at the same time each year using the same methods from early August to mid-August and again in late September near the end of the ablation season. Any additional ablation that occurs after the last visit to a glacier is measured during the subsequent hydrologic year. NCGCP methods emphasize surface mass balance measurements with a relatively high density of sites on each glacier (>100 sites

km^{-2}), consistent measurement methods, applied on fixed dates, at fixed measurement locations with consistent supervision (Pelto 1996; Pelto and Riedel 2001; Pelto and Brown 2012). The use of a high measurement density and consistent methods generates errors resulting from an imperfectly representative measurement network that are largely consistent and correctable, the error range has been estimated at between 100 and 150 kg m^{-2} yr^{-1}.

The USGS has been studying the South Cascade Glacier since 1959 (Meier and Tangborn 1965; Krimmel 1996), which is a WGMS reference glacier.

For all sites, average annual glaciological mass balance rates for available records between 2000 and 2018 were calculated. A conservative error of 300 kg m^{-2} yr^{-1} was applied to all glaciological B_a estimates (Cogley et al., 1996; Zemp et al., 2013), and ASTER/WorldView error estimates are taken from the uncertainty analysis (Figure S2).

2 Detailed elevation trend methodology

Below, we detail our workflow (Figure S2) we used to extract trends in elevation for WNA glaciers. Our methods stem from the methodology first developed by Berthier et al. (2016) and later refined by Brun et al. (2017).

2.1 Data sources used in trend analysis

First, we downloaded all day-only ASTER L1A granules within 1x1 degree tiles with a maximum cloud coverage of 95% from NASA EarthData (https://earthdata.nasa.gov/). We selected 1x1 degree tiles within WNA that contained more than 5 km^2 of ice as defined in the Randolph Glacier Inventory (v. 6.0). Mount Shasta was also included in our selection yielding 90 tiles. Collectively, these granules covered 99.5% of the ice area of WNA.

We processed raw ASTER L1A scenes with the NASA Ames Stereo Pipeline (ASP) 2.6.1 using high performance computing facilities at the University of Northern British Columbia and at LEGOS (parameters used for DEM generation are available upon request). These ASTER DEMs were supplemented by DEMs generated from very high resolution (0.5 m) optical stereo imagery from Worldview 1-3 satellite campaigns (2010 to present) and Pleiades (2015) for glaciers in Garibaldi Provincial Park (subregion 2) and Nahanni National Park (subregion 6). Unlike ASTER, these sub-meter optical satellite campaigns began in 2010 with a median acquisition date of 2014 for the scenes utilized in this study. We also included DEMs from the ArcticDEM (release 6) for Nahanni National Park (subregion 6) where the number of recent (post-2009) ASTER DEMs were low. These data do not appear to temporally bias our results, but their inclusion reduces spatial gaps at highest elevations for some of the largest icefields of the study.

Glacier	*Area [km^2]*	*ASTER/WV/Pleiades Ba [kg m^{-2} yr^{-1}]*	*Glaciological [kg m^{-2} yr^{-1}]*	*Period of comparison (summer to summer)*
Lower Curtis (LC)	0.56	-810 ± 250	-1050 ± 300	2000-2017
Rainbow (RB)	2.38	-450 ± 120	-760 ± 300	2000-2017
Peyto (PY)	9.68	-800 ± 240	-1100 ± 300	2000-2017
Place (PL)	3.02	-1040 ± 190	-950 ± 300	2000-2017
Lynch (LY)	0.88	-80 ± 170	-850 ± 300	2000-2017
Ice Worm (IW)	0.19	-200 ± 330	-960 ± 300	2000-2017
Columbia (CB)	0.80	-1160 ± 210	-800 ± 300	2000-2017
Noisy (NY)	2.81	-630 ± 120	-720 ± 300	2000-2016
Easton (ES)	2.88	-340 ± 100	-760 ± 300	2000-2017
Daniels (DA)	0.44	10 ± 230	-790 ± 300	2000-2017
Sholes (SH)	1.18	-320 ± 140	-880 ± 300	2000-2017
Helm (HE)	0.97	-1180 ± 240	-1410 ± 300	2000-2017
Silver (SI)	0.77	-370 ± 190	-410 ± 300	2000-2016
North Klawatti (NK)	1.76	-540 ± 150	-800 ± 300	2000-2016
South Cascade (SC)	2.92	-140 ± 120	-380 ± 300	2000-2012
Sperry (SP)	1.27	100 ± 190	-450 ± 300	2004-2017

Table S2: Average ASTER/Worldview geodetic and glaciological mass balance rates for monitoring sites in western North America over the period 2000-2017

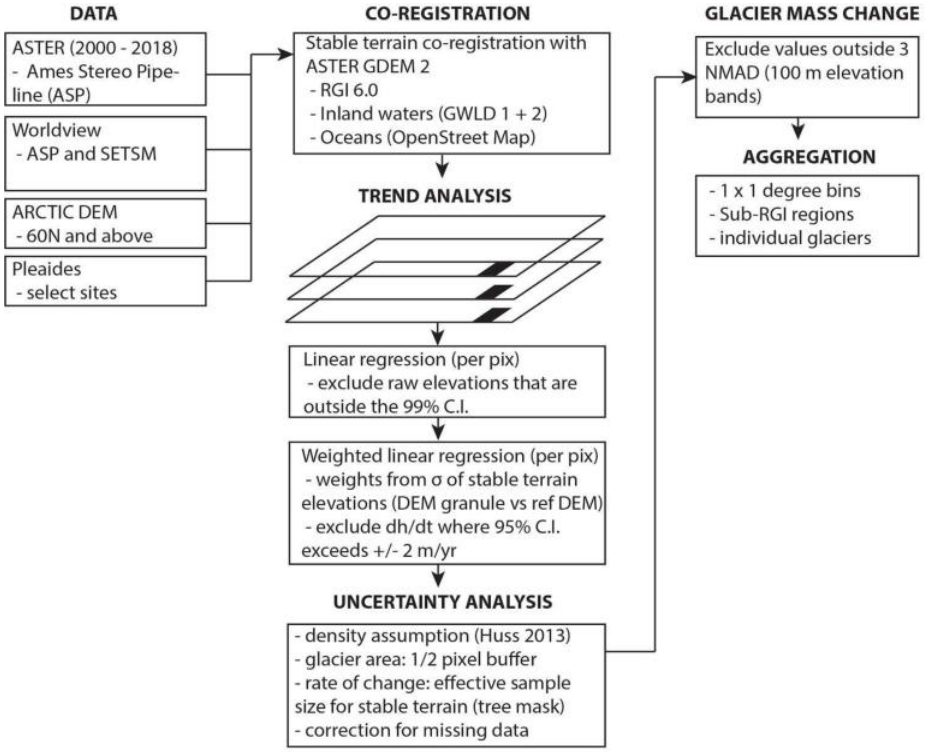

Figure S2. Workflow used to process satellite imagery used in this study.

2.2 Coregistration

Excluding unstable terrain we coregistered all DEMs to the GDEM2 (Tachikawa et al., 2011) using the relation between elevation difference and terrain aspect (Nuth & Kääb, 2011). We then corrected the ASTER DEMs for the across-track, along-track and curvature bias by fitting fifth-order polynomials to the elevation difference on stable terrain (Berthier et al., 2016). Unstable terrain was mapped using the intersection of the following inventories: RGI 6.0 for ice cover, the Global Land and Water Database was used to map inland water bodies, and OpenStreetMapData water polygons for the coastline. Attempts to co-register DEMs using only non-vegetated terrain yielded poor results, presumably because the co-registration method requires large-scale topographic features for success. We used vegetation masks to later isolate stable terrain for error analysis.

2.3 Trend analysis

To filter elevation outliers before the final weighted least squares (WLS) regression, an initial ordinary least squares (OLS) regression is performed for each given map coordinate. All elevation values lying outside the 99% confidence interval (on the elevation) for this first OLS fit are removed. Then, we assess the confidence in our derived dh/dt values (i.e. slope of the final fit) by deriving the 95% confidence

interval (on the slope) in the WLS. If this interval is wider than ±2 m yr^{-1}, those dh/dt values are removed from subsequent analysis (mass balance and uncertainty estimates). To minimize the impact of outliers on the estimate of volume change, we also removed any dh/dt values that lie outside ±3 times the normalized median absolute deviation (NMAD) of all dh/dt estimates for 100-m elevation bins using all valid data in the 1x1° tile.

In addition to glaciers, our trend analysis also reveals elevation change in areas adjacent to ice masses that, based on visual inspection, reflect unmapped debris-covered ice, ice bodies missed in glacier inventory mapping (Bolch et al., 2010), regions prone to landsliding (Roberti et al., 2017), sites of current mineral extraction and major changes in forest cover (logging and regrowth).

2.4 Uncertainty analysis

Our results are subject to both random and systematic errors typical of studies that employ geodetic methods to estimate glacier mass change. We follow the uncertainty analysis and terminology from Brun et al., (2017) and explain refinements made in our approach. One of the greatest challenges we found was the ability to isolate sufficient terrain that experienced negligible elevation change over the last 18 years. Land use, specifically forestry (forest harvesting and later tree growth), as well as natural phenomena such as wildfires, beetle kill, channel change and landslides substantially reduced stable areas available to quantify the magnitude of random errors inherent in our data. Our assessment of stable terrain was also hindered by the presence of unmapped termini and debris-covered ice that thinned over the period of study. In order to isolate stable terrain for uncertainty analysis we excluded tree cover using the 300 m ESA CCI LC product of 2010. Using these masks we noticed that, in some cases, logging areas were not excluded because they were mapped by the LC product as “grasslands”, which affected our original assessment of stable terrain.

The total uncertainty of the mass change estimate (ϵ_m) is defined as the quadratic sum of random $\left(\sigma_{\Delta M,rdn}\right)$ and systematic $\left(\sigma_{\Delta M,sys}\right)$ error terms:

$$\epsilon_m = \sqrt{\left(\sigma_{\Delta M,rdn}\right)^2 + \left(\sigma_{\Delta M,sys}\right)^2} \quad (1)$$

2.4.1 Random error

Random error arises from three sources that we assume to be independent: 1) the uncertainty on the rate of elevation change ($\sigma_{\Delta z}$); 2) the uncertainty on glacierized area (σ_A); and 3) the uncertainty on volume to mass conversion ($\sigma_{f\Delta V}$).

Elevation change ($\sigma_{\Delta z}$) error is derived from the uncertainty on stable terrain $\left(\sigma_{\Delta h}\right)$ after correction for effective sample size (Rolstad et al., 2009):

$$\sigma_{\Delta z} = \sigma_{\Delta h} \cdot \sqrt{\frac{A_{cor}}{5A}} \quad (2)$$

where A is the glacier area, and $A_{cor} = \pi L^2$ where L is the decorrelation length. We determined L by plotting semivariance (variogram) for randomly selected coordinate pairs (n=10,000) against distance for ten different realizations and determined the distance at which semivariance failed to substantially change. In most cases we found that L was around 500 m, a value commonly used by previous geodetic studies (Brun et al., 2017; Nuth & Kääb, 2011), and 300 m on average for the high resolution geodetic data sources considered in our study. These two average decorrelation lengths values were used to derive effective sample size for each dataset.
The uncertainty on glacierized area (σ_A), or planimetric uncertainty, was assessed by using a buffering method (Granshaw & Fountain, 2006) for each glacier in our inventory:

$$\sigma_A = P \cdot \frac{dx}{2} \quad (3)$$

where the buffer is defined as half the resolution of a pixel dx and P denotes the perimeter of a given glacier. Since most of the ice polygons from RGI02 are derived from 30 m imagery (Bolch et al., 2010), we use this value for dx for all glaciers. Our approach yields planimetric uncertainties that, when translated as a percentage of the area of a glacier, vary between 3% for large glaciers that are larger than 100 km^2 and 25% for glaciers smaller than 0.5 km^2. Collectively, these two uncertainties are combined to yield the total non-systematic error in volume change:

$$\sigma_{\Delta V} = \sqrt{\left(\sigma_{\Delta z}\left(p_A + 5\left(1 - p_A\right)\right)A\right)^2 + \left(\sigma_A \Delta_z\right)^2} \quad (4)$$

where A is the area of a given glacier and P_A is the percentage of surveyed area. We assume a factor of 5 in the elevation change uncertainty of non-surveyed areas (Berthier et al., 2014). We used a constant value for the mass to volume conversion factor $f\Delta V$ of 850 kg m^{-3} and an uncertainty $\sigma_{f\Delta V}$ of ± 60 kg m^{-3} (Huss, 2013).

The random uncertainty on geodetic mass balance is then derived as:

$$\sigma_{\Delta M,rdn} = \sqrt{\left(\sigma_{\Delta V} f_{\Delta V}\right)^2 + \left(\sigma_{f_{\Delta V}} \Delta V\right)^2} \quad (5)$$

where ΔV is the volume change. Our methods to derive $\sigma_{\Delta V}$ and σ_A both tend toward conservative estimates of the total random error ($\sigma_{\Delta M,rdn}$).

2.4.2 Systematic error

Due to departure from a linear glacier surface evolution hypothesis, imperfect sensor geometry and unidentified sources of error, the sum of glacier mass balance calculated for the two sub-periods do not exactly correspond to the mass balances calculated for the entire period. Consequently, and in line with the geodetic mass balance literature (Nuth and Kääb, 2011; Paul et al., 2017), we evaluate the systematic error following a similar approach as the one described elsewhere (Brun et al., 2017; Nuth & Kääb, 2011). That work considers the absolute value of the residuals of triangulation that are derived from decadal estimates of mass change (i.e. 2000-2009 and 2009-2018) that are differenced with the full period (2000-2018). These residuals, calculated tile-wise (as ensembles of similar size using approximately the same amount of scenes), are defined by:

$$r = \left|\Delta M_{2000-2018} - \frac{1}{2}\left(\Delta M_{2000-2009} + \Delta M_{2009-2018}\right)\right| \quad (6)$$

Similar to Brun et al., (2017) we found that the distribution of the residuals is related to the number of DEMs used in the trend. Unlike Brun et al., (2017), however, our number of DEMs greatly varied from five (e.g. subperiod analysis for some areas) to 32 (Sierras region for the full period). We derived the 68th percentile of the residuals distribution ($\pm$ 1σ) in a moving window of associated number of DEMs, large enough to contain at least five samples. Tile-associated residuals contain heterogeneous coverage over glaciers related to data gaps and various other filters. We thus weighted the percentile calculation with the minimum value of percent surveyed area from each of the three periods [2000-2009, 2009-2018 and 2000-2018] for each tile.

Finally, an inverse function was fitted to the observed trend of 68th percentile of residuals for each window of DEMs (see Figure S3). The systematic error is thus approximated by the relation:

$$\sigma_{\Delta M,sys} = a + \frac{b}{N_{DEM}} \quad (7)$$

where $a = -0.015$ and $b = 2$ and N_{DEM} is the average number of DEMs used in the trend. Our systematic error varies from ± 0.05 m yr^{-1} for trends derived from 30 DEMs to ± 0.40 m yr^{-1} for trends derived from approximately five DEMs.

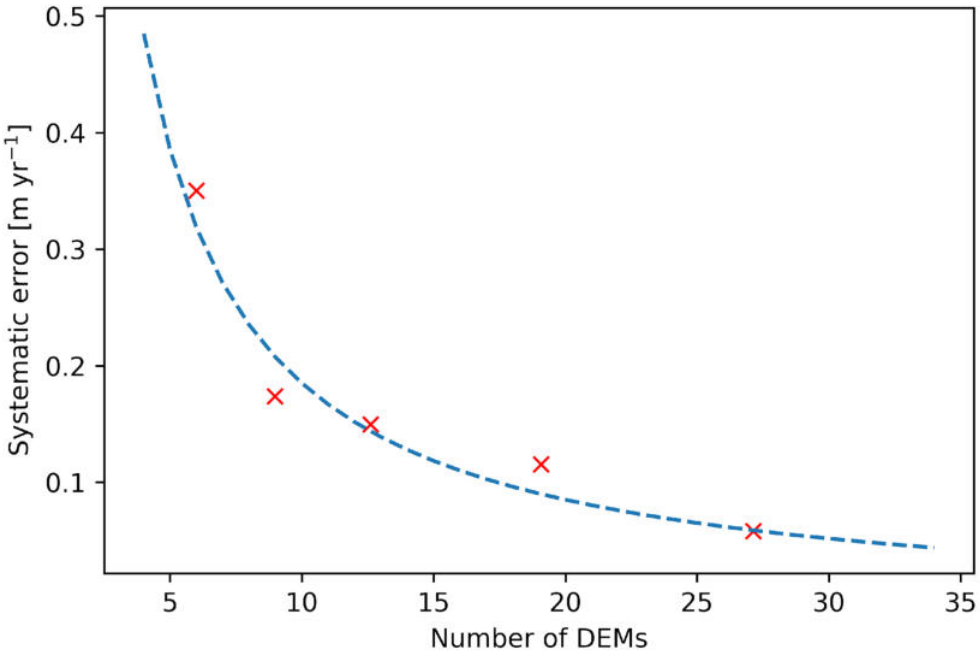

Figure S3. Systematic error versus number of DEMs.

3 Comparisons with independent mass change observations

3.1 Glaciological measurements

Additional ASTER/WV/Pleiades trends were derived (summer to summer) for the periods corresponding to the glaciological records availability (Table S2). The geodetic mass balances estimates calculated from these trends differ from traditional glaciological mass balances for some small glaciers (Figure S4). For most sites, the ASTER/WV/Pleiades estimates are within the bounds of uncertainty. ASTER/WV/Pleiades mass balances are occasionally less negative than traditional mass balances, especially for several sites with average balance tending towards

zero. These glaciers tend to occur in the North Cascades, where errors in RGI glacier delineation will bias the ASTER/WV/Pleiades mass balance towards less negative values due to inclusion of non-glacierized (stable) terrain in the glacier outline. Measurement error is considered in the error bounds given for the glaciological mass balance data (±300 kg m^{-2} yr^{-1}), but systematic errors due to biased sampling or calculation method may also exist.

3.2 Geodetic measurements

We compared our elevation trends obtained from ASTER/WV/Pleiades to independent estimates of elevation change derived from Lidar, SPOT and aerial photography, herein defined as independent geodetic measurements. ASTER/WV/Pleiades trends are calculated to match specific epochs of each geodetic site (Table S1). In practice, this typically corresponded to scenes selected for endpoints where they contained at least 50% coverage of the glacier. The inability to exactly match these endpoints to the independent geodetic data could thus introduce a seasonal bias into our comparison. The fewer the number of DEMs available for trend analysis, the stronger this bias can be. We performed mass balance calculations and uncertainty analysis similarly for both datasets following the methods described above and in the main paper.

We only report the random error for the independent geodetic data using parameters calculated for each dataset at highest spatial resolution (e.g. $\sigma_{\Delta z}$, L). Mass balance estimates were also derived after resampling the independent geodetic data to 30 m, but those estimates showed no significant difference from estimates made on higher resolution data. For the ASTER/WV/Pleiades trends, a systematic error was assessed from the number of valid DEMs used in the subperiod of each geodetic site, and quadratically summed with the random error.

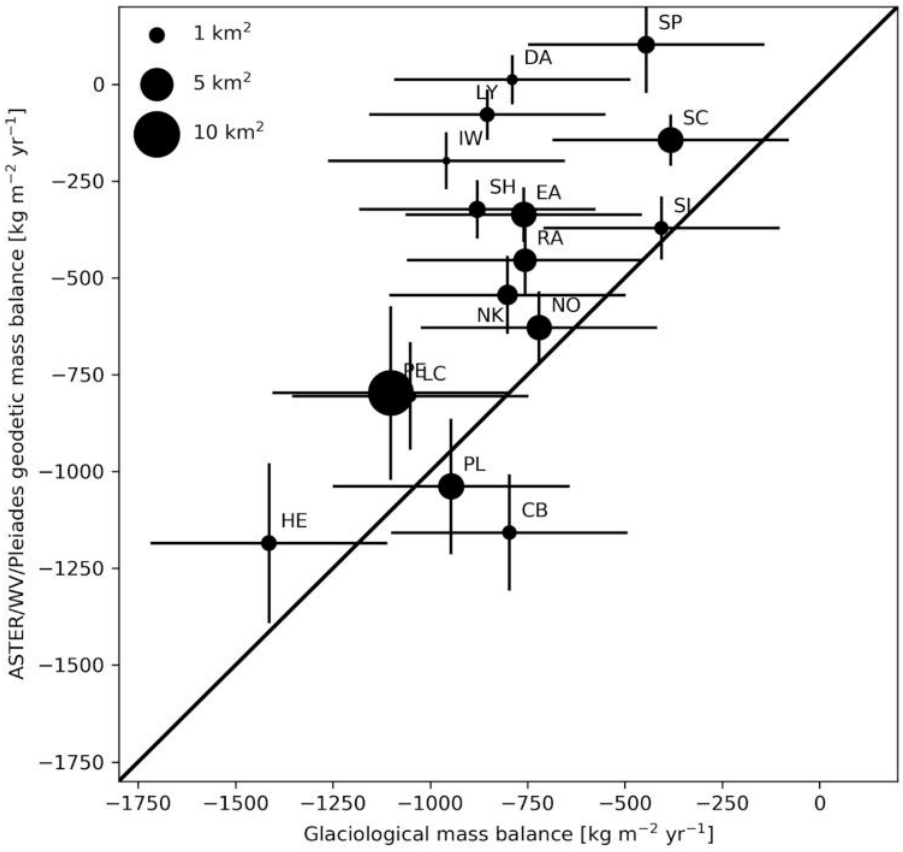

Figure S4. Geodetic and glaciological mass balance rates (± annual errors) for select observation sites in western North America (1:1 line shown in black). Symbol diameter is scaled (square root) to glacier area and point labels correspond to mass balance sites identified in Table S2.

ASTER/WV/Pleiades derived rates of mass change compare favorably to independently derived estimates of mass change (Table S1). Comparison of ASTER/WV derived rates to a LiDAR-SPOT5 dh/dt map for the Columbia Icefield (Table S1) was hampered by poor base to height geometry of the SPOT5 pair and fresh snowfall. We were unable to remove systematic bias in elevation from this DEM, so those data were excluded from subsequent analysis.

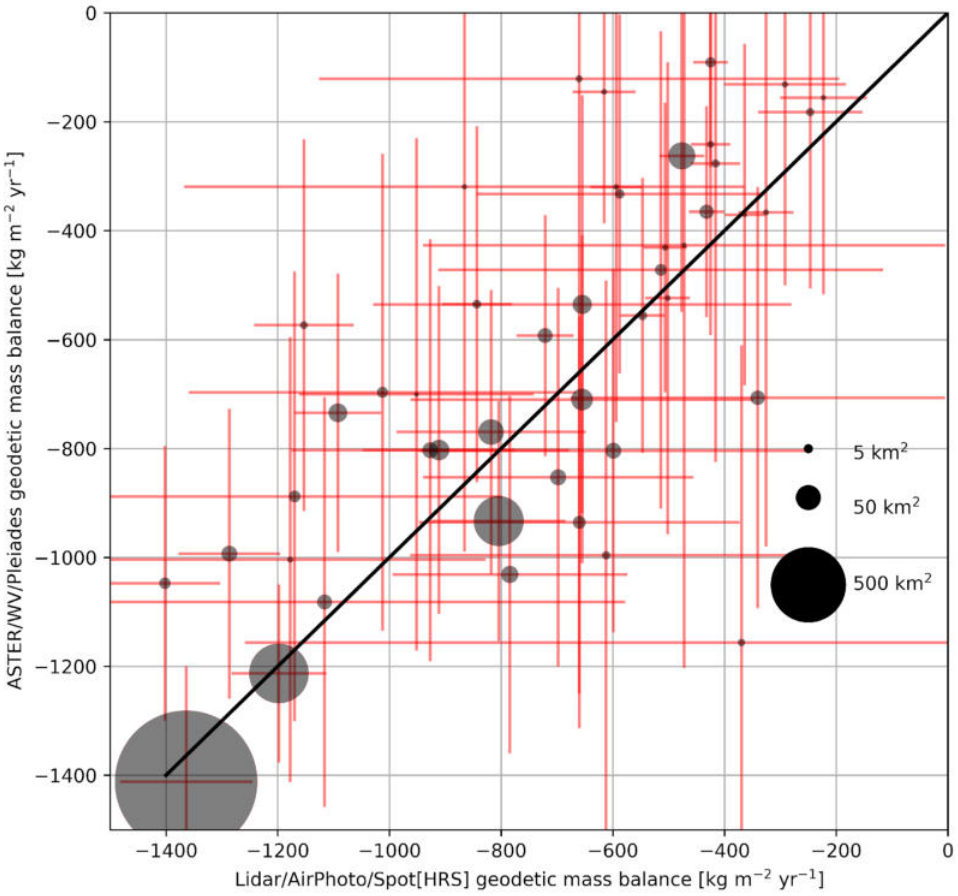

Figure S5. Independent geodetic measurements versus elevation trend analysis methods of this study (1:1 line shown in black). Symbol diameter is scaled (square root) to glacier area. Only glaciers with a minimum surface area (> 0.5 km^2) and sufficient proportion of surveyed area (> 50%) in both datasets are shown. Thirty four glaciers are between 0.5-5.0 km^2. Error bars denote ±1σ uncertainties.

4 Climate data supplementary figures

As described in our paper we used ERA5 (Hersbach & Dee, 2016) to assess the response of meteorological forcing on decadal changes in glacier mass. We downloaded monthly fields from the primary server used for ERA5 (http://apps.ecmwf.int/data-catalogues/era5). Maps shown in the paper (Figure 3) are based on composite anomalies of monthly averaged fields between the late

[2009-2017] and early periods [2000-2009]. The strongest relation between changes in glacier mass and meteorological fields are for the winter season (Figure S6).

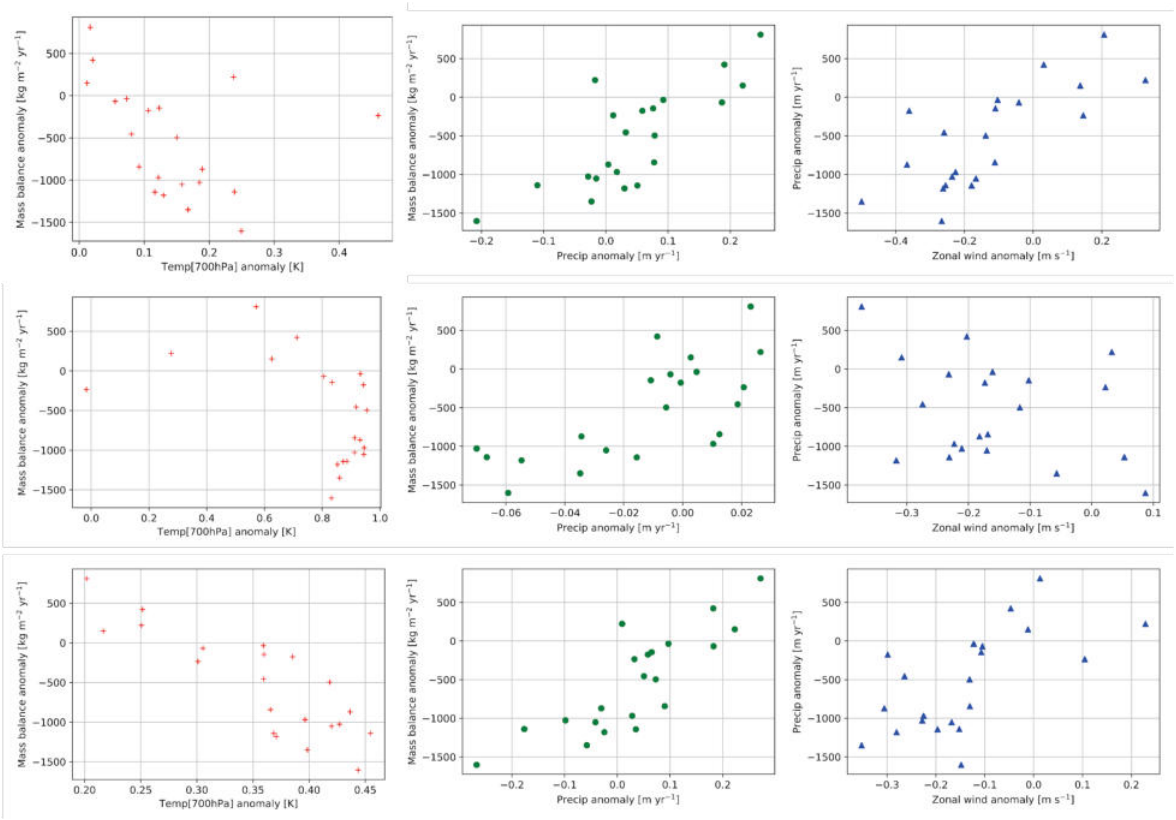

Figure S6. Relation between changes in mass balance [kg m^{-2} yr^{-1}] between the early and later periods at grid point (dots of Figure 1) and averaged composite anomalies ([2017-2009] - [2000-2009]) of monthly ERA5 fields for temperature [K] at 700 hPa, surface precipitation [m yr^{-1}] and zonal wind speed at 250 hPa [m s^{-1}]. Top row: winter [Oct-May] season anomalies. Middle row: summer [June-September]. Bottom row: annual [January-December]. Correlation coefficients (not shown) increase marginally (2-3%) when adjacent ERA5 grid points for a given grid point are averaged with its neighbors.

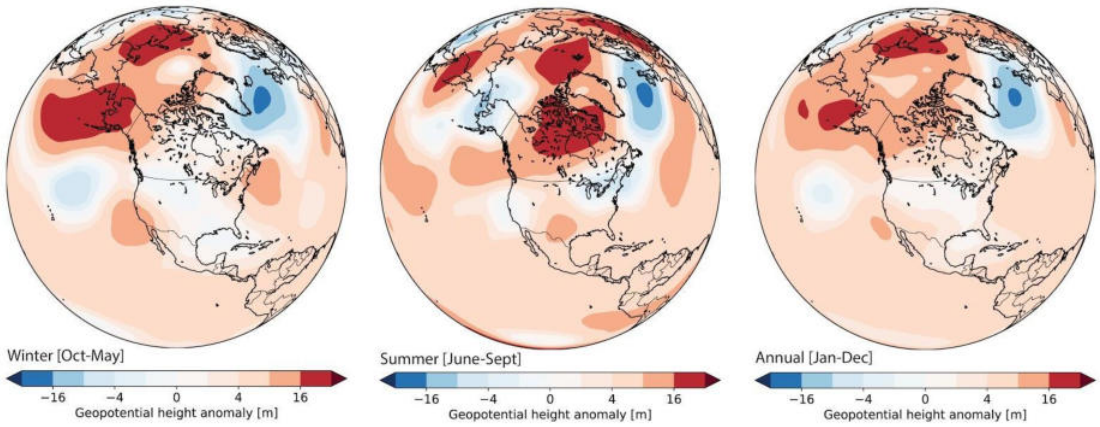

Figure S7. Geopotential height [500 hPa] anomalies for monthly composites ([2009-2017] - [2000-2009] for winter (left), summer (middle) and annual (right).

Examination (not shown) of linear correlation between zonal wind and climate indices over the last decade and for the period 1948-2017 (https://www.esrl.noaa.gov/psd/data/correlation/) reveals no obvious climate state (winter or annual) that can adequately explain the north-south dipole of zonal wind anomalies. Geopotential height [500 hPa] anomalies (Figure S7) reveal a general strengthening of high pressure over high latitudes and a deepening area of low pressure of eastern Greenland during the last decade.

5 References

Berthier, E., Vincent, C., Magnússon, E., Gunnlaugsson, Á., Pitte, P., Le Meur, E., et al. (2014). Glacier topography and elevation changes derived from Pléiades sub-meter stereo images. Cryosphere, 8(6), 2275–2291.

Berthier, E., Cabot, V., Vincent, C., & Six, D. (2016). Decadal Region-Wide and Glacier-Wide Mass Balances Derived from Multi-Temporal ASTER Satellite Digital Elevation Models. Validation over the Mont-Blanc Area. Frontiers of Earth Science, 4. https://doi.org/10.3389/feart.2016.00063

Bolch, T., Menounos, B., & Wheate, R. (2010). Landsat-based inventory of glaciers in western Canada, 1985–2005. Remote Sensing of Environment, 114(1), 127–137.

Brun, F., Berthier, E., Wagnon, P., Kääb, A., & Treichler, D. (2017). A spatially resolved estimate of High Mountain Asia glacier mass balances, 2000-2016. Nature Geoscience, 10(9), 668–673.

Clark, A., Fagre, D., Peitzsch, E., Reardon, B., & Harper, J. (2017). Glaciological measurements and mass balances from Sperry Glacier, Montana, USA, years 2005-2015. Earth System Science Data, 9(1), 47–61.

Cogley, G., Adams, W., Ecclestone, M., Jung-Rothenhäusler, F., & Ommanney, C. S. L. (1996). Mass balance of White Glacier, Axel Heiberg Island, NWT, Canada, 1960–91. Journal of Glaciology, 42(142), 548–563.

Demuth, M., & Keller, R. (2006). An assessment of the mass balance of Peyto Glacier (1966-1995) and its relation to recent and past-century climatic variability. Peyto Glacier: One Century of Science, 8, 83–132.

Granshaw, F., & Fountain, A. (2006). Glacier change (1958–1998) in the North Cascades National Park Complex, Washington, USA. Journal of Glaciology, 52(177), 251–256.

Hersbach, H., & Dee, D. (2016). ERA5 reanalysis is in production. ECMWF Newsletter, 147(7).

Hopkinson, C., & Demuth, M. (2006). Using airborne lidar to assess the influence of glacier downwasting on water resources in the Canadian Rocky Mountains. Canadian Journal of Remote Sensing, 32(2), 212–222.

Huss, M. (2013). Density assumptions for converting geodetic glacier volume change to mass change. The Cryosphere, 7(3), 877–887.

Josberger, E., Bidlake, W., March, R., & Kennedy, B. (2007). Glacier mass-balance fluctuations in the Pacific Northwest and Alaska, USA. Annals of Glaciology, 46(1), 291–296.

Korona, J., Berthier, E., Bernard, M., Rémy, F., & Thouvenot, E. (2009). SPIRIT. SPOT 5 stereoscopic survey of Polar Ice: Reference Images and Topographies during the fourth International Polar Year (2007–2009). ISPRS Journal of Photogrammetry and Remote Sensing: Official Publication of the International Society for Photogrammetry and Remote Sensing , 64(2), 204–212.

Krimmel, R. M. (1997). Water, ice, meteorological, and speed measurements at South Cascade Glacier, Washington, 1996 balance year. USGS. https://doi.org/10.3133/wri994049

Krimmel, R.(1999). Analysis of Difference Between Direct and Geodetic Mass Balance Measurements at South Cascade Glacier, Washington. Geografiska Annaler: Series A, Physical Geography, 81(4), 653–658.
Meier, M., & Tangborn, W. (1965). Net Budget and Flow of South Cascade Glacier, Washington. Journal of Glaciology, 5(41), 547–566.
Moore, D., & Demuth, M. (2001). Mass balance and streamflow variability at Place Glacier, Canada, in relation to recent climate fluctuations. Hydrological Processes, 15(18), 3473–3486.
National Park Service, Larrabee, M., & Riedel, J. (2017). GLACIAL MASS BALANCE 2003-2016 ON MOUNT RAINIER. Presented at the GSA Annual Meeting in Seattle, Washington, USA - 2017, Geological Society of America. https://doi.org/10.1130/abs/2017AM-302746
Nuth, C., & Kääb, A. (2011). Co-registration and bias corrections of satellite elevation data sets for quantifying glacier thickness change. The Cryosphere, 5(1), 271–290.
Pelto, M., & Brown, C. (2012). Mass balance loss of Mount Baker, Washington glaciers 1990-2010. Hydrological Processes, 26(17), 2601–2607.
Pelto, M. (1996). Changes in glacier and alpine runoff in the North Cascade Range, Washington, USA 1985-1993. Hydrological Processes, 10(9), 1173–1180.
Pelto, M., & Riedel, J. (2001). Spatial and temporal variations in annual balance of North Cascade glaciers, Washington 1984–2000. Hydrological Processes, 15(18), 3461–3472.
Roberti, G., Friele, P., de Vries, B. van W., Ward, B., Clague, J., Perotti, L., & Giardino, M. (2017). Rheological evolution of the Mount Meager 2010 debris avalanche, southwestern British Columbia. Geosphere, 13(2), 369–390.
Rolstad, C., Haug, T., & Denby, B. (2009). Spatially integrated geodetic glacier mass balance and its uncertainty based on geostatistical analysis: application to the western Svartisen ice cap, Norway. Journal of Glaciology, 55(192), 666–680.
Schiefer, E., Menounos, B., & Wheate, R. (2007). Recent volume loss of British Columbian glaciers, Canada. Geophysical Research Letters, 34(16), L16503.
Tachikawa, T., Hato, M., Kaku, M., & Iwasaki, A. (2011). Characteristics of ASTER GDEM version 2. In 2011 IEEE International Geoscience and Remote Sensing Symposium (pp. 3657–3660).
Tennant, C., & Menounos, B. (2013). Glacier change of the Columbia Icefield, Canadian Rocky Mountains, 1919–2009. Journal of Glaciology, 59(216), 671–686.
Tennant, C., Menounos, B., Ainslie, B., Shea, J., & Jackson, P. (2012/2). Comparison of modeled and geodetically-derived glacier mass balance for Tiedemann and Klinaklini glaciers, southern Coast Mountains, British Columbia, Canada. Global and Planetary Change, 82–83, 74–85.
VanLooy, J., & Forster, R. (2008). Glacial changes of five southwest British Columbia icefields, Canada, mid-1980s to 1999. Journal of Glaciology, 54(186), 469–478.
Young, G. J. (1981). The Mass Balance of Peyto Glacier, Alberta, Canada, 1965 TO 1978. Arctic and Alpine Research, 13(3), 307–318.

Zemp, M., Thibert, E., Huss, M., Stumm, D., Rolstad Denby, C., Nuth, C., et al. (2013). Reanalysing glacier mass balance measurement series. The Cryosphere, 7(4), 1227–1245.

Zemp, M., Nussbaumer, S., Gartner-Roer, I., Huber, J., Machguth, H., Paul, F., & Hoelzle, M. (2017). Global Glacier Change Bulletin (No. 2). World Glacier Monitoring Service, Switzerland.

Appendix C: Supplementary Information of *Accelerated global glacier mass loss in the early twenty-first century*

nature portfolio

https://doi.org/10.1038/s41586-021-03436-z

Supplementary information

Accelerated global glacier mass loss in the early twenty-first century

In the format provided by the authors and unedited

Supplementary Information for

Accelerated global glacier mass loss in the early twenty-first century

Romain Hugonnet, Robert McNabb, Etienne Berthier, Brian Menounos, Christopher Nuth, Luc Girod, Daniel Farinotti, Matthias Huss, Ines Dussaillant, Fanny Brun and Andreas Kääb

Correspondence to: romain.hugonnet@gmail.com

This document includes (navigation links embedded):

Supplementary Methods

1. ASTER processing

We downloaded 440,548 ASTER L1A[43] granules totalling around 30TB of data from NASA's Land Processes Distributed Active Archive Center via EarthData Search (https://search.earthdata.nasa.gov). Daytime granules with a cloud coverage below 99% were selected, from the first acquisition date of 4th March 2000 until 30th September 2019. Spatially, they cover all terrain in 1 by 1 degree tiles containing glaciers. Our tiling was extended both in latitude and longitude to retrieve at least one additional granule in each direction, based on a 60 km by 60 km granule footprint and the along-track angle of the Terra satellite (boarding ASTER) at a given latitude.

This coverage extension increased the amount of stable terrain available in each DEM in order to improve the along-track corrections and co-registration (later described) and mitigate correction errors at the edges. We bypassed the arbitrary 60 km by 60 km splitting of the ASTER archive and combined granules containing a valid 3N and 3B Visible and Near Infra-Red (VNIR) band in groups of at most three, depending on whether they were acquired sequentially (less than 12s apart), thereby forming 60 km by 180 km image strips. This "stitching" was done in image geometry, before stereo matching. We chose a maximum of three granules in order to avoid effects from the curvature of the Earth appearing in our corrections. We also observed that three granules were sufficient to improve corrections for the frequencies typically observed in ASTER along-track undulations biases[50]. For occurences with less than three consecutives granules, we stitched two granules if possible or kept only one. We left one overlapping granule in between sequential strips to mitigate the edge effects of later corrections. The resulting ASTER L1A strips were processed in UTM zones based on their new centroid. To generate ASTER DEMs, we used MicMac ASTER (MMASTER)[50], a procedure that is part of the MicMac photogrammetric processing library[49]. In total, we generated 198,339 ASTER DEM strips posted at 30 m resolution (Table S1) which required about 5 million compute hours.

Our last step was to correct ASTER DEM strips for systematic biases using TanDEM-X as a reference. In this last step, prior to any correction, we performed an initial co-registration. We first removed cross-track biases by selecting the best-performing polynomial fit within orders 1 to 6 based on their RMSE (Fig. S1a). We then corrected along-track low-frequency and high-frequency undulations simultaneously using a sum of sinusoids with specific frequencies and amplitudes (Fig. S1b), conditioned by priors and optimized through basin-hopping[51]. Finally, ice-free terrain from the DEMs was co-registered a second time off-ice to TanDEM-X. We successfully corrected and co-registered 154,565 ASTER DEM strips (Extended Data Fig. 2, Table S1).

2. Elevation time series

The ASTER elevations are annotated as $h_{AST}(t,x,y)$. The ArcticDEM and REMA elevations, originating mainly from the WorldView satellite sensors, are annotated as $h_{WV}(t,x,y)$. The TanDEM-X reference elevations are annotated as $h_{TDX}(x,y)$.

2.1. Time stacking

Following co-registration, we created three-dimensional arrays (time t, space x and y; hereafter referred to as "stacks") of elevation using all available ASTER DEMs, ArcticDEM DEMs and REMA DEMs within a 1 by 1 degree tiling. For ASTER DEMs generated with MicMac, a raster indicating the quality of stereo-correlation was also stacked in time for each corresponding DEM. We did not filter low-correlation pixels and relied solely on the statistical filtering and measurement error assessment later described. Only pixels (x,y) within a buffer of 10 km of the glacier inventory were kept for further processing. They together represent a surface of about 4,000,000 km² including about 700,000 km² of glacierized terrain[85].

The stacked elevations from ASTER $h_{AST}(t,x,y)$ and ArcticDEM/REMA $h_{WV}(t,x,y)$ are annotated as $h_{AST/WV}(t,x,y)$. The stacked quality of stereo-correlation from ASTER are annotated as $q(t,x,y)$ and varies from 0 to 100%.

2.2. Elevation filtering step 1: reference elevations

A large number of outliers is present in elevation data due to photogrammetric blunders, presence of clouds or low image contrast. We performed an initial filtering of stacked elevations to remove extreme outliers using our reference DEM TanDEM-X (Extended Data Fig. 3c).

First, we implemented a spatial filter. We excluded elevation observations $h_{AST/WV}$ for which the absolute elevation difference to the maximum or minimum reference elevation h_{TDX} found within a disk D of radius r was larger than a vertical elevation threshold Δh_D:

$$min(h_{TDX}(x_D,y_D)) - \Delta h_D < h_{AST/WV}(t,x,y) < max(h_{TDX}(x_D,y_D)) + \Delta h_D \quad \text{(S1)}$$

where (x_D,y_D) are pixels in the disk D of radius r centered on (x,y).

This procedure was performed for each pixel with $r = 200\,m$, $\Delta h_D = 700\,m$ and repeated with $r = 500\,m$, $\Delta h_D = 500\,m$ and $r = 1000\,m$, $\Delta h_D = 300\,m$. These large threshold values and the ones detailed hereafter were defined and tested over the glacier HPS12, Southern Patagonian Icefield, experiencing to our knowledge the most rapid sustained elevation change in the world[53].

Then, we applied a temporal filter to all pixels (x,y) with a valid reference value $h_{TDX}(x,y)$ (Extended Data Fig. 3c). To constrain this filtering, we assumed the time stamp of TanDEM-X, t_{TDX}, to be 1st January 2013 which corresponds to the middle of the period

used to generate the TanDEM-X mosaic DEM[46]. To account for possible time differences, we included all values within a vertical threshold Δh_0 of 100 m starting 1st January 2013. From this date, we propagated the filtering in time allowing for a maximum and minimum linear elevation change rate $\frac{\Delta h}{\Delta t}_T$ of 50 meters per year (glacier HPS12). The vertical threshold ensures the conservation of observations of rapidly evolving surfaces, for example that of surging glaciers, near the reference date t_{TDX}.

$$h_{AST/WV}(t,x,y) < \left| h_{TDX}(x,y) + \Delta h_0 + (t - t_{TDX}) \cdot \frac{\Delta h}{\Delta t}_T \right| \quad \text{(S2)}$$

2.3. Elevation measurement error

Inspection of our elevation observations $h_{AST/WV}$ revealed a significant variability in elevation precision (heteroscedasticity). To account for it in subsequent analysis, we evaluated the dependence of the elevation variance $\sigma_{h_{AST/WV}}^2$ on two factors: terrain slope $\alpha(x,y)$ and quality of stereo correlation $q(t,x,y)$. To assess this dependency, we randomly drew without replacement up to 10,000 off-ice elevation differences to the reference TanDEM-X, $h_{AST/WV} - h_{TDX}$, for varying categories of terrain slope and quality of stereo-correlation. We did this for all tiles globally. For each category, we estimated the variance as the square of the Normalized Median Absolute Deviation (NMAD) to mitigate the effect of elevation outliers[58].

Elevation measurement error $\sigma_{h_{AST/WV}}$ increased with terrain slope and, for ASTER DEMs, decreased with quality of stereo-correlation (Extended Data Fig. 3a). The dependency of error on surface slope is well documented[55,56] while the one to the quality of stereo-correlation is inherent to photogrammetry[49] but, despite this, both are rarely accounted for. As an example, for a typical ASTER DEM with a co-registration RMSE of 5 m, we found the NMAD to be about 3 m over low slopes (0 to 10 degrees) and exceeding 20 m for steep slopes (> 40 degrees). Similarly, we found the NMAD of elevation differences for $q = 100\%$ to be around 3 m, while it was over 30 m for $q = 40\%$.

The elevation measurement error $\sigma_{h_{AST/WV}}$ was estimated by a simple model, calibrated on the empirical variance (Extended Data Fig. 3a), to yield an error for all elevation observations in space (x,y) and time t (Equation 1, repeated below).

$$\sigma_{h_{AST/WV}}^2(t,x,y) = \sigma_c^2(t,x,y) + \sigma_\alpha^2(\alpha,q) + \sigma_q^2(q) \quad \text{(1)}$$

where $\alpha(x,y)$ is the terrain slope, $q(t,x,y)$ is the quality of stereo-correlation and $\sigma_c(t,x,y)$ is the co-registration error, specific to the DEM from which the elevation observation $h_{AST/WV}(t,x,y)$ originates. The co-registration error σ_c would ideally have to be estimated on pixels with low slopes and good qualities of stereo-correlation to avoid double-counting the effect of other errors. However, as this is not possible for some DEMs because of the limited amount of flat terrain available, we conservatively used the RMSE of elevation differences over all available stable terrain to derive σ_c.

The errors due to slope σ_α and quality of stereo-correlation σ_q were described as:

$$\sigma_\alpha = (a_\alpha + a_q(1 - q)^{b_\alpha}) \cdot \tan(\alpha) \quad \text{(S3)}$$

$$\sigma_q = a_q \cdot (1 - q)^{b_q} \quad \text{(S4)}$$

where we found $a_\alpha \approx 20$ m, $b_\alpha \approx 1$, $a_q \approx 20$ m and $b_q \approx 1.25$ by manually combining independent least squares optimizations for the slope and the quality of stereo-correlation on the empirical variance (Extended Data Fig. 3a). Against the above-mentioned approximations, the simplicity of this process was sufficient to calibrate the elevation variance at the right order of precision. The slope and quality of stereo-correlation errors were not independent, as it proved necessary to integrate some effects of the quality of stereo-correlation in the slope error to yield satisfying results (Equation S3). ArcticDEM and REMA DEMs being already filtered for low stereo-correlations without any product on quality of stereo-correlation provided[44,45,52], we assigned them a constant worst-case quality of stereo-correlation of 60%.

Over vegetated terrain, the variance in elevation increased by a factor of 1.5-2. We interpreted this high variance from vegetation that can dynamically change over time due to forest harvesting, wildfire, regrowth and snow-covered vegetation[60]. This does not significantly affect elevation measurement error over glacierized terrain and thus was omitted from our workflow. We did, however, verify its limited impact in subsequent analysis of elevation time series (Section 3).

2.4. Elevation filtering step 2: linear elevation change and reference elevations

In most regions of the world, the largest glacier elevation change rates are far lower than the extreme rate $\frac{\Delta h}{\Delta t}_T$ of 50 meters per year previously adopted. In order to improve the performance of our filtering (Extended Data Fig. 3c), we estimated a maximum and minimum acceptable linear elevation change rate at the pixel-scale.

First, we estimated a robust linear elevation change rate $\frac{dh}{dt}_{WLS}(x,y)$. For each pixel, we performed two successive weighted least-squares (WLS) fits, filtering outliers outside the 99 percent confidence interval of the first fit, and keeping only the second fit[54]. The elevation measurement error $\sigma_{h_{AST/WV}}$ (see above) was used for weighting.

Then, for each pixel, we derived the 20th and 80th percentiles of linear elevation change rate within a disk. We computed the maximum absolute value of the two percentiles and conservatively used twice this value to constrain the maximum linear elevation change rate allowed at the pixel-scale.

$$\frac{\Delta h}{\Delta t}_T(x,y) = 2 \cdot max\left(\left|\frac{dh}{dt}_{WLS}(x_D,y_D)_{20th}\right|, \left|\frac{dh}{dt}_{WLS}(x_D,y_D)_{80th}\right|\right) \quad \text{(S5)}$$

where (x_D,y_D) are pixels in the disk D of radius $r = 1000$ m centered on (x,y) and the subscripts 20th and 80th denote the 20th and 80th distribution percentiles.

We refined the temporal filter previously described (Equation S2, Extended Data Fig. 3c) with the linear elevation change rate $\frac{\Delta h}{\Delta t}_T(x,y)$ (instead of a constant of 50 meters per year). We also modified the vertical threshold Δh_0 to better account for the varying timestamp of TanDEM-X:

$$\Delta h_0(x,y) = \Delta h_0 + \Delta t_{TDX-TDX} \cdot \frac{\Delta h}{\Delta t}_T(x,y) \quad \text{(S6)}$$

where $\Delta t_{TDX-TDX} = 2$ yr is the maximum number of years that can separate a TanDEM-X acquisition and the middle date t_{TDX} chosen as 1st January 2013.

We refined the spatial filter previously described (Section 2.2, Equation S1, Extended Data Fig. 3c) by further constraining the vertical elevation threshold Δh_D:

$$\Delta h_D(x,y) = \Delta h_0 + \Delta t_{AST-TDX} \cdot \frac{\Delta h}{\Delta t}_T(x,y) \quad \text{(S7)}$$

with $\Delta h_0 = 100$ m, and $\Delta t_{AST-TDX} = 15$ yr is the maximum number of years that can separate a TanDEM-X acquisition in 2015 to the furthest observation in 2000. We applied the spatial filter with $r = 1000$ m. This step was especially helpful to filter remaining outliers for pixels with no valid reference elevation h_{TDX} where the temporal filter cannot be applied.

2.5. Temporal covariance of glacier elevation

Extracting a continuous time series from glacier elevation data is complex[61,62,76]. At the pixel scale, glacier surface elevation undergoes changes at different time scales (seasonal, annual, decadal) with trends and amplitudes that significantly vary in space (region, glacier, zone of the glacier). Parametric methods such as least squares are thus not particularly well-suited to fitting a temporal series to glacier elevation data. If an underlying parametrization is erroneous, both the temporal interpolation and the propagation of uncertainties will be negatively affected.

We instead chose to interpolate our elevation measurements using non-parametric, empirically-based interpolation methods based on the covariance of the data, a technique referred to as Gaussian Processes[59]. These methods find the local minima of variance propagated from observations. Assuming that the covariance model chosen is statistically representative of the underlying process, it provides the best unbiased estimator. These methods also yield empirical confidence intervals, having the benefit of being representative of the uneven temporal sampling inherent to the data.

We harnessed the repeat temporal coverage of DEMs to study the temporal covariance of glacier elevation change in order to better constrain both our temporal filtering and interpolation. Once the temporal covariance is estimated, we derive our best interpolator using Gaussian Process (GP) regression[63]. For this type of application, GP regression is equivalent to kriging[71,78,79]. Here, we do not optimize covariances for each pixel based on priors with a maximum likelihood function, as is usually the case in machine learning applications. Instead, our objective is to model variograms with characteristics representative

of many pixels at once, and to apply these variograms directly in the regression. The rationale behind this approach is to mitigate the sparse sampling of elevations in time at the pixel scale by utilizing the repeat spatial coverage of our observations.

To derive temporal variograms, we randomly drew up to 10,000 pixels (x, y) of locations $h_{AST/WV}(t, x, y)$ containing at least 10 valid observations in time. We did so for all RGI regions. To reduce the effect of outliers, the variograms were estimated by the median of squared residuals for each time lag instead of the mean.

We aggregated our variograms depending on the linear trend of elevation of pixels $\frac{dh}{dt}_{WLS}(t, x, y)$ (Section 2.4) to better identify variance components independent of this underlying linear elevation change. The empirical temporal variances varied little between regions, and we found no significant variability with external factors (such as slope), as we did for the elevation measurement error.

Through analysis of the empirical variograms, we found that the data temporal covariance (Extended Data Fig. 3b) consisted of a sum of:

- a pairwise linear (PL) kernel, manifesting parabolically in variance, that represents the long-term, decadal linear elevation trend of the pixel (over 20 years in our case)
- a periodic, exponential sine-squared (ESS) kernel, corresponding to how seasonality is captured by the elevation data, for example by the fact that summer-to-summer observations of glacier elevations can be much closer than summer-to-winter observations
- a local, radial basis-function (RBF) kernel, showing how close elevation observations are to each other with varying time differences
- white noise, representative the average of the measurement errors $\sigma_{h_{AST/WV}}$.

To capture nonlinear elevation change trends (with time scales larger than the local RBF kernel), we added a local linear kernel, described by a rational quadratic (RQ) kernel multiplied by the pairwise linear kernel. We chose to model local linear changes using a RQ kernel times PL kernel instead of solely a RQ kernel. The latter was discarded after initial testing due to undesired effects at the temporal boundaries (2000 and 2020). The RQ times PL implies that the "mean" linear trend can vary locally and, when no observation is available at the boundaries, the extrapolated trend falls back towards the local "mean" linear trend. Physically, this is behaviour consistent with existing observations and with known decadal and sub-decadal climatic oscillations that influence glacier change. In practice, there is little extrapolation made in our study due to the dense repeat data coverage (Fig. 1).

We used our measurement error $\sigma_{h_{AST/WV}}$, having a value specific to each elevation observation in space and time, instead of the average measurement error (white noise) sampled by the empirical variograms. We semi-automatedly modelled the temporal covariance with time scales and amplitudes estimated from the empirical covariance (Extended Data Fig. 3b) and used the same ESS, RBF and RQ parameters for all pixels given the absence of significant nonstationarities. The pairwise linear kernel was estimated independently for each pixel (x, y) (Equation 2, repeated below):

$$\sigma_{h_{AST/WV}}(x,y,\Delta t)^2 = PL(x,y,\Delta t) + ESS(\phi_p, \sigma_p{}^2, \Delta t) + RBF(\Delta t_l, \sigma_l{}^2, \Delta t) + RQ(\Delta t_{nl}, \sigma_{nl}{}^2, \alpha_{nl}, \Delta t) \cdot PL(x,y,\Delta t) + \sigma_{h_{AST/WV}}(t,x,y)^2 \quad (2)$$

where Δt is the time lag between observations.

We found $\phi_p = 1$ yr, $\sigma_p \approx 5$ m, implying a seasonal periodicity component of 5 m on average. We found that the local signal was best decomposed into a sum of three RBF kernels with $\Delta t_{l1} \approx 0.75$ yr, $\sigma_{l1} \approx 5$ m, $\Delta t_{l2} \approx 1.5$ yr, $\sigma_{l2} \approx 4$ m and $\Delta t_{l3} \approx 3$ yr, $\sigma_{l3} \approx 2$ m, which suggests that, once the underlying linear trend and periodicity is removed, inter-annual glacier elevations are on average within 5 m of each other within a year, within 9 m within 1.5 year and within 11 m within 3 years. Finally, based on pixel-scale testing (for filtering purposes) and the temporal range of the underlying linear trend observed in our empirical variograms, we constrained the local linear values to $\sigma_{nl} \approx 10$ m, $\alpha_{nl} \approx 10$ and $\frac{1}{2\alpha_{nl}} \cdot \Delta t_{nl} \approx 5$ yr. Those values mean that, on average, local nonlinearity lasts around 5 years and within 10 m of the underlying linear trend. Our primary objective was to ensure a low sensitivity to outliers, which were not effectively filtered out when using shorter-time scale parameters. In order to avoid removing glacier surges, we included a conditional loop in our procedure, which was calibrated on Nathorstbreen glacier, Svalbard (the largest surge observed during our period of study, Fig. S3).

The variances described above do not directly condition the mean of the GP elevation time series, which is interpolated from available observations, but only leave the opportunity to find periodicity and local variations in those observations within an order of magnitude. For example, the periodic kernel (with $\sigma_p \approx 5$ m) applied to elevation observations in the Low Latitudes yields elevation temporal series with no marked seasonality, despite leaving the opportunity to find amplitudes of the order of 5 m. This is because, in this region, the elevation observations categorized by seasons do not show a significant seasonal trend (in front of linear, local trends) and thus the periodic kernel does not find significant seasonality to propagate from observations.

With the same rationale, sensitivity tests showed limited influence of the seasonal, local and non-linear variances σ_p, σ_l and σ_{nl}, time parameters Δt_l and Δt_{nl}, and scale parameter α_{nl} for values within the same order of magnitude (Supplementary Discussion section “Sensitivity to the Gaussian Process hyperparameters”.). The limited influence of GP parameters within the same order of magnitude is due to the dense repeat coverage, and the relatively large measurement error of ASTER elevations (of about 5 m) which generally prevents complete deconvolution of local and periodic signals. This effect is later accounted for by our uncertainty propagation of interpolation biases (Section 4.3) and, when aggregated at different spatial scales, is essentially what defines the temporal resolution of our dataset (Supplementary Discussion section “Time series comparison and temporal resolution”). We found that the credible interval of the GP regression was the most impacted by parameter changes and was thus validated in a later analysis (Section 3.4). For estimating changes over stable terrain in the surroundings of glaciers, we used only a linear and seasonal kernel.

2.6. Elevation filtering step 3: iterative GP filtering of elevation

We applied GP regression iteratively, fitting an interpolated time series $h_{GP}(t,x,y)$ to our elevations $h_{AST/WV}(t,x,y)$ at a monthly temporal resolution from January 1st, 2000 to January 1st, 2020 for each pixel at a posting of 100 m. The interpolation period is 20 years, with boundaries positioned exactly three months before the earliest (early March, 2000) and after the latest (late September, 2019) observations. We used the GP error $\sigma_{h_{GP}}(t,x,y)$ propagated in time to filter any remaining outliers.

Ideally, we would filter the largest outliers first, and repeat this process iteratively outlier by outlier to avoid biasing new fits with previous outliers. However, as this process would be too computationally intensive, we chose instead to remove several outliers at once. For each pixel, we performed five iterative GP regressions for filtering, where we removed outliers successively from a 20-sigma ($\sigma_{h_{GP}}$) interval, a 12-sigma interval, a 9-sigma interval, a 6-sigma interval and, finally, a 4-sigma interval (Extended Data Fig. 3d).

2.7. Temporal GP interpolation of glacier elevation

After excluding the outliers, we performed a final GP regression at a monthly temporal resolution, to yield the final interpolated elevation time series $h_{GP}(t,x,y)$ with error $\sigma_{h_{GP}}(t,x,y)$ (Extended Data Fig. 3e). The repeat temporal coverage allowed us to correctly identify the expected seasonal minimum of glacier elevation at the pixel-scale (e.g. around the end of September in the Northern Hemisphere, and around the end of March in the Southern Hemisphere).

Qualitative evaluation of the time series showed that the fit and the GP credible interval performed well for typical glacier elevation change signals (Fig. S2). However, in the case of abrupt changes such as glacier surges, the method fails to represent the true temporal evolution of elevation even if the overall elevation change signal is captured (Fig. S3). Improving these aspects would require a classification of glacierized terrain for extreme events prior to constraining the temporal covariance and performing temporal interpolation, which was not feasible at a global scale.

3. Validation of elevation time series

The ICESat elevations are annotated as $h_{ICS}(t,x,y)$. The IceBridge elevations are annotated as $h_{ICB}(t,x,y)$. The elevations from high-resolution DEMs are annotated as $h_{HR}(t,x,y)$.

3.1. Comparing to ICESat

Before comparing ICESat elevations $h_{ICS}(t,x,y)$ to our interpolated elevation time series $h_{GP}(t,x,y)$, we verified that ICESat was aligned off-ice with our reference TanDEM-X $h_{TDX}(x,y)$ by computing the co-registration shifts between the two datasets over all stable terrain in the region[48]. ICESat showed very negligible horizontal and vertical shifts with the reference TanDEM-X in all regions. This is expected given that during its production the

TanDEM-X was co-registered to ICESat data[46]. Thus, we chose not to apply any horizontal or vertical shift.

To compare ICESat elevations $h_{ICS}(t,x,y)$ at the same points in time t_{ICS} as our elevation time series $h_{GP}(t,x,y)$, we performed a linear interpolation of our monthly elevation time series to extract elevation at the center date of each ICESat campaign. Most ICESat campaigns last 30 to 40 days, thus the longest possible time lag to their center date is 15 to 20 days. This 15 to 20-day period of time corresponds to about half of the temporal resolution of our monthly time series, which is why we considered using the middle ICESat campaign date a sufficient approximation for this analysis.

Finally, for each individual ICESat laser shot (point data), we performed a spatial bilinear interpolation of our elevations $h_{GP}(t,x,y)$ (gridded data) to estimate the elevation $h_{GP}(t_{ICS},x_{ICS},y_{ICS})$ at the center of each ICESat footprint (x_{ICS},y_{ICS}).

3.2. Comparing to IceBridge

For IceBridge elevations, we bilinearly downsampled our two sets of IceBridge elevations $h_{ICB}(t,x,y)$ (DMS-based and lidar-based) to 50 m (half the horizontal resolution of our time series). This resampling aimed simply at reducing the large amount of repeat spatial samples while conserving the vertical precision of the data. We then extracted elevations at the center of each pixel containing valid data, and subsequently compared to our interpolated time series by estimating $h_{GP}(t_{ICB},x_{ICB},y_{ICB})$ using the same procedure as described for ICESat data.

3.3. Systematic errors

We intersected over ten million ICESat and a hundred million IceBridge measurements in space and time with our interpolated elevation time series on both glacierized and stable terrain. We annotate validation elevations composed of both ICESat and IceBridge h_{IC}.

$$\Delta h_{GP/IC} = h_{GP} - h_{IC} \tag{S8}$$

To assess whether our elevation estimates were unbiased, we studied the median of elevation differences $\Delta h_{GP/IC}$. For all statistical operations, IceBridge points - about 40 times more dense spatially than ICESat points - were weighted at 1/40th of ICESat points to represent a comparable spatial sampling.

On average, glacierized terrain was found to be lower than true elevation, while stable terrain was slightly higher (Fig. S4a,b). These biases between stable terrain and glacierized terrain varied between regions (Table S3) and seasons (Fig. S4c). Our reference, TanDEM-X was also found to be higher over stable terrain, while we previously described the absence of vertical shift with ICESat (Section 3.1). The reason for this difference is that terrain here is limited to a 10 km buffer around glaciers instead of the whole region.

We attributed these biases to snow cover, originating from two distinct sources. First, we explained the seasonal variations by the fact that snow-covered terrain is not masked out from stable terrain during co-registration of the ASTER, ArcticDEM and REMA DEMs (Fig.

S5). The varying height of snow-cover in those DEMs directly leads to the observed seasonal biases. Second, we attributed the average differences between stable, glacierized terrain and our reference TanDEM-X to the fact that TanDEM-X has no defined timestamp but is a mosaic of different seasons, which also unevenly contains snow-covered terrain (Fig. S5a). At present, the lack of a homogeneous and global DEM with a well-defined seasonal timestamp prevents correcting these issues to improve the co-registration in regards to snow-covered terrain.

In order to derive volume change, our interest however lies in elevation change and not absolute elevation. Thus, the mean elevation bias between stable and glacierized terrain does not have an impact on elevation differences. The seasonal cycle of this bias has a systematic impact on seasonal elevation differences, however. We estimated this seasonal bias of co-registration by fitting a sinusoidal function (Fig. S4c ; Table S3). These sinusoidal fits revealed that the maximum and minimum bias occurred symmetrically around the dates of September 30th and March 30th for the Northern and Southern hemispheres, agreeing with prior knowledge. Additionally, the amplitude of the snow-cover biases were found to be relatively small for Arctic regions (RGI regions 3, 4, 5, 7, 9), large for mountainous areas (RGI regions 2, 8, 11, 12, 13, 14, 15, 17, 18) and absent in the Tropics (RGI region 16) (Table S3).

We used these sinusoidal fits to remove the seasonal biases in our elevation differences for further validation purposes. We derived a linear trend (WLS) in time from the remaining differences to ICESat and IceBridge (Extended Data Fig. 4d). We thereby verified the absence of elevation change bias in our GP time series globally and along several variables of interest. Less sampled regions yield larger trends, but do not statistically differ from zero (Table S3).

We also identified elevation biases with curvature (Fig. S4d), on both stable and glacierized terrain. This bias was also observable when differencing to the reference DEM TanDEM-X on stable terrain, suggesting that it originates from an inherent difference between the datasets rather than our temporal interpolation method, as shown in previous studies[69]. The lower resolution of our DEMs does not allow us to reliably capture elevation in places of high curvatures such as peaks, ridges or narrow valleys. Being independent of time, this bias does not need to be accounted for when differencing the elevation time series into elevation change and does not affect our glacier mass balance estimates.

3.4. Random errors

For each ICESat and IceBridge observation, we also derived a z-score, or elevation difference divided by our time series error at a given point of time and space:

$$z_{GP/IC} = \frac{(h_{GP} - h_{IC})}{\sigma_{h_{GP}}} \tag{S9}$$

This standardized metric allows us to compare the performance of the elevation time series h_{GP} in relation to its GP credible interval $\sigma_{h_{GP}}$ which varies significantly in space and time

based on factors such as elevation measurement errors, number of observations, or time lag to the closest observations (Figs. S2, S3). Ideally, for a performant interpolation method, the z-score would be normally distributed, centered on 0 with a standard deviation of 1. A mean of 0 would signify that our elevation estimates h_{GP} are unbiased and a standard deviation of 1 would signify that our modelled error $\sigma_{h_{GP}}$ is representative of the elevation error at the right confidence level.

We used the NMAD as a robust estimator of the standard deviation of the z-score distribution (Fig. S6). The standard deviation of z-scores was verified to be independent of several factors: the terrain slope, the terrain curvature, the time of the year, the time lag to the closest elevation observation, and the size of the GP credible interval. The lack of dependency on these two last factors validates the reliability of our empirically-based GP parameters (Section 2.5). The z-score standard deviation was found to be very close to 0.5 for glaciers (Fig. S6, Extended Data Fig. 4d) and close to 1 for stable terrain (Table S3) in all regions, implying that our GP method is able to estimate elevation in space and time at the right confidence level. Over glaciers, our elevation uncertainties are thus conservative by a factor of over two.

4. Spatial correlation of elevation change time series

We identified three sources of correlation to account for when propagating uncertainties from our elevation change time series into volume change time series. The first source is the short range spatial correlation originating from instrument resolution (Section 4.1). The second is the long range spatial correlation originating from instrument noise, generally not accounted for in earlier studies (Section 4.2). The third and final source originates from our temporal interpolation (Section 4.3). We accounted for these three sources of spatial correlation when aggregating both from pixels to individual glaciers and from glaciers to regional volume change estimates (see Aggregation to regions in Methods).

4.1. Spatial correlation due to instrument resolution

Conservatively, we estimated spatial uncertainties that originate from instrument resolution solely on ASTER, which has the coarsest resolution. We derived a short-range spatial variogram[80] over ASTER DEMs to assess the short-range spatial correlation that can be attributed to the effects of spatial resolution $\sigma_{dh,res}$:

$$\sigma_{dh,res}(d)^2 = S(d, s_0, r_0) \quad \text{(S10)}$$

where d is the spatial lag, or distance between pixels, $S(d, s, r)$ the spherical model of partial sill s and range r. We found a range of $r_0 = 150$ m. The partial sill s_0 derived in our spatial variograms is only a representative average of the many factors affecting elevation variance (Section 2.3). Instead of using this average, we estimated s_0 from our individual pixel errors

$\sigma_{dh_{GP}}$ over glacierized terrain after removing contributions from longer range correlations (described in Section 4.3).

4.2. Spatial correlation due to instrument noise

We accounted for long-range correlations due to instrument noise, such as the ones present in ASTER DEMs that we described in Section 1[50,82]. Depending on the distribution of stable terrain in a specific DEM, it can be difficult to fully correct the low-frequency along-track undulations, and even more so for the high-frequency along-track undulations (also called "jitter")[83]. We know from ASTER corrections that the low-frequency along-track undulation has a range of about 5 to 20 km, while the jitter has a range of 2 km. Residuals from this correlated noise can be described by a sum of nested spatial variograms at these correlation lengths with specific variances, which in turn can be used to derive the uncertainty in the volume changes obtained by spatial aggregation[72].

In order to account for improvements brought by corrections (Section 1), filtering and interpolation (Section 2) we deduced our spatial correlations directly from the elevation differences to ICESat and IceBridge data $\Delta h_{GP/IC}$ (Section 3). The procedure for estimating the spatial correlation is the same as used for longer range correlation which is described extensively in the next section. We modelled our empirical variogram by a sum of spherical variograms $\sigma_{dh,noise}$ with correlation lengths of 2 km, 5 km and 20 km:

$$\sigma_{dh,noise}(d)^2 = S(d, s_1, r_1) + S(d, s_2, r_2) + S(d, s_3, r_3) \quad \text{(S11)}$$

with $r_1 = 2$ km, $r_2 = 5$ km and $r_3 = 20$ km.

The sills we estimated indicate that, for the average ASTER DEM, we corrected on average around 90% of the typically observed low-frequency along-track undulation of range 20 km, and about 70% of the high-frequency undulation (jitter) of range 2 km.

4.3. Spatial correlation due to temporal interpolation

Previously, we treated our elevation time series uncertainty $\sigma_{h_{GP}}$ as a random error term (Section 3.4), but this qualification does not always hold. Because of the nature of the spatial coverage of DEMs, temporal data gaps are often spatially correlated over large areas. Although we know that our GP credible interval $\sigma_{h_{GP}}$ contains the true elevation at the right confidence level, the elevation difference to the true elevation might be spatially correlated. For example, let's assume that there are three years without data for the entire region of Svalbard and that we independently interpolate all pixels of the region in time. Assume also that in the middle of that period, one winter had stronger accumulation than usual. At this point in time, our GP credible interval might still contain the true values of glacier elevations at the pixel scale (Figs. S2, S3), but at the regional scale this stronger accumulation manifests as a systematic error, or as a random error correlated over large distances.

We accounted for the spatial correlation inherent to the temporal interpolation to correctly propagate uncertainties into the resulting volume changes. For this, we used the ICESat validation data only, which has a more diverse regional coverage than IceBridge. We categorized our validation elevation differences $\Delta h_{GP/ICS}$ by date, corresponding to ICESat campaigns. For each campaign, at the pixel scale, we also categorized $\Delta h_{GP/ICS}$ by time lag $\Delta t_{AST/WV}$. The time lag is the time between the ICESat acquisition and the closest valid ASTER/WV observation $h_{AST/WV}(t_{AST/WV}, x, y)$ used to derive the time series during the temporal interpolation:

$$\Delta t_{AST/WV}(t, x, y) = \left| t - t_{AST/WV} \right| \tag{S12}$$

For each region, date and time lag bin, we randomly drew up to 10,000 observations of validation elevation differences $\Delta h_{GP/ICS}$ and quantified their spatial correlation[81]. We did so by computing their variance correlations at distances of 0.15 km, 2 km, 5 km, 20 km, 50 km, 200 km and 500 km (Extended Data Fig. 5a,b). The first four ranges of 0.15 km, 2 km, 5 km and 20 km correspond to the correlation ranges for instrument resolution and instrument noise (preceding sections). We found similar variograms between well-sampled regions and chose to aggregate and apply a single variogram globally for robustness in less-sampled regions. This approach is expected to be conservative for instrument noise, due to the larger residuals of correlated signals captured over large ice caps (corrected with less stable terrain) that dominate the ICESat sample. Aggregating all available variograms, we derived the median variance of elevation differences $\Delta h_{GP/IC}$ at different correlation lengths depending on the time lag to the closest observation. We showed that there was no significant correlation in the variance beyond 500 km, a finding consistent with known estimates of correlations of glacier mass balances[77], and we thus considered elevation differences to be independent beyond this range. We modelled these correlations as a sum of spherical variograms:

$$\sigma_{dh}(d, \Delta t)^2 = \sum_{i=0}^{6} S(d, s_i(\Delta t), r_i) \tag{S13}$$

where $r_4 = 50$ km, $r_5 = 200$ km. We found $s_6(\Delta t) = 0$ for $r_6 = 500$ km. The partial sills s_0 to s_5 depend on the time lag to the closest valid observation Δt. For s_1 to s_5, we used the empirical values of the partial sills to estimate it as a function of the time lag. We found a good fit between the complete sills (sum of partials sill) and a sum of quadratic and squared sinusoidal functions by least squares optimization (Extended Data Fig. 5b):

$$\sum_{i=1}^{k} s_i(\Delta t) = (a_k \cdot \Delta t + b_k)^2 + c \cdot sin(d \cdot \Delta t)^2 \tag{S14}$$

where we found two constants for the sinusoidal component $c = 1.4$ m^2 and $d = 1$ yr. At $\Delta t = 0$, we deduced the values of $s_1(0)$, $s_2(0)$ and $s_3(0)$ described in the previous section on instrument noise.

We accounted for the random error due to instrument resolution, represented by the partial sill s_0 at a correlation length of $r_0 = 150$ m, using the original pixel error $\sigma_{dh}(t,x,y)$. To avoid double-counting errors in s_0, we quadratically subtracted the partial sills of range r_1 to r_5 to $\sigma_{dh}(t,x,y)$:

$$\sigma_{dh,0}(t,x,y)^2 = \sigma_{dh}(t,x,y)^2 - \sum_{i=1}^{6} s_i(\Delta t) \quad \text{(S15)}$$

For each glacier and time step, we used the mean of all pixel errors $\sigma_{dh,0}{}^2$ over glacierized terrain to estimate s_0. We then spatially integrated this sum of variograms[72] over each glacier, for each time step, accounting for each individual glacier pixel's distance to the closest observation Δt at this time step to yield the uncertainty in the mean elevation change $\sigma_{\overline{dh}}$ (see Methods, Equations 4 and 5).

Supplementary Discussion

Improved elevation change estimation

Our surface elevation change maps (Extended Data Fig. 6, and Data availability statement) visually testify to the improved quality brought out by our novel methodology in comparison to preceding ASTER-based studies[28,53,54,74]. It is most notable through the reduction of elevation change outliers and through stable terrain surfaces that consistently show elevation changes close to 0 m. The improved quality and increased spatial coverage is the combined result of (i) the inclusion of low stereo-matching correlation data that is statistically weighted, (ii) a multi-step filtering of outliers conditioned by a reference elevation model, an elevation measurement error and temporal covariances throughout the different steps of our statistical modelling approach, (iii) the mitigation of seasonality, and other non-linear responses during the final interpolation into surface elevation time series. Although having fewer data gaps than preceding studies, our time series of elevation change still contain uncertainties that vary in space and time for different regions, periods, and for different areas of a given glacier (e.g. low-contrast accumulation areas). Stable terrain is not directly comparable to glacierized terrain, as it only includes a pairwise linear kernel and a periodic kernel during GP regression (i.e. a linear trend with mitigated seasonality). Non-linear kernels were not applied to stable terrain as those were estimated using glacier elevation observations only, non-applicable to other types of terrain (bare-ground, vegetated, ...). Nonetheless, the linear estimation allows similar 20-year changes to be captured at the boundary of glacierized and stable terrain. For instance, unmapped debris-covered tongues treated as stable terrain show long-term elevation changes consistent with the rest of the glacier.

Subaqueous mass loss

Our analysis is limited to measuring glacier elevation change above water by assessing only topographic changes and not bathymetric ones. The subaqueous mass loss due to retreat of ice fronts over water for marine- or lake-terminating glaciers cannot be captured, leading to an underestimation of the total glacier mass loss[29]. This omitted underwater contribution is largely dominated by marine-terminating glaciers, however, and thus does not impact the contribution to sea-level rise. This limitation is shared between geodetic, gravimetric (for marine-terminating glaciers) and altimetric (ICESat) estimates.

Time series comparison and temporal resolution

We compare our results to the time series of previous studies[19,21] (Fig. S7) and, for this exercise, use the same density conversion factor and errors for annual mass change rates despite the known limitations of density conversion assumptions at such short time scales[23]. We find good agreement to gravimetric time series[19] in regions where competing mass change signals are weak (e.g., Russian Arctic), and to geodetic and glaciological-based time

series in regions with dense in-situ measurements[21]. At the regional scale, we generally observe a temporal autocorrelation, or "smoothing" of extreme glaciological years in our time series, either due to the limits of local and seasonal elevation change deconvolution from our Gaussian Processes method (where repeat data coverage is good, e.g. Iceland), or originating from the near-linear interpolation over long observational data gaps (where data coverage is more limited). In practice, the rapid change of extreme years is redistributed into adjacent years. This effect is accounted for by our improved uncertainty approaches calibrated on spatial correlations with observational time lag, validated with high-resolution data (Extended Data Fig. 5d-f). Based on our volume change uncertainties, the temporal resolution at which volume changes are statistically significant at the regional scale (95% confidence interval <0.2 m yr^{-1}) is of 3-7 years depending on the spatial domain and temporal coverage. This is confirmed by the inter-comparison to regional estimates of temporally resolved, gravimetric studies.

Decadal changes in summer temperature and winter precipitation

For the Northern Hemisphere, we define winter to coincide with the accumulation period which, for high-altitude glaciers is typically October-April whereas we define the summer season to include the months May-September. Winter and summer seasons in the Southern Hemisphere are respectively defined as the months April-October and November-March. Decadal changes between annual and seasonal components show minor differences of precipitation patterns (Fig. S8). However, the increase of summer temperature over glaciers (corresponding to a global trend of 0.037 K yr^{-1}) is slightly larger than that of annual temperature (0.031 K yr^{-1}) and thus yields a slightly lower global mass balance sensitivity to temperature of -0.24 m w.e. yr^{-1} K^{-1}. We also find little difference in temperature and precipitation change conditions between tidewater and non-tidewater glaciers aggregated at the global-scale.

Uncertainty propagation and limits of density-based mass change uncertainties

Volume change uncertainties sources are dominated by short- to long-range spatial correlations (2-200 km) and our pixel-wise GP uncertainties only have influence for very small glaciers (<0.1 km^2, Extended Data Fig. 5h,g). While our volume change time series have rigorously constrained uncertainties (Extended Data Fig. 5d-f), density-based mass change uncertainties are still poorly known. We thus use conservative approaches that likely lead to an overestimation of mass change uncertainties. We conservatively applied our uncertainties by considering them completely correlated in space at the scale of RGI regions, which leads to larger regional mass change uncertainties than previous DEM-based studies[29,53,54] that considered subregions of RGI regions as independent. Additionally, the current formulation of the density uncertainty[23] linearly scales with specific elevation changes while it is known that it is with most negative elevation change rates that the density conversion factor is best constrained towards 850 kg m^{-3}. This effect likely provides uncertainties that are too large, especially for regions with strong mass losses (e.g., Fig. 3).

Supplementary Figures

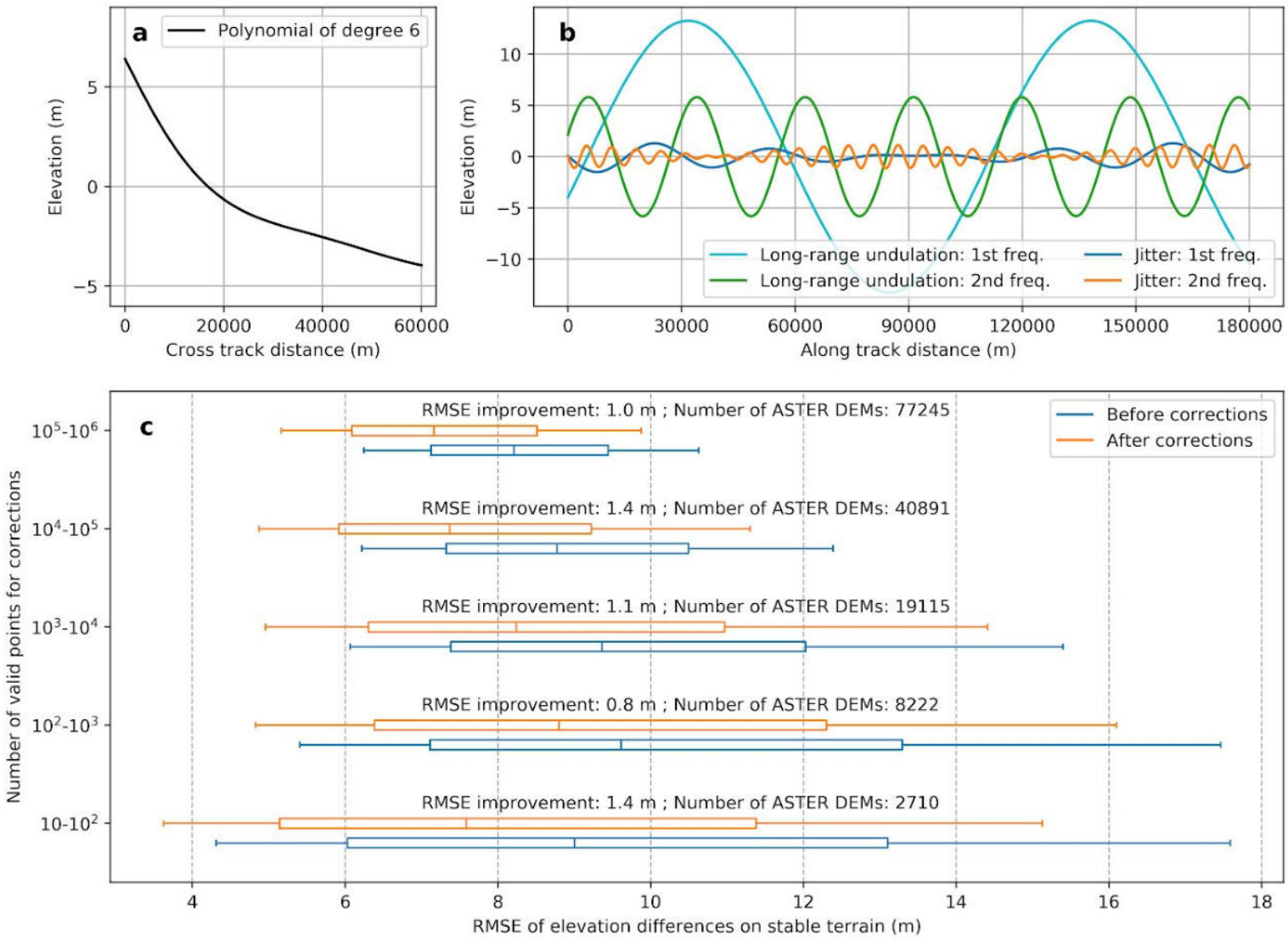

Fig. S1. ASTER bias corrections.

MMASTER corrections[50] for cross-track (**a**) and along-track biases (**b**) and overall (**c**). For (**a**) and (**b**), elevation corrections shown correspond to the median of parameters (i.e. the most typical case of correction, which vary greatly between images) found when optimizing corrections individually for 154,565 ASTER DEM strips. For the along-track corrections, we show the median of parameters decomposed by additive frequencies of long range undulations and jitter. **c**, Boxplots of off-ice RMSE between ASTER DEMs and the reference TanDEM-X before (blue) and after (orange) bias correction with the number of valid points for corrections. Boxes show the distribution from first to third quartiles, with the median represented as a line and the whiskers extending to the 10th and 90th percentiles. RMSE improvement is a limited but simple indicator of the underlying removal of large-scale correlated noise on top of the inherent random noise, typically observed at an amplitude of 5 to 10 m in ASTER DEMs. Most DEMs are confidently corrected with a large number of points which reflects in their lesser spread of RMSE, later used to assess measurement error and weighting.

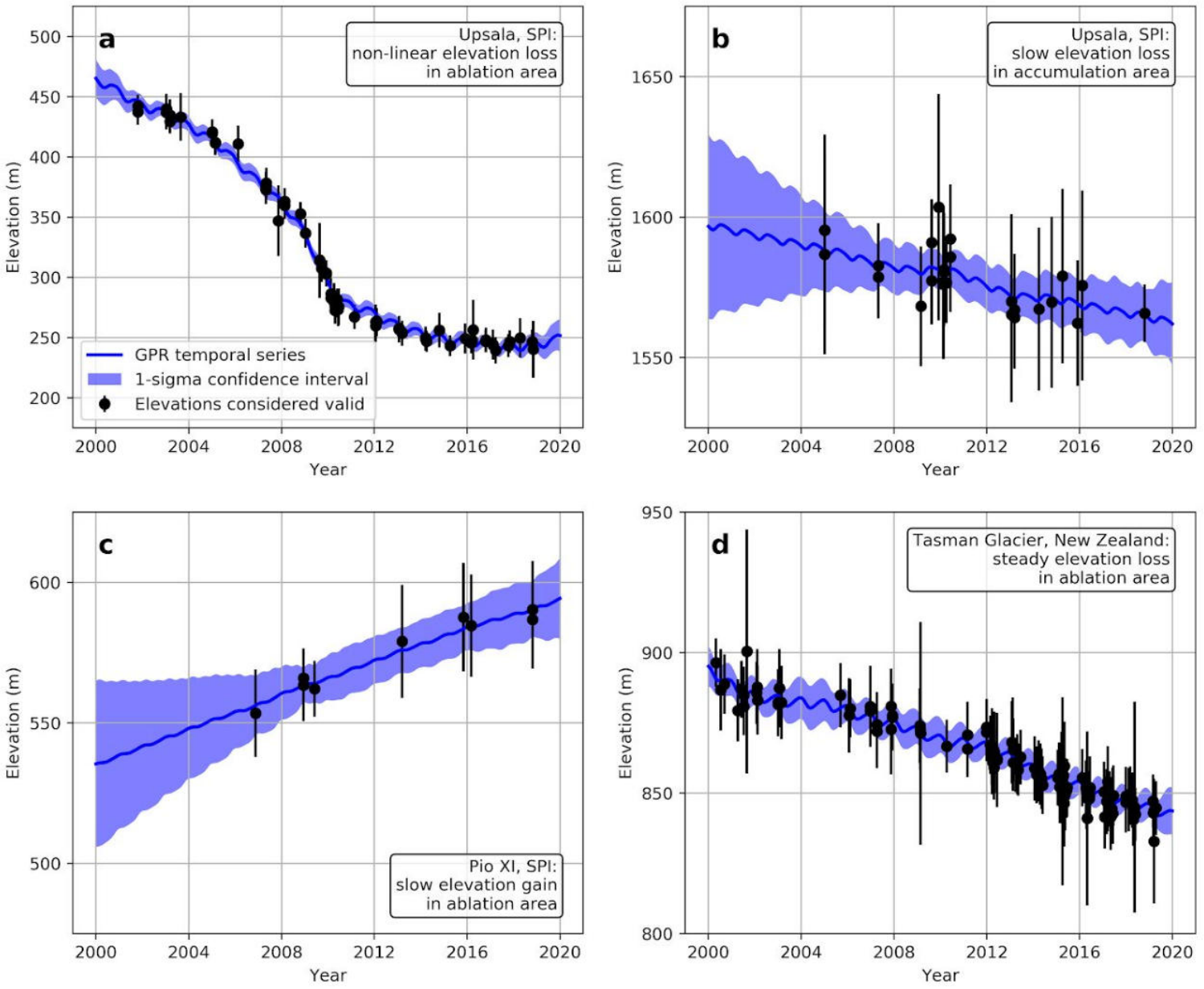

Fig. S2. Gaussian Process regression elevation time series.

Time series of final Gaussian Process Regression fits and standard deviation after the removal of outliers. These temporal fits are shown for: a pixel in the ablation area of Upsala where a strongly nonlinear elevation loss occurred[99] which is used as an example in Extended Data Fig. 3c-e (**a**), a zone of low quality of stereo-correlation in the accumulation area of Upsala, Southern Patagonian Icefield, Argentina that is undergoing slow elevation loss (**b**), the data-scarce ablation area of Pio XI, Southern Patagonian Icefield, Chile, facing a steady elevation gain (**c**) and the highly sampled tongue of Tasman Glacier, New Zealand showing steady elevation loss (**d**).

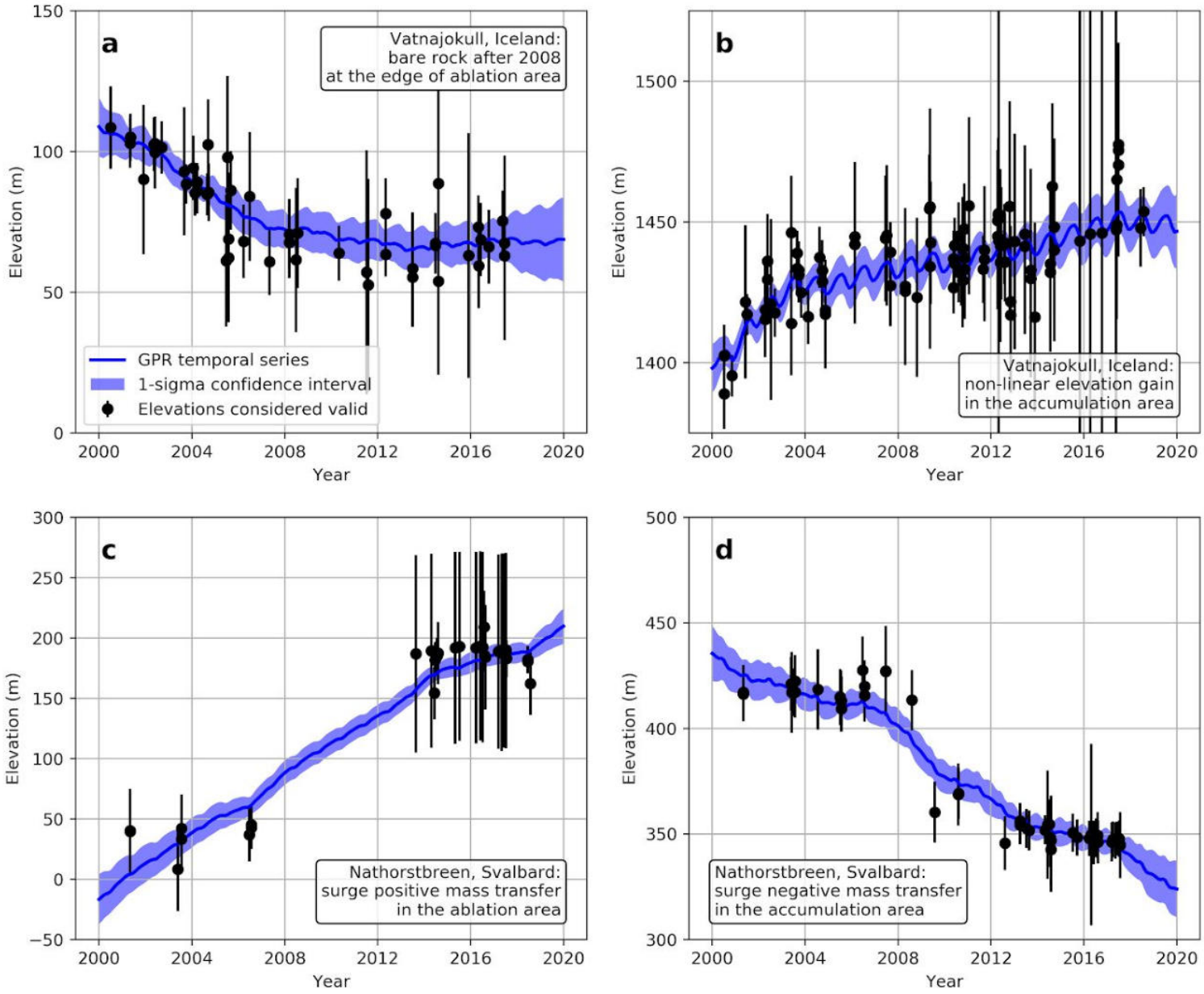

Fig. S3. Gaussian Process regression elevation time series for extreme observations.

Time series of final Gaussian Process Regression fits and standard deviation over extreme elevation observations, after the removal of outliers. We show pixels in: the edge of the ablation area of outlet glacier Breidamerkurjökull of Vatnajökull, Iceland, showing rapid thinning and then no elevation change after 2008 due to complete deglaciation (**a**), the nonlinear thickening on the outlet glacier Dyngjujökull, in the accumulation area of Vatnajökull, Iceland (**b**), the elevation gain at the bottom of Nathorstbreen glacier, Svalbard, after a massive surge in 2009[40] (**c**) and the mass loss in the accumulation area of Nathorstbreen glacier, Svalbard, from the same surge event (**d**).

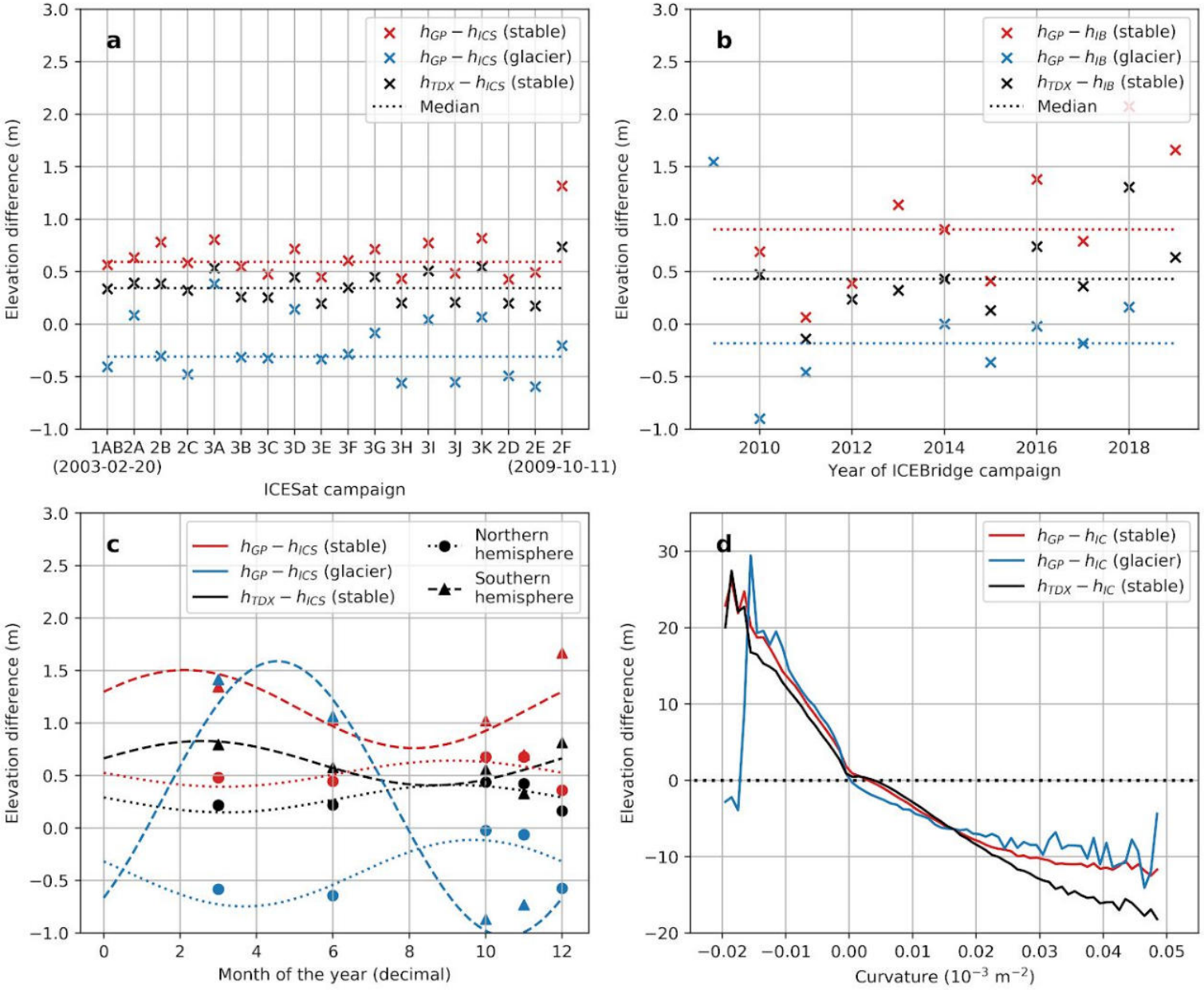

Fig. S4. Systematic error analysis.

Median elevation differences between ICESat/IceBridge and our GP regression elevation time series on stable and glacierized terrain, and for TanDEM-X on stable terrain. Elevation differences are shown globally for all ICESat campaigns (**a**), all IceBridge campaigns (**b**), seasonal timestamps independently for the Northern and Southern hemisphere (ICESat samples only, Antarctic and Subantarctic excluded) (**c**) and terrain maximum curvature (**d**). Panels (**a**), (**b**) and (**c**) are shown on the same scale.

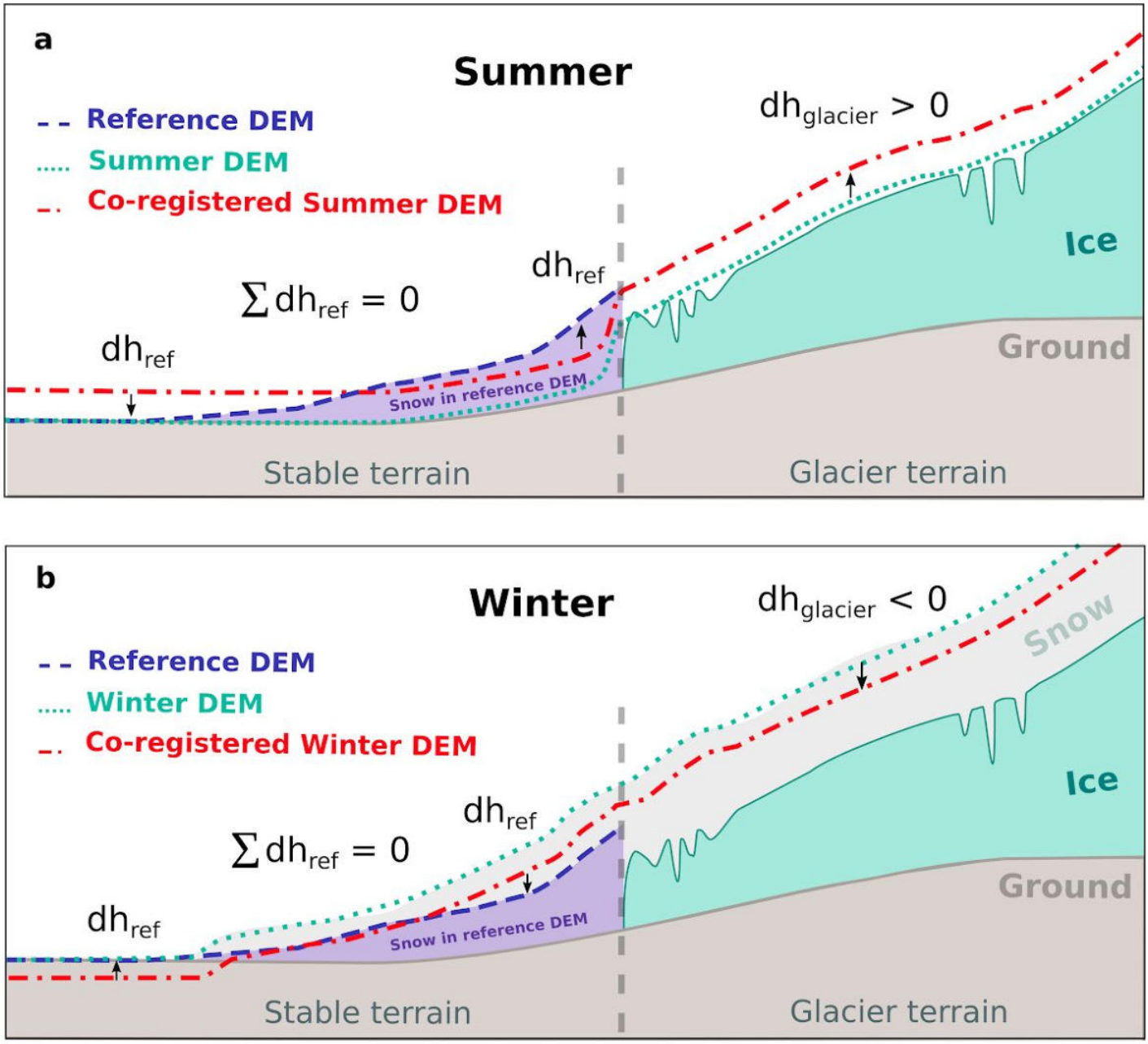

Fig. S5. Schematic representation of the effects of snow-covered terrain on co-registration.

Summer and winter co-registration biases. **a**, The coregistration of summer ASTER DEMs to a reference DEM (TanDEM-X) that includes snow cover on stable terrain creates a positive elevation bias over glaciers. **b**, The coregistration of winter ASTER DEMs to a reference DEM (TanDEM-X) that, on average, includes less snow, creates a negative elevation bias over glaciers.

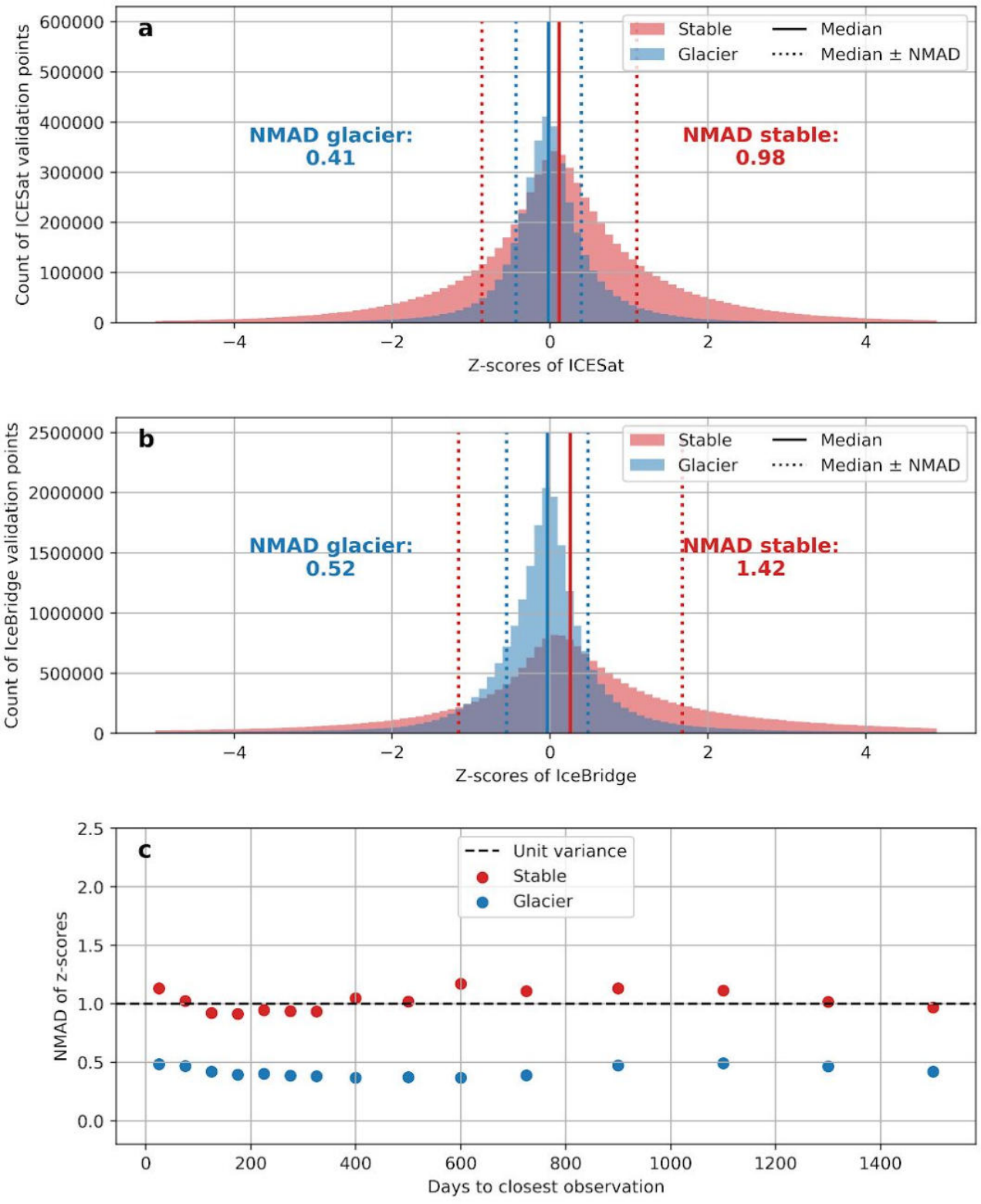

Fig. S6. Random error analysis.

Distribution of z-scores of elevation differences for stable and ice-free surfaces. The distribution of ICESat (**a**) and IceBridge (**b**) z-scores for stable and glacierized terrain with the corresponding median and Normalized Median Absolute Deviation. **c**, NMAD of the z-score with the time lag to the closest observation. IceBridge points are weighted 1/40th to represent similar spatial sampling as ICESat points.

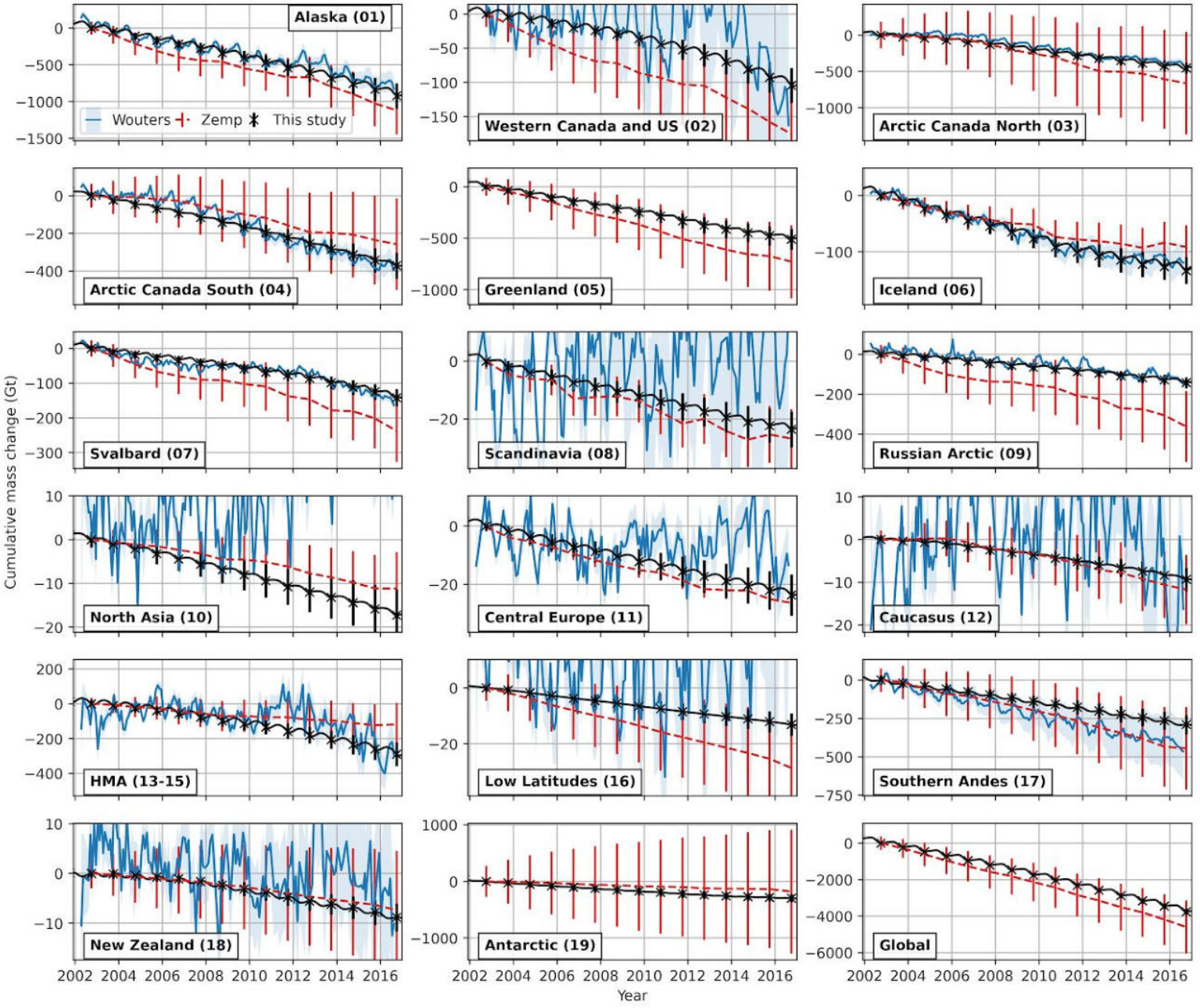

Fig. S7. Comparison of mass change time series with earlier studies.

Regional and global time series of cumulative glacier mass change between 2002 to 2016 compared to earlier global or near-global studies[19,21]. Time series are zeroed at the starting date of September 2002 to coincide with the northern hemisphere glaciological years reported in an earlier global study[21]. Uncertainties are shown at 95%. For our study, we show annual uncertainties despite known limitations for density assumptions and show our monthly time series uncorrected for seasonal biases.

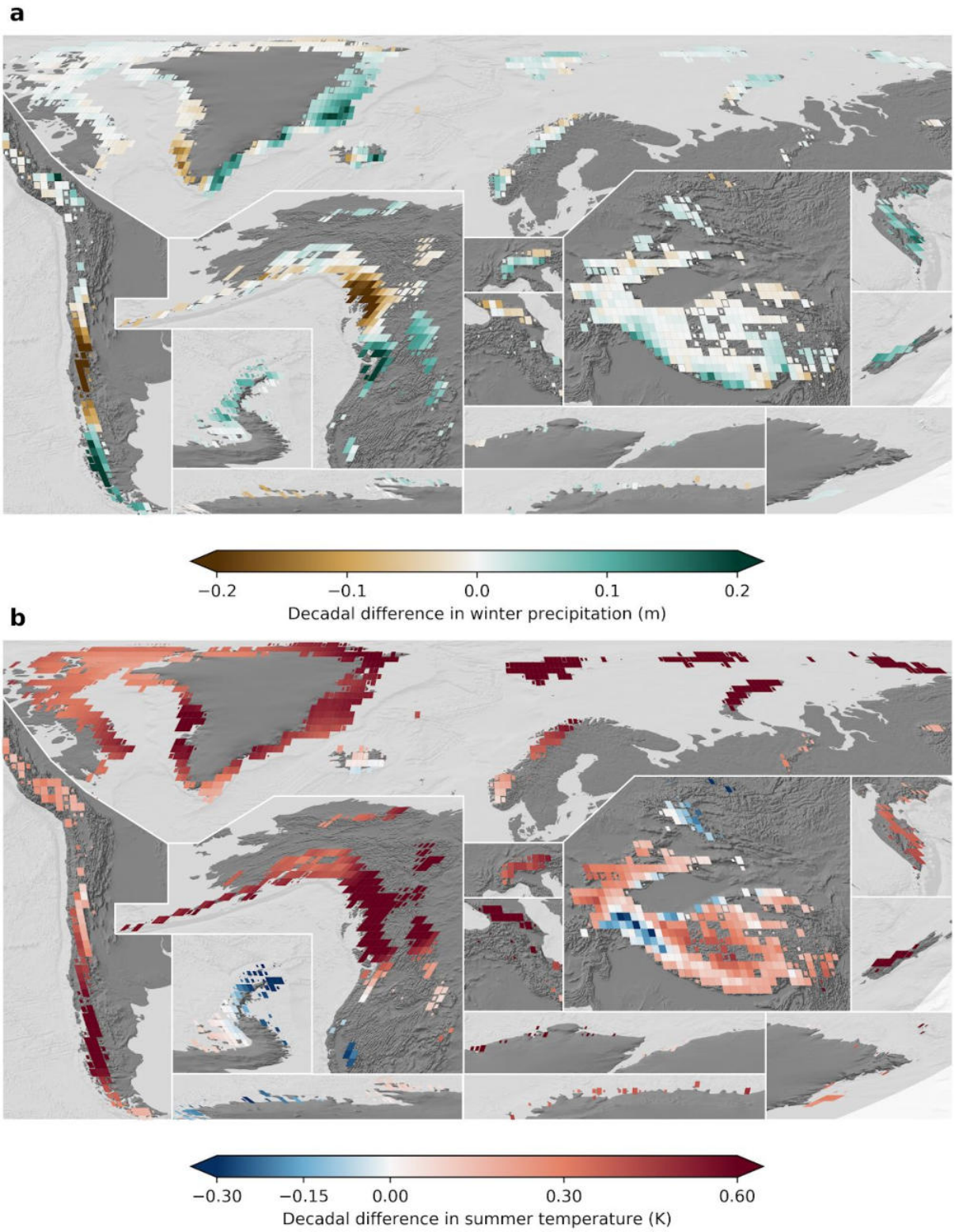

Fig. S8. Decadal changes in summer temperature and winter precipitation.

Difference between 2010-2019 and 2000-2009 for summer temperature (May-September in the northern hemisphere, October-April for southern hemisphere) (**a**) and winter precipitation (November-March in the northern hemisphere, April-October in the southern hemisphere) (**b**). Decadal patterns are similar to those of annual temperature and precipitation (Fig. 4).

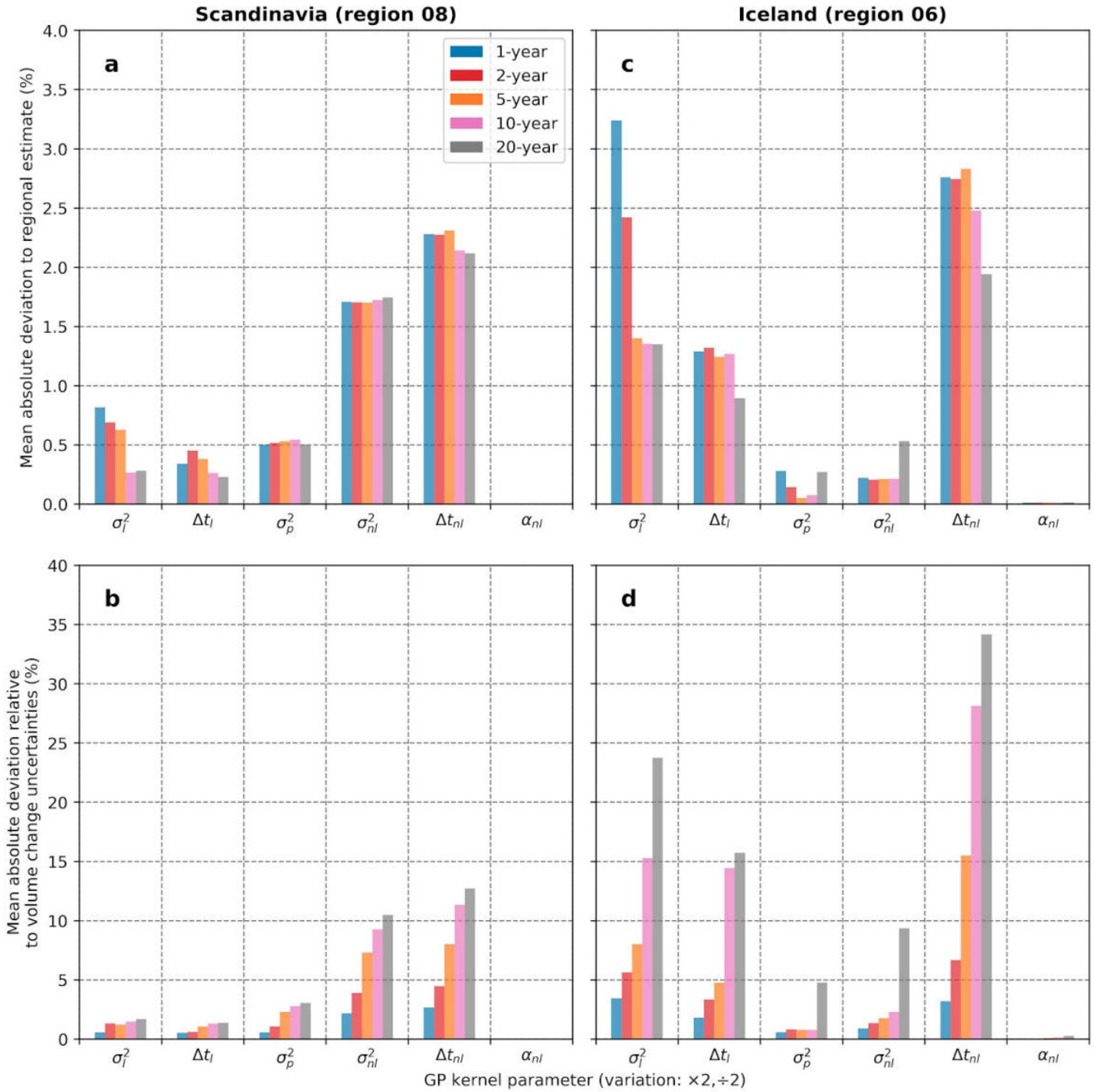

Fig. S9. Sensitivity to Gaussian Process kernel parameters.

Sensitivity of the regional estimates of glacier volume changes to the Gaussian Process kernels parameters for Scandinavia **(a,b)** and Iceland **(c,d)**. The kernel parameters are varied by multiplying and dividing the value used in this study by 2, and refer to Equation 2 (see Methods, or Supplementary Methods section 2.5). Iceland and Scandinavia were selected as they are potentially the most sensitive to Gaussian Process kernel parameters. This is due to both their small size (spatially correlated signal) and the fact that they show strong nonlinear changes during the past two decades (Extended Data Table 1). Additionally, they

include a wide spectrum of temporal coverage, as Iceland is the region with the largest repeat coverage (~66 observations in 20 years per pixel) while Scandinavia is the region with the lowest repeat coverage (~27 observations in 20 years per pixel), excluding the Antarctic and Subantarctic. Panels **(a)** and **(c)** show the mean absolute deviation relative to the regional estimate and panels **(b)** and **(d)** the mean absolute deviation relative to the estimated volume change uncertainty. The mean absolute deviation is computed from all possible successive time periods of a certain length in 2000-2019 (e.g., 5-year periods indicate 2000-2004, 2005-2009, 2010-2014 and 2015-2019) and varied parameters (x2,÷2). Overall, varying all Gaussian Process kernel parameters within this order of magnitude impacts the estimates less than 3%, which is well within estimated volume change uncertainties (at most 30% of uncertainty range) and estimated mass change uncertainties (at most 10% of uncertainty range). The maximum absolute deviation is within the same range and does not exceed 1.5 times the mean absolute deviation.

Supplementary Tables

Region	ASTER initial DEMs	ASTER final DEMs	ArcticDEM & REMA final DEMs	ICESat points	IceBridge DEMs
01, 02 Alaska & Western Canada and USA	28,705	24,681	3,763	1,137,548	273
03 Arctic Canada North	9,610	7,645	4,209	2,220,084	78,434
04 Arctic Canada South	3,702	3,013	2,832	584,499	39,113
05 Greenland	24,290	16,837	14,353	2,375,214	334,721
06 Iceland	3,439	2,569	701	72,811	0
07 Svalbard and Jan Mayen	2,870	1,750	3,507	350,053	4,882
08 Scandinavia	3,432	2,770	1,143	16,157	0
09 Russian Arctic	9,137	4,485	5,635	596,456	0
10 North Asia	15,693	12,867	4,248	309,226	0
11 Central Europe	4,499	4,304	0	2,277	0
12 Caucasus and Middle East	5,745	5,563	0	31,580	0
13-15 High Mountain Asia	31,676	30,774	0	2,169,746	0
16 Low Latitudes	15,689	14,800	0	61,845	0
17 Southern Andes	9,076	8,124	0	237,559	495
18 New Zealand	2,221	1,922	0	13,998	0
19 Antarctic and Subantarctic	28,555	12,461	3,456	559,639	154,770

Table S1. Regional data coverage for ASTER, ArcticDEM, REMA and IceBridge DEMs.

Number of DEMs and corresponding area covered for RGI regions. ASTER initial DEMs are the strips generated from stereo imagery. ASTER, ArcticDEM and REMA final DEMs are the DEM strips successfully corrected (for ASTER), merged (for ArcticDEM and REMA) and co-registered to TanDEM-X (for both). ASTER initial and final DEM footprint is generally 180 km x 60 km, ArcticDEM and REMA DEM footprint is on average 50 km x 15 km and IceBridge DEMs 500 x 500 m. ICESat points are only considered in a buffer of 10 km around glaciers, the count of points on glacier and stable terrain is reported in Table S3.

Region	Site	Early DEM date	Early DEM source	Late DEM date	Late DEM source	Resolution (m)	Glacier area (km²)	Number of glaciers covered
01 Alaska	Yukon	2007-09-03	SPOT-5HRS	2018-10-01	SPOT6/7	20	2387.4	139
02 Western Canada and USA	Place	2006-08-15	LiDAR	2018-09-04	LiDAR	1	4.9	7
02 Western Canada and USA	Sentinel	2006-08-15	LiDAR	2018-09-04	LiDAR	1	22.3	10
02 Western Canada and USA	Bridge	2006-08-15	LiDAR	2017-09-27	LiDAR	1	142.6	23
02 Western Canada and USA	Weart	2006-08-15	LiDAR	2018-09-04	LiDAR	1	12.8	9
02 Western Canada and USA	Conrad	2005-07-31	Aerial Photo	2017-09-17	Aerial Photo	5	19.4	11
02 Western Canada and USA	Nordic	2004-08-21	Aerial Photo	2017-09-27	Aerial Photo	5	5	3
11 Central Europe	Mont Blanc	2003-08-21	SPOT5-HRG	2018-08-09	Pleiades	10	141.1	105
11 Central Europe	Gries	2012-08-27	Aerial Photo	2018-08-19	Aerial Photo	1	6	10
11 Central Europe	Silvretta	2012-08-20	Aerial Photo	2018-08-16	Aerial Photo	1	6.8	7
11 Central Europe	Plaine Morte	2012-09-14	Aerial Photo	2018-08-28	Aerial Photo	1	11.6	10
11 Central Europe	Aletsch	2009-09-08	Aerial Photo	2017-08-29	Aerial Photo	25	120	61
11 Central Europe	Gorner	2007-09-13	Aerial Photo	2015-08-26	Aerial Photo	25	54.1	8
11 Central Europe	Rhone	2000-08-24	Aerial Photo	2007-09-12	Aerial Photo	25	16	6
11 Central Europe	Morteratsch	2008-09-09	Aerial Photo	2015-08-29	Aerial Photo	25	17	14
11 Central Europe	Unteraar	2003-07-14	Aerial Photo	2009-08-19	Aerial Photo	25	23.9	6
13 Central Asia	Abramov	2003-08-27	SPOT5-HRS	2015-09-01	Pleiades	40	114.7	121
14 South Asia West	Mera	2012-11-25	Pleiades	2018-10-28	Pleiades	4	33.6	44
14 South Asia West	Chhota Shigri	2005-09-21	SPOT5-HRG	2014-09-26	Pleiades	10	97.9	65
15 South Asia East	Gangotri	2004-11-26	SPOT5-HRG	2014-08-25	Pleiades	10	199.9	17

Table S2. High-resolution DEMs.

High-resolution DEM pairs used to validate glacier volume changes and their related uncertainty propagation. Only glaciers covered over more than 70% of their surface are considered. A minimum time interval of 5 years between the DEMs was chosen, corresponding to the length of the periods reported in our study.

RGI Region number	*Glacierized terrain (Stable terrain)*						
	ICESat points	IceBridge points	Elevation bias			Elevation change bias (m yr^{-1})	Standardized elevation uncertainty
			Amplitude (m)	Phase (decimal month)	Summer vertical bias (m)		
01	330,297 (658,370)	8,523,287 (463,310)	2.0 (0.1)	5.5 (3.5)	0.8 (1.1)	-0.046±0.033 (0.076±0.055)	0.51 (0.99)
02	30,011 (118,880)	0 (0)	1.8 (0.3)	5.9 (2.8)	2.2 (2.4)	0.035±0.216 (0.043±0.165)	0.54 (1.31)
03	1,139,069 (1,081,015)	4,833,055 (1,789,711)	1.8 (0.9)	6.6 (0.2)	2.1 (-0.6)	0.029±0.048 (0.007±0.104)	0.47 (1.01)
04	178,770 (405,729)	2,060,069 (1,381,223)	0.1 (0.1)	3.2 (1.8)	0.0 (0.5)	-0.001±0.014 (0.013±0.018)	0.32 (0.60)
05	878,141 (1,497,073)	3,150,014 (13,772,122)	0.4 (0.1)	6.3 (1.0)	0.0 (0.3)	0.008±0.014 (0.007±0.018)	0.47 (1.02)
06	27,480 (45,331)	0 (0)	1.3 (0.3)	4.3 (6.2)	1.0 (0.7)	0.023±0.071 (-0.041±0.034)	0.32 (0.77)
07	214,912 (135,141)	179,851 (18,227)	0.6 (0.4)	5.7 (5.5)	0.2 (0.4)	-0.026±0.039 (-0.046±0.037)	0.38 (0.63)
08	5,421 (10,736)	0 (0)	2.3 (0.4)	4.5 (4.3)	1.7 (1.6)	-0.092±0.160 (0.062±0.145)	0.55 (0.97)
09	383,224 (213,232)	0 (0)	0.2 (0.3)	6.0 (5.4)	-0.4 (0.1)	-0.015±0.022 (-0.013±0.014)	0.28 (0.45)
10	3,183 (306,043)	0 (0)	1.4 (0.3)	3.2 (6.0)	1.2 (0.8)	0.206±0.126 (-0.007±0.067)	0.60 (0.93)
11	1,891 (46,722)	0 (0)	1.2 (0.0)	6.2 (4.7)	2.1 (1.5)	0.052±0.263 (0.066±0.189)	0.67 (1.48)
12	929 (30,651)	0 (0)	1.7 (0.4)	6.0 (3.3)	1.3 (0.3)	-0.183±0.440 (-0.031±0.378)	0.69 (1.67)
13	105,218 (1,238,894)	0 (0)	0.5 (0.1)	3.5 (0.9)	1.2 (0.4)	0.110±0.090 (0.018±0.062)	0.68 (1.16)
14	54,382 (423,848)	0 (0)	0.7 (0.0)	3.2 (0.4)	1.4 (0.4)	0.102±0.083 (0.017±0.070)	0.64 (1.15)
15	19,961 (327,443)	0 (0)	0.2 (0.2)	4.3 (1.5)	1.1 (0.5)	0.122±0.106 (0.050±0.074)	0.63 (1.10)
16	897 (60,948)	0 (0)	0.0 (0.4)	2.7 (1.7)	0.3 (1.0)	0.045±0.500 (0.086±0.159)	0.58 (1.14)
17	21,157 (216,402)	109,339 (178,910)	2.5 (1.0)	11.8 (0.8)	2.0 (2.0)	-0.007±0.082 (0.010±0.215)	0.44 (1.29)
18	401 (13,597)	0 (0)	2.5 (0.8)	9.5 (1.2)	-0.4 (2.7)	-0.142±0.671 (0.167±0.685)	0.71 (1.47)
19	445,523 (114,116)	2,208,460 (3,997,523)	0.0 (0.9)	2.2 (3.0)	2.2 (4.4)	-0.004±0.048 (0.150±0.214)	0.33 (1.47)

Table S3. Validation of elevation time series with ICESat and IceBridge.

Elevation biases are decomposed in a sinusoidal function of amplitude, phase at maximum and vertical bias at the end of summer: mid-September for the northern hemisphere (decimal month: 8.5), mid-March for the southern hemisphere (decimal month: 2.5). Elevation change bias is the residual linear trend in time (weighted least squares) of seasonally de-biased mean elevation differences, shown with 95% CI. Standardized elevation uncertainty is the standard deviation of z-scores (conservative if less than 1).

Bibliography

Abdalati, W., Zwally, H.J., Bindschadler, R., Csatho, B., Farrell, S.L., Fricker, H.A., Harding, D., Kwok, R., Lefsky, M., Markus, T., Marshak, A., Neumann, T., Palm, S., Schutz, B., Smith, B., Spinhirne, J., Webb, C., 2010. The ICESat-2 laser altimetry mission. Proc. IEEE 98, 735–751.

Abdel Jaber, W., Rott, H., Floricioiu, D., Wuite, J., Miranda, N., 2019. Heterogeneous spatial and temporal pattern of surface elevation change and mass balance of the patagonian ice fields between 2000 and 2016. The Cryosphere 13, 2511–2535.

Abdullahi, S., Wessel, B., Huber, M., Wendleder, A., Roth, A., Kuenzer, C., 2019. Estimating Penetration-Related X-Band InSAR elevation bias: A study over the greenland ice sheet. Remote Sensing 11, 2903.

Abrams, M., 2000. The advanced spaceborne thermal emission and reflection radiometer (ASTER): Data products for the high spatial resolution imager on NASA's terra platform. Int. J. Remote Sens. 21, 847–859.

Abrams, M., Crippen, R., Fujisada, H., 2020. ASTER global digital elevation model (GDEM) and ASTER global water body dataset (ASTWBD). Remote Sensing 12, 1156.

Abrams, M., Hook, S., others, 2002. ASTER user handbook, version 2.

Altena, B., Scambos, T., Fahnestock, M., Kääb, A., 2019. Extracting recent short-term glacier velocity evolution over southern alaska and the yukon from a large collection of landsat data. The Cryosphere 13, 795–814.

An, L., Wang, J., Huang, J., Pokhrel, Y., Hugonnet, R., Wada, Y., Cáceres, D., Schmied, H.M., Song, C., Berthier, E., Yu, H., Zhang, G., 2021. Divergent causes of terrestrial water storage decline between drylands and humid regions globally. Geophys. Res. Lett. .

Baltsavias, E.P., 1999. Airborne laser scanning: basic relations and formulas. ISPRS J. Photogramm. Remote Sens. 54, 199–214.

Bamber, J.L., Oppenheimer, M., Kopp, R.E., Aspinall, W.P., Cooke, R.M., 2019. Ice sheet contributions to future sea-level rise from structured expert judgment. Proc. Natl. Acad. Sci. U. S. A. 116, 11195–11200.

Bamber, J.L., Westaway, R.M., Marzeion, B., Wouters, B., 2018. The land ice contribution to sea level during the satellite era. Environ. Res. Lett. 13.

Barandun, M., Pohl, E., Naegeli, K., McNabb, R., Huss, M., Berthier, E., Saks, T., Hoelzle, M., 2021. Hot spots of glacier mass balance variability in central asia. Geophys. Res. Lett. 48, e2020GL092084.

Barnes, R., 2016. RichDEM: Terrain Analysis Software.

Bauder, A., Funk, M., Huss, M., 2007. Ice-volume changes of selected glaciers in the swiss alps since the end of the 19th century. Ann. Glaciol. 46, 145–149.

Belart, J.M.C., Berthier, E., Magnússon, E., Anderson, L.S., Pálsson, F., Thorsteinsson, T., Howat, I.M., Aðalgeirsdóttir, G., Jóhannesson, T., Jarosch, A.H., 2017. Winter mass balance of drangajökull ice cap (NW iceland) derived from satellite sub-meter stereo images. The Cryosphere 11, 1501–1517.

Berthier, E., Arnaud, Y., Vincent, C., Rémy, F., 2006. Biases of SRTM in high-mountain areas: Implications for the monitoring of glacier volume changes. Geophys. Res. Lett. 33, 382.

Berthier, E., Cabot, V., Vincent, C., Six, D., 2016. Decadal Region-Wide and Glacier-Wide mass balances derived from Multi-Temporal ASTER satellite digital elevation models. validation over the Mont-Blanc area. Front Earth Sci. 4, 63.

Berthier, E., Schiefer, E., Clarke, G.K.C., Menounos, B., Rémy, F., 2010. Contribution of alaskan glaciers to sea-level rise derived from satellite imagery. Nat. Geosci. 3, 92–95.

Berthier, E., Vincent, C., Magnússon, E., Gunnlaugsson, P., Pitte, P., Le Meur, E., Masiokas, M., Ruiz, L., Pálsson, F., Belart, J.M.C., Wagnon, P., 2014. Glacier topography and elevation changes derived from pléiades sub-meter stereo images. Cryosphere 8, 2275–2291.

Besl, P.J., McKay, N.D., 1992. A method for registration of 3-D shapes. IEEE Trans. Pattern Anal. Mach. Intell. 14, 239–256.

Beyer, R.A., Alexandrov, O., McMichael, S., 2018. The ames stereo pipeline: NASA's open source software for deriving and processing terrain data. Earth and Space Science 5, 537–548.

Bhambri, R., Hewitt, K., Kawishwar, P., Kumar, A., Verma, A., Snehmani, Tiwari, S., Misra, A., 2019. Ice-dams, outburst floods, and movement heterogeneity of glaciers, karakoram. Glob. Planet. Change 180, 100–116.

Bhushan, S., Shean, D., Alexandrov, O., Henderson, S., 2021. Automated digital elevation model (DEM) generation from very-high-resolution planet SkySat triplet stereo and video imagery. ISPRS J. Photogramm. Remote Sens. 173, 151–165.

Biggs, J., Wright, T.J., 2020. How satellite InSAR has grown from opportunistic science to routine monitoring over the last decade. Nat. Commun. 11, 3863.

Blazquez, A., Meyssignac, B., Lemoine, J.M., Berthier, E., Ribes, A., Cazenave, A., 2018. Exploring the uncertainty in GRACE estimates of the mass redistributions at the earth surface: implications for the global water and sea level budgets. Geophys. J. Int. 215, 415–430.

Bolch, T., Kulkarni, A., Kääb, A., Huggel, C., Paul, F., Cogley, J.G., Frey, H., Kargel, J.S., Fujita, K., Scheel, M., Bajracharya, S., Stoffel, M., 2012. The state and fate of himalayan glaciers. Science 336, 310–314.

Bradski, G., 2000. The openCV library. Dr. Dobb's Journal: Software Tools for the Professional Programmer 25, 120–123.

Braithwaite, R.J., 1984. Can the mass balance of a glacier be estimated from its Equilibrium-Line altitude? J. Glaciol. 30, 364–368.

Braun, M.H., Malz, P., Sommer, C., Farías-barahona, D., Sauter, T., Casassa, G., Soruco, A., Skvarca, P., Seehaus, T.C., 2019. Constraining glacier elevation and mass changes in south america. Nat. Clim. Chang. .

Bretherton, C.S., Widmann, M., Dymnikov, V.P., Wallace, J.M., Bladé, I., 1999. The effective number of spatial degrees of freedom of a time-varying field. J. Clim. 12, 1990–2009.

van den Broeke, M., Bamber, J., Ettema, J., Rignot, E., Schrama, E., van de Berg, W.J., van Meijgaard, E., Velicogna, I., Wouters, B., 2009. Partitioning recent greenland mass loss. Science 326, 984–986.

Brun, F., Berthier, E., Wagnon, P., Kääb, A., Treichler, D., 2017. A spatially resolved estimate of high mountain asia glacier mass balances, 2000-2016. Nat. Geosci. 10, 668–673.

Brunt, K.M., Neumann, T.A., Smith, B.E., 2019. Assessment of ICESat-2 ice sheet surface heights, based on comparisons over the interior of the antarctic ice sheet. Geophys. Res. Lett. 46, 13072–13078.

Bühler, Y., Kumar, S., Veitinger, J., Christen, M., Stoffel, A., Others, 2013. Automated identification of potential snow avalanche release areas based on digital elevation models. Nat. Hazards Earth Syst. Sci. 13, 1321–1335.

Burgess, T.M., Webster, R., 1980. Optimal interpolation and isarithmic mapping of soil properties. J. Soil Sci. 31, 315–331.

Bürgmann, R., Rosen, P.A., Fielding, E.J., 2000. Synthetic aperture radar interferometry to measure earth's surface topography and its deformation. Annu. Rev. Earth Planet. Sci. 28, 169–209.

Canters, F., Genst, W.D., Dufourmont, H., 2002. Assessing effects of input uncertainty in structural landscape classification. Int. J. Geogr. Inf. Sci. 16, 129–149.

Carabajal, C.C., Harding, D.J., 2005. ICESat validation of SRTM c-band digital elevation models. Geophys. Res. Lett. 32.

Carrivick, J.L., Tweed, F.S., 2016. A global assessment of the societal impacts of glacier outburst floods. Glob. Planet. Change 144, 1–16.

Cauvy-Fraunié, S., Dangles, O., 2019. A global synthesis of biodiversity responses to glacier retreat. Nat Ecol Evol 3, 1675–1685.

Ciracì, E., Velicogna, I., Swenson, S., 2020. Continuity of the mass loss of the world's glaciers and ice caps from the GRACE and GRACE Follow-On missions. Geophys. Res. Lett. 47, 226.

Cogley, J.G., Hock, R., Rasmussen, L.A., Arendt, A.A., Bauder, A., Braithwaite, R.J., Jansson, P., Kaser, G., Möller, M., Nicholson, L., Zemp, M., 2011. Glossary of glacier mass balance and related terms. IHP-VII Technical Documents in Hydrology 86, 114.

Cressie, N., Wikle, C.K., 2015. Statistics for Spatio-Temporal Data. John Wiley & Sons.

Cressie, N.A.C., 1993. Statistics for spatial data. volume 4. Wiley, New York.

Cuffey, K.M., Paterson, W.S.B., 2010. The Physics of Glaciers. Academic Press.

Dall, J., Madsen, S.N., Keller, K., Forsberg, R., 2001. Topography and penetration of the greenland ice sheet measured with airborne SAR interferometry. Geophys. Res. Lett. 28, 1703–1706.

Dartnell, P., Gardner, J.V., 2004. Predicting seafloor facies from multibeam bathymetry and backscatter data. Photogrammetric Engineering & Remote Sensing 70, 1081–1091.

Davaze, L., Rabatel, A., Dufour, A., Hugonnet, R., Arnaud, Y., 2020. Region-Wide annual glacier surface mass balance for the european alps from 2000 to 2016. Front Earth Sci. 8, 149.

Dehecq, A., Gardner, A.S., Alexandrov, O., McMichael, S., Hugonnet, R., Shean, D., Marty, M., 2020. Automated processing of declassified KH-9 hexagon satellite images for global elevation change analysis since the 1970s. Front Earth Sci. 8, 516.

Dehecq, A., Gourmelen, N., Gardner, A.S., Brun, F., Goldberg, D., Nienow, P.W., Berthier, E., Vincent, C., Wagnon, P., Trouvé, E., 2019. Twenty-first century glacier slowdown driven by mass loss in high mountain asia. Nat. Geosci. 12, 22–27.

Dehecq, A., Millan, R., Berthier, E., Gourmelen, N., Trouvé, E., Vionnet, V., 2016. Elevation changes inferred from TanDEM-X data over the Mont-Blanc area: Impact of the X-Band interferometric bias. IEEE Journal of Selected Topics in Applied Earth Observations and Remote Sensing 9, 3870–3882.

Deschamps-Berger, C., Gascoin, S., Berthier, E., Deems, J., Gutmann, E., Dehecq, A., Shean, D., Dumont, M., 2020. Snow depth mapping from stereo satellite imagery in mountainous terrain: evaluation using airborne laser-scanning data. The Cryosphere 14, 2925–2940.

Dubayah, R.O., Drake, J.B., 2000. Lidar remote sensing for forestry. J. For. 98, 44–46.

Dussaillant, I., Berthier, E., Brun, F., 2018. Geodetic mass balance of the northern patagonian icefield from 2000 to 2012 using two independent methods. Front Earth Sci. 6, 8.

Dussaillant, I., Berthier, E., Brun, F., Masiokas, M., Hugonnet, R., Favier, V., Rabatel, A., Pitte, P., Ruiz, L., 2019. Two decades of glacier mass loss along the andes. Nat. Geosci. 12, 802–808.

Eberhard, L.A., Sirguey, P., Miller, A., Marty, M., Schindler, K., Stoffel, A., Bühler, Y., 2021. Intercomparison of photogrammetric platforms for spatially continuous snow depth mapping. The Cryosphere 15, 69–94.

Edwards, T.L., Nowicki, S., Marzeion, B., Hock, R., Goelzer, H., Seroussi, H., Jourdain, N.C., Slater, D.A., Turner, F.E., Smith, C.J., McKenna, C.M., Simon, E., Abe-Ouchi, A., Gregory, J.M., Larour, E., Lipscomb, W.H., Payne, A.J., Shepherd, A., Agosta, C., Alexander, P., Albrecht, T., Anderson, B., Asay-Davis, X., Aschwanden, A., Barthel, A., Bliss, A., Calov, R., Chambers, C., Champollion, N., Choi, Y., Cullather, R., Cuzzone, J., Dumas, C., Felikson, D., Fettweis, X., Fujita, K., Galton-Fenzi, B.K., Gladstone, R., Golledge, N.R., Greve, R., Hattermann, T., Hoffman, M.J., Humbert, A., Huss, M., Huybrechts, P., Immerzeel, W., Kleiner, T., Kraaijenbrink, P., Le Clec'h, S., Lee, V., Leguy, G.R., Little, C.M., Lowry, D.P., Malles, J.H., Martin, D.F., Maussion, F., Morlighem, M., O'Neill, J.F., Nias, I., Pattyn, F., Pelle, T., Price, S.F., Quiquet, A., Radić, V., Reese, R., Rounce, D.R., Rückamp, M., Sakai, A., Shafer, C., Schlegel, N.J., Shannon, S., Smith, R.S., Straneo, F., Sun, S., Tarasov, L., Trusel, L.D., Van Breedam, J., van de Wal, R., van den Broeke, M., Winkelmann, R., Zekollari, H., Zhao, C., Zhang, T., Zwinger, T., 2021. Projected land ice contributions to twenty-first-century sea level rise. Nature 593, 74–82.

Farinotti, D., Brinkerhoff, D.J., Fürst, J.J., Gantayat, P., Gillet-Chaulet, F., Huss, M., Leclercq, P.W., Maurer, H., Morlighem, M., Pandit, A., Rabatel, A., Ramsankaran, R., Reerink, T.J., Robo, E., Rouges, E., Tamre, E., van Pelt, W.J.J., Werder, M.A., Azam, M.F., Li, H., Andreassen, L.M., 2021. Results from the ice thickness models intercomparison experiment phase 2 (ITMIX2). Front Earth Sci. 8, 484.

Farinotti, D., Huss, M., Bauder, A., Funk, M., Truffer, M., 2009. A method to estimate the ice volume and ice-thickness distribution of alpine glaciers. J. Glaciol. 55, 422–430.

Farinotti, D., Huss, M., Fürst, J.J., Landmann, J., Machguth, H., Maussion, F., Pandit, A., 2019a. A consensus estimate for the ice thickness distribution of all glaciers on earth. Nat. Geosci. 12, 168–173.

Farinotti, D., Round, V., Huss, M., Compagno, L., Zekollari, H., 2019b. Large hydropower and water-storage potential in future glacier-free basins. Nature 575, 341–344.

Farr, T.G., Rosen, P.A., Caro, E., Crippen, R., Duren, R., Hensley, S., Kobrick, M., Paller, M., Rodriguez, E., Roth, L., Seal, D., Shaffer, S., Shimada, J., Umland, J., Werner, M., Oskin, M., Burbank, D., Alsdorf, D., 2007. The shuttle radar topography mission. Rev. Geophys. 45, 1485.

Fell, S.C., Carrivick, J.L., Cauvy-Fraunié, S., Crespo-Pérez, V., Hood, E., Randall, K.C., Nicholass, K.J.M., Tiegs, S.D., Dumbrell, A.J., Brown, L.E., 2021. Fungal decomposition of river organic matter accelerated by decreasing glacier cover. Nat. Clim. Chang. 11, 349–353.

Feng, S., Fu, Q., 2013. Expansion of global drylands under a warming climate. Atmos. Chem. Phys. 13, 10081–10094.

Fischer, A., 2009. Calculation of glacier volume from sparse ice-thickness data, applied to schaufelferner, austria. J. Glaciol. 55, 453–460.

Fischer, G., Papathanassiou, K.P., Hajnsek, I., 2020. Modeling and compensation of the penetration bias in InSAR DEMs of ice sheets at different frequencies. IEEE Journal of Selected Topics in Applied Earth Observations and Remote Sensing 13, 2698–2707.

Fischer, M., Huss, M., Hoelzle, M., 2015. Surface elevation and mass changes of all swiss glaciers 1980-2010. Cryosphere 9, 525–540.

Fricker, H.A., 2005. Assessment of ICESat performance at the salar de uyuni, bolivia. Geophys. Res. Lett. 32.

Friedl, P., Seehaus, T., Braun, M., 2021. Global time series and temporal mosaics of glacier surface velocities derived from sentinel-1 data. Earth System Science Data 13, 4653–4675.

Fürst, J.J., Durand, G., Gillet-Chaulet, F., Tavard, L., Rankl, M., Braun, M., Gagliardini, O., 2016. The safety band of antarctic ice shelves. Nat. Clim. Chang. 6, 479–482.

Galiatsatos, N., Donoghue, D.N.M., Philip, G., 2007. High resolution elevation data derived from stereoscopic CORONA imagery with minimal ground control. Photogrammetric Engineering & Remote Sensing 73, 1093–1106.

Garbe, J., Albrecht, T., Levermann, A., Donges, J.F., Winkelmann, R., 2020. The hysteresis of the antarctic ice sheet. Nature 585, 538–544.

Gardelle, J., Berthier, E., Arnaud, Y., 2012. Impact of resolution and radar penetration on glacier elevation changes computed from DEM differencing. J. Glaciol. 58, 419–422.

Gardelle, J., Berthier, E., Arnaud, Y., Kääb, A., 2013. Region-wide glacier mass balances over the Pamir-Karakoram-Himalaya during 1999–2011. The Cryosphere 7, 1263–1286.

Gardner, A., Moholdt, G., Cogley, J.G., Wouters, B., Arendt, A.A., Wahr, J., Berthier, E., Hock, R., Pfeffer, W.T., Kaser, G., Ligtenberg, S.R.M., Bolch, T., Sharp, M.J., Hagen, J.O., Van Den Broeke, M.R., Paul, F., 2013. A reconciled estimate of glacier contributions to sea level rise: 2003 to 2009. Science 340, 852–857.

Gardner, A.S., Fahnestock, M.A., Scambos, T.A., 2019. ITS_LIVE regional glacier and ice sheet surface velocities.

Gardner, A.S., Moholdt, G., Scambos, T., Fahnstock, M., Ligtenberg, S., van den Broeke, M., Nilsson, J., 2018a. Increased west antarctic and unchanged east antarctic ice discharge over the last 7 years. The Cryosphere 12, 521–547.

Gardner, J.R., Pleiss, G., Bindel, D., Weinberger, K.Q., Wilson, A.G., 2018b. GPyTorch: Blackbox Matrix-Matrix gaussian process inference with GPU acceleration `arXiv:1809.11165`.

GDAL/OGR contributors, 2022. GDAL/OGR geospatial data abstraction software library.

Geyman, E.C., J J van Pelt, W., Maloof, A.C., Aas, H.F., Kohler, J., 2022. Historical glacier change on svalbard predicts doubling of mass loss by 2100. Nature 601, 374–379.

Gillies, S., Others, 2013. Rasterio: geospatial raster I/O for Python programmers.

Girod, L., Nuth, C., Kääb, A., McNabb, R., Galland, O., 2017. MMASTER: Improved ASTER DEMs for elevation change monitoring. Remote Sensing 9, 704.

Girod, L.M.R., 2018. Improved measurements of cryospheric processes using advanced photogrammetry. Ph.D. thesis. Universitetet i Oslo.

Girotto, M., Rodell, M., 2019. Chapter two - terrestrial water storage, in: Maggioni, V., Massari, C. (Eds.), Extreme Hydroclimatic Events and Multivariate Hazards in a Changing Environment. Elsevier, pp. 41–64.

Goodchild, M.F., Gopal, S., 1989. The Accuracy Of Spatial Databases. CRC Press.

Goovaerts, P., 1997. Geostatistics for Natural Resources Evaluation. Oxford University Press.

Gräler, B., Pebesma, E., Heuvelink, G., 2016. Spatio-Temporal interpolation using gstat.

Grove, J.M., 2019. Little ice ages: ancient and modern. Routledge.

Gruber, A., Wessel, B., Huber, M., Roth, A., 2012. Operational TanDEM-X DEM calibration and first validation results. ISPRS J. Photogramm. Remote Sens. 73, 39–49.

Grünewald, T., Bühler, Y., Lehning, M., 2014. Elevation dependency of mountain snow depth. The Cryosphere 8, 2381–2394.

Guan, L., Pan, H., Zou, S., Hu, J., Zhu, X., Zhou, P., 2020. The impact of horizontal errors on the accuracy of freely available digital elevation models (DEMs). Int. J. Remote Sens. 41, 7383–7399.

Haeberli, W., 1983. Frequency and characteristics of glacier floods in the swiss alps. Ann. Glaciol. 4, 85–90.

Hall, D.K., Riggs, G.A., 2021. MODIS/Terra snow cover monthly L3 global 0.05deg CMG, version 61.

Harris, C.R., Millman, K.J., van der Walt, S.J., Gommers, R., Virtanen, P., Cournapeau, D., Wieser, E., Taylor, J., Berg, S., Smith, N.J., Kern, R., Picus, M., Hoyer, S., van Kerkwijk, M.H., Brett, M., Haldane, A., Del Río, J.F., Wiebe, M., Peterson, P., Gérard-Marchant, P., Sheppard, K., Reddy, T., Weckesser, W., Abbasi, H., Gohlke, C., Oliphant, T.E., 2020. Array programming with NumPy. Nature 585, 357–362.

Harrison, S., Kargel, J.S., Huggel, C., Reynolds, J., Shugar, D.H., Betts, R.A., Emmer, A., Glasser, N., Haritashya, U.K., Klimeš, J., Reinhardt, L., Schaub, Y., Wiltshire, A., Regmi, D., Vilímek, V., 2018. Climate change and the global pattern of moraine-dammed glacial lake outburst floods. The Cryosphere 12, 1195–1209.

Hawker, L., Bates, P., Neal, J., Rougier, J., 2018. Perspectives on digital elevation model (DEM) simulation for flood modeling in the absence of a High-Accuracy open access global DEM. Front Earth Sci. 6, 233.

Hebeler, F., Purves, R.S., 2009. The influence of elevation uncertainty on derivation of topographic indices. Geomorphology 111, 4–16.

Heritage, G.L., Milan, D.J., Large, A.R.G., Fuller, I.C., 2009. Influence of survey strategy and interpolation model on DEM quality. Geomorphology 112, 334–344.

Herreid, S., Pellicciotti, F., 2020. The state of rock debris covering earth's glaciers. Nat. Geosci. .

Hersbach, H., Bell, B., Berrisford, P., Hirahara, S., Horányi, A., Muñoz-Sabater, J., Nicolas, J., Peubey, C., Radu, R., Schepers, D., Simmons, A., Soci, C., Abdalla, S., Abellan, X., Balsamo, G., Bechtold, P., Biavati, G., Bidlot, J., Bonavita, M., Chiara, G., Dahlgren, P., Dee, D., Diamantakis, M., Dragani, R., Flemming, J., Forbes, R., Fuentes, M., Geer, A., Haimberger, L., Healy, S., Hogan, R.J., Hólm, E., Janisková, M., Keeley, S., Laloyaux, P., Lopez, P., Lupu, C., Radnoti, G., Rosnay, P., Rozum, I., Vamborg, F., Villaume, S., Jean-Noël Thépaut, 2020. The ERA5 global reanalysis. Quart. J. Roy. Meteor. Soc. 146, 1999–2049.

Heuvelink, G.B.M., 1998. Error propagation in environmental modelling with GIS. CRC press.

Heuvelink, G.B.M., 2006. Analysing uncertainty propagation in GIS: Why is it not that simple?, in: Uncertainty in Remote Sensing and GIS. John Wiley & Sons, Ltd, Chichester, UK, pp. 155–165.

Heuvelink, G.B.M., Burrough, P.A., Stein, A., 1989. Propagation of errors in spatial modelling with GIS. International Journal of Geographical Information Systems 3, 303–322.

Hock, R., Bliss, A., Marzeion, B., Giesen, R.H., Hirabayashi, Y., Huss, M., Radić, V., Slangen, A.B.A., 2019a. GlacierMIP – a model intercomparison of global-scale glacier mass-balance models and projections. J. Glaciol. 65, 453–467.

Hock, R., Jensen, H., 1999. Application of kriging interpolation for glacier mass balance computations. Geogr. Ann. Ser. A. Phys. Geogr. 81, 611–619.

Hock, R., Rasul, G., Adler, C., Caceres, B., Gruber, S., Hirabayashi, Y., Jackson, M., Kääb, A., Kang, S., Kutuzov, S., Milner, A., Molau, U., Morin, S., Orlove, B., Steltzer, H., Allen, S., Arenson, L., Baneerjee, S., Barr, I., Bórquez, R., Brown, L., Cao, B., Carey, M., Cogley, G., Fischlin, A., de Sherbinin, A., Eckert, N., Geertsema, M., Hagenstad, M., Honsberg, M., Hood, E., Huss, M., Jimenez Zamora, E., Kotlarski, S., Lefeuvre, P., Ignacio López Moreno, J., Lundquist, J., McDowell, G., Mills, S., Mou, C., Nepal, S., Noetzli, J., Palazzi, E., Pepin, N., Rixen, C., Shahgedanova, M., McKenzie Skiles, S., Vincent, C., Viviroli, D., Gesa, A.W., Yangjee Sherpa, P., Weyer, N., Wouters, B., Yasunari, T., You, Q., Zhang, Y., 2019b. High mountain areas, in: Pörtner, H.O., Roberts, D.C., Masson-Delmotte, V., Zhai, P., Tignor, M., Poloczanska, E., Mintenbeck, K., Alegría, A., Nicolai, M., Okem, A., Petzold, J., Rama, B., Weyer, N.M. (Eds.), IPCC Special Report on the Ocean and Cryosphere in a Changing Climate. USA, pp. 131–202.

Höhle, J., Höhle, M., 2009. Accuracy assessment of digital elevation models by means of robust statistical methods. ISPRS J. Photogramm. Remote Sens. 64, 398–406.

Horn, B.K.P., 1981. Hill shading and the reflectance map. Proc. IEEE 69, 14–47.

Howat, I.M., Porter, C., Smith, B.E., Noh, M.J., Morin, P., 2019. The reference elevation model of antarctica. The Cryosphere 13, 665–674.

Hoyer, S., Hamman, J., 2017. xarray: ND labeled arrays and datasets in python. Journal of Open Research Software 5.

Hugonnet, R., Brun, F., Berthier, E., Dehecq, A., Mannerfelt, E.S., Eckert, N., accepted. Uncertainty analysis of digital elevation models by spatial inference from stable terrain.

Hugonnet, R., McNabb, R., Berthier, E., Menounos, B., Nuth, C., Girod, L., Farinotti, D., Huss, M., Dussaillant, I., Brun, F., Kääb, A., 2021. Accelerated global glacier mass loss in the early twenty-first century. Nature 592, 726–731.

Humphrey, V., Gudmundsson, L., 2019. GRACE-REC: A reconstruction of climate-driven water storage changes over the last century.

Huss, M., 2013. Density assumptions for converting geodetic glacier volume change to mass change. The Cryosphere 7, 877–887.

Huss, M., Bauder, A., Funk, M., 2009. Homogenization of long-term mass-balance time series. Ann. Glaciol. 50, 198–206.

Huss, M., Bauder, A., Linsbauer, A., Gabbi, J., Kappenberger, G., Steinegger, U., Farinotti, D., 2021. More than a century of direct glacier mass-balance observations on claridenfirn, switzerland. J. Glaciol. 67, 697–713.

Huss, M., Farinotti, D., 2012. Distributed ice thickness and volume of all glaciers around the globe. Journal of Geophysical Research: Earth Surface 117, 1–10.

Huss, M., Hock, R., 2015. A new model for global glacier change and sea-level rise. Front Earth Sci. 3, 54.

Huss, M., Hock, R., 2018. Global-scale hydrological response to future glacier mass loss. Nat. Clim. Chang. .

Huss, M., Hugonnet, R., Compagno, L., Landmann, J., Farinotti, D., in prep. Converting geodetic ice volume to mass change: a global-scale assessment.

IMBIE team, 2018. Mass balance of the antarctic ice sheet from 1992 to 2017. Nature 558, 219–222.

IMBIE Team, 2020. Mass balance of the greenland ice sheet from 1992 to 2018. Nature 579, 233–239.

Immerzeel, W.W., Lutz, A.F., Andrade, M., Bahl, A., Biemans, H., Bolch, T., Hyde, S., Brumby, S., Davies, B.J., Elmore, A.C., Emmer, A., Feng, M., Fernández, A., Haritashya, U., Kargel, J.S., Koppes, M., Kraaijenbrink, P.D.A., Kulkarni, A.V., Mayewski, P.A., Nepal, S., Pacheco, P., Painter, T.H., Pellicciotti, F., Rajaram, H., Rupper, S., Sinisalo, A., Shrestha, A.B., Viviroli, D., Wada, Y., Xiao, C., Yao, T., Baillie, J.E.M., 2020. Importance and vulnerability of the world's water towers. Nature 577, 364–369.

IPCC, 2019. IPCC special report on the ocean and cryosphere in a changing climate.

IPCC, 2021. Climate Change 2021: The Physical Science Basis. Contribution of Working Group I to the Sixth Assessment Report of the Intergovernmental Panel on Climate Change. Cambridge University Press.

ISO (International Organisation for Standardisation), 1994. ISO 5725-1: 1994: Accuracy (Trueness and Precision) of Measurement Methods and Results-Part 1: General Principles and Definitions. ISO, Geneva.

Jacob, T., Wahr, J., Pfeffer, W.T., Swenson, S., 2012. Recent contributions of glaciers and ice caps to sea level rise. Nature 482, 514–518.

Jacobsen, D., Milner, A.M., Brown, L.E., Dangles, O., 2012. Biodiversity under threat in glacier-fed river systems. Nat. Clim. Chang. 2, 361–364.

Jakob, L., Gourmelen, N., Ewart, M., Plummer, S., 2021. Spatially and temporally resolved ice loss in high mountain asia and the gulf of alaska observed by CryoSat-2 swath altimetry between 2010 and 2019. The Cryosphere 15, 1845–1862.

Jóhannesson, T., Raymond, C., Waddington, E., 1989. Time–Scale for adjustment of glaciers to changes in mass balance. J. Glaciol. 35, 355–369.

Jonas, T., Marty, C., Magnusson, J., 2009. Estimating the snow water equivalent from snow depth measurements in the swiss alps. J. Hydrol. 378, 161–167.

Jordahl, K., Van den Bossche, J., Fleischmann, M., Wasserman, J., McBride, J., Gerard, J., Tratner, J., Perry, M., Badaracco, A.G., Farmer, C., Hjelle, G.A., Snow, A.D., Cochran, M., Gillies, S., Culbertson, L., Bartos, M., Eubank, N., maxalbert, Bilogur, A., Rey, S., Ren, C., Arribas-Bel, D., Wasser, L., Wolf, L.J., Journois, M., Wilson, J., Greenhall, A., Holdgraf, C., Filipe, Leblanc, F., 2020. geopandas/geopandas: v0.8.1.

Joughin, I., Smith, B.E., Howat, I.M., Scambos, T., Moon, T., 2010. Greenland flow variability from ice-sheet-wide velocity mapping. J. Glaciol. 56, 415–430.

Journel, A.G., Huijbregts, C.J., 1978. Mining geostatistics. volume 600. Academic press London.

Kääb, A., 2008. Glacier volume changes using ASTER satellite stereo and ICESat GLAS laser altimetry. a test study on edgeøya, eastern svalbard. IEEE Trans. Geosci. Remote Sens. 46, 2823–2830.

Kääb, A., Berthier, E., Nuth, C., Gardelle, J., Arnaud, Y., 2012. Contrasting patterns of early twenty-first-century glacier mass change in the himalayas. Nature 488, 495–498.

Kääb, A., Leinss, S., Gilbert, A., Bühler, Y., Gascoin, S., Evans, S.G., Bartelt, P., Berthier, E., Brun, F., Chao, W.A., Farinotti, D., Gimbert, F., Guo, W., Huggel, C., Kargel, J.S., Leonard, G.J., Tian, L., Treichler, D., Yao, T., 2018. Massive collapse of two glaciers in western tibet in 2016 after surge-like instability. Nat. Geosci. 11, 114–120.

Kaser, G., Cogley, J.G., Dyurgerov, M.B., Meier, M.F., Ohmura, A., 2006. Mass balance of glaciers and ice caps: Consensus estimates for 1961-2004. Geophys. Res. Lett. 33, 1–5.

Kaser, G., Grosshauser, M., Marzeion, B., 2010. Contribution potential of glaciers to water availability in different climate regimes. Proc. Natl. Acad. Sci. U. S. A. 107, 20223–20227.

Kochtitzky, W., Copland, L., 2022. Retreat of northern hemisphere marine-terminating glaciers, 2000–2020. Geophys. Res. Lett. 49.

Kochtitzky, W., Copland, L., Van Wychen, W., Hugonnet, R., Hock, Regineand Dowdeswell, J.A., Benham, T., Strozzi, T., Glazovsky, A., Lavrentiev, I., Rounce, D., Millan, R., Cook, A., Dalton, A., Jiskoot, H., Cooley, J., Jania, J., Navarro, F., in review. Frontal ablation: the unquantified mass loss of marine-terminating glaciers, 2000-2020.

Korona, J., Berthier, E., Bernard, M., Rémy, F., Thouvenot, E., 2009. SPIRIT. SPOT 5 stereoscopic survey of polar ice: Reference images and topographies during the fourth international polar year (2007–2009). ISPRS J. Photogramm. Remote Sens. 64, 204–212.

Krieger, G., Moreira, A., Fiedler, H., Hajnsek, I., Werner, M., Younis, M., Zink, M., 2007. TanDEM-X: A satellite formation for High-Resolution SAR interferometry. IEEE Trans. Geosci. Remote Sens. 45, 3317–3341.

Kulp, S.A., Strauss, B.H., 2019. New elevation data triple estimates of global vulnerability to sea-level rise and coastal flooding. Nat. Commun. 10, 4844.

Kyriakidis, P.C., Shortridge, A.M., Goodchild, M.F., 1999. Geostatistics for conflation and accuracy assessment of digital elevation models. Int. J. Geogr. Inf. Sci. 13, 677–707.

Lam, S.K., Pitrou, A., Seibert, S., 2015. Numba: a LLVM-based python JIT compiler, in: Proceedings of the Second Workshop on the LLVM Compiler Infrastructure in HPC, Association for Computing Machinery, New York, NY, USA. pp. 1–6.

Lambeck, K., Esat, T.M., Potter, E.K., 2002. Links between climate and sea levels for the past three million years. Nature 419, 199–206.

Lambrecht, A., Mayer, C., Wendt, A., Floricioiu, D., Völksen, C., 2018. Elevation change of fedchenko glacier, pamir mountains, from GNSS field measurements and TanDEM-X elevation models, with a focus on the upper glacier. J. Glaciol. 64, 637–648.

Leinss, S., Bernhard, P., 2021. TanDEM-X:Deriving InSAR height changes and velocity dynamics of great aletsch glacier. IEEE Journal of Selected Topics in Applied Earth Observations and Remote Sensing 14, 4798–4815.

Li, J., Li, Z.W., Hu, J., Wu, L.X., Li, X., Guo, L., Liu, Z., Miao, Z.L., Wang, W., Chen, J.L., 2021. Investigating the bias of TanDEM-X digital elevation models of glaciers on the tibetan plateau: impacting factors and potential effects on geodetic mass-balance measurements. J. Glaciol. 67, 613–626.

Lievens, H., Demuzere, M., Marshall, H.P., Reichle, R.H., Brucker, L., Brangers, I., Rosnay, P.D., Dumont, M., Girotto, M., Immerzeel, W.W., Jonas, T., Kim, E.J., Koch, I., Marty, C., Saloranta, T., Schöber, J., Lannoy, G.J.M.D., 2019. Snow depth variability in the northern hemisphere mountains observed from space. Nat. Commun. , 1–12.

Lliboutry, L., 1965. Traité de glaciologie: Glaciers, variations du climat, sols gelés. Masson.

Magruder, L., Neuenschwander, A., Klotz, B., 2021. Digital terrain model elevation corrections using space-based imagery and ICESat-2 laser altimetry. Remote Sens. Environ. 264, 112621.

Mälicke, M., Schneider, H.D., 2019. Scikit-GStat 0.2.6: A scipy flavored geostatistical analysis toolbox written in python.

Malz, P., Meier, W., Casassa, G., Jaña, R., Skvarca, P., Braun, M.H., 2018. Elevation and mass changes of the southern patagonia icefield derived from TanDEM-X and SRTM data. Remote Sensing 10, 1–17.

Mannerfelt, E.S., Dehecq, A., Hugonnet, R., Hodel, E., Huss, M., Bauder, A., Farinotti, D., 2022. Halving of swiss glacier volume since 1931 observed from terrestrial image photogrammetry.

Marti, R., Gascoin, S., Berthier, E., Pinel, M.d., Houet, T., Laffly, D., 2016. Mapping snow depth in open alpine terrain from stereo satellite imagery. The Cryosphere 10, 1361–1380.

Marzeion, B., Cogley, J.G., Richter, K., Parkes, D., 2014. Attribution of global glacier mass loss to anthropogenic and natural causes. Science 345, 919–921.

Marzeion, B., Hock, R., Anderson, B., Bliss, A., Champollion, N., Fujita, K., Huss, M., Immerzeel, W.W., Kraaijenbrink, P., Malles, J., Maussion, F., Radić, V., Rounce, D.R., Sakai, A., Shannon, S., Wal, R., Zekollari, H., 2020. Partitioning the uncertainty of ensemble projections of global glacier mass change. Earth's Future 8, F01003.

Matheron, G., 1965. Les variables régionalisées et leur estimation: une application de la théorie de fonctions aléatoires aux sciences de la nature. volume 4597. Masson et CIE.

Matiu, M., Crespi, A., Bertoldi, G., Carmagnola, C.M., Marty, C., Morin, S., Schöner, W., Cat Berro, D., Chiogna, G., De Gregorio, L., Kotlarski, S., Majone, B., Resch, G., Terzago, S., Valt, M., Beozzo, W., Cianfarra, P., Gouttevin, I., Marcolini, G., Notarnicola, C., Petitta, M., Scherrer, S.C., Strasser, U., Winkler, M., Zebisch, M., Cicogna, A., Cremonini, R., Debernardi, A., Faletto, M., Gaddo, M., Giovannini, L., Mercalli, L., Soubeyroux, J.M., Sušnik, A., Trenti, A., Urbani, S., Weilguni, V., 2021. Observed snow depth trends in the european alps: 1971 to 2019. The Cryosphere 15, 1343–1382.

Maussion, F., TimoRoth, Bell, R., Li, F., Landmann, J., Dusch, M., tbridel, 2021. fmaussion/salem: v0.3.7.

McKinney, W., 2010. Data Structures for Statistical Computing in Python, in: van der Walt, S., Millman, J. (Eds.), Proceedings of the 9th Python in Science Conference, pp. 56–61.

McNabb, R., Nuth, C., Kääb, A., Girod, L., 2019. Sensitivity of glacier volume change estimation to DEM void interpolation. The Cryosphere 13, 895–910.

Melkonian, A.K., Willis, M.J., Pritchard, M.E., 2014. Satellite-derived volume loss rates and glacier speeds for the juneau icefield, alaska. J. Glaciol. 60, 743–760.

Menounos, B., Hugonnet, R., Shean, D., Gardner, A., Howat, I., Berthier, E., Pelto, B., Tennant, C., Shea, J., Noh, M.J., Brun, F., Dehecq, A., 2019. Heterogeneous changes in western north american glaciers linked to decadal variability in zonal wind strength. Geophys. Res. Lett. 46, 200–209.

Menthon, M., 2020. Global cartography of radar penetration in glaciers from the shuttle radar topographic mission.

Meyssignac, B., Cazenave, A., 2012. Sea level: A review of present-day and recent-past changes and variability. J. Geodyn. 58, 96–109.

Mikhail, E.M., Bethel, J.S., McGlone, J.C., 2001. Introduction to Modern Photogrammetry. volume 19. John Wiley & Sons, Nashville, TN.

Miles, E., McCarthy, M., Dehecq, A., Kneib, M., Fugger, S., Pellicciotti, F., 2021. Health and sustainability of glaciers in high mountain asia. Nat. Commun. 12, 2868.

Miles, E.S., Scott Watson, C., Brun, F., Berthier, E., Esteves, M., Quincey, D.J., Miles, K.E., Hubbard, B., Wagnon, P., 2018. Glacial and geomorphic effects of a supraglacial lake drainage and outburst event, everest region, nepal himalaya. The Cryosphere 12, 3891–3905.

Millan, R., Mouginot, J., Rabatel, A., Morlighem, M., 2022. Ice velocity and thickness of the world's glaciers. Nat. Geosci. 15, 124–129.

Milner, A.M., Khamis, K., Battin, T.J., Brittain, J.E., Barrand, N.E., Füreder, L., Cauvy-Fraunié, S., Gíslason, G.M., Jacobsen, D., Hannah, D.M., Hodson, A.J., Hood, E., Lencioni, V., Ólafsson, J.S., Robinson, C.T., Tranter, M., Brown, L.E., 2017. Glacier shrinkage driving global changes in downstream systems. Proc. Natl. Acad. Sci. U. S. A. 114, 9770–9778.

Morlighem, M., Rignot, E., Binder, T., Blankenship, D., Drews, R., Eagles, G., Eisen, O., Ferraccioli, F., Forsberg, R., Fretwell, P., Goel, V., Greenbaum, J.S., Gudmundsson, H., Guo, J., Helm, V., Hofstede, C., Howat, I., Humbert, A., Jokat, W., Karlsson, N.B., Lee, W.S., Matsuoka, K., Millan, R., Mouginot, J., Paden, J., Pattyn, F., Roberts, J., Rosier, S., Ruppel, A., Seroussi, H., Smith, E.C., Steinhage, D., Sun, B., van den Broeke, M.R., van Ommen, T.D., van Wessem, M., Young, D.A., 2019. Deep glacial troughs and stabilizing ridges unveiled beneath the margins of the antarctic ice sheet. Nat. Geosci. 13, 132–137.

Morlighem, M., Williams, C.N., Rignot, E., An, L., Arndt, J.E., Bamber, J.L., Catania, G., Chauché, N., Dowdeswell, J.A., Dorschel, B., Fenty, I., Hogan, K., Howat, I., Hubbard, A., Jakobsson, M., Jordan, T.M., Kjeldsen, K.K., Millan, R., Mayer, L., Mouginot, J., Noël, B.P.Y., O'Cofaigh, C., Palmer, S., Rysgaard, S., Seroussi, H., Siegert, M.J., Slabon, P., Straneo, F., van den Broeke, M.R., Weinrebe, W., Wood, M., Zinglersen, K.B., 2017. BedMachine v3: Complete bed topography and ocean bathymetry mapping of greenland from multibeam echo sounding combined with mass conservation. Geophys. Res. Lett. 44, 11051–11061.

Morris, A., Moholdt, G., Gray, L., Schuler, T.V., Eiken, T., 2022. CryoSat-2 interferometric mode calibration and validation: A case study from the austfonna ice cap, svalbard. Remote Sens. Environ. 269, 112805.

Mukherjee, S., Joshi, P.K., Mukherjee, S., Ghosh, A., Garg, R.D., Mukhopadhyay, A., 2013. Evaluation of vertical accuracy of open source digital elevation model (DEM). Int. J. Appl. Earth Obs. Geoinf. 21, 205–217.

Müller, S., Schüler, L., Zech, A., Heße, F., 2021. GSTools v1.3: A toolbox for geostatistical modelling in python.

Müller Schmied, H., Cáceres, D., Eisner, S., Flörke, M., Herbert, C., Niemann, C., Peiris, T.A., Popat, E., Portmann, F.T., Reinecke, R., Others, 2021. The global water resources and use model WaterGAP v2.2d: model description and evaluation. Geoscientific Model Development 14, 1037–1079.

Naegeli, K., Damm, A., Huss, M., Wulf, H., Schaepman, M., Hoelzle, M., 2017. Cross-comparison of albedo products for glacier surfaces derived from airborne and satellite (sentinel-2 and landsat 8) optical data. Remote Sensing 9, 1–22.

NASA JPL, 2020. NASADEM SRTM-only height and height precision mosaic global 1 arc second.

NASA/METI/AIST/Japan Spacesystems, and U.S./Japan ASTER Science Team, 2001. ASTER level 1A data set - reconstructed, unprocessed instrument data.

NASA/METI/AIST/Japan Spacesystems and U.S./Japan ASTER Science Team, 2007. ASTER On-Demand L3 DEM and orthorectified images, GeoTIF format.

Nefeslioglu, H.A., San, B.T., Gokceoglu, C., Duman, T.Y., 2012. An assessment on the use of terra ASTER L3A data in landslide susceptibility mapping. Int. J. Appl. Earth Obs. Geoinf. 14, 40–60.

Noh, M.J., Howat, I.M., 2014. Automated coregistration of repeat digital elevation models for surface elevation change measurement using geometric constraints. IEEE Trans. Geosci. Remote Sens. 52, 2247–2260.

Noh, M.J., Howat, I.M., 2017. The surface extraction from TIN based search-space minimization (SETSM) algorithm. ISPRS J. Photogramm. Remote Sens. 129, 55–76.

Nolan, M., Larsen, C., Sturm, M., 2015. Mapping snow depth from manned aircraft on landscape scales at centimeter resolution using structure-from-motion photogrammetry. The Cryosphere 9, 1445–1463.

Nuimura, T., Fujita, K., Yamaguchi, S., Sharma, R.R., 2012. Elevation changes of glaciers revealed by multitemporal digital elevation models calibrated by GPS survey in the khumbu region, nepal himalaya, 1992-2008. J. Glaciol. 58, 648–656.

Nuth, C., Kääb, 2011. Co-registration and bias corrections of satellite elevation data sets for quantifying glacier thickness change. The Cryosphere 5, 271–290.

Nuth, C., McNaab, R., Girod, L., Hugonnet, R., in prep. The aster dem legacy: precise elevation extraction for change detection.

Nuth, C., Moholdt, G., Kohler, J., Hagen, J.O., Kääb, A., 2010. Svalbard glacier elevation changes and contribution to sea level rise. J. Geophys. Res. 115.

Oerter, H., Reinwarth, O., Rufli, H., 1982. Core drilling through a temperate alpine glacier (vernagtferner, oetztal alps) in 1979. Z. Gletscherkd. Glazialgeol. 18, 1–11.

Oksanen, J., 2006. Digital elevation model error in terrain analysis. Ph.D. thesis. University of Helsinki, Faculty of Science.

Oksanen, J., Sarjakoski, T., 2005. Error propagation analysis of DEM-based drainage basin delineation. Int. J. Remote Sens. 26, 3085–3102.

Painter, T.H., Flanner, M.G., Kaser, G., Marzeion, B., VanCuren, R.A., Abdalati, W., 2013. End of the little ice age in the alps forced by industrial black carbon. Proc. Natl. Acad. Sci. U. S. A. 110, 15216–15221.

Parkes, D., Marzeion, B., 2018. Twentieth-century contribution to sea-level rise from uncharted glaciers. Nature 563, 551–554.

Pebesma, E.J., Wesseling, C.G., 1998. gstat : A program for geostatistical modelling, prediction and simulation. Comput. Geosci. 24, 17–31.

Pedregosa, F., Varoquaux, G., Gramfort, A., Michel, V., Thirion, B., Grisel, O., Blondel, M., Prettenhofer, P., Weiss, R., Dubourg, V., Vanderplas, J., Passos, A., Cournapeau, D., Brucher, M., Perrot, M., Duchesnay, E., 2011. Scikit-learn: Machine learning in Python. J. Mach. Learn. Res. 12, 2825–2830.

Pelto, B.M., Menounos, B., Marshall, S.J., 2019. Multi-year evaluation of airborne geodetic surveys to estimate seasonal mass balance, columbia and rocky mountains, canada. The Cryosphere 13, 1709–1727.

Perko, R., Raggam, H., Roth, P.M., 2019. Mapping with Pléiades—End-to-End workflow. Remote Sensing 11, 2052.

Pfeffer, T.W., Arendt, A.A., Bliss, A., Bolch, T., Graham Cogley, J., Gardner, A.S., Hagen, J.O., Hock, R., Kaser, G., Kienholz, C., Miles, E.S., Moholdt, G., Mölg, N., Paul, F., Radić, V., Rastner, P., Raup, B.H., Rich, J., Sharp, M.J., The Randolph Consortium, 2014. The randolph glacier inventory: a globally complete inventory of glaciers. J. Glaciol. 60, 537–552.

Pleiss, G., Gardner, J.R., Weinberger, K.Q., Wilson, A.G., 2018. Constant-Time predictive distributions for gaussian processes `arXiv:1803.06058`.

Pokhrel, Y., Felfelani, F., Satoh, Y., Boulange, J., Burek, P., Gädeke, A., Gerten, D., Gosling, S.N., Grillakis, M., Gudmundsson, L., Hanasaki, N., Kim, H., Koutroulis, A., Liu, J., Papadimitriou, L., Schewe, J., Müller Schmied, H., Stacke, T., Telteu, C.E., Thiery, W., Veldkamp, T., Zhao, F., Wada, Y., 2021. Global terrestrial water storage and drought severity under climate change. Nat. Clim. Chang. 11, 226–233.

Porter, C., Morin, P., Howat, I., Noh, M.J., Bates, B., Peterman, K., Keesey, S., Schlenk, M., Gardiner, J., Tomko, K., Willis, M., Kelleher, C., Cloutier, M., Husby, E., Foga, S., Nakamura, H., Platson, M., Wethington, Jr, M., Williamson, C., Bauer, G., Enos, J., Arnold, G., Kramer, W., Becker, P., Doshi, A., D'Souza, C., Cummens, P., Laurier, F., Bojesen, M., 2018. ArcticDEM.

Pritchard, H.D., 2019. Asia's shrinking glaciers protect large populations from drought stress. Nature 569, 649–654.

PROJ contributors, 2022. PROJ coordinate transformation software library.

Rabatel, A., Dedieu, J.P., Vincent, C., 2005. Using remote-sensing data to determine equilibrium-line altitude and mass-balance time series: validation on three french glaciers, 1994–2002.

Racoviteanu, A.E., Manley, W.F., Arnaud, Y., Williams, M.W., 2007. Evaluating digital elevation models for glaciologic applications: An example from nevado coropuna, peruvian andes. Glob. Planet. Change 59, 110–125.

Rankl, M., Braun, M., 2016. Glacier elevation and mass changes over the central karakoram region estimated from TanDEM-X and SRTM/X-SAR digital elevation models. Ann. Glaciol. 57, 273–281.

Raup, B., Racoviteanu, A., Khalsa, S.J.S., Helm, C., Armstrong, R., Arnaud, Y., 2007. The GLIMS geospatial glacier database: A new tool for studying glacier change. Glob. Planet. Change 56, 101–110.

Raup, B.H., Kieffer, H.H., Hare, T.M., Kargel, J.S., 2000. Generation of data acquisition requests for the ASTER satellite instrument for monitoring a globally distributed target: glaciers. IEEE Trans. Geosci. Remote Sens. 38, 1105–1112.

Reuter, H.I., Nelson, A., Jarvis, A., 2007. An evaluation of void-filling interpolation methods for SRTM data. Int. J. Geogr. Inf. Sci. 21, 983–1008.

RGI Consortium, 2017. Randolph glacier inventory – a dataset of global glacier outlines: Version 6.0: Technical report, global land ice measurements from space, colorado, USA.

Rignot, E., Echelmeyer, K., Krabill, W., 2001. Penetration depth of interferometric synthetic-aperture radar signals in snow and ice. Geophys. Res. Lett. 28, 3501–3504.

Riley, S.J., DeGloria, S.D., Elliot, R., 1999. Index that quantifies topographic heterogeneity. Intermt. J. Sci. 5, 23–27.

Rizzoli, P., Martone, M., Gonzalez, C., Wecklich, C., Tridon, D.B., Bräutigam, B., Bachmann, M., Schulze, D., Fritz, T., Huber, M., Wessel, B., Krieger, G., Zink, M., Moreira, A., 2017. Generation and performance assessment of the global TanDEM-X digital elevation model. ISPRS J. Photogramm. Remote Sens. 132, 119–139.

Rocklin, M., 2015. Dask: Parallel computation with blocked algorithms and task scheduling, in: Proceedings of the 14th Python in Science Conference, SciPy.

Rodell, M., Famiglietti, J.S., Wiese, D.N., Reager, J.T., Beaudoing, H.K., Landerer, F.W., Lo, M.H., 2018. Emerging trends in global freshwater availability. Nature 557, 651–659.

Roe, G.H., Christian, J.E., Marzeion, B., 2021. On the attribution of industrial-era glacier mass loss to anthropogenic climate change. The Cryosphere 15, 1889–1905.

Rolstad, C., Haug, T., Denby, B., 2009. Spatially integrated geodetic glacier mass balance and its uncertainty based on geostatistical analysis: Application to the western svartisen ice cap, norway. J. Glaciol. 55, 666–680.

Rosen, J., 2021. Shifting ground. Science 371, 876–880.

Rosen, P.A., Hensley, S., Joughin, I.R., Li, F.K., Madsen, S.N., Rodriguez, E., Goldstein, R.M., 2000. Synthetic aperture radar interferometry. Proc. IEEE 88, 333–382.

Rott, H., Scheiblauer, S., Wuite, J., Krieger, L., Floricioiu, D., Rizzoli, P., Libert, L., Nagler, T., 2021. Penetration of interferometric radar signals in antarctic snow. The Cryosphere 15, 4399–4419.

Rounce, D., Maussion, F., Hock, R., Hugonnet, R., Kochtitzky, W., Huss, M., Berthier, E., Brinkerhoff, D., Compagno, L., Copland, L., Farinotti, D., Menounos, B., McNabb, R., in review. Global glacier change in the 21st century: every tenth of a degree temperature increase matters.

Rounce, D.R., Hock, R., McNabb, R.W., Millan, R., Sommer, C., Braun, M.H., Malz, P., Maussion, F., Mouginot, J., Seehaus, T.C., Shean, D.E., 2021. Distributed global debris thickness estimates reveal debris significantly impacts glacier mass balance. Geophys. Res. Lett. 48, e2020GL091311.

Rounce, D.R., Khurana, T., Short, M.B., Hock, R., Shean, D.E., Brinkerhoff, D.J., 2020. Quantifying parameter uncertainty in a large-scale glacier evolution model using bayesian inference: application to high mountain asia. J. Glaciol. 66, 175–187.

Rupnik, E., Daakir, M., Pierrot Deseilligny, M., 2017. MicMac – a free, open-source solution for photogrammetry. Open Geospatial Data, Software and Standards 2, 14.

Scherler, D., Wulf, H., Gorelick, N., 2018. Global assessment of supraglacial Debris-Cover extents. Geophys. Res. Lett. , 798–805.

Schiefer, E., Menounos, B., Wheate, R., 2007. Recent volume loss of british columbian glaciers, canada. Geophys. Res. Lett. .

Schiefer, E., Menounos, B., Wheate, R., 2008. An inventory and morphometric analysis of british columbia glaciers, canada. J. Glaciol. 54, 551–560.

Schöner, W., Koch, R., Matulla, C., Marty, C., Tilg, A.M., 2019. Spatiotemporal patterns of snow depth within the Swiss-Austrian alps for the past half century (1961 to 2012) and linkages to climate change. Int. J. Climatol. 39, 1589–1603.

Schwitter, M.P., Raymond, C.F., 1993. Changes in the longitudinal profiles of glaciers during advance and retreat. J. Glaciol. 39, 582–590.

Seehaus, T., Morgenshtern, V.I., Hübner, F., Bänsch, E., Braun, M.H., 2020. Novel techniques for void filling in glacier elevation change data sets. Remote Sensing 12, 3917.

Shaw, T.E., Ulloa, G., Farías-Barahona, D., Fernandez, R., Lattus, J.M., McPhee, J., 2021. Glacier albedo reduction and drought effects in the extratropical andes, 1986–2020. J. Glaciol. 67, 158–169.

Shean, D., Bhushan, S., Lilien, D., Knuth, F., Schwat, E., Meyer, J., Sharp, M., Hu, M., 2021. dshean/demcoreg: v1.1.0.

Shean, D., Lilien, D., 2019. dshean/pygeotools: Zenodo DOI release.

Shean, D.E., Alexandrov, O., Moratto, Z.M., Smith, B.E., Joughin, I.R., Porter, C., Morin, P., 2016. An automated, open-source pipeline for mass production of digital elevation models (DEMs) from very-high-resolution commercial stereo satellite imagery. ISPRS J. Photogramm. Remote Sens. 116, 101–117.

Shean, D.E., Bhushan, S., Montesano, P., Rounce, D.R., Arendt, A., Osmanoglu, B., 2020. A systematic, regional assessment of high mountain asia glacier mass balance. Front. Earth Sci. 7, 435.

Shekhar, P., Csathó, B., Schenk, T., Roberts, C., Patra, A.K., 2021. ALPS: A unified framework for modeling time series of land ice changes. IEEE Trans. Geosci. Remote Sens. 59, 6466–6481.

Shugar, D.H., Burr, A., Haritashya, U.K., Kargel, J.S., Watson, C.S., Kennedy, M.C., Bevington, A.R., Betts, R.A., Harrison, S., Strattman, K., 2020. Rapid worldwide growth of glacial lakes since 1990. Nat. Clim. Chang. .

Shugar, D.H., Jacquemart, M., Shean, D., Bhushan, S., Upadhyay, K., Sattar, A., Schwanghart, W., McBride, S., de Vries, M.V.W., Mergili, M., Emmer, A., Deschamps-Berger, C., McDonnell, M., Bhambri, R., Allen, S., Berthier, E., Carrivick, J.L., Clague, J.J., Dokukin, M., Dunning, S.A., Frey, H., Gascoin, S., Haritashya, U.K., Huggel, C., Kääb, A., Kargel, J.S., Kavanaugh, J.L., Lacroix, P., Petley, D., Rupper, S., Azam, M.F., Cook, S.J., Dimri, A.P., Eriksson, M., Farinotti, D., Fiddes, J., Gnyawali, K.R., Harrison, S., Jha, M., Koppes, M., Kumar, A., Leinss, S., Majeed, U., Mal, S., Muhuri, A., Noetzli, J., Paul, F., Rashid, I., Sain, K., Steiner, J., Ugalde, F., Watson, C.S., Westoby, M.J., 2021. A massive rock and ice avalanche caused the 2021 disaster at chamoli, indian himalaya. Science 373, 300–306.

Snow, A.D., Brochart, D., Raspaud, M., Bell, R., Chegini, T., Amici, A., Braun, R., Annex, A., Hoese, D., Bunt, F., Hamman, J., Zehner, M., Cordeiro, M., RichardScottOZ, Henderson, S., Miller, S., The Gitter Badger, Augspurger, T., pmallas, 2022. corteva/rioxarray: 0.10.1 release.

Sommer, C., Malz, P., Seehaus, T.C., Lippl, S., Zemp, M., Braun, M.H., 2020. Rapid glacier retreat and downwasting throughout the european alps in the early 21st century. Nat. Commun. 11, 3209.

Stevens, N.F., Garbeil, H., Mouginis-Mark, P.J., 2004. NASA EOS terra ASTER: Volcanic topographic mapping and capability. Remote Sens. Environ. 90, 405–414.

Stoffel, M., Huggel, C., 2012. Effects of climate change on mass movements in mountain environments. Progress in Physical Geography: Earth and Environment 36, 421–439.

Stuart-Smith, R.F., Roe, G.H., Li, S., Allen, M.R., 2021. Increased outburst flood hazard from lake palcacocha due to human-induced glacier retreat. Nat. Geosci. 14, 85–90.

Surazakov, A.B., Aizen, V.B., 2006. Estimating volume change of mountain glaciers using SRTM and map-based topographic data. IEEE Trans. Geosci. Remote Sens. 44, 2991–2995.

Tachikawa, T., Hato, M., Kaku, M., Iwasaki, A., 2011. Characteristics of ASTER GDEM version 2, in: 2011 IEEE International Geoscience and Remote Sensing Symposium, pp. 3657–3660.

Tao, C.V., Hu, Y., 2001. A comprehensive study of the rational function model for photogrammetric processing. Photogramm. Eng. Remote Sens. .

Taud, H., Parrot, J.F., Alvarez, R., 1999. DEM generation by contour line dilation. Comput. Geosci. 25, 775–783.

Teshima, Y., Iwasaki, A., 2008. Correction of attitude fluctuation of terra spacecraft using ASTER/SWIR imagery with parallax observation. IEEE Trans. Geosci. Remote Sens. 46, 222–227.

Tsuchida, S., Yamamoto, H., Kouyama, T., Obata, K., Sakuma, F., Tachikawa, T., Kamei, A., Arai, K., Czapla-Myers, J.S., Biggar, S.F., Thome, K.J., 2020. Radiometric degradation curves for the ASTER VNIR processing using vicarious and lunar calibrations. Remote Sensing 12, 427.

Uuemaa, E., Ahi, S., Montibeller, B., Muru, M., Kmoch, A., 2020. Vertical accuracy of freely available global digital elevation models (ASTER, AW3D30, MERIT, TanDEM-X, SRTM, and NASADEM). Remote Sensing 12, 3482.

Vaughan, D.G., Comiso, J.C., Allison, I., Carrasco, J., Kaser, G., Kwok, R., Mote, P., Murray, T., Paul, F., Ren, J., Rignot, E., Solomina, O., Steffen, K., Zhang, T., 2013. Observations: Cryosphere, in: Stocker, T.F., D. Qin, G.-K. Plattner, M. Tignor, S.K. Allen, J. Boschung, A. Nauels, Y. Xia, V. Bex and P.M. Midgley (eds.) (Ed.), Climate Change 2013: The Physical Science Basis. Contribution of Working Group I to the Fifth Assessment Report of the Intergovernmental Panel on Climate Change. Cambridge University Press, Cambridge, United Kingdom and New York, NY, USA.

Veh, G., Korup, O., von Specht, S., Roessner, S., Walz, A., 2019. Unchanged frequency of moraine-dammed glacial lake outburst floods in the himalaya. Nat. Clim. Chang. 9, 379–383.

Veh, G., Korup, O., Walz, A., 2020. Hazard from himalayan glacier lake outburst floods. Proc. Natl. Acad. Sci. U. S. A. 117, 907–912.

Veh, G., Lützow, N., Kharlamova, V., Petrakov, D., Hugonnet, R., Korup, O., 2022. Trends, breaks, and biases in the frequency of reported glacier lake outburst floods. Earths Future .

Veh, G., Lützow, N., Tamm, J., , Hugonnet, R., Geertsema, M., Clague, J.J., Korup, O., in review. Smaller and earlier outbursts from ice-dammed lakes with ongoing glacier decay.

Velicogna, I., Mohajerani, Y., Geruo, A., Landerer, F., Mouginot, J., Noel, B., Rignot, E., Sutterley, T., Broeke, M., Wessem, M., Wiese, D., 2020. Continuity of ice sheet mass loss in greenland and antarctica from the GRACE and GRACE Follow-On missions. Geophys. Res. Lett. 47, L11501.

Vidaller, I., Revuelto, J., Izagirre, E., Rojas-Heredia, F., Alonso-González, E., Gascoin, S., René, P., Berthier, E., Rico, I., Moreno, A., Serrano, E., Serreta, A., López-Moreno, J.I., 2021. Toward an ice-free mountain range: Demise of pyrenean glaciers during 2011–2020. Geophys. Res. Lett. 48.

Vincent, C., Fischer, A., Mayer, C., Bauder, A., Galos, S.P., Funk, M., Thibert, E., Six, D., Braun, L., Huss, M., 2017. Common climatic signal from glaciers in the european alps over the last 50 years. Geophys. Res. Lett. 44, 1376–1383.

Vionnet, V., Marsh, C.B., Menounos, B., Gascoin, S., Wayand, N.E., Shea, J., Mukherjee, K., Pomeroy, J.W., 2021. Multi-scale snowdrift-permitting modelling of mountain snowpack. The Cryosphere 15, 743–769.

Viviroli, D., Kummu, M., Meybeck, M., Kallio, M., Wada, Y., 2020. Increasing dependence of lowland populations on mountain water resources. Nature Sustainability 3, 917–928.

Vörösmarty, C.J., McIntyre, P.B., Gessner, M.O., Dudgeon, D., Prusevich, A., Green, P., Glidden, S., Bunn, S.E., Sullivan, C.A., Liermann, C.R., Davies, P.M., 2010. Global threats to human water security and river biodiversity. Nature 467, 555–561.

Wales, D.J., Doye, J.P.K., 1997. Global optimization by Basin-Hopping and the lowest energy structures of Lennard-Jones clusters containing up to 110 atoms. J. Phys. Chem. A 101, 5111–5116.

Walker, A.S., 1995. Analogue, analytical and digital photogrammetric workstations: Practical investigations of peformance. The Photogrammetric Record .

Wang, F., Bamber, J.L., Cheng, X., 2015. Accuracy and performance of CryoSat-2 SARIn mode data over antarctica. IEEE Geoscience and Remote Sensing Letters 12, 1516–1520.

Wang, G., Gertner, G.Z., Fang, S., Anderson, A.B., 2005. A methodology for spatial uncertainty analysis of remote sensing and GIS products. Photogrammetric Engineering & Remote Sensing 71, 1423–1432.

Wang, J., Song, C., Reager, J.T., Yao, F., Famiglietti, J.S., Sheng, Y., MacDonald, G.M., Brun, F., Schmied, H.M., Marston, R.A., Wada, Y., 2018. Recent global decline in endorheic basin water storages. Nat. Geosci. 11, 926–932.

WCRP Global Sea Level Budget Group, 2018. Global sea-level budget 1993–present. Earth Syst. Sci. Data 10, 1551–1590.

Webster, R., Oliver, M.A., 2007. Geostatistics for Environmental Scientists. 2nd ed., Wiley.

Wechsler, S.P., 2003. Perceptions of digital elevation model uncertainty by DEM users. URISA Journal 15, 57–64.

Wechsler, S.P., 2007. Uncertainties associated with digital elevation models for hydrologic applications: a review. Hydrol. Earth Syst. Sci. 11, 1481–1500.

Weiss, A., 2001. Topographic position and landforms analysis, in: Poster presentation, ESRI user conference, San Diego, CA, jennessent.com.

Welty, E., Zemp, M., Navarro, F., Huss, M., Fürst, J.J., Gärtner-Roer, I., Landmann, J., Machguth, H., Naegeli, K., Andreassen, L.M., Farinotti, D., Li, H., GlaThiDa Contributors, 2020. Worldwide version-controlled database of glacier thickness observations. Earth Syst. Sci. Data 12, 3039–3055.

Weng, Q., 2002. Quantifying uncertainty of digital elevation models derived from topographic maps, in: Advances in Spatial Data Handling, Springer Berlin Heidelberg. pp. 403–418.

WGMS, 2019. Fluctuations of glaciers database.

Williams, C.K.I., Rasmussen, C.E., 2006. Gaussian processes for machine learning. volume 2. MIT press Cambridge, MA.

Willis, M.J., Melkonian, A.K., Pritchard, M.E., Rivera, A., 2012. Ice loss from the southern patagonian ice field, south america, between 2000 and 2012. Geophys. Res. Lett. 39.

Wilson, M.F.J., O'Connell, B., Brown, C., Guinan, J.C., Grehan, A.J., 2007. Multiscale terrain analysis of multibeam bathymetry data for habitat mapping on the continental slope. Mar. Geod. 30, 3–35.

Wouters, B., Gardner, A.S., Moholdt, G., 2019. Global glacier mass loss during the GRACE satellite mission (2002-2016). Front. Earth Sci. 7, 535.

xdem contributors, 2021. xdem.

Xiong, Z., 2021. Large-scale snow depth mapping from moderate resolution satellite imagery.

Zdanowicz, C., Krümmel, E.M., Lean, D., Poulain, A.J., Yumvihoze, E., Chen, J., Hintelmann, H., 2013. Accumulation, storage and release of atmospheric mercury in a glaciated arctic catchment, baffin island, canada. Geochim. Cosmochim. Acta 107, 316–335.

Zemp, M., Huss, M., Thibert, E., Eckert, N., McNabb, R., Huber, J., Barandun, M., Machguth, H., Nussbaumer, S.U., Gärtner-Roer, I., Thomson, L., Paul, F., Maussion, F., Kutuzov, S., Cogley, J.G., 2019. Global glacier mass changes and their contributions to sea-level rise from 1961 to 2016. Nature 568, 382–386.

Zemp, M., Thibert, E., Huss, M., Stumm, D., Denby, C.R., Nuth, C., Nussbaumer, S.U., Moholdt, G., 2013. Reanalysing glacier mass balance measurement series. The Cryosphere , 1227–1245.

Zevenbergen, L.W., Thorne, C.R., 1987. Quantitative analysis of land surface topography. Earth Surf. Processes Landforms 12, 47–56.

Zhao, J., Floricioiu, D., 2017. The penetration effects on TanDEM-X elevation using the GNSS and laser altimetry measurements in antarctica. Int. Arch. Photogramm. Remote Sens. Spatial Inf. Sci. XLII-2/W7, 1593–1600.

Zheng, Z., Kirchner, P.B., Bales, R.C., 2016. Topographic and vegetation effects on snow accumulation in the southern sierra nevada: a statistical summary from lidar data. The Cryosphere 10, 257–269.

Zink, M., Moreira, A., Hajnsek, I., Rizzoli, P., Bachmann, M., Kahle, R., Fritz, T., Huber, M., Krieger, G., Lachaise, M., Martone, M., Maurer, E., Wessel, B., 2021. TanDEM-X: 10 years of formation flying bistatic SAR interferometry. IEEE Journal of Selected Topics in Applied Earth Observations and Remote Sensing 14, 3546–3565.